

Conformal Electromagnetic Wave Propagation using Primal Mimetic Finite Elements

Dissertation

zur Erlangung des akademischen Grades

Doktoringenieur (Dr.-Ing.)

vorgelegt der
Fakultät für Elektrotechnik und Informationstechnik der
Technischen Universität Ilmenau

von
M. Sc. Thomas Reum
geboren am 10.06.1988 in Schmalkalden

Gutachter:

Herr Univ.-Prof. Dr.-Ing. habil. Hannes Töpfer (Betreuer)

Technische Universität Ilmenau

Herr Prof. Dr.-Ing. Jürgen Ulm

Hochschule Heilbronn Campus-Künzelsau

Herr Dr. Dr.-Ing. Ralf Theo Jacobs

Technische Universität Dresden

Datum der Einreichung: 03.09.2021

Datum der wissenschaftlichen Aussprache: 02.06.2022

DOI: 10.22032/dbt.52276

URN: urn:nbn:de:gbv:ilm1-2022000212

Pflichterfüllung reicht nicht, man muß Freude an seiner Arbeit haben.

- Jonathan Adolf Wilhelm Zenneck

Fulfillment of duty is not enough, one has to enjoy one's work.

- English translation

Abstract

Electromagnetic wave propagation provides the physical basis for countless applications in various subjects of today's world. In order to model spatial scenarios, the continuous space must be converted to an appropriate computational domain. Ordinarily discretized models – which are based on distinct quantities – consider the connection between field variables by relations which are represented by partial differential equations. To reproduce mathematical relationships between dependent variables in a convenient manner, hypercomplex number systems build a suitable alternative framework. This approach aims to incorporate certain system properties and covers, in addition to the modeling of field problems where all variables are present, also simplified models.

To provide a competitive alternative to the ordinary numerical handling of electromagnetic fields in an observation-based way, the electric and magnetic field of electromagnetic wave fields is understood as only one combined field variable embedded in the function space. This procedure is intuitive since both fields occur together in electrodynamics and are directly measurable.

The focus of this thesis is twofold. On the one side, a reformulated Maxwell system is broadly investigated in a metric-free environment by the use of the so-called "bicomplex approach". On the other side, a possible numerical implementation concerning the Finite Element Method is evaluated in a modern way by the use of discrete exterior calculus with focus on accuracy matters.

It is shown on several analytical formulations and numerical examples, whether the used alternative concept is advantageous or not in the given cases. This is accompanied by a quaternionization of the de Rham cohomology. In this context, different relations to ordinary electromagnetic field variables are turned out where appropriate. Regarding the numerical accuracy evaluation, it is demonstrated that the presented approach yields a higher exactness in general when comparing it to formulations which are based on the Helmholtz equation.

This thesis contributes generalized hypercomplex alternative representations of ordinary electrodynamic expressions to the topic of wave propagation. By the use of a direct formulation of the electric field in conjunction with the magnetic field, the computational accuracy of boundary value problems is improved. In order to achieve this increase of accuracy, a profound investigation and an appropriate enhancement of the de Rham cohomology is proposed.

Although essential context is provided and many recommendations on further reading are given, general knowledge on discrete exterior calculus is advised.

Zusammenfassung

Elektromagnetische Wellenausbreitung bildet die physikalische Grundlage für unzählige Anwendungen in verschiedenen Bereichen der heutigen Welt. Um räumliche Szenarien zu modellieren, muss der kontinuierliche Raum in geeigneter Weise in ein Rechengebiet umgewandelt werden. Üblich diskretisierte Modelle – welche auf verschiedenen Größen beruhen – berücksichtigen die Beziehungen zwischen Feldvariablen mittels Relationen, welche durch partielle Differentialgleichungen repräsentiert werden. Um mathematische Beziehungen zwischen abhängigen Variablen in zweckdienlicher Art nachzubilden, schaffen hyperkomplexe Zahlensysteme ein passendes alternatives Rahmenwerk. Dieser Ansatz bezweckt das Einbinden bestimmter Systemeigenschaften und umfasst zusätzlich zur Modellierung von Feldproblemen, bei denen alle Variablen vorkommen, auch vereinfachte Modelle.

Um eine wettbewerbsfähige Alternative zur üblichen numerischen Behandlung elektromagnetischer Felder in beobachtungsorientierter Weise darzubieten, wird das elektrische und magnetische Feld elektromagnetischer Wellenfelder als eine zusammengefasste Feldgröße, eingebettet im Funktionenraum, verstanden. Dieses Vorgehen ist intuitiv, da beide Felder in der Elektrodynamik gemeinsam auftreten und direkt messbar sind.

Der Schwerpunkt dieser Arbeit ist in zwei Ziele untergliedert. Auf der einen Seite wird ein umformuliertes Maxwell-System in einer metrikfreien Umgebung mittels dem sogenannten „bikomplexen Ansatz“ umfassend untersucht. Auf der anderen Seite wird eine mögliche numerische Implementierung hinsichtlich der Finite-Elemente-Methode auf modernem Wege durch Nutzung der diskreten äußeren Analysis mit Fokus auf Genauigkeitsbelange bewertet.

Anhand einiger analytischer Formulierungen und numerischer Beispiele wird gezeigt, ob das genutzte alternative Konzept in den jeweiligen Fällen vorteilhaft ist oder nicht. Dies wird von einer Quaternionisierung der de Rham-Kohomologie begleitet. In diesem Zusammenhang werden Beziehungen zu gewöhnlichen elektromagnetischen Feldgrößen an geeigneten Stellen aufgezeigt. Hinsichtlich der numerischen Genauigkeitsbewertung wird demonstriert, dass der vorgelegte Ansatz grundsätzlich eine höhere Exaktheit zeigt, wenn man ihn mit Formulierungen vergleicht, welche auf der Helmholtz-Gleichung beruhen.

Diese Dissertation trägt eine generalisierte hyperkomplexe alternative Darstellung von gewöhnlichen elektrodynamischen Ausdrucksweisen zum Themengebiet der Wellenausbreitung bei. Durch die Nutzung einer direkten Formulierung des elektrischen Feldes in Verbindung mit dem magnetischen Feld wird die Rechengenauigkeit von Randwertproblemen erhöht. Um diese Genauigkeitserhöhung zu erreichen, wird eine fundierte Untersuchung und eine geeignete Erweiterung der de Rham-Kohomologie unterbreitet.

Wenngleich wesentlicher Kontext bereitgestellt wird und viele Empfehlungen hinsichtlich weiterführender Literatur gegeben werden, sind generelle Kenntnisse über diskrete äußere Analysis angeraten.

Acknowledgments

At first, I would like to especially thank my supervisor Univ.-Prof. Dr.-Ing. habil. Hannes Töpfer, who provided me with the time, the place and the surroundings for my research and findings. His encouraging empathic attitude and professional knowledge was essential for my progress and well-being.

I would also like to thank my colleague and tutor Prof. Dr.-Ing. habil. Marek Ziółkowski for the stimulating discussions. He supported me many times on difficult points. Also the pleasant mutual dealings have to be emphasized.

I would like to extend my thanks to Prof. Dr.-Ing. Jürgen Ulm for the pleasant atmosphere at our meetings as well as for being a reviewer of the present thesis.

Further thanks are issued to Dr. Dr.-Ing. Ralf Theo Jacobs for being a reviewer of this thesis.

Thanks to Dr.-Ing. Michael Naß, who endowed me with the opportunity to work in a self-organized manner and provided me with interesting and interdisciplinary tasks.

Special thanks are dedicated to Prof. em. Dr.-Ing. Reinhold Michelfeit, who motivated me in the preceding years of study to the topics of high-frequency engineering and especially advanced electromagnetics.

I like to thank my colleagues M.S. Frank Feldhoff and M.S. Maximilian Krey for the fruitful discussions on various subjects.

Lastly, I would like to thank my mother Heidrun, who is always there for me and supported me over all the years in various ways.

Nomenclature

Abbreviation	
pD	p -dimensional
ABC	Absorbing boundary condition
ANA	Analytical
BEM	Boundary Element Method
BVP	Boundary value problem
CONV	Convection matrix in FEM
CPU	Central processing unit
DEC	Discrete exterior calculus
DGFEM	Discontinuous Galerkin FEM
DOF	Degree of freedom
EM	Electromagnetic
FEM	Finite Element Method
FEM BC	Bicomplex FEM
FEM C	Complex FEM
GA	Geometric algebra (\equiv Clifford algebra)
GaLS	Galerkin / Least-Squares
GR	General relativity
LHS	Left-hand side
MASS	Mass matrix in FEM
MoM	Method of Moments
MST	Maxwell stress tensor
NRMSE	Normalized root mean square error
PDE	Partial differential equation
RAM	Random access memory
RHS	Right-hand side
S-parameter	Scattering parameter

SI	International system of units
SRC	Sommerfeld radiation condition
STIFF	Stiffness matrix in FEM
SUPG	Streamline Upwind Petrov Galerkin
TEM	Transversal electromagnetic
TE	Transversal electric
TM	Transversal magnetic
USFEM	Unusual Stabilized FEM

General framework

Symbol	Meaning	Unit
\mathbb{BC}	Set of bicomplex numbers	
\mathbb{BC}_6	Non-Abelian bicomplex group	
c	Speed of light	m s^{-1}
\mathbb{C}	Set of complex numbers	
\mathbf{Cl}_3	Specific Clifford algebra	
$\det(\dots)$	Determinant of a matrix	
\dim	Dimension of a quotient space	
f	Frequency	Hz
\underline{f}	General bicomplex number	
$F(\dots)$	Functional	
g_{pq}	Metric coefficients of the metric tensor	
$[g_{pq}]$	Matrix representation of the metric tensor	
\mathbb{H}	Set of quaternions	
$\mathbf{H}(\Omega)$	Generalized Hilbert space for vector fields	
$\mathbf{H}(\text{curl}; \Omega)$	Sobolev space for edge approximation	
$\mathbf{H}(\text{div}; \Omega)$	Sobolev space for face approximation	
$H^1(\Omega)$	Sobolev space for nodal approximation	
i	Spatial / vectorial imaginary unit	
image	Image of a differential operator	
j	Temporal / scalar imaginary unit	
k	Third imaginary unit of quaternions	
K	Number of dimensions of a vector space	
${}^p K(\Omega)$	Space of p -chains	

$L^2(\Omega)$	Lebesgue space of square-integrable functions	
$\mathbf{L}^2(\Omega)$	Vectorial Lebesgue space	
null space	Null space of a differential operator	
\mathbb{O}	Set of octonions	
p	Number of an object's / a space's dimensions	
\mathbb{Q}_8	Non-Abelian quaternion group	
\mathbb{R}	Set of real numbers	
$r_{1\dots 4}$	General real numbers	
\mathbb{R}^p	Euclidean p -manifold / real spatial space	
\mathbb{S}	Set of sedenions	
$\text{SO}(3)$	Specific rotation group	
t	Time	s
$[T]$	Transformation matrix	
$u_{x/y}, v_{x/y}$	Terms of Vekua equation system	
ω	Angular frequency	s^{-1}
Ω	Manifold / computational domain	
∂_t	Temporal derivative	
\dots	Complex-valued quantity	
\dots	Bicomplex-valued quantity	
\dots	Discretized objects	
\dots^*	Ordinary complex conjugation regarding j	
\dots^+	Complex conjugation regarding i	
\dots'	Derivative with respect to the subscript	
\dots^A	Adjoint of a matrix	
\dots^T	Transpose of a matrix	
$ \dots _j$	Bicomplex modulus regarding j	
$ \dots _i$	Bicomplex modulus regarding i	
\in	Set membership	
\subset	Proper subset	
$\xrightarrow{\sim}$	Isomorphic	
\exists	Existential quantifier	
\oplus	Direct sum of two spaces	

Vector calculus

Symbol	Meaning	Unit
a	Width of a rectangular waveguide	m
A	General surface / wave port surface	m^2
$\underline{\mathbf{A}}$	Magnetic vector potential	V s m^{-1}
$\mathbf{a}, \mathbf{b}, \mathbf{c}, \mathbf{d}$	Generalized vector quantities	
a^p, b^q	Generalized contravariant vector components	
b	Height of a rectangular waveguide	m
$\underline{\mathbf{B}}$	Magnetic flux density	V s m^{-2}
$\text{CG}(\Omega)$	Curly gradient space	
$\underline{\mathbf{D}}$	Electric flux density	A s m^{-2}
$d\mathbf{A}$	Differential surface element	m^2
ds	Differential line element	m
dx, dy, dz	Cartesian coordinate differentials	m
$\underline{\mathbf{E}}$	Electric field strength	V m^{-1}
\mathbf{e}, \mathbf{h}	Generalized complex-valued vector quantities	
E_0	Electric field strength given at boundaries of the computational domain	V m^{-1}
$\underline{\mathbf{E}}_c / \underline{\mathbf{E}}_i / \underline{\mathbf{E}}_1$	Computed / reflected / excited electric field strength on waveguide port	V m^{-1}
$\underline{\mathbf{E}}_{\text{cum}} / \underline{\mathbf{H}}_{\text{cum}}$	Resulting wave field portion	$\text{V m}^{-1} / \text{A m}^{-1}$
\mathbf{E}_{im}	Imaginary part of electric field strength	V m^{-1}
$\underline{\mathbf{E}}_{\text{inc}} / \underline{\mathbf{H}}_{\text{inc}}$	Incident wave field portion	$\text{V m}^{-1} / \text{A m}^{-1}$
$\mathbf{e}_{p/q}$	Generalized covariant base vectors	
\mathbf{E}_{re}	Real part of electric field strength	V m^{-1}
$\underline{\mathbf{E}}_{\text{ref}} / \underline{\mathbf{H}}_{\text{ref}}$	Reflected wave field portion	$\text{V m}^{-1} / \text{A m}^{-1}$
$\underline{\mathbf{E}}_{\text{tra}} / \underline{\mathbf{H}}_{\text{tra}}$	Transmitted wave field portion	$\text{V m}^{-1} / \text{A m}^{-1}$
$\mathbf{e}_x, \mathbf{e}_y, \mathbf{e}_z$	Cartesian unit vectors	
$\underline{\underline{\mathbf{f}}}$	Generalized bicomplex-valued vector quantity	
$\underline{\underline{\mathbf{F}}}$	Electromagnetic field strength	$\sqrt{\text{V A}} \text{ m}^{-1}$
$\underline{\underline{\mathbf{F}}}_{+/-}$	Electromagnetic field strength with indicated propagation direction	$\sqrt{\text{V A}} \text{ m}^{-1}$
$\text{FK}(\Omega)$	Fluxless knot space	
$\text{G}(\Omega)$	Gradient space	
$\text{GG}(\Omega)$	Grounded gradient space	

h	Strain (relative change of length caused by gravitational waves)	
$\underline{\mathbf{H}}$	Magnetic field strength	A m ⁻¹
H_0	Magnetic field strength given at boundaries of the computational domain	A m ⁻¹
\mathbf{H}_{im}	Imaginary part of magnetic field strength	A m ⁻¹
\mathbf{H}_{re}	Real part of magnetic field strength	A m ⁻¹
HG (Ω)	Harmonic gradient space	
HK (Ω)	Harmonic knot space	
$\underline{\mathbf{J}}$	Electric current density	A m ⁻²
k	Wave number	m ⁻¹
\mathbf{k}	Wave vector	m ⁻¹
K (Ω)	Knot space	
L	Absolute length of an object	m
\mathbf{n}	Surface normal	
P	Wave port excitation power	W
$q(x)$	Function q of x	
$Q(c) / Q(d)$	Antiderivative Q of $q(x)$ at the point c / d	
r	Distance from the origin	m
$[r_{\text{bc}}]$	Matrix describing the reflection coefficient of a bicomplex wave field	
r_e / r_m	Reflection coefficient of electric / magnetic field strength	
s	Generalized boundary contour of a surface / integration line	m
$\underline{\mathbf{S}}$	Poynting vector	V A m ⁻²
$[S]_{2 \times 2}$	Scattering matrix of a two port network	
\underline{S}_{mn}	Scattering parameter from port n to port m	
$[t_{\text{bc}}]$	Matrix describing the transmission coefficient of a bicomplex wave field	
t_e / t_m	Transmission coefficient of electric / magnetic field strength	
\underline{U}	Electric voltage	V
V	Volume	m ³
VF (Ω)	Vector space	
v_{phase}	Phase velocity of an electromagnetic wave	m s ⁻¹

W_{EM}	Energy content of an electromagnetic wave	W s
X	Arbitrary complex subspace	
$x^{p/q}$	Generalized contravariant coordinates	m
x, y, z	Global Cartesian coordinates	m
Y	Arbitrary complex auxiliary subspace	
Z	General wave impedance	V A ⁻¹
Z_0	Wave impedance of free space	V A ⁻¹
$\underline{z}_{1/2}\{\dots\}$	Outer real / imaginary part of an electromagnetic wave field	
β	Wave number in propagation direction	m ⁻¹
ΔL	Absolute change of length of an object	m
ε	Electric permittivity	A s V ⁻¹ m ⁻¹
ε_r	Relative electric permittivity	
λ	General wavelength	m
λ_0	Wavelength of free space	m
μ	Magnetic permeability	V s A ⁻¹ m ⁻¹
μ_r	Relative magnetic permeability	
ξ, η, ζ	Local coordinates	
$\tau_{e/m}$	Electric / magnetic part of MST	V A s m ⁻³
$\underline{\phi}$	Electric scalar potential	V
ψ	Generalized scalar quantity	
$ \dots $	Magnitude of a vector quantity	
∇	Nabla / gradient operator	
$\nabla \times$	Curl operator	
$\nabla \cdot$	Divergence operator	
\times	Cross product	
\cdot	Dot product	
\otimes	Tensor product	
\circ	Hadamard product	

Exterior calculus

Symbol	Meaning	Unit
${}^1\mathcal{A}$	Differential magnetic vector potential	V s
${}^2\mathcal{B}$	Differential magnetic flux density	V s
$b_p(\Omega)$	p -th Betti number of Ω	
${}^1\mathcal{CG}(\Omega)$	Differential curly gradient space	
${}^2\mathcal{D}$	Differential electric flux density	A s
${}^p d$	Exterior derivative / coboundary operator	
\mathbb{D}_p	Matrix representation of ${}^p d$	
${}^1\mathcal{E}$	Differential electric field strength	V
${}^1\mathcal{F}$	Differential electromagnetic field strength	$\sqrt{V A}$
${}^1\mathcal{FK}(\Omega)$	Differential fluxless knot space	
${}^1\mathcal{H}$	Differential magnetic field strength	A
H_{dR}^p	p -th de Rham cohomology group	
\mathcal{I}_p	Whitney interpolation map for p -cochains	
${}^2\mathcal{J}$	Differential electric current density	A
\mathbb{M}_p	Matrix representation of Hodge star operator (the order ${}^p \dots$ is not explicitly given)	
$n_p(\Omega)$	Number of p -entities contained in the computational domain	
\mathcal{P}_p	De Rham projection map for vector fields	
${}^2\mathcal{S}$	Differential Poynting vector	V A
${}^1\mathcal{X}$	Differential subspace	
${}^1\mathcal{Y}$	Differential auxiliary subspace	
${}^3\mathcal{Q}$	Differential space charge density	A s
${}^p\sigma$	p -chain	
${}^0\phi$	Differential electric scalar potential	V
$\chi(\Omega)$	Euler / Euler-Poincaré characteristic	
${}^p\psi$	p -form	
${}^p\partial$	Boundary operator	
★	Hodge star operator	
\flat	Flat operator	
‡	Sharp operator	
\wedge	Wedge product	

Finite element framework

Symbol	Meaning	Unit
$[A], [B], [C], [D]$	Submatrices of FEM matrices	
C^p	Primal p -cochain space	
\overline{C}^p	Dual p -cochain space	
D_a	Damköhler number	
$\ e\ _{\text{BWD}}^{\%}$	Backward NRMSE	%
$\ e\ _{\text{FWD}}^{\%}$	Forward NRMSE	%
E_u / F_u	Unknown coefficients of electric / electromagnetic field strength	See <u>E</u> / <u>F</u>
\mathbf{e}_u	Unit vectors of basis functions	
h_{ele}	Size of a one-dimensional finite element	m
$[J]$	Jacobian matrix	
l_x, l_y, l_z	Global lengths of linear brick element	m
M / N	Number of interpolated points / unknowns	
M_{ij}, S_{ij}, C_{ij}	Entries of FEM matrices	
n	One-dimensional discretization parameter	
N_p^e	Edge shape function p of a finite element	
q	Three-dimensional discretization parameter	
sign_p	Local sign of the edge shape function p	
T_{CPU}	Calculation time / CPU runtime	s
x_m, y_m, z_m	Global center coordinates of a finite element	m
$\alpha_{\dots}, f_{ij}, b_{\dots}^e, c_{\dots}^e, d_{\dots}^e$	Auxiliary parameters for FEM matrix entries	
τ_{STAB}	Stabilization factor	
$\varphi / \underline{\varphi}$	Scalar / vectorial shape functions of FEM	
$\underline{\varphi}_u / \underline{\underline{\varphi}}_u$	Scalar / vectorial basis functions of FEM	
$\underline{\varphi}_w / \underline{\underline{\varphi}}_w$	Scalar / vectorial test functions of FEM	
$\underline{\psi}$	Differential shape functions of FEM	
$\underline{\psi}_u$	Differential basis functions of FEM	
$\underline{\psi}_w$	Differential test functions of FEM	
\dots^e	Locally described object	

Contents

Abstract	iii
Zusammenfassung	v
Acknowledgment	vii
Nomenclature	ix
Contents	xvii
List of Figures	xix
List of Tables	xxv
1 Introduction	1
1.1 Motivation	2
1.2 Thesis Aims	3
1.3 Thesis Layout	3
2 Formulations in Electrodynamics	5
2.1 Bicomplex Number System	6
2.1.1 Quick Survey of Modeling	6
2.1.2 Several Geometrical Interpretations	8
2.2 Homogeneous Material Distribution	13
2.2.1 Complex-valued Helmholtz Equation	13
2.2.2 Bicomplex-valued Pseudo-Helmholtz Equation	14
2.3 Inhomogeneous Material Distribution and Variational Approaches	15
2.3.1 Complex-valued Helmholtz Equation	15
2.3.2 Bicomplex-valued Pseudo-Helmholtz Equation	18
2.4 Discrete Exterior Calculus	20
2.4.1 From Covariant Vector Calculus to Contravariant Cohomology	24
2.4.2 Quaternionized De Rham Cohomology	28
2.4.3 Whitney Forms and Spurious Solutions	32
2.4.4 Generalized Conformal Discretization of the Pseudo-Helmholtz Equation	34
2.4.5 Generalized Conformal Discretization of the Helmholtz Equation	37
2.4.6 Topological Concept	38
2.4.7 Topological Study	42
2.5 Relation to Potential Formulations	48
2.6 Derivation of Wave Quantities from the Bicomplex-valued Field	51
2.6.1 Energy Content	51

2.6.2	Poynting Vector	52
2.6.3	Scattering Parameters	53
2.6.4	Maxwell Stress Tensor	54
2.7	Wave Splitting of the Bicomplex-valued Field	55
2.8	Conjecture Regarding Gravitational Waves	59
3	Finite Element Method	61
3.1	Concept of Finite Element Modeling	62
3.2	State-of-the-Art in the Finite Element Method	64
3.3	Variational Formulations for 3D-FEM	65
3.4	Implementation Specifics of Bicomplex p D-FEM	66
3.5	Associated Matrices for Elements in 3D-FEM	68
3.6	Absorbing Boundary Conditions for 3D-FEM	72
4	Simulation Studies	77
4.1	One-dimensional Finite Element Method	78
4.1.1	Discussion of the Same Discretization Parameter n	78
4.1.2	Discussion of the Same Accuracy of L^2 -norm	81
4.2	Three-dimensional Finite Element Method	82
4.2.1	TEM-wave in Free Space	82
4.2.2	TEM-wave Passing a Dielectric Step	87
4.2.3	TE ₁₀ -wave in a Hollow Rectangular Waveguide	93
4.2.4	TE ₁₀ -wave in a Partially Dielectric-filled Rectangular Waveguide	97
4.2.5	Qualitative Hodge Decomposition	101
4.3	Findings of the Simulation Studies	103
4.3.1	Discussion of the Electric Field's Real Part	103
4.3.2	Discussion of the Poynting Vector Field's Real Part	104
5	Summary and Outlook	107
5.1	Summary	107
5.2	Outlook and Future Work	108
	Appendices	109
A	Green's Identities	109
B	Vector Identities and Integral Theorems	110
C	Derivation of Tetrahedral Shape Functions	111
D	Classification of Pseudo-Helmholtz Equation	115
E	Stabilization Technique for Bicomplex-valued Convection-Reaction Equation	116
F	Guideline to Stabilize the Bicomplex FEM	116
	Bibliography	119

List of Figures

2.1	Fundamental strategy of designing mathematical representations of physical phenomena. In section 2.5, this will be done exemplarily in order to gauge potentials.	5
2.2	Plane wave propagation in three-dimensional space.	6
2.3	Interpretation of bicomplex electromagnetism in the function space. Note that no classification on embedding this structure is arranged so far.	7
2.4	Overview of compared approaches to determine EM wave fields.	7
2.5	Cayley graph of the non-Abelian group \mathbb{BC}_6 .	8
2.6	Clifford algebra as the generic term of several hypercomplex number systems.	10
2.7	Tensor product of several algebras to form the desired algebra \mathbb{BC} for the calculation approach described in this thesis.	10
2.8	Rotated coordinate systems due to spatial mapping as an alternative to embedding the bicomplex structure in the function space.	11
2.9	Construction of the trivector (pseudoscalar) by combining lower-dimensional multivectors in Clifford algebra \mathbf{Cl}_3 through the wedge product.	12
2.10	Near-field to far-field conversion of a vertically polarized electric dipole described by the two time-harmonic Maxwell's equations (2.7a, 2.7b), exemplified on the positive z -axis.	14
2.11	Manifold Ω as a subset of the real spatial space \mathbb{R}^p .	20
2.12	Base vectors of the two concepts vector calculus and exterior calculus.	20
2.13	A two-dimensional manifold (depicted in gray) with a two-dimensional tangential space (drawn in orange) to demonstrate a possible orientation of an exemplary differential 1-form.	21
2.14	Tonti diagram of three-dimensional electromagnetism.	23
2.15	Contravariant (depicted in orange) and invariant (colored in black) quantities of the ordinary covariant vector calculus are presented on the top. The middle shows a simple analytical example, where furthermore a covariant (drawn in blue) quantity arises. Exemplary, the two possibilities of implementing a changed measure (caused e.g. by a deformation of the metric) of Ω are shown on the bottom. The bottom left shows the common way in physics called change of base vectors (here: other units), whereas the bottom right shows changed coordinates (changed length scale of the integration line) by keeping the base vectors constant.	25
2.16	Example of integration in vector (left) and exterior (right) calculus: Integration of a vector over a line s from point a to point b described by the differential line element ds , which may be expressed as the sum of a point-wise scalar product. This can be thought in exterior calculus as integration of a 1-form (differential form, a covector which lives in the cotangential space) over a 1-chain (geometric entity, a vector which lives in the tangential space, defined on Ω).	26
2.17	Matrix representation of the metric expressed in (2.38).	27

2.18	The DEC-de Rham diagram for contractible domains in \mathbb{R}^3 is drawn on the top, where the relevant part is marked in red. After elimination of the constitutive equations on the bottom left, the blue lines depict Faraday's law, whereas the violet lines show Ampère's law. The orange lines indicate the Helmholtz equation for the electric field. The bicomplex-valued Pseudo-Helmholtz equation is drawn on the bottom right, which is called "quaternionized de Rham cohomology" throughout this thesis, since the p -forms are bicomplex- instead of complex-valued.	28
2.19	Principle of the mimetic operators \mathcal{P}_p and \mathcal{I}_p demonstrated on a brick element. They transform between the continuous and discrete setting. On the continuous left side, the color gradient indicates the intensity of an x -oriented vectorial function with reference to a line, which varies over z . On the discretized right side, only the four nonzero edge values are highlighted.	30
2.20	Geometric relations of several important operators and operations. Left side: correlation of the Hodge operator to the wedge product. Right side: transformation of the differential bicomplex EM field (drawn in blue) by the exterior derivative and the Hodge operator in accordance to the bottom right of Fig. 2.18.	31
2.21	Possible p -forms defined on a three-dimensional manifold. For oriented p -forms, an arrow indicates the orientation.	32
2.22	Principle of tangential continuity of a normalized field intensity using Whitney edge DOFs (1-forms, compare to the second illustration from the left in Fig. 2.21) on brick elements. See Fig. 2.23 below for the three-dimensional behavior of one edge-based shape function's normalized field intensity.	32
2.23	Exemplary normalized field intensity of a Whitney edge-based shape function in the unit cell of the brick element. It shows the 3D alternative of Fig. 2.22 on one finite element.	33
2.24	Exemplary normalized field intensity of a Whitney nodal-based shape function in the unit cell of a brick element.	33
2.25	Primal and dual brick mesh. The circumcenters of the primal mesh are used as nodes for the dual mesh. For relations between the discretized primal C^1 and dual \bar{C}^1 cochain spaces, see Fig. 2.18 in section 2.4.2.	34
2.26	Connection of the bicomplex-valued EM field between vector calculus and exterior calculus by the use of the metric tensor, valid for generalized coordinates in GR. Contravariant quantities are illustrated in orange, whereas covariant quantities are depicted in blue. Invariant quantities as well as operations are drawn in black. The explicit contravariant metric tensor is marked in violet, whereas the implicit covariant metric tensor is encoded in the scalar product of the covariant base vectors. Regarding the effect of the musical operators, see Fig. 2.27.	35
2.27	The musical operators (drawn in violet) map as isomorphisms between the cotangential space (placed on the top) and the tangential space (placed on the bottom). Applied to the bicomplex-formulated EM field components on the left, they map between co- and contravariant vector field components, respectively. On the right, they map between contra- and covariant coordinate differentials, respectively. For an overview of the used quantities, see Fig. 2.26.	36
2.28	Solution spaces of the two used kinds of PDEs.	37
2.29	Duality in different spaces: Cochain and chain complex on the manifold Ω . The generalized Stokes' theorem (2.34) further shows this duality between cohomology and homology.	38
2.30	Possible embeddings of bicomplex EM wave field.	40

2.31	Intuitive process to determine the first Betti number $b_1(\Omega)$ for H_{dR}^1 . Since an arbitrary 1-circle overdetermines the system, it has to be subtracted as $b_1(\Omega) = 6 - 1 = 5$. This is summarized for various H_{dR}^p and two kinds of entities in Fig. 2.35, see later on section 2.4.7.	41
2.32	Visualization of the field pattern of the five mutually orthogonal subspaces presented in (2.59) which are the result of the Hodge decomposition theorem applied to an arbitrary vector field in 3D space. The definitions on the right are oriented on [87], where the fields are illustrated on the manifolds: torus, ball, or a ball with a three-dimensional hole in its center. Here, these manifolds are adapted to several brick meshes, which have the same topology, respectively.	43
2.33	The two types of Hodge decomposition split an arbitrary three-dimensional vector field into two or five mutually orthogonal subspaces, respectively, which is shown on the top (a). Concerning the bicomplex PDE on the top, this allows for C^1 on the left and C^2 on the right in (b), respectively. C^1 and C^2 lead to conformal Whitney 1- and 2-forms, respectively, with associated DOFs in (c). Through the use of divergence-free brick elements, only C^1 is of interest.	44
2.34	Process of wave propagation in a waveguide with assigned field types of Hodge decomposition by assuming a trivial topology of Ω . The EM field components which are included in the bicomplex PDE's solution space and the corresponding field types are marked in red. In blue, the two possibilities of generating the first bicomplex component (electric field) are indicated.	45
2.35	Euler / Euler-Poincaré characteristics and related Betti numbers of the tetrahedral and brick element in the respective de Rham cohomology group. On the first row, (2.55) is used and on the second row, (2.56) is utilized, respectively, which yield the same number.	47
2.36	Principle of gauging potentials and relation of physical and mathematical field quantities as one possibility of designing mathematical representations of physical phenomena shown in Fig. 2.1, see Chapter 2. See Fig. 2.14 in section 2.4 for the connection of these quantities in the language of differential forms.	48
2.37	Relation of the bicomplex-formulated Maxwell system to the ordinary potential formulation.	49
2.38	Several wave quantities derived from the bicomplex-valued field. The following definitions of the quantities on the left need the embedding of the bicomplex structure in the homology / tangential space (see the right side of Fig. 2.30), whereas the quantities on the right are valid for both the cohomology and the homology approach.	51
2.39	Bicomplex wave components of (2.89) for waves incoming from the positive and negative z -direction by assuming wave splitting at a step of material properties.	57
2.40	Equivalence of derivation of the bicomplex equation (2.6) in section 2.2.2 and the process of wave splitting discussed here. (a) shows the impedance normalization without formatting, (b) the generation of the bicomplex format and (c) the diagonalization procedure.	57
2.41	Principle of a bicomplex SRC (2.91) concerning the qualitative energy content W_{EM} of incoming and outgoing waves generated by finite sources. (a) shows the two possible asymptotical behaviors of waves, and (b) describes the situation after the application of the SRC in an infinite domain, a radially asymptotic decrease of the EM field strength is obvious.	58

2.42	Proposed topological concept of both electromagnetic and gravitational waves. The chain complex (defined on the tangential space) is the observer’s reference frame.	60
3.1	Principle of handling BVPs defined on the manifold Ω using brick finite elements.	61
3.2	Progressive deduction of the used three-dimensional FEM variants.	62
3.3	Intuitive interpretation of FEM linear equation system. In (a), the full linear equation system is shown. For both FEM C and FEM BC, it is represented by real numbers, see later on Fig.3.4 in section 3.4. Below in (b), the integration procedure building the real-valued first entry of the RHS vector (drawn in orange) is implemented by matrix multiplication of the first row of the real-valued system matrix and the real-valued vector containing the DOFs (drawn in violet).	63
3.4	Real matrix representation of the bicomplex system matrix, which is included in the FEM linear equation system in Fig.3.3, see section 3.1.	66
3.5	Workflow of bicomplex FEM.	67
3.6	Relation of three-dimensional bicomplex FEM to the de Rham complex presented in Fig.2.18 by consideration of the respective function spaces.	67
3.7	Atlas of two types of finite elements defined on the real spatial space \mathbb{R}^3	68
3.8	DOF numbering of the brick element where edges (drawn in black) and nodes (highlighted in red) are considered.	69
3.9	Relation of the terms of the variational formulations / weak form of the bicomplex PDE (3.6) and the Helmholtz PDEs (3.5) to their matrix representation in FEM based on Whitney edge DOFs.	70
3.10	Direct manipulation of the 3D MASS matrix instead of a separate 2D handling of the port plane (the gray face in front) to consider ABCs for FEM BC and FEM C. To implement the reflecting wave portion, the part of the tensor product which involves edges 10 and 11 in the gray drawn port plane A is manipulated.	74
4.1	Electric field E_{re} distribution calculated by means of various methods, where $n = 3$ is used in FEM.	78
4.2	Forward NRMSE $\ e\ _{\text{FWD}}^{\%}$ for selected values of the discretization parameter n	79
4.3	Backward NRMSE $\ e\ _{\text{BWD}}^{\%}$ for selected values of the discretization parameter n	80
4.4	Calculation time T_{CPU} for selected values of the discretization parameter n	80
4.5	Detail of Fig.4.2 (see section 4.1.1) to indicate a comparable accuracy of L^2 -norm for the two distinct bicomplex and complex FEM models.	81
4.6	Investigated numerical examples using the three-dimensional bicomplex FEM.	82
4.7	Analytical solution of the real electric field concerning TEM-wave propagation.	83
4.8	Field evaluation points (11x11x21) for TEM-wave propagation in Ω	83
4.9	Field pattern of TEM-wave propagating over z , arbitrary placed in the xy -plane.	83
4.10	q -times refined regular brick meshes of Ω with a length of 1 m.	84
4.11	$\ e\ _{\text{FWD}}^{\%}$ of $E_{re, \text{FEM}}$ for wave propagation on the meshes in Fig.4.10, calculated at the points shown in Fig.4.8.	84
4.12	q -times refined irregular brick meshes of Ω with a length of 1 m.	85
4.13	$\ e\ _{\text{FWD}}^{\%}$ of $E_{re, \text{FEM}}$ for wave propagation on the meshes in Fig.4.12, calculated on the points shown in Fig.4.8.	85
4.14	Longitudinal cross section of the dielectric step.	87
4.15	Wave behavior on a dielectric / permeable interface.	87

4.16	Process of consecutive bicomplex FEM depicted on the half space TEM-wave problem. On the material step, the wave splitting occurs. FEM 1 calculates the initial Dirichlet boundary conditions of FEM 2, whereas on the respective other side of Ω , ABCs are invoked.	88
4.17	Handling of the interface at the dielectric step among the process of consecutive bicomplex FEM shown in Fig. 4.16 exemplified on a TE_{10} -wave guided by a rectangular waveguide. In [250], the presented impedance relations are derived in detail.	89
4.18	Propagation behavior of the transversal field intensities of the TEM-wave which passes a material step.	90
4.19	Real \underline{E}_y of FEM C for inhomogeneous material distribution and $q = 3$, numerical dispersion is evident on the right.	91
4.20	Real \underline{E}_y of consecutive FEM BC for inhomogeneous material distribution and $q = 3$, no numerical dispersion is apparent.	91
4.21	$\ e\ _{\text{FWD}}^{\%}$ of $E_{\text{re, FEM}}$ for wave propagation on regular brick meshes based on Fig. 4.10, calculated at the interpolation points (11x11x101).	92
4.22	Sketch of the hollow rectangular waveguide.	93
4.23	Analytical solution of the real electric field concerning TE_{10} -mode propagation evaluated at the center line of Ω	94
4.24	Mesh for TE_{10} -mode propagation in Ω	94
4.25	Field pattern for TE_{10} -mode propagation in Ω	94
4.26	Real part of \underline{E}_y calculated by FEM C, numerical dispersion is evident (displacement at the left side).	95
4.27	Real part of \underline{E}_y calculated by FEM BC, no numerical dispersion is apparent.	95
4.28	Sketch of the partially dielectric-filled rectangular waveguide.	97
4.29	Propagation behavior of transversal field intensities of the partially dielectric-filled waveguide.	98
4.30	Propagation behavior of the longitudinal field intensity of the partially dielectric-filled waveguide.	98
4.31	Real \underline{E}_y of the partially filled waveguide, calculated by FEM C.	99
4.32	Real \underline{E}_y of the partially filled waveguide, calculated by FEM BC.	99
4.33	Field pattern for TE_{10} -wave propagation in Ω of the partially filled waveguide.	100
4.34	Qualitative EM field pattern of the fundamental modes in free space on the left and in a rectangular waveguide on the right, respectively. In (a), the electric field is illustrated, (b) shows the magnetic field. The decrease of EM field intensity over the distance is not visualized.	102
4.35	Postprocessing quantities for error investigation of the 3D benchmark problems.	103
B1	Visualization of integral theorems as important special cases of the generalized Stokes' theorem (2.34), see section 2.4. Note that on the top right, the orange-colored objects indicate the surface of the manifold $\partial\Omega$, whereas on the top left, the volume Ω is highlighted.	110
C1	DOF numbering of tetrahedral element, where edges and nodes are considered.	111

List of Tables

2.1	Selected features of the de Rham cohomology compared to vector calculus. . . .	27
2.2	Wording of the discrete p -dimensional setting in DEC.	29
3.1	ABCs for the benchmark problems investigated in section 4.2. For both versions of FEM BC, an additional factor is necessary, which is described subsequently. . . .	75
4.1	Memory requirements for two specific values of the discretization parameter n . . .	81
4.2	Mesh Properties for regular / irregular meshes.	86
4.3	Time consumption for regular / irregular meshes.	86
4.4	Memory requirements for regular / irregular meshes.	86
4.5	Time consumption regarding several values of q for inhomogeneous material distribution.	92
4.6	Error Comparison of $\ e\ _{\text{FWD}}^{\%}$ regarding the respective real field component of the TE ₁₀ -mode.	96
4.7	Time / Memory requirements for TE ₁₀ -mode.	96
4.8	Error Comparison of $\ e\ _{\text{FWD}}^{\%}$ regarding the respective real field component of TE ₁₀ -mode in partially filled waveguide.	100
4.9	Time / Memory requirements for TE ₁₀ -wave in partially filled waveguide.	100
4.10	Qualitative Hodge decomposition of the EM fields (calculated in the 3D topologically trivial numerical examples) into curly gradients and fluxless knots, respectively. . .	101
4.11	Error improvements of FEM BC compared to FEM C regarding the real electric field. The numerator shows the accuracy of FEM C and the denominator shows that of FEM BC.	103
4.12	Error improvements of FEM BC concerning the real Poynting vector field \mathbf{S} . . .	105

The advent of wireless communication, which started at the end of the forelast century, is nowadays more relevant than never before. Various applications are developed for data transmission, where the physical foundation are the transmission of electromagnetic (EM) waves. Novel technologies lead to progressively increasing data rates of these systems. To predict the application-specific behavior of EM wave fields, a variety of numerical methods has been established. It is usual in EM modeling to use a reduced or rather adapted set of Maxwell's equations, which fits well the physical relations. Following this idea, the authors D. E. Fernandes et al. use a quasistatic approximation to describe the scattering of EM waves by metamaterials in [89]. Another example is presented by S. Schoos and O. Schwanitz, where a quasistationary approach is used to simulate complicated filter chokes in [217]. The "bicomplex" EM wave field concept – discussed throughout this thesis – aims at the same objective of adaptation.

The system of bicomplex numbers is a kind of hypercomplex number system. Applied to the EM field, bicomplex numbers are obtained by combining the usual complex numbers (time-harmonic behavior) with quaternions in a way that both the outer real and imaginary part (which are connected in a quaternionic sense) contains an ordinary complex number, respectively. H. Anastassiou et al. have shown a lower order alternative to the Helmholtz equation in [7], which aims to describe EM wave propagation analytically in a bicomplex manner. Since the term "bicomplex" used there describes the desired construct of subspaces which contain their own subspaces in an appropriate manner, this term is also used in this thesis. Note that in this context, the ordinary temporal complex subspaces is based on a distinct meaning compared to the spatial complex connection of the EM field as indicated above.

Historically, bicomplex numbers emerged in the 19th century. C. Segre proposed a bicomplex algebra as an extension of the complex algebra in [222]. Nowadays, the variety of hypercomplex number systems is versatile. The bicomplex-formulated electromagnetism reproduces directly the physical occurrence of wave propagation, where the electric and magnetic fields arise together. In contrast to common approaches like the use of potentials, no auxiliary quantities are involved.

The calculation of the EM field in the high-frequency regime is traditionally based on real- or complex-valued Helmholtz equations, which can be numerically evaluated for complicated domains using for instance the Finite Element Method (FEM). To give a practice-oriented introduction and possibly evaluate some advantages of this approach, different EM wave propagation problems will be examined using FEM. For the above-mentioned approach based on Helmholtz equations, one has to perform the FEM twice in order to compute the full EM field, or calculate one field quantity from the other one. A common alternative is to solve for the magnetic vector potential and deduce the EM field from this auxiliary quantity. The bicomplex FEM offers in this sense an advantage compared to this approach: the whole EM field is calculated in only one step by

using a combined field quantity, which is constructed due to symmetry considerations of the Maxwell system. This is possible, since the bicomplex field maintains intrinsically the connection between the electric field and the magnetic field in one function space instead of using two distinct function spaces. A fundamental difference between the common and the proposed FEM approach is, that the bicomplex-valued FEM is based on a 1st-order partial differential equation (PDE), whereas the complex-valued FEM is based on a 2nd-order PDE. Nowadays, FEM models are often advantageously enhanced by the use of discrete exterior calculus (DEC) in a way that physical quantities are discretized in a conformal manner. This technique will be adequately adopted.

The advantage of the presented approach in comparison to classical DEC is a conformal approximation of both the electric and magnetic field quantity at the same spatial locations without the use of a dual mesh. As FEM is widespread in computational engineering, the proposed hypercomplex approach can be applied to reformulate a multitude of tasks, which requires the numerical handling of PDEs either in electromagnetics as well as in engineering and research areas beyond, such as fluid dynamics. Caused by the needed high degree of freedom concerning the software implementation, all calculations are carried out using MATLAB[®] [166] environment.

1.1 Motivation

It is not usual to use bicomplex numbers in the context of computational electromagnetism. Therefore, a comprehensive investigation is appropriate. Since the origin of spurious modes concerning FEM lies in special properties of numerical differential operators, a profound investigation using the cohomology approach instead of only using standard nodal finite elements is suitable. This cohomology approach is based on the differential structure of the manifold instead of the Euclidean metric (as usual in vector calculus). Therefore, the coordinate system can be arbitrarily chosen. Several practical EM wave propagation problems will be reviewed in terms of the de Rham cohomology, which is convenient for three-dimensional (3D) electromagnetism. The cohomology theory is presented with focus on the discrete setting by the use of differential forms. This procedure allows for a bicomplex description of the EM field, which explains well the beneficial conformal discretization of observable field quantities. The conformal approximation of both the electric and the magnetic field together through the use of a specific geometric algebra – which is implemented using DEC as a mimetic method – fundamentally increases the accuracy of calculations overall. This leads among other things to a conformally approximated Poynting vector. An essential motivation for the use of bicomplex calculus is furthermore to calculate the electric and magnetic field with merely one calculation procedure instead of successive conversions.

An advantage concerning differentiation of differential forms compared to vectors in general is, that the covariant derivative is replaced by the exterior derivative, since differential forms are independent of the underlying metric. Therewith, no consideration of the product rule as for the covariant derivative is necessary for problems which involve non-Euclidean metrics, like curved space of general relativity. Also special relativity (which is a special case of general relativity since it is based on one possible metric, called the Minkowski metric¹) is addressed briefly in terms of the bicomplex-expressed EM field's relation to potential formulations.

To be compatible with general relativity, the usage of the metric tensor (which is commonly used to describe general spaces which differ from the Euclidean space) is extensively outlined to allow for an incorporation of an arbitrarily desired metric. Since both the electric and the magnetic field are subspaces of the bicomplex-valued EM field, the presented investigations cover in addition these ordinary complex-valued field quantities in a profound manner.

¹This metric describes the Minkowski space-time, see e.g. [172] for a geometric interpretation.

1.2 Thesis Aims

To return to the basic idea of formulating EM wave propagation in different frameworks such as vector calculus or geometric algebra, the present thesis aims at discussing fundamental relationships. Often, they are not common in today's modern course schemes on universities and, therefore, they will be outlined in adequate detail. By applying these ideas in a suitable finite element framework, practical wave propagation problems are investigated and numerical results are compared to common state-of-the-art approaches to achieve an improved numerical accuracy as a general aim. Therein, this thesis aims at a more theoretical and a mainly practical aspect, respectively, as to

- complexifying or rather quaternionizing the de Rham cohomology in an appropriate way to conformally represent the physical behavior of the recasted EM field.
- reveal an implementation of the bicomplex-valued EM field's associated PDEs in the finite element environment. Through an alternative field representation, it is possible to reformulate other physical quantities derived from this recasted EM field.

1.3 Thesis Layout

In this thesis, the starting point are the time-harmonic Maxwell's equations. For a more fundamental step, see for example the investigation of R. Feynman, which is discussed in [80].

At first, an in-depth discussion on several hypercomplex formulations concerning electrodynamics is outlined in Chapter 2, including the proposed bicomplex-formulated electromagnetism. To consider independence of metric, a general definition of the proposed concept is desired. This definition will be achieved through a quaternionization of the de Rham cohomology. Invariants of the corresponding cohomology groups are further investigated to cover e.g. mesh deformation, while the connectivity of the mesh remains the same. A reformulation of different EM field quantities is done, which is followed by several important fundamentals with regard to the intended implementation of three-dimensional EM wave propagation in a finite element environment.

Chapter 3 shows the addressed implementation in a finite element environment, where special features are pointed out. A specific FEM formulation based on the problem class of EM wave fields is presented, which is constructed using DEC instead of vector calculus. The underlying PDEs and their corresponding weak forms / variational formulations used for the numerical implementation are derived in detail. Since only field problems with non-vanishing rotation are investigated, edge-based finite elements are chosen. They refer to a conformal discretization of the EM field.

In Chapter 4, the numerical investigation of the implemented features in FEM is started in one dimension. Several practical examples in 3D are presented afterwards accompanied by a topological classification of the calculated wave fields. Both the electric field and active power flow are discussed in terms of the numerical accuracy improvement achieved for benchmark problems.

This thesis is concluded by a summary and extended by an outlook in Chapter 5.

The following remarks are given as an advice for reading the present thesis. Note in general that indices which refer to a context are written in standard font, whereas indices which act as running indices or indicate variables are noted in italic font. Without loss of generality, Cartesian coordinates (with only one exception at the end of section 2.7 in terms of the Sommerfeld radiation condition) are assumed when vector calculus is used. The used level of applied mathematics aims at addressing mainly engineers and avoids, therefore, formal details where appropriate.

CHAPTER 2

Formulations in Electrodynamics

In all times in history, mathematical models are build up to represent natural phenomena in an appropriate manner. An example of this idea is the range of possibilities to gauge the magnetic vector potential \underline{A} . As a starting point, Fig. 2.1 shows the fundamental strategy of designing artificial mathematical representations of natural observable physical phenomena.

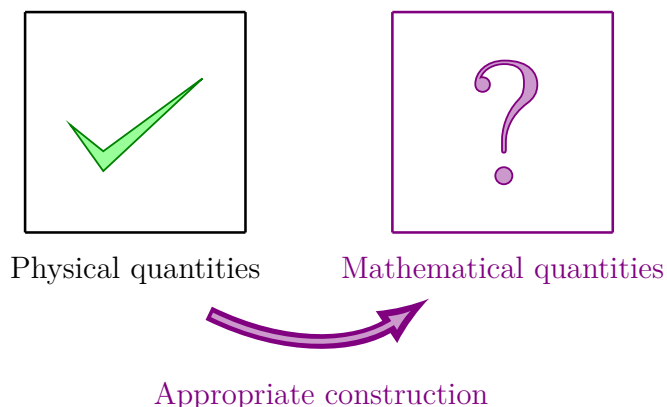


Figure 2.1 Fundamental strategy of designing mathematical representations of physical phenomena. In section 2.5, this will be done exemplarily in order to gauge potentials.

In general, only physical observations are fixed and the mathematical framework behind this can be arbitrarily chosen. The bicomplex number system can be chosen in order to mathematically represent physical observations in an equivalent way, as e.g. the complex number system, since the electric field \underline{E} and the magnetic field \underline{H} appear together in EM waves.

In 1873, J. C. Maxwell stated that "Physical vector quantities may be divided into two classes, in one of which the quantity is defined with reference to a line, while in the other the quantity is defined with reference to an area." [167] Following this idea in the scope of the de Rham cohomology, the electric and magnetic field are conformally expressed by 1-forms in the context of exterior calculus and discretized using Whitney edge elements in the FEM environment. Contrary, the electric displacement current, the magnetic flux density and the current density would be conformally expressed by 2-forms and discretized by the use of Whitney face elements in FEM. The mentioned Whitney forms are a today's standard in FEM, for an overview and an application to eddy current problems, see e.g. [32].

A brief explanation of bicomplex-formulated electrodynamics using different approaches is presented in section 2.1. After deriving all relevant equations in sections 2.2 and 2.3, the

topological discussion on cohomology and homology started from vector calculus creates a profound understanding of embedding possibilities of bicomplex electrodynamics, which is discussed especially in section 2.4. The relation to commonly used potential formulations is clarified in section 2.5, which is followed by reformulations of several physical quantities based on the bicomplex EM field in section 2.6. Due to the properties of the bicomplex EM formulation, an appropriate wave splitting is investigated in section 2.7. Conclusively, a possible generalization of the proposed approach to considering gravitational waves is discussed in section 2.8.

2.1 Bicomplex Number System

As stated in Chapter 1, the variety and possible uses of today's hypercomplex number systems are versatile. A general overview of quaternionic systems is discussed in [110], regarding an assessment of fundamentals and EM applications of quaternions, see e.g. [221]. A deep mathematical discussion of the bicomplex calculus and related context is given in [164]. Regarding several applications of bicomplex calculus to quantum mechanics, see e.g. [204] or [205]. To return to the subject of electromagnetism, analytical investigations of transversal electromagnetic (TEM) wave propagation can be found e.g. in [3], [4], [7] and [161].

The basic definitions and properties of bicomplex calculus presented in [7] are used throughout this work. As a first step, the electromagnetic field is illustrated for time-harmonic TEM-waves. Figure 2.2 shows well-known plane wave propagation in z -direction observed in 3D space.

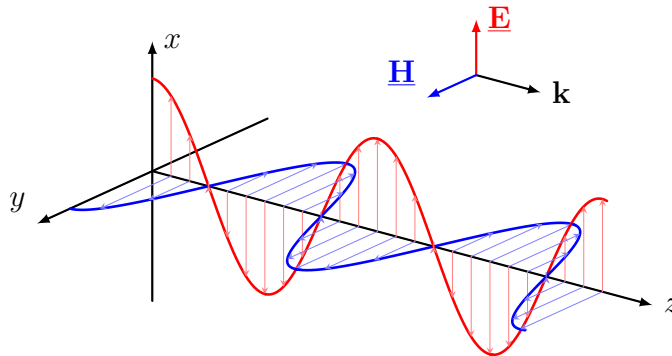


Figure 2.2 Plane wave propagation in three-dimensional space.

There are many conceivable ways to describe the relations of the field quantities electric field $\underline{\mathbf{E}}$ and magnetic field $\underline{\mathbf{H}}$, associated with the wave vector \mathbf{k} to each other. The following sections cover reinterpretations of bicomplex electromagnetism in several ways through the geometrical meaning of the imaginary units in the area of differential geometry.

2.1.1 Quick Survey of Modeling

Following [201, 202], bicomplex numbers $\underline{\underline{f}}$ are constructed from real numbers $r_{1\dots 4}$ in a way that

$$\underline{\underline{f}} = (r_1 + j r_2) + i (r_3 + j r_4), \quad (2.1)$$

where j is the inner imaginary unit of the bicomplex number and i is the outer one. An elaborated mathematical investigation of bicomplex calculus is described in [164], which examines, among other things, the possible conjugations of bicomplex numbers, the bicomplex derivative or the

bicomplex exponential function. Using structure (2.1), the electric and magnetic field can be intuitively gathered into a normalized bicomplex EM field $\underline{\underline{\mathbf{F}}}$ as

$$\underline{\underline{\mathbf{F}}} = \frac{1}{\sqrt{Z}} (\mathbf{E}_{\text{re}} + j \mathbf{E}_{\text{im}}) + i\sqrt{Z} (\mathbf{H}_{\text{re}} + j \mathbf{H}_{\text{im}}), \quad (2.2)$$

where $\underline{\mathbf{E}} = \mathbf{E}_{\text{re}} + j \mathbf{E}_{\text{im}}$ is the ordinary complex-valued electric field, $\underline{\mathbf{H}} = \mathbf{H}_{\text{re}} + j \mathbf{H}_{\text{im}}$ is the magnetic field and $Z = \sqrt{\mu/\varepsilon} = Z_0 \sqrt{\mu_r/\varepsilon_r}$ is the wave impedance. This wave impedance is determined by the material properties permeability μ and permittivity ε and differs – depending on the corresponding relative quantities μ_r and ε_r – from the wave impedance of free space Z_0 . Figure 2.3 shows an interpretation of the bicomplex EM field $\underline{\underline{\mathbf{F}}}$ concerning $\underline{\mathbf{E}}$ and $\underline{\mathbf{H}}$ in the function space.

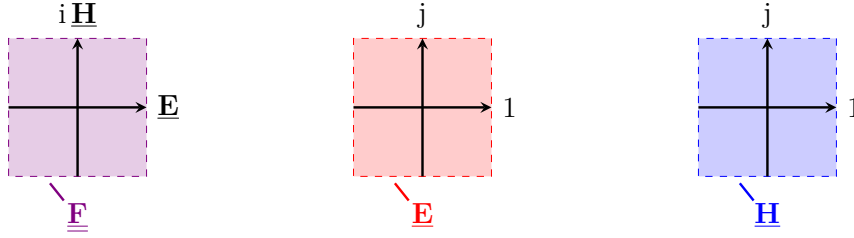


Figure 2.3 Interpretation of bicomplex electromagnetism in the function space. Note that no classification on embedding this structure is arranged so far.

On the left of Fig. 2.3, the outer imaginary unit i connects the electric field $\underline{\mathbf{E}}$ with the magnetic field $\underline{\mathbf{H}}$. On the middle and on the right, the complex-valued subspaces are shown, which can be interpreted as ordinary complex vector amplitudes. The left one might be intuitively interpreted as the transversal field of a plane TEM-wave (see Fig. 2.2 in section 2.1), the propagation direction of the wave points to the observer, who is located at the wave front.

A common way to computationally determine EM wave fields is the use of a Helmholtz equation, sketched on the right in Fig. 2.4.

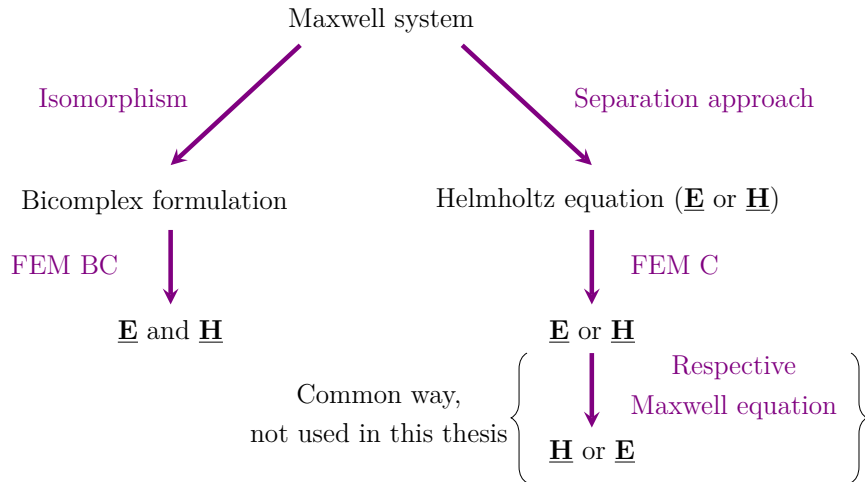


Figure 2.4 Overview of compared approaches to determine EM wave fields.

Contrary, the left side shows the bicomplex formulation, where both $\underline{\mathbf{E}}$ and $\underline{\mathbf{H}}$ are calculated together. Especially how to handle the isomorphism¹ on the top left and furthermore the FEM

¹Regarding vector spaces, isomorphisms are invertible linear maps / transformations [20], or, in other words, invertible mappings between vector spaces, where vector addition and scalar multiplication are preserved.

implementation of the bicomplex FEM (FEM BC) is content of this thesis. For both complex FEM (FEM C) calculations of $\underline{\mathbf{E}}$ and $\underline{\mathbf{H}}$ of the numerical examples in Chapter 4, separate Helmholtz equations are used, respectively. This is further reasoned through the numerical disadvantage in FEM that a derivation of $\underline{\mathbf{H}}$ from $\underline{\mathbf{E}}$ – or vice versa – reduces the order of shape functions by one (since a spatial derivative is necessary), which lowers the accuracy in general.

2.1.2 Several Geometrical Interpretations

In this section, several approaches will be applied to describe the bicomplex formulation of the EM field. After starting with the conversion rules using group theory, the combination of hypercomplex algebras is investigated with respect to historical developments. Then, the spatial relationships in the Euclidean space \mathbb{R}^3 will be clarified and alternatively expressed through a rotation matrix. Furthermore, an interpretation through rotation groups will be considered.

According to [54], the quaternion symbols i, j, k represent rectangular versors; that is to say, they are operations which will turn an object through a right angle in the three coordinate planes respectively. It is a common way to interpret the three imaginary units i, j and k of quaternions in a spatial manner. In this thesis, the bicomplex formulation of the EM field is considered. For this, the interpretation of the imaginary units is done in a different manner. To represent time-harmonic Maxwell’s equations, the inner imaginary unit j is used to represent the temporal behavior, which is assumed to be time-harmonic. Merely the outer imaginary unit i is used as a spatial one, which represents the orthogonality between the electric and the magnetic field. One can conceive that by assuming only one specific time step, the temporal dependency vanishes and the bicomplex system can be understood like a complex system, which describes spatial relations.

A first approach originates from the context of group theory. Here, the proposed non-Abelian² group \mathbb{BC}_6 describes the conversion rules of multiplication well. It has got the 6 quaternions $\{1, i, j, -1, -i, -j\}$ and is noncommutative, which leads to $ij = -ji$. The first quaternion 1 is the neutral element of multiplication, the fourth quaternion -1 yields a sign inversion. To investigate the relationship between the two imaginary units, the possible products of them are of interest. A Cayley graph³ of the group \mathbb{BC}_6 can be obtained by simply replacing the third imaginary unit k in the Cayley graph of the commonly used quaternion group \mathbb{Q}_8 ⁴ by ij , see Fig. 2.5 below.

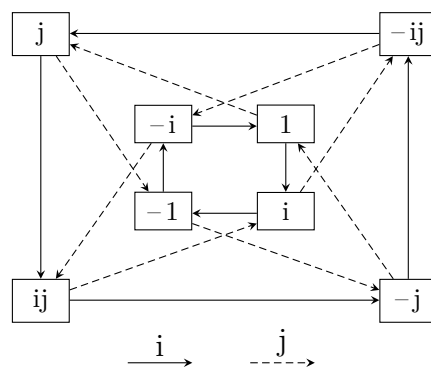


Figure 2.5 Cayley graph of the non-Abelian group \mathbb{BC}_6 .

²Abelian groups are commutative, which means that the result of a group operation based on two group elements is independent of their order.

³Cayley graphs were first considered for finite groups by A. Cayley [43] and encode the abstract structure of a group.

⁴This group has got 8 quaternions $\{1, i, j, k, -1, -i, -j, -k\}$ and is also noncommutative, see e.g. [116] for details.

Figure 2.5 shows all possible left multiplications, which are fundamental for the derivation of the bicomplex-valued Pseudo-Helmholtz equation (2.6) discussed later on in section 2.2.2. This graph is an intuitive alternative to the multiplication table, which will not be presented here.

J. C. Maxwell revealed the difference in the interpretation of the relation of physical quantities to directions in space [167]. Two ways of interrelating physical quantities to a coordinate system are usual. The first one, which is provided by R. Descartes⁵, is the association of physical quantities by the axes of the coordinate system as absolute directions, called Cartesian coordinates. The second one, which is done by W. R. Hamilton, is to fix in mind a point in space and describe the physical quantities as a magnitude and angles relative to that point. This is done by the quaternions, which are established in [113]. Various examples using quaternions to express geometrical relations are known and can be found e.g. in [167] or [168]. Furthermore, hypercomplex numbers are interpreted in different ways concerning the calculation rules. C. Segre [222] proposed a bicomplex algebra, which has the property that the multiplication of the two imaginary units is commutative. It will be shown later on in this section, that this is not the appropriate choice for three-dimensional electromagnetism. J. Cockle [56] identified four essentially distinct systems of quadruple algebra. They are the quaternions, the tessarines, the coquaternions and the cotessarines. Whatever the number of imaginary units is, the tessarine algebra is fundamentally different from the quaternion algebra. The tessarines are a complexification of a complex algebra in the sense that the imaginary units are interpreted in an algebraic / scalar way. In contrast, the quaternions are interpreted in a spatial / vectorial manner. It is important to note that algebras can be combined to form new algebras. This is done by the tensor product of these algebras, denoted as \otimes . Regarding the content presented in this thesis, the tensor product can be understood as a matrix containing all possible combinations of the base vectors of two vector spaces. Following [224], this is given as

$$\mathbf{a} \otimes \mathbf{b} = \mathbf{a} \mathbf{b}^T \xrightarrow{\mathbb{R}^3} \sum_{p=1}^3 \sum_{q=1}^3 (a^p \mathbf{e}_p) \cdot (b^q \mathbf{e}_q) = \begin{pmatrix} a^1 b^1 (\mathbf{e}_1 \cdot \mathbf{e}_1) & a^1 b^2 (\mathbf{e}_1 \cdot \mathbf{e}_2) & a^1 b^3 (\mathbf{e}_1 \cdot \mathbf{e}_3) \\ a^2 b^1 (\mathbf{e}_2 \cdot \mathbf{e}_1) & a^2 b^2 (\mathbf{e}_2 \cdot \mathbf{e}_2) & a^2 b^3 (\mathbf{e}_2 \cdot \mathbf{e}_3) \\ a^3 b^1 (\mathbf{e}_3 \cdot \mathbf{e}_1) & a^3 b^2 (\mathbf{e}_3 \cdot \mathbf{e}_2) & a^3 b^3 (\mathbf{e}_3 \cdot \mathbf{e}_3) \end{pmatrix}, \quad (2.3)$$

where \mathbf{a} and \mathbf{b} are generalized vector quantities, \dots^T means the transpose, a^p and b^q are generalized vector components and $\mathbf{e}_{p/q}$ are generalized base vectors, see later on section 2.4.1 for a detailed discussion. Also the position of indices will be clarified there. The tensor product represents a bilinear or a similar form, which will be further discussed in section 2.3.1. Details can be found e.g. in [79] or [224]. The common way is to construct the algebra with respect to the physical laws of the system of interest. Contrary by following the opposite way, physical phenomena could arise from a certain interpretation of the used algebra. This leads in a recently published paper [96] to the self-interaction of the magnetic vector potential \mathbf{A} .

A possible generalization of complex numbers and quaternions is the Clifford algebra [72], which is also known as geometric algebra (GA). In [252], a detailed introduction to the basic mathematical handling of GA is given, whereas [186] shows geometric relations in several dimensions. According to [252], GA proposes an alternative vectorial framework where different geometrical objects are structures endowed with magnitude and orientation. These structures are called multivectors, which include scalars, vectors, bivectors, pseudovectors and pseudoscalars, or linear combinations of them. GA is an extension of the exterior algebra (in which the wedge product is defined) through the geometric product⁶. Reformulations of various physical problems are thinkable.

⁵See [74] for an english version of the original one, which was published in 1637.

⁶The geometric product is the sum of the inner product and the outer product. These correspond to the scalar product and the cross product in vector calculus, respectively.

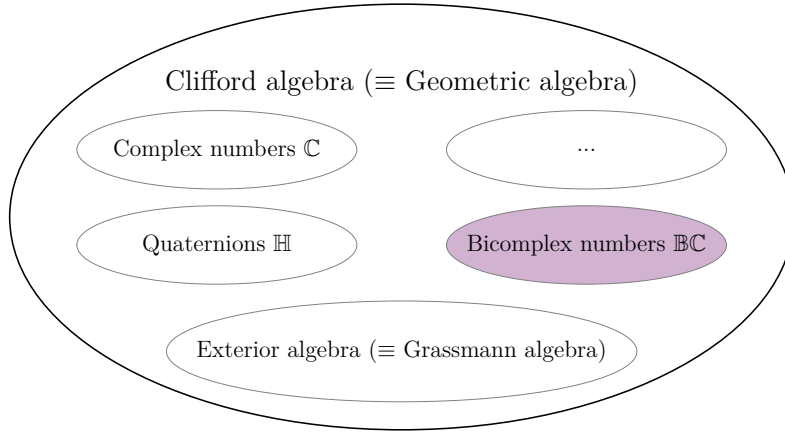


Figure 2.6 Clifford algebra as the generic term of several hypercomplex number systems.

Figure 2.6 shows several hypercomplex number systems, which are assigned to the term “Clifford algebra”. Only a few conceivable number systems are inserted in Fig. 2.6, they might be also combined to form new ones. Remember that the aim is to derive a suitable bicomplex formulation of electromagnetism. For example, the biquaternions can be generated through the tensor product of complex numbers and quaternions $\mathbb{C} \otimes \mathbb{H}$. Therefore, they are a complex combination of two real quaternions. This would lead to the opposite of what is convenient for the formalism of electromagnetism, the inner imaginary unit would be spatial and the outer one would be algebraic. See for example [72], where the biquaternions are used to combine gravitational theory and electromagnetism. Also Sedenions \mathbb{S} [45] and Octonions \mathbb{O} [46] might be used for this purpose. As mentioned previously, classical quaternions \mathbb{H} [113] assign imaginary units to directions in space. In order to derive the bicomplex formulation, $\mathbb{H} \otimes \mathbb{C}$ generates the desired algebra for this thesis. The inner imaginary unit behaves algebraic for the time-harmonic (or time-discrete) property of the electric and magnetic field. Contrary, the outer imaginary unit is spatial and describes the orthogonality between the electric and magnetic field.

The just discussed two combinations are sketched below in Fig. 2.7.

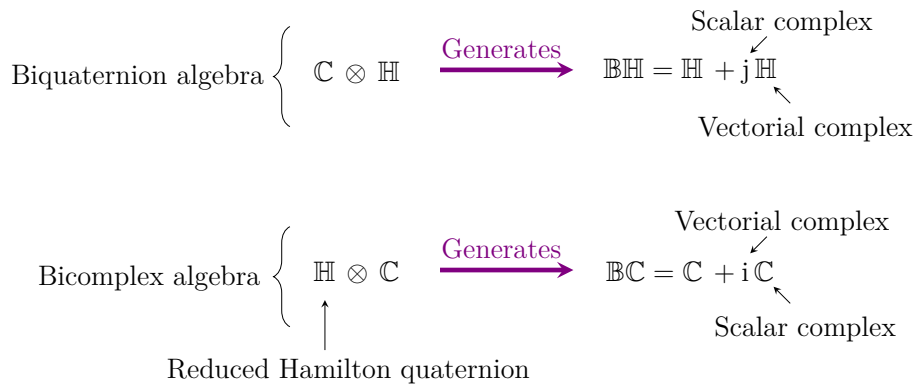


Figure 2.7 Tensor product of several algebras to form the desired algebra \mathbb{BC} for the calculation approach described in this thesis.

Regarding the investigated combination of algebras using the tensor product, the resulting tensor is of type $(p \times pp, q \times qq)$, where in (2.3), \mathbf{a} is of type (p, q) and \mathbf{b} is of type (pp, qq) . This is in accordance with (2.3). Note that in the second case which is sketched on the bottom of Fig. 2.7, a reduced Hamilton quaternion⁷ is used. According to [7], an isomorphism from the set

⁷A common Hamilton quaternion contains three imaginary units, the reduced one here contains only one, which corresponds to the outer imaginary unit i of bicomplex numbers.

of quaternions to the set of bicomplex numbers exists. It is stated there that the third imaginary unit k will not be used. The bicomplex numbers constructed above for electromagnetism form a skew field / division ring⁸. They are used for various applications in physics and mathematics in the context of rotation groups. Also in relativistic calculations they are applied, for example the Minkowski form and Lorentz transformations can be represented by quaternions [181].

To understand the geometrical relations, the commutative property has to be discussed in-depth. The effect of the outer imaginary unit i can be alternatively understood as a geometrical shift of the coordinate system. As previously mentioned, the underlying space is \mathbb{R}^3 . Consequently, the de Rham cohomology is valid for the desired system. To solve the bicomplex equation for homogeneous space, the orientation of the magnetic field can further be shifted to the electric field's orientation. In the one-dimensional (1D) bicomplex electromagnetism presented in [202], it is merely assumed that the electric and magnetic field are orthogonal to each other in the transversal plane, since only the propagation direction is modeled. Especially for three-dimensional problems, the geometrical relations between all field components become complicated.

According to [236], the interpretation of imaginary units can be divided into spatial / vectorial (physical space) and algebraic / scalar (function space). This choice has direct influence on the geometrical meaning and calculation rules like commutativity. The quaternionic sense is spatial. Imagine to calculate a vector product of two vectors. If the order of multiplication is changed, the sign of the result changes. The time-complex sense is algebraic. Imagine to calculate a scalar product of two vectors. If the order of multiplication is changed, the sign of the result is still the same. The desired bicomplex electromagnetism is a combination of algebraic and spatial imaginary units. One can ask about noncommutativity of the product of the two imaginary units. As mentioned, the inner imaginary unit j is an algebraic one. This would lead to a product between a vector and a scalar, which would be commutative. The answer is that the algebraic imaginary unit is oriented as its underlying space. No spatial rotation is involved between the reference system and the algebraic imaginary unit, but between the reference system and the spatial imaginary unit i . Therefore, the relation between the algebraic j and the spatial i is vectorial. This leads finally to noncommutativity of their product.

A possible influence of the spatial i will be discussed next on the rotations of the three reference planes. Following the convention of the vector product, assume a right-handed coordinate system in Fig. 2.8. For common EM problems in DEC, a real-valued differentiable manifold with Cartesian coordinates is often assumed. According to [181], it is possible to use complex coordinates, which would lead to a complex-valued manifold. However, as mentioned previously, the underlying space for the electric and the magnetic subsystem is the \mathbb{R}^3 . Since the exterior derivative $^p d$ acts in a linear manner on both of these subspaces, the de Rham cohomology is valid for bicomplex electromagnetism. Possible spatial issues are addressed by means of the right-handed coordinate system in Fig. 2.8, see also [203].

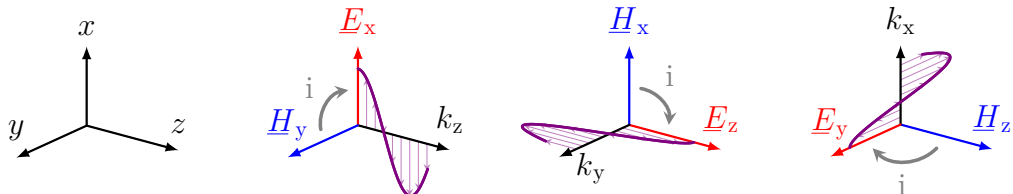


Figure 2.8 Rotated coordinate systems due to spatial mapping as an alternative to embedding the bicomplex structure in the function space.

⁸A skew field is an algebraic structure like a field, where the multiplication may be not commutative, like e.g. the quaternions of Hamilton, see [113].

For the left one of the three colored coordinate systems, the propagation direction is z , the electric field's orientation is x and the magnetic field points in the y -direction. A rotation of \underline{H}_y around 90° is a mapping to \underline{E}_x , which is defined as the orientation of the bicomplex-valued EM wave (drawn in violet). The other two right-handed trihedrons are handled similarly. Quite naturally, the orthogonality between transversal and longitudinal wave components holds. A rotation of 180° changes the sign and corresponds to $i^2 = -1$, equivalently to quaternions. By superposing these three systems, all possible wave directions are possible. In summary, the imaginary unit i rotates the magnetic field back to the electric field's orientation. For this purpose, a transformation matrix $[T]$ is used, which reads as

$$[T] = \begin{pmatrix} 0 & 0 & 1 \\ 1 & 0 & 0 \\ 0 & 1 & 0 \end{pmatrix}. \quad (2.4)$$

A further classification of the rotation caused by i is based on the general description of rotations of vectors, which can be described through Euler angles or quaternions [220]. Euler angles use 3×3 rotation matrices, whereas quaternions use spatial imaginary units. To examine the properties of similar transformations in general, like symmetries, it is suitable to use group theory. A basic introduction to group theory, quaternions and Lie groups is given in [220]. Lie groups can be applied to EM wave propagation as a formal structure for studying the nature of elementary transformations of the PDE's solutions [55]. Other physical problems, such as propagation of light in curved space-time or heat diffusion, are handled in this manner by the authors of [133]. In the context of differential forms, Lie groups are used in [91]. Following the first-mentioned approach of Euler angles, the $SO(3)$ rotation group [220] is suitable. The elements of the $SO(3)$ group are the rotation matrices, which can be applied at once or consecutively to the several coordinate axes. In comparison to the $SO(3)$ group – where all possible rotations in the respective space exist – the bicomplex formulation needs only one rotation matrix $[T]$ and its inverse. This matrix is later on applied to the magnetic part of the bicomplex-valued EM field to express physical quantities directly without transforming them back from the bicomplex function space to the physical space in section 2.6.

For the investigations covered by this thesis, a real-valued differentiable manifold equipped with Cartesian coordinates is assumed. As shown in [7], it is also possible to choose another common coordinate system, like the cylindrical or the spherical one. As previously mentioned, it is also possible to use a complex-valued manifold by assuming complex coordinates. Complex manifolds⁹ have applications, for instance, in string theory, see e.g. [104]. For an overview of orthogonal coordinate systems in Euclidean 3-space concerning differential equations in EM field theory, see e.g. [174].

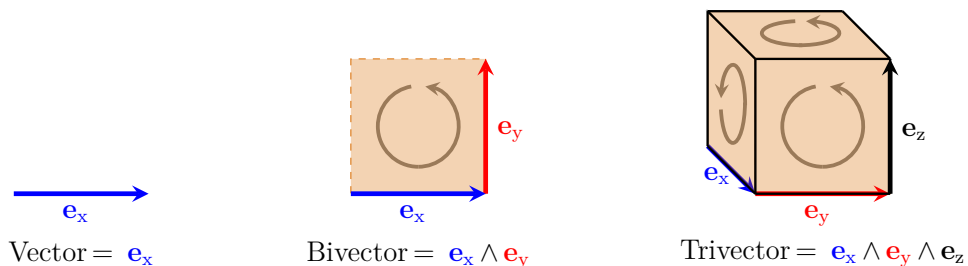


Figure 2.9 Construction of the trivector (pseudoscalar) by combining lower-dimensional multi-vectors in Clifford algebra \mathbf{Cl}_3 through the wedge product.

⁹For a complex manifold, the tangential space is complex instead of the cotangential space, see e.g. [93] for mathematical handling. The (co)tangential space is of central interest in section 2.4.

It is important to distinguish the outer imaginary unit i from the trivector (pseudoscalar) of the Clifford algebra \mathbf{Cl}_3 ; details to the latter can be found e.g. in [76] or [252]. According to [186], pseudoscalars act as rotating operators. A trivector can be formed by the wedge product (denoted as \wedge) of the three unit vectors \mathbf{e}_x , \mathbf{e}_y and \mathbf{e}_z of Cartesian coordinates, as sketched in Fig. 2.9. The shown concept of the bivector further clarifies the difference of the used bicomplex formulation to the bivector formulation, which has got applications in the context of geometric algebra. Introductory discussions of geometric algebra in electromagnetism can be found e.g. in [16] and [47]. For the bicomplex formulation, the outer imaginary unit i separates the electric field from the magnetic field, whereas the bivector notation combines these fields [7]. The bivector formulation is apparently demonstrated in [53], where the Riemann-Silberstein complex vector [226, 227] is applied to represent the complete set of Maxwell's equations. A comprehensive examination of these formulations is given in [77]. Also applications of GA in other topics exist, see e.g. [171], where GA is applied to represent the Fourier space of EM power.

2.2 Homogeneous Material Distribution

In this section, the conventional calculus for TEM-wave propagation in homogeneous media is shown first. Next, an alternative way to calculate the electric and magnetic field simultaneously is presented, which is based on only one bicomplex equation. For convenience, this equation is derived in detail from the familiar time-harmonic Maxwell's equations.

Throughout this thesis, a real-valued wavenumber k is assumed. Therefore, a real-valued Poynting vector follows, since solely active power transfer and no oscillating reactive power takes place. Note that this assumption is no restriction to the derivations presented in this thesis, it is just made to keep them simple. In the following, the term "complex" refers to the ordinary description of time-harmonic behavior of real-valued waves through the usage of complex vector amplitudes. Contrary, the bicomplex concept uses also complex vector amplitudes, which are furthermore spatially connected (discussed in section 2.1.2).

2.2.1 Complex-valued Helmholtz Equation

The governing equation for the propagation of a TEM-wave in homogeneous, lossless, source-free medium along one coordinate – commonly known as vector Helmholtz equation – under time-harmonic conditions, is given by [115] as

$$\nabla \times (\nabla \times \underline{\mathbf{E}}) - k^2 \underline{\mathbf{E}} = 0 \quad \text{or} \quad \nabla \times (\nabla \times \underline{\mathbf{H}}) - k^2 \underline{\mathbf{H}} = 0, \quad (2.5)$$

where $\nabla \times$ is the curl operator and $k = \omega/c \sqrt{\mu_r \epsilon_r}$ is the wavenumber. In the definition of k , ω is the angular frequency and c is the speed of light. Later on in section 2.3.1, they are enhanced to inhomogeneous material distribution, see (2.13a, 2.13b). By assuming lossless media, k is real-valued. The derivation of (2.5) is well-known and therefore not presented here. Nevertheless, the following references could be helpful. A mathematical introduction to PDEs, like the wave equation, can be found, for instance, in [30], [162] or [185]. Regarding a physical discussion of waves, see e.g. [253]. An elaborative discussion of several conventional time-harmonic EM field problems is done e.g. in [115]. Concerning the so-called pollution effect, which is important to consider when using Helmholtz equations for FEM calculations, see for example [27]. To avoid this effect, an appropriate number of elements per wavelength is assumed. According to [135] and [136], the application of Helmholtz problems in high-frequency regime of FEM suffers from the linear dependency of the wavelength on the number of degrees of freedom (DOFs). This will be further discussed by means of numerical examples later on in Chapter 4.

2.2.2 Bicomplex-valued Pseudo-Helmholtz Equation

In order to express the source-free time-harmonic Maxwell's equations in the framework of bicomplex numbers, a suitable equation is given by [7], which reads as

$$\nabla \times \underline{\underline{\mathbf{F}}} = ij k \underline{\underline{\mathbf{F}}}^+ . \quad (2.6)$$

This is called the "Pseudo-Helmholtz equation" throughout this thesis. Here, $\underline{\underline{\mathbf{F}}}^+$ denotes the outer conjugate¹⁰ of $\underline{\underline{\mathbf{F}}}$. Again, k is the wave number and should be not mixed-up with the third imaginary unit of Hamilton quaternions. Caused by the inherent geometrical structure, only one spatial derivative (1st-order) is needed instead of two (2nd-order), as necessary for the Helmholtz equations (2.5) discussed in the previous section 2.2.1. As a guide, the derivation of (2.6) is given below. The starting point is the source-free time-harmonic Maxwell system, which is

$$\nabla \times \underline{\underline{\mathbf{E}}} = -j k Z_0 \underline{\underline{\mathbf{H}}} \quad (2.7a)$$

$$\nabla \times \underline{\underline{\mathbf{H}}} = j k \frac{1}{Z_0} \underline{\underline{\mathbf{E}}} \quad (2.7b)$$

$$\nabla \cdot \underline{\underline{\mathbf{B}}} = 0 \quad (2.7c)$$

$$\nabla \cdot \underline{\underline{\mathbf{D}}} = 0, \quad (2.7d)$$

where $\underline{\underline{\mathbf{B}}}$ is the magnetic flux density, $\underline{\underline{\mathbf{D}}}$ is the electric flux density and $\nabla \cdot$ is the divergence operator. Note that, contrary to section 2.3, where inhomogeneous material distribution yields a general wave impedance Z , the wave impedance assumed here is that of the free space Z_0 . System (2.7a, 2.7b) is also valid for inhomogeneous material distribution by substituting Z_0 by Z .

It is suitable here to clarify at first the meaning of (2.7a, 2.7b) regarding wave propagation. Figure 2.10 shows the near-field to far-field conversion of an electric dipole described by the time-harmonic Maxwell system for vertical wave polarization ($\underline{\underline{\mathbf{E}}}$ is parallel to the x -axis).

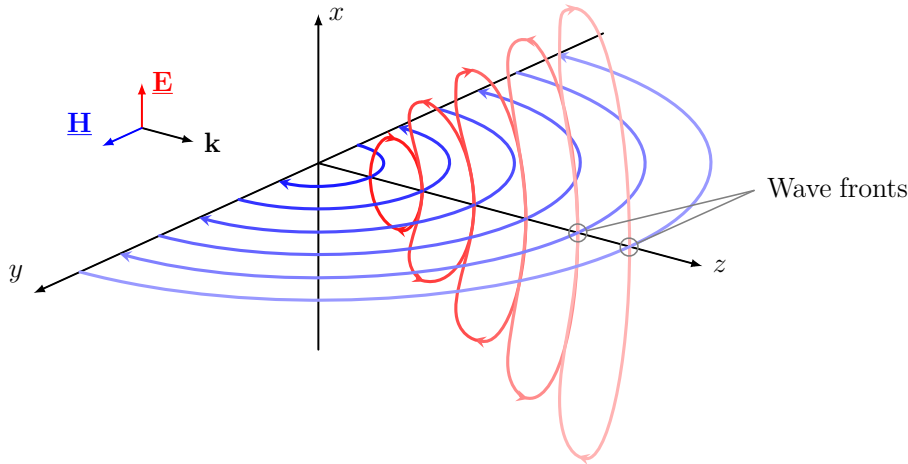


Figure 2.10 Near-field to far-field conversion of a vertically polarized electric dipole described by the two time-harmonic Maxwell's equations (2.7a, 2.7b), exemplified on the positive z -axis.

For simplification, the drawn field lines (red and blue) are representative for radially decreasing vector fields from the source point, which is here the origin of coordinates. Assume that the first magnetic loop (depicted in blue) – drawn close to the origin – is generated through (2.7b) by a time-harmonic current element¹¹ placed at the origin of coordinates, which points in the positive

¹⁰This means the inverse sign for the magnetic part, so the conjugation with respect to the outer imaginary unit i , see e.g. [164] or (2.12) presented at the end of this section.

¹¹Note that current densities are omitted on the right-hand side (RHS) of (2.7b).

x -direction. The direction of this magnetic loop is reversed, since it is placed a half wavelength away from the current element. This magnetic loop generates an electric loop (drawn in red) through (2.7a). Based on this electric loop, a magnetic loop is generated again through (2.7b) and so forth. The different signs on the RHS of (2.7a) and (2.7b) define the orientation of the loops, respectively. In the far-field, the loops expand transversally to infinity. From then on, they build plane wave fronts. These phase planes result in plane TEM-waves, as shown earlier in Fig. 2.2, see section 2.1. For further reading, the radiation of EM waves from a resonant antenna is excellently described by [265]. Since k is used explicitly in (2.7a, 2.7b), they describe only the wave direction $+z$. To describe wave propagation in the negative z -direction, a second bicomplex equation is needed, which is explained in-depth in section 2.7. For convenience, the following derivations assume one bicomplex equation.

Coming back to the derivation of (2.6), Ampère's law in (2.7b) is multiplied by the outer imaginary unit i times $\sqrt{Z_0}$ and added to Faraday's law (2.7a) divided by $\sqrt{Z_0}$

$$\nabla \times \left(\frac{1}{\sqrt{Z_0}} \mathbf{E} + i\sqrt{Z_0} \mathbf{H} \right) = -j k \sqrt{Z_0} \mathbf{H} + ij k \frac{1}{\sqrt{Z_0}} \mathbf{E}. \quad (2.8)$$

Bicomplex numbers are commutative with respect to addition, but not regarding multiplication [7]. Thus, $ij = -ji$ leads to

$$\nabla \times \left(\frac{1}{\sqrt{Z_0}} \mathbf{E} + i\sqrt{Z_0} \mathbf{H} \right) = -j k \sqrt{Z_0} \mathbf{H} - ji k \frac{1}{\sqrt{Z_0}} \mathbf{E}. \quad (2.9)$$

After factoring out j and k , the equation is converted to

$$\nabla \times \left(\frac{1}{\sqrt{Z_0}} \mathbf{E} + i\sqrt{Z_0} \mathbf{H} \right) = -j k \left(\sqrt{Z_0} \mathbf{H} + i \frac{1}{\sqrt{Z_0}} \mathbf{E} \right). \quad (2.10)$$

Now, i is factored out and the order of the components on the RHS is changed, which leads to

$$\nabla \times \left(\frac{1}{\sqrt{Z_0}} \mathbf{E} + i\sqrt{Z_0} \mathbf{H} \right) = ji k \left(-\frac{1}{\sqrt{Z_0}} \mathbf{E} + i\sqrt{Z_0} \mathbf{H} \right). \quad (2.11)$$

Flipping again the RHS with $ij = -ji$ gives

$$\nabla \times \left(\frac{1}{\sqrt{Z_0}} \mathbf{E} + i\sqrt{Z_0} \mathbf{H} \right) = ij k \left(\frac{1}{\sqrt{Z_0}} \mathbf{E} - i\sqrt{Z_0} \mathbf{H} \right), \quad (2.12)$$

which is exactly the same as in (2.6). In [4], the derivation of a similar equation can be found.

2.3 Inhomogeneous Material Distribution and Variational Approaches

To generalize the content of the previous section 2.2, the ordinary calculus for the electric field of TEM-wave propagation in inhomogeneous media is shown first. Subsequently, an alternative formulation with only one bicomplex equation is derived. To lead the discussion to the context of FEM, nodal-based variational formulations are derived, which are adjusted later on for edge elements in section 3.3. In [7], both bicomplex equations for homogeneous and inhomogeneous media are given analytically, but not derived in detail.

2.3.1 Complex-valued Helmholtz Equation

Discussions of Helmholtz problems in one, two and three dimensions are given e.g. in [11] or [66]. The general wave impedance $Z = \sqrt{\mu/\varepsilon}$ of inhomogeneous media depends on the location, where

μ is the permeability and ε is the permittivity of the media. For ordinary numerical handling, see e.g. [48] or [194]. There, the incidence angle of the EM wave is taken into account as a parameter.

Throughout this thesis, a wave vector orthogonal to the material transition plane is assumed. The following investigation starts with the time-harmonic Maxwell's equations in a stationary reference system for no losses described by (2.7a, 2.7b) presented in section 2.2.2. In the case of inhomogeneous material properties, elimination of $\underline{\mathbf{H}}$ or $\underline{\mathbf{E}}$, respectively, leads – using vector identity (B.4) from appendix B as well as $-\mu \nabla (1/\mu) = \nabla \mu / \mu$ or $-\varepsilon \nabla (1/\varepsilon) = \nabla \varepsilon / \varepsilon$ – to

$$\nabla \times (\nabla \times \underline{\mathbf{E}}) - k^2 \underline{\mathbf{E}} - \frac{\nabla \mu}{\mu} \times (\nabla \times \underline{\mathbf{E}}) = 0, \quad (2.13a)$$

$$\nabla \times (\nabla \times \underline{\mathbf{H}}) - k^2 \underline{\mathbf{H}} - \frac{\nabla \varepsilon}{\varepsilon} \times (\nabla \times \underline{\mathbf{H}}) = 0, \quad (2.13b)$$

where ∇ in front of μ and ε is the gradient operator. See e.g. [169] for a detailed derivation of these equations. Later on in the FEM implementation, the curl operator ($\nabla \times$) will be conformally discretized by the use of Whitney edge DOFs defined on divergence-free brick elements. Therefore, the first and the third term on the left-hand side (LHS) of (2.13a) and (2.13b) will be not further splitted off using vector identity (B.1) from appendix B or a similar one. Rather Green's theorem (A.1) from appendix A will be imposed to obtain the weak form (2.21) later on in this section. In the following, only the electric field (2.13a) is discussed in detail. The shown procedure applies for (2.13b) in a similar manner.

In the context of the de Rham cohomology, the vectorial differential equation is discretized into p -cochains (see later on section 2.4) for the FEM, where the number of these object's dimensions p can be 0, 1, 2 or 3. Following [243], any discretized vector field $\tilde{\underline{\mathbf{E}}}$ can be written as the sum of linearly independent base vectors, which are called basis functions $\underline{\varphi}_u$ in the context of FEM as

$$\tilde{\underline{\mathbf{E}}} = \sum_{u=1}^U E_u \underline{\varphi}_u \mathbf{e}_u, \quad (2.14)$$

where E_u are the unknown coefficients, \mathbf{e}_u are the unit vectors of the basis functions and $\tilde{\underline{\mathbf{E}}} \in H^1(\Omega)$ is the approximated vector field. The Sobolev space of scalar shape functions $\underline{\varphi}$ for nodal approximation¹² of the electric field is

$$H^1(\Omega) = \{ \underline{\varphi} \in L^2(\Omega); \nabla \underline{\varphi} \in L^2(\Omega) \}. \quad (2.15)$$

Let Ω be an open¹³, bounded Lipschitz domain in \mathbb{R}^p . Since a physical EM field has a finite energy in a bounded region, the field quantities at the stationary state are square-integrable [200]. The Lebesgue space of square-integrable functions $L^2(\Omega)$ [151] is defined for shape functions as

$$L^2(\Omega) = \left\{ \underline{\varphi} : \int_{\Omega} |\underline{\varphi}|^2 \, d\Omega < \infty \right\}. \quad (2.16)$$

The norm of this space in the context of FEM leads to the error norm (4.2) discussed later on in section 4.1.1. By defining a scalar product on the Sobolev space $H^1(\Omega)$, it becomes a Hilbert space [151] endowed with a metric. In the FEM, the solutions of the field problem are approximated in this space as the tensor product of test and basis functions, which can be in this thesis a bilinear, sesquilinear or +-sesquilinear (defined later on for the bicomplex case) form¹⁴. The inner product of two base vectors contained in a finite-dimensional complex Hilbert

¹²Variational formulations for vector-valued edge approximation are discussed in section 3.3.

¹³Open means that every point has its own neighborhood [214].

¹⁴A bilinear form assigns a scalar value to two vectors and is linear in both arguments, examples are the dot product or the tensor product. If these two vectors are real-valued, the term "bilinear" is used, if they are complex-valued, a "sesquilinear form" is present. One possible bicomplex-valued analog is called "+-sesquilinear form".

space $H^1(\Omega)$ can be defined according to [111] as a sesquilinear form by the scalar product of its arguments $\tilde{\mathbf{E}}_w$ and $\tilde{\mathbf{E}}_u$ integrated over the domain Ω , where $\tilde{\mathbf{E}}_w, \tilde{\mathbf{E}}_u \in H^1(\Omega)$ as

$$\langle \tilde{\mathbf{E}}_w, \tilde{\mathbf{E}}_u \rangle = \int_{\Omega} \tilde{\mathbf{E}}_w \cdot \tilde{\mathbf{E}}_u^* \, d\Omega, \quad (2.17)$$

where the superscript $*$ denotes the complex conjugate of the argument. It is important to emphasize that $\tilde{\mathbf{E}}_w$ and $\tilde{\mathbf{E}}_u$ are not p -dimensional vectors as usually assumed in vector calculus, respectively, rather they are oriented projections of the physical quantity of interest \mathbf{E} regarding the respective base vector indicated by the subscript w / u . In the context of shape functions in FEM, these arguments are used as test functions φ_w and basis functions φ_u . Note that (2.17) represents one entry of the tensor product shown in (2.3), see section 2.1.2. To clarify the bicomplex analogon (2.28) discussed later on in section 2.3.2, the integral kernel of (2.17) is exemplarily investigated by using the structure of a general complex number $(r_1 + j r_2)$, where r_1 and r_2 are real numbers, respectively, as

$$(\mathbf{a} + j \mathbf{b}) \cdot (\mathbf{a} - j \mathbf{b}). \quad (2.18)$$

In (2.18), \mathbf{a} and \mathbf{b} are generalized real-valued vector quantities. The multiplication of a complex number by its common conjugation yields the squared complex modulus, which reads as

$$\mathbf{a}^2 + \mathbf{b}^2. \quad (2.19)$$

A similar formulation is generated by the bicomplex version (2.31), see later on section 2.3.2.

Following Galerkin's method, under consideration of $\nabla\mu/\mu = \nabla \ln \mu$ and by switching one Nabla operator (∇) of the first term on the LHS using integration by parts, (2.13a) reads in the weak sense¹⁵ for the one-dimensional case by using nodal finite elements and assuming zero Neumann boundary conditions as

$$\int_{\Omega} \left[-\nabla\varphi_w \cdot \nabla\varphi_u^* - k^2 \varphi_w \cdot \varphi_u^* - \nabla(\ln \mu) \nabla\varphi_w \cdot \varphi_u^* \right] d\Omega = 0. \quad (2.20)$$

Caused by the resolve of the cross product using (B.1) of appendix B, the third term on the LHS of (2.20) is expressed with a gradient and the sign is changed compared to (2.13a). There arises also a convective¹⁶ contribution to the FEM system matrix by the third term on LHS in (2.20). Therefore, the FEM system matrix is potentially not positive definite for specific elements and has to be stabilized in an appropriate manner to receive reasonable results from the FEM.

If one handles the solution of (2.20) by setting up a variational formulation, a non-self-adjoint operator follows. The process of building a functional deals with the combined solution of the problem and the corresponding adjoint problem, see e.g. [49] or [140] for details. Concerning Maxwell's equations, basic introductions to functional issues can be found in [57] or [114]. A 3D-Helmholtz equation for inhomogeneous media can be constructed in this way by consideration of the inhomogeneous Dirichlet boundary conditions via a modified functional, which is done by using the first (A.1) and second (A.2) vector Green's identity of appendix A (see also [142]) as

$$F(\tilde{\mathbf{E}}) = \frac{1}{2} \iiint_{\Omega} \left[(\nabla \times \tilde{\mathbf{E}}_w) \cdot (\nabla \times \tilde{\mathbf{E}}_u)^* - k^2 \tilde{\mathbf{E}}_w \cdot \tilde{\mathbf{E}}_u^* - \frac{\nabla\mu}{\mu} \times (\nabla \times \tilde{\mathbf{E}}_w) \cdot \tilde{\mathbf{E}}_u^* \right] d\Omega, \quad (2.21)$$

¹⁵In a weak formulation of a PDE, that PDE has to be no longer fulfilled in an absolute sense (by one function which is defined on the whole domain Ω). Rather shape functions, which are defined on subdomains (finite elements) approximate the exact solution in FEM.

¹⁶The convection matrix (convective term), which is also known as advection matrix in the field of heat transfer [59], is the weak form of a first order derivative. In contrast, the weak form of the second order derivative is the stiffness matrix (diffusive term) and for the unknown itself, one has to use the mass matrix (reactive term).

which is the generalization of (2.20) and is non-self-adjoint.

This approach leads to the same result as the tensor product in Galerkin FEM by neglecting discretization errors, where the test functions and basis functions lie in the same function space. Unfortunately, the third term of (2.20) has got different test and basis function spaces, which is why the FEM has to be stabilized in certain cases. The effect and appropriate solutions will be discussed later on for the bicomplex FEM in appendix E and appendix F, respectively.

2.3.2 Bicomplex-valued Pseudo-Helmholtz Equation

As derived previously in section 2.2.2, the Pseudo-Helmholtz equation for the homogeneous case is (2.6). For inhomogeneous media, it is extended by following [7] to

$$\nabla \times \underline{\underline{\mathbf{E}}} + \frac{\nabla \sqrt{Z}}{\sqrt{Z}} \times \underline{\underline{\mathbf{E}}} = ij k \underline{\underline{\mathbf{F}}}^+. \quad (2.22)$$

As for the Helmholtz equation for inhomogeneous material distribution (2.13a) or (2.13b) presented in section 2.3.1, the additional second term on the LHS covers the behavior of the EM field at positions where the impedance changes. The derivation of (2.22) takes less steps than its traditional counterparts (2.13a) and (2.13b). Anymore, only one equation covers inhomogeneities of both μ and ε . Dividing Faraday's law (2.7a) by \sqrt{Z} and multiplying Ampère's law in (2.7b) by \sqrt{Z} (see section 2.2.2 for both equations) gives

$$\frac{1}{\sqrt{Z}} \nabla \times \underline{\underline{\mathbf{E}}} = -j k \sqrt{Z} \underline{\underline{\mathbf{H}}} \quad (2.23a)$$

$$\sqrt{Z} \nabla \times \underline{\underline{\mathbf{H}}} = j k \frac{1}{\sqrt{Z}} \underline{\underline{\mathbf{E}}}. \quad (2.23b)$$

Usage of the product rule and some minor trivial transformations on the LHS creates

$$\nabla \times \left(\frac{1}{\sqrt{Z}} \underline{\underline{\mathbf{E}}} \right) - \nabla \frac{1}{\sqrt{Z}} \times \underline{\underline{\mathbf{E}}} = -j k \sqrt{Z} \underline{\underline{\mathbf{H}}} \quad (2.24a)$$

$$\nabla \times \left(\sqrt{Z} \underline{\underline{\mathbf{H}}} \right) - \nabla \sqrt{Z} \times \underline{\underline{\mathbf{H}}} = j k \frac{1}{\sqrt{Z}} \underline{\underline{\mathbf{E}}}. \quad (2.24b)$$

If (2.24b) is multiplied by the outer imaginary unit i and added to (2.24a), it follows

$$\nabla \times \left(\frac{1}{\sqrt{Z}} \underline{\underline{\mathbf{E}}} + i\sqrt{Z} \underline{\underline{\mathbf{H}}} \right) - \nabla \frac{1}{\sqrt{Z}} \times \underline{\underline{\mathbf{E}}} - \nabla \sqrt{Z} \times \underline{\underline{\mathbf{H}}} = -j k \sqrt{Z} \underline{\underline{\mathbf{H}}} + ij k \frac{1}{\sqrt{Z}} \underline{\underline{\mathbf{E}}}. \quad (2.25)$$

The manipulation of the RHS of (2.25) is done in accordance to [202]. A combination of the second and third term on the LHS of (2.25) leads under consideration of the final result of the RHS of (2.22), which is derived in [202], to

$$\nabla \times \left(\frac{1}{\sqrt{Z}} \underline{\underline{\mathbf{E}}} + i\sqrt{Z} \underline{\underline{\mathbf{H}}} \right) + \frac{\nabla \sqrt{Z}}{\sqrt{Z}} \times \left(\frac{1}{\sqrt{Z}} \underline{\underline{\mathbf{E}}} - i\sqrt{Z} \underline{\underline{\mathbf{H}}} \right) = ij k \left(\frac{1}{\sqrt{Z}} \underline{\underline{\mathbf{E}}} - i\sqrt{Z} \underline{\underline{\mathbf{H}}} \right), \quad (2.26)$$

which is exactly the same as (2.22). Note that the second term on the LHS of (2.25) needs to be rearranged using $-\sqrt{Z} \nabla \left(1/\sqrt{Z} \right) = \nabla \left(\sqrt{Z} \right) / \sqrt{Z}$.

Analogous to the complex-valued counterpart in (2.14) discussed in section 2.3.1, discretization of $\underline{\underline{\mathbf{F}}}$ via bicomplex-valued shape functions $\underline{\underline{\varphi}}$ leads exemplary for basis functions $\underline{\underline{\varphi}}_u$ to

$$\underline{\underline{\tilde{\mathbf{F}}}} = \sum_{u=1}^U F_u \underline{\underline{\varphi}}_u \mathbf{e}_u, \quad (2.27)$$

where F_u are the unknown coefficients, \mathbf{e}_u are the unit vectors of the basis functions and $\underline{\underline{\tilde{\mathbf{F}}}} \in H^1(\Omega)$ is the approximated vector field. The Sobolev and Lebesgue spaces of $\underline{\underline{\varphi}}$ are defined

according (2.15) and (2.16) of section 2.3.1, respectively, for bicomplex $\underline{\varphi}$ instead of complex shape functions φ .

According to [157], the inner product of a finite-dimensional bicomplex Hilbert space $H^1(\Omega)$ can be defined as a +-sesquilinear form by the scalar product of its arguments $\tilde{\underline{\mathbf{F}}}_w$ and $\tilde{\underline{\mathbf{F}}}_u$, where $\tilde{\underline{\mathbf{F}}}_w, \tilde{\underline{\mathbf{F}}}_u \in H^1(\Omega)$ as

$$\langle \tilde{\underline{\mathbf{F}}}_w, \tilde{\underline{\mathbf{F}}}_u \rangle = \int_{\Omega} | \tilde{\underline{\mathbf{F}}}_w \cdot \tilde{\underline{\mathbf{F}}}_u^+ |_{\mathbf{j}} \, d\Omega, \quad (2.28)$$

where the integral kernel proposed in (2.28) is discussed below. As mentioned in section 2.2.2, the superscript "+" denotes the i-conjugation.

A particular modulus of bicomplex numbers $|\dots|_{\mathbf{j}}$ reduced to common complex numbers is used additionally to both complex subspaces, respectively, as

$$|\mathbf{e}|_{\mathbf{j}} = \sqrt{\mathbf{a}^2 + \mathbf{b}^2} \quad \text{for } \mathbf{e} = \mathbf{a} + \mathbf{j} \mathbf{b}. \quad (2.29)$$

This produces a real-valued result of (2.28). See e.g. [164] for details. A generalized complex-valued vector quantity $\underline{\mathbf{e}}$ instead of a bicomplex vector quantity can be assumed here, which consists of two real-valued vector quantities \mathbf{a} and \mathbf{b} , since the scalar product in (2.28) produces a common complex number by elimination of the outer imaginary unit i . To show that (2.28) yields a real-valued integral kernel, the structure of a general bicomplex number in (2.1) of section 2.1.1 is taken to express the part inside the integral of (2.28) as

$$|[(\mathbf{a} + \mathbf{j} \mathbf{b}) + i(\mathbf{c} + \mathbf{j} \mathbf{d})] \cdot [(\mathbf{a} + \mathbf{j} \mathbf{b}) - i(\mathbf{c} + \mathbf{j} \mathbf{d})]|_{\mathbf{j}}, \quad (2.30)$$

which yields after performing multiplication followed by the modulus

$$\sqrt{(\mathbf{a}^2 + \mathbf{b}^2 + \mathbf{c}^2 + \mathbf{d}^2)^2 + (2 \mathbf{a} \mathbf{b} + 2 \mathbf{c} \mathbf{d})^2}. \quad (2.31)$$

Obviously, the result of 2.31 is real-valued and shows a structure similar to (2.19), see section 2.3.1. Further possible approaches of complexifying a real Hilbert space or quaternionizing a complex Hilbert space are given e.g. in [225].

Following Galerkin's method as done to produce (2.20) in section 2.3.1, (2.22) reads in the weak sense by using nodal finite elements, assuming zero Neumann boundary conditions and resolve the rotations for the 1D-case as

$$\int_{\Omega} \left| \left[\nabla \underline{\varphi}_w \cdot \underline{\varphi}_u^+ - \frac{\nabla \sqrt{Z}}{\sqrt{Z}} \underline{\varphi}_w^+ \cdot \underline{\varphi}_u^+ - ij k \underline{\varphi}_w^+ \cdot \underline{\varphi}_u^+ \right] \right|_{\mathbf{j}} \, d\Omega = 0. \quad (2.32)$$

Note that the minus sign in the second term of the LHS in (2.32) arises because of the resolve of the cross product, similar to (2.20).

The equivalent functional for the 3D-case is

$$F(\tilde{\underline{\mathbf{F}}}) = \frac{1}{2} \iiint_{\Omega} \left| \left[(\nabla \times \tilde{\underline{\mathbf{F}}}_w) \cdot \tilde{\underline{\mathbf{F}}}_u^+ + \frac{\nabla \sqrt{Z}}{\sqrt{Z}} \times \tilde{\underline{\mathbf{F}}}_w^+ \cdot \tilde{\underline{\mathbf{F}}}_u^+ - ij k \tilde{\underline{\mathbf{F}}}_w^+ \cdot \tilde{\underline{\mathbf{F}}}_u^+ \right] \right|_{\mathbf{j}} \, d\Omega, \quad (2.33)$$

which is the generalization of (2.32) and is non-self-adjoint.

Since discontinuities arise when using the one-way wave equations (2.32) or (2.33) to describe material transitions caused by reflected wave parts, an implementation by continuous FEM is not possible. This problem can be solved e.g. with an implementation in a discontinuous FEM, which is outside the scope of this thesis. An alternative derivation for consideration of inhomogeneous media from a quaternionic view can be found in [153].

2.4 Discrete Exterior Calculus

Mimetic numerical methods handle physical properties in a continuous way instead of only solving PDEs on discrete nodes and interpolate between them. As the approximation of the continuum is far better, no spurious modes arise, e.g. by using Whitney elements (see e.g. [241]). Concerning physics-compatible discretization techniques, mimetic methods are discussed, for instance, in [188]. Since DEC is a mimetic method, the operators used therein are called mimetic operators [28]. Mainly in the earlier literature, exterior algebra is also known as Grassmann algebra. The merits of differential calculus are that it provides a rigorous description of EM theory through the differentiation between field intensities and flux densities and yields computational simplifications compared to vector calculus [255]. To describe EM field quantities in geometric algebra, differential forms (or: multivectors) are used. Differential forms allow the factorization of the field equations into a topological part and a metric part [241]. In recent years, DEC become widely applied in several fields of physical problems. For a general introduction to DEC, see e.g. [73], [93] or [98]. Especially concerning electromagnetism, [75], [99], [117], [240,241], [244,245], [255] and [260] are recommended. Exemplary further applications of DEC are relativistic problems addressed for example in [58], or fluid mechanics discussed e.g. in [128].

At first, it is convenient to introduce the concept of a manifold. In DEC, the manifold is a generalization for describing p -dimensional objects, and can be understood as a set of local Euclidean subregions. These subregions are formed by a point set and a map from the standard Euclidean space \mathbb{R}^p to this set. Individual regions on a manifold can be described by individual maps (\equiv charts), which form an atlas. Through the use of this atlas, integrations on p -dimensional manifolds are reduced to integrations on the standard \mathbb{R}^p . A mathematical handling is done for example in [144], where a topological definition of the term "manifold" is given and also integration on manifolds is discussed. Historical points of view are reported e.g. in [137] or [216]. Following [147], a convenient way for the interpretation of modeling purposes is shown in Fig. 2.11.

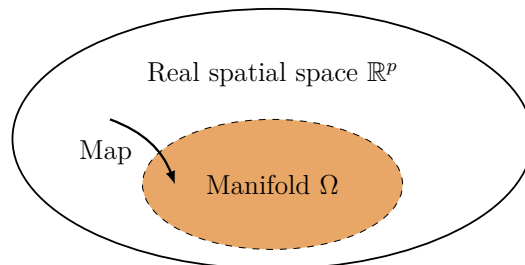


Figure 2.11 Manifold Ω as a subset of the real spatial space \mathbb{R}^p .

The manifold Ω is a subset of the real spatial space \mathbb{R}^p , which is also a manifold itself. Since the aim is to model real world geometries in \mathbb{R}^p , an Euclidean metric¹⁷ is introduced on Ω . Therefore, Ω is a submanifold of \mathbb{R}^p . Concerning the FEM, Ω is the set of all entities of the mesh. These entities are described by vector spaces (tangential spaces) defined on Ω . In Fig. 2.12, the two concepts of exterior calculus and vector calculus are indicated regarding their bases.



Figure 2.12 Base vectors of the two concepts vector calculus and exterior calculus.

¹⁷The proximity of points in Ω is measurable by the Euclidean distance formula [214].

On the left of Fig. 2.12, the Cartesian unit vectors \mathbf{e}_x , \mathbf{e}_y and \mathbf{e}_z represent the base of the Euclidean 3-space. For exterior calculus depicted on the right, the three-dimensional tangential space of a manifold is described by the Cartesian coordinate differentials dx , dy and dz .

More abstract topologies may be analyzed by introducing a Riemannian metric on a Riemannian manifold. There, an inner product is defined on the tangential space, where the distance is expressed more abstractly compared to the Euclidean metric using the geodesic distance instead of the well-known Euclidean distance as the square-root of the summed squared coordinate differences. A basic mathematical discussion on Riemannian manifolds is done e.g. in [39], for further reading concerning other subjects as, for instance, classification problems in the field of machine learning, see for example [132]. In this thesis, closed manifolds of \mathbb{R}^1 and \mathbb{R}^3 are used as the computational domains. The one-dimensional manifold assumed in section 4.1 is the unit interval. It is divided into distinct independent segments, which are called linear finite elements after they are equipped with a suitable vector space. Three-dimensional manifolds are used in section 4.2. Two different meshings are done on them, which generate the linear brick and the linear tetrahedral finite element, respectively. These two elements are common in FEM modeling.

The crossover from classical vector calculus to the calculus of differential forms will be discussed later on in section 2.4.1. For further reading, [75], [144] and [188] are recommended. According to [192], the main difference between vectors and differential forms is the different point of view, so differential forms are functionals on vectors rather than vectors themselves. Regarding the used language of differential forms, electromagnetic field quantities are subject to respective differentials, see (2.35) in section 2.4.1. A suitable vector space for defining differential forms on a manifold is the tangential space. In the context of FEM, the differential forms are connected directly to Whitney shape functions. The relationship of the manifold to the tangential space is shown in Fig. 2.13.

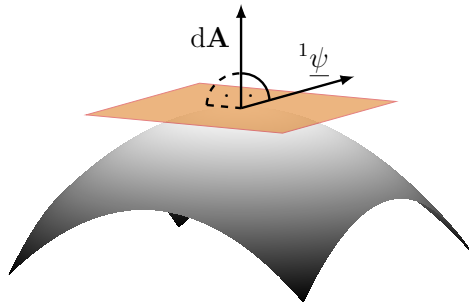


Figure 2.13 A two-dimensional manifold (depicted in gray) with a two-dimensional tangential space (drawn in orange) to demonstrate a possible orientation of an exemplary differential 1-form.

A two-dimensional (2D) tangential space (drawn in orange) touches the boundary of the two-dimensional manifold (which is drawn in gray). This two-dimensional manifold might be also interpreted as a part of the boundary of a three-dimensional manifold, or as the boundary of the computational domain in 3D-FEM. The differential surface element of the plane tangential space $d\mathbf{A}$ is oriented in the normal direction, whereas the differential 1-form ${}^1\psi$ is oriented in the tangential plane and includes the differential in the same way as the electric field (later on presented in (2.35), see section 2.4.1). Note that the superscript in front of the differential form reveals its order. As usual, EM quantities of vector calculus are expressed using the Latin alphabet. Differential forms of EM quantities are written using fracture font, as e.g. the electric, magnetic or bicomplex field. The tangential space is a spatial description of the manifold, so the place where functions (which exist in the cotangential space) are defined. This will be discussed in detail later on, see Fig. 2.16 in section 2.4.1.

The bicomplex formulation of the EM field yields a bicomplex-valued cotangential space which is defined on a real-valued manifold, see especially section 2.4.6. Since the FEM uses integration of differential forms ${}^p\psi$ on a manifold Ω , it is suitable to introduce the generalized Stokes' theorem (see e.g. [93] or [144]), which reads as

$$\int_{{}^{p+1}\sigma} {}^p d {}^p \psi = \int_{{}^{p+1}\partial} {}^p \psi, \quad (2.34)$$

where ${}^p d$ is the exterior derivative / coboundary operator and ${}^p \partial$ is the boundary operator. It states that the integration of a differential form's derivative ${}^p d {}^p \psi$ over the whole manifold Ω is equal to the integration of the differential form ${}^p \psi$ itself over the manifold's boundary $\partial\Omega$. This means duality in different spaces, which will be broadly discussed in section 2.4.6. The manifold's boundary might be also described by the p -chains ${}^p\sigma$ which form the manifold in the discrete setting. Stokes' theorem in its general form (2.34) for \mathbb{R}^3 yields several further theorems as special cases, which are the divergence theorem (B.5) for $p = 2$, the Stokes' theorem of vector calculus (B.6) for $p = 1$, and the fundamental theorem of algebra (B.7) for $p = 0$. In Fig. B1 (see appendix B), a graphical interpretation of these three special cases of (2.34) is depicted. Also Green's theorems are based on the generalized Stokes' theorem, see appendix A. The two sides of (2.34) are connected by an operator switch commonly used in the weak formulation of PDEs. Integration of differential forms is discussed, for instance, in [41] and [91].

Regarding differential forms, there are for example the ordinary vector (1-form), which is known from vector calculus. The bivector (2-form) is defined by the wedge product of two 1-forms as shown previously on Fig. 2.9 in section 2.1.2. In the context of wave propagation, these two equivalence classes¹⁸ are used to describe field strengths and flux densities, respectively. A mathematical investigation of differential forms is done in [41], where also the variational calculus discussed in section 2.3 and later on in section 3.3 is addressed. Differential forms in the field of electromagnetism are examined e.g. in [120] or [159], where in the latter also wave equations are considered. The connection from the mathematical to the physical context of differential forms is presented in [91]. An introduction to Maxwell's equations expressed in differential forms is also given there. The two musical operators flat \flat and sharp \sharp transform between p -vectors and p -covectors¹⁹. A map from p -vectors to p -covectors is done by \flat and vice versa by \sharp , which are detailed investigated in [127]. As stated in [100], the musical operators can be used to transform between vectors of vector calculus and p -forms of exterior calculus. This is shown later on in section 2.4.4. Following [188], a p -form is not directly observable. However, its action on various elements of the vector space can be shown. For this reason, in order to obtain representable vector fields, the Whitney interpolation map \mathcal{I}_p is applied to a p -form when its behavior is of interest. Since in classical vector calculus there is no distinction between 1-forms and 2-forms, and further no distinction between 0-forms and 3-forms, it does not fit into the de Rham complex. The de Rham complex will be introduced later on in Fig. 2.29, see section 2.4.6. If one considers these distinctions, the vectorial operators ∇ , $\nabla \times$ and $\nabla \cdot$ can be associated with the appropriate grade of the exterior derivative ${}^0 d$, ${}^1 d$ and ${}^2 d$, respectively.

¹⁸Equivalence classes are in the context of cohomology the respective set of p -forms which are defined on the cotangential space of Ω and in the context of homology the respective set of p -chains which are defined on the tangential space of Ω . This is subsequently clarified later on especially in section 2.4.1 and further in Fig. 2.29, see section 2.4.6.

¹⁹In section 2.4.1, the concept of p -vectors and p -covectors is discussed in detail.

It is appropriate now to introduce all relevant quantities in electromagnetism and their connection in DEC in a graphical way. The usage of vector calculus hides the metric-independence of Maxwell's equations, since the topological structure is intertwined with their metric structure [241]. This graphical representation is known as Tonti diagram. It is shown in Fig. 2.14 for three-dimensional electromagnetism in the context of DEC, see e.g. [33] or [246] for further reading. The Tonti diagram can be also derived from another possibility to illustrate the relations between differential forms, which are called flow diagrams, as used e.g. in [75].

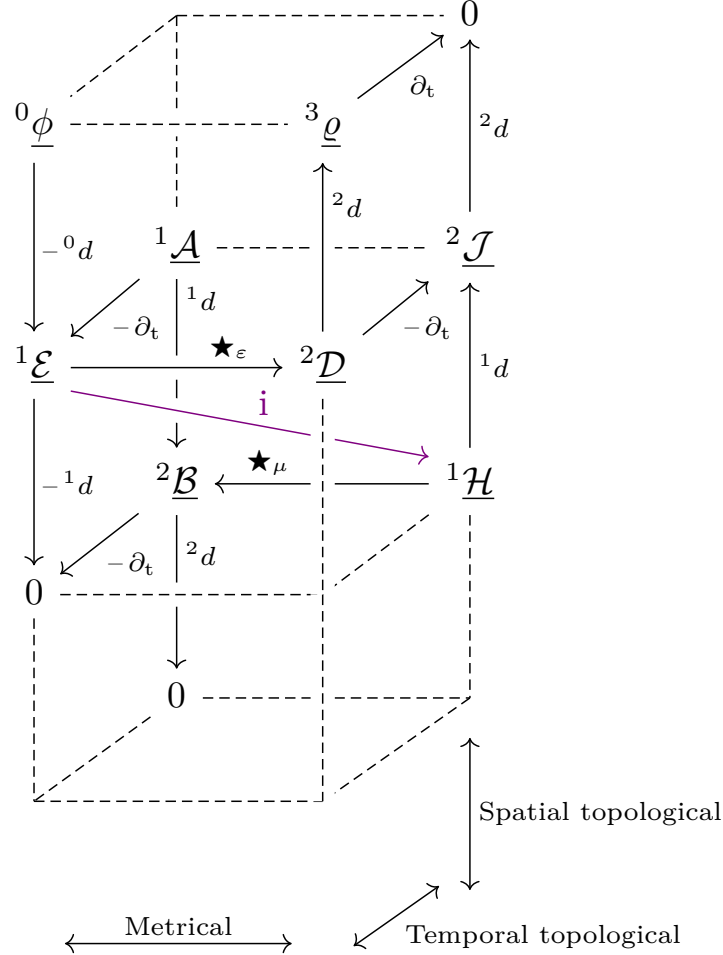


Figure 2.14 Tonti diagram of three-dimensional electromagnetism.

Field quantities²⁰ lying on the corners of the diagram depicted in Fig. 2.14 are differential p -forms, the connection between them is established by operators. The horizontal Hodge operators (\star_μ and \star_ε) act as metrical operators. Contrary, in vertical direction, the exterior derivative ${}^p d$ operates spatially topological. For completion, temporal derivatives ∂_t transform from the front to the back and vice versa. The separation of operators in these three classes is important for discretization purposes. In violet, the effect of the outer imaginary unit i of bicomplex electromagnetism is shown. Later on in Fig. 2.18 (see section 2.4.2), this context will be expressed by the use of the DEC-de Rahm diagram.

²⁰The differential EM field quantities shown in Fig. 2.14 are the 0-forms electric scalar potential ${}^0\phi$ (note that the same symbol is used for both vector and exterior calculus, the superscript in front of the symbol indicates the context), the 1-forms electric field ${}^1\mathcal{E}$, magnetic field ${}^1\mathcal{H}$ and magnetic vector potential ${}^1\mathcal{A}$, the 2-forms electric flux density ${}^2\mathcal{D}$, magnetic flux density ${}^2\mathcal{B}$ and electric current density ${}^2\mathcal{J}$ and finally the 3-form space charge density ${}^3\rho$.

2.4.1 From Covariant Vector Calculus to Contravariant Cohomology

It is convenient now to clarify the meaning of co- and contravariant tensors. Vectors in classical vector calculus are tensors of rank one [230]. As common in literature, the subscripts indicate covariant components (lower index notation), whereas the superscripts indicate contravariant components (upper index notation). Since in this thesis base changes are considered, as next it will be outlined how transformations are to be understood. Transformations between coordinate systems are discussed e.g. in [230]. For the used orthonormal Cartesian coordinate system of \mathbb{R}^3 , it does not matter whether vector components transform in a covariant or contravariant manner. However, in order to provide a general concept by the use of differential forms in a metric-free²¹ environment, a clarification of the transformation behavior is important. Following [188], the transformation behavior of a covector when a base change occurs is different to that of a vector.

By assuming the covariant notation of vector calculus (see e.g. [172]), the generalized covariant base vectors \mathbf{e}_p of the coordinate system are the reference of an integration. They are defined later on in this section, see (2.39). The components of contravariant tensors transform inversely to the base vectors of the coordinate system, whereas the components of covariant tensors transform in the same way as the base vectors. A covector has typically units related to the inverse of distance. This is the case for vector quantities in general such as the vectorial bicomplex EM field $\underline{\mathbf{F}}$, which is expressed in $\sqrt{V} \text{ A m}^{-1}$. In general, all spatial derivatives transform in a covariant manner, since they are all defined with respect to the base vectors. Furthermore, also the metric tensor²² (later on defined in (2.48), see section 2.4.4) transforms covariantly, indicated by subscripts. Contrary, contravariant tensors transform inversely to the base vectors. Examples are the length scales of the coordinate axes (expressed as absolute coordinates) or the velocity vector, which has typically units of distance included.

Integrals of differential forms over manifolds can be represented by the inner product of a differential form and the manifold. This is equivalent to the inner product of an element defined on the cotangential space (where covectors live in) with one element of the tangential space (where vectors live in). For clarity, an example of using this notation is given below in (2.35). The electric field's differential form ${}^1\mathcal{E}$ derived from three-dimensional vector calculus (see e.g. [256]) is a linear combination of contravariant coordinate differentials (dx, dy, dz) instead of unit vectors, which are scaled by covariant vector components ($\underline{E}_x, \underline{E}_y, \underline{E}_z$) as

$${}^1\mathcal{E} = \underline{\mathbf{E}} \cdot d\mathbf{s} = \underline{E}_x dx + \underline{E}_y dy + \underline{E}_z dz. \quad (2.35)$$

This is in accordance to the tangential space shown on the right of Fig. 2.12, see section 2.4. Note that through the inclusion of the corresponding contravariant coordinate differential in a differential form, the unit is changed to be metric-free. So is the unit of $\underline{\mathbf{F}}$ expressed in $\sqrt{V} \text{ A m}^{-1}$, whereas the unit of ${}^1\mathcal{F}$ is $\sqrt{V} \text{ A}$. This indicates that the units of differential forms do not reveal the distinction between covector and vector. In exterior calculus, this is rather indicated by the used reference framework, so if it is cohomology or homology, respectively.

In Fig. 2.15, the covariant vector calculus (so called, since the base vectors transform covariantly) is explained on the simple example of integrating an electric field $\underline{\mathbf{E}}$ over a straight line s , which is described by the invariant²³ line element $d\mathbf{s}$. The points a and b are described by ordered triples of contravariant generalized coordinates x^p , where p is the index of the dimension. Due

²¹In a metric-free space, no norm is induced.

²²The metric tensor $[g_{pq}]$ represents the scalar products of all possible pairs of the used metrics' base vectors (tangential vectors) in matrix form.

²³An invariant quantity is unchanged when a base change / basis transformation occurs.

to charge conservation, the magnitude of the integral quantity \underline{U} (electric voltage) is invariant under a base change. Thus, it is constant in every case. On the bottom left, the contravariant coordinate function compensates the effect of the changed basis, it acts "contra" to the change of basis. The covariant electric field components change in the same way as the basis does, so "co" to the basis. On the bottom right, the z -coordinates are contracted, whereas the base vectors are unchanged. Since again the integration's result has to be constant, the covariant electric field components change in the opposite sense as the contravariant z -coordinates does.

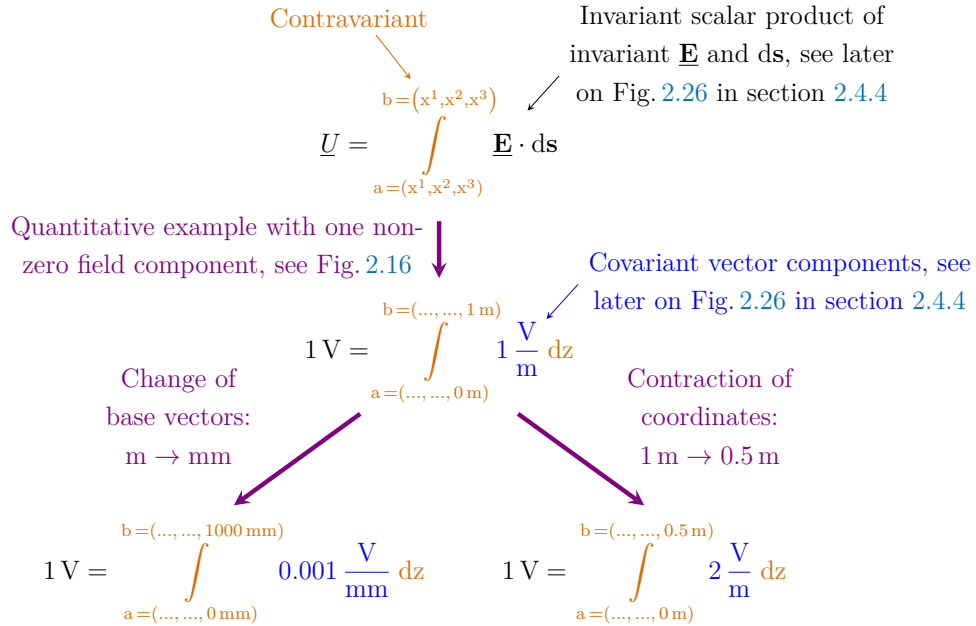


Figure 2.15 Contravariant (depicted in orange) and invariant (colored in black) quantities of the ordinary covariant vector calculus are presented on the top. The middle shows a simple analytical example, where furthermore a covariant (drawn in blue) quantity arises. Exemplary, the two possibilities of implementing a changed measure (caused e.g. by a deformation of the metric) of Ω are shown on the bottom. The bottom left shows the common way in physics called change of base vectors (here: other units), whereas the bottom right shows changed coordinates (changed length scale of the integration line) by keeping the base vectors constant.

Contrary to vector calculus, cohomology allows for metric-free definitions of the above concept, so the geometric term "metric" is exchanged by the topological term "chain complex". Ordinary vector calculus is a covariant theory, since the covariant base vectors are the reference. Cohomology is a contravariant theory, since the chain complexes (which are the reference and are defined in a tangential space) transform in a contravariant manner. This is more natural for electromagnetism than the homology²⁴ concept. Contrary, the covariant homology concept is rather useful, for example, in topological data analysis.

The top of Fig. 2.15 is exemplarily sketched on the left of Fig. 2.16, where additionally the connection to exterior calculus is shown on the right. Following Fig. 2.15, the electric field depicted in Fig. 2.16 is constant along the integration path. Note that both $\underline{\mathbf{E}}$ and ${}^1\underline{\mathcal{E}}$ seem to have got a spatial expansion in Fig. 2.16 caused by illustration purposes. Obviously, they describe instead the field intensity along the z -axis and dz -axis, respectively, as usual in literature.

²⁴In terms of this thesis, homology relates the possible transformation behavior of the boundary operator ${}^p\partial$ between the p -chains in order to detect holes in a topological sense.

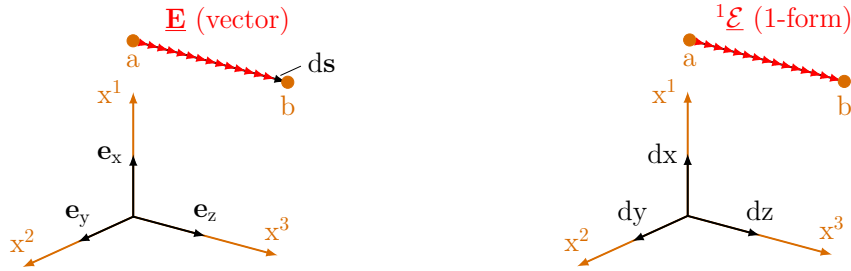


Figure 2.16 Example of integration in vector (left) and exterior (right) calculus: Integration of a vector over a line s from point a to point b described by the differential line element ds , which may be expressed as the sum of a point-wise scalar product. This can be thought in exterior calculus as integration of a 1-form (differential form, a covector which lives in the cotangential space) over a 1-chain (geometric entity, a vector which lives in the tangential space, defined on Ω).

The two ways of integration presented above in Fig. 2.16 yield the same result as

$$\underline{U} = \int_a^b \underline{\mathbf{E}} \cdot d\mathbf{s} = \int_a^b {}^1\xi. \quad (2.36)$$

For more general cases, such as a discussion of gravitational waves (see later on section 2.8), it is of further importance to examine the behavior of ds in general curvilinear coordinates (p -dimensional space). This can be done by the use of the metric tensor, which incorporates an arbitrary desired metric. As usual for matrix notation, the first index p stands for the row and the second index q denotes the column. The metric on a manifold Ω is induced by setting up an inner product, as discussed in section 2.3.1 (see e.g. [172] for details). Since the FEM directly includes coordinates from the mesh data, the following approach from vector calculus is preferredly discussed. Note that this is no restriction to Euclidean spaces in general. It is convenient now to introduce two equivalent representations of an invariant vector (K is the number of dimensions which are spanning this vector space) commonly used in vector calculus (see e.g. [228]) as

$$\underline{\mathbf{E}} = \sum_{p=1}^K \underline{E}^p \mathbf{e}_p = \sum_{p=1}^K \underline{E}_p \mathbf{e}^p. \quad (2.37)$$

The left one of the two representations in (2.37) is usual in vector calculus and will be used throughout this thesis. According to [93], [181], [228] or [230], a squared differential line element ds^2 is build from the matrix representation of generalized contravariant coordinate differentials $[dx^p]$ and $[dx^q]$, which are reordered for matrix multiplication as

$$ds^2 = \sum_{p=1}^K \sum_{q=1}^K g_{pq} dx^p dx^q = [dx^p]^T [g_{pq}] [dx^q], \quad (2.38)$$

where p and q indicate members of the same (co)vector space. This corresponds to the general definition of the tensor product (2.3) presented in section 2.1.2 and can be understood as the Pythagorean theorem valid for general curvilinear coordinate systems. By the use of (2.38), the metric is represented by the squared invariant coordinate differential ds^2 in every point of the space. The symmetric metric tensor can be formulated as a $K \times K$ matrix, denoted as $[g_{pq}]$, which represents all possible pairs of base vectors. In Fig. 2.17, the matrix multiplication of (2.38) is depicted to show the correct dimensionality. Note that in (2.38), the transpose of the contravariant column vector $[dx^p]^T$ is necessary to change its notation, since for building the tensor product in (2.3), one vector has to be transposed, too. By setting the covariant metric coefficients $g_{pq} = 0$ for $p \neq q$, the coordinate system is orthogonal [230]. If $[g_{pq}]$ varies locally, a deformed space can

be represented by changed components of $[g_{pq}]$ at the respective local coordinates, as done on the left in Fig. 2.15 earlier in this section.

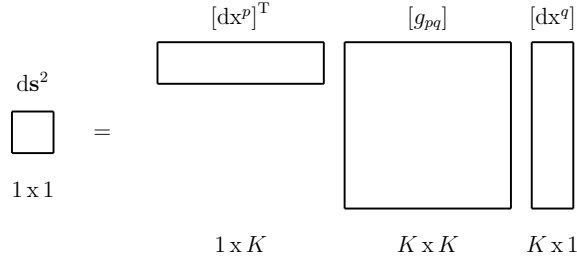


Figure 2.17 Matrix representation of the metric expressed in (2.38).

The Einstein summation convention²⁵ is avoided to achieve improved clarity. Following [181], a generalized tangent / base vector \mathbf{e}_p tangential to a curve / coordinate axis is given by the directional derivative of the generalized coordinates x^p as

$$\mathbf{e}_p = \frac{\partial}{\partial x^p}. \tag{2.39}$$

The covariant \mathbf{e}_p together with the contravariant x^p is in accordance to the concept of covariant vector calculus presented throughout this section. Furthermore, spatial derivatives transform covariantly in general. If the distance between two points becomes smaller, the value of their derivative rises, which confirms these opposite transformation behaviors. It is further useful to introduce the index cancellation rule of raising and lowering indices on the action of the metric tensor elements on base vectors [228] as (see e.g. [228] for the inverse transformation)

$$\mathbf{e}_p = g_{pq} \mathbf{e}^q. \tag{2.40}$$

Only their use as subscript (covector space) or superscript (vector space) distinguishes the membership of these objects. The index cancellation applies also for (2.38), where invariant ds are produced. Note that (2.40) is valid for one element. For matrix representation, (2.40) is rewritten by consideration of correct dimensionality as done in (2.38) to

$$[\mathbf{e}_p]^T = [g_{pq}] [\mathbf{e}^q]. \tag{2.41}$$

To summarize the framework of the de Rham cohomology, Table 2.1 represents important features compared to vector calculus discussed in this section. In Table 2.1, the dots in the last row stand for an arbitrary unit of EM quantities excluding metric dependence.

Table 2.1 Selected features of the de Rham cohomology compared to vector calculus.

Category	(Topological) de Rham cohomology		(Metrical) Calculus
Subcategory	Cohomology	Homology	Vector calculus
Algebraic objects	differential p -forms	p -entities (nodes, edges,...)	vector fields
Differential operator	${}^p d$ (coboundary operator)	${}^p \partial$ (boundary operator)	∇ (Nabla operator)
Reference	dx^p (coordinate differentials)		\mathbf{e}_p (base vectors)
Units of EM quantities	...		$\dots \cdot \text{m}^{-p}$

²⁵The sigma sign (\sum) in front of terms where an index appears more than once is omitted.

Note that in the content of this thesis, cohomology is produced by dualizing homology. Therefore, the de Rham cohomology contains the term "cohomology", furthermore the reference is the homology (p -chain complex). In the following section 2.4.2, the quaternionized cohomology part of the de Rham cohomology will be discussed in detail. Relations between cohomology and homology are especially discussed later on in section 2.4.6. Throughout this thesis, the notation of EM quantities is changed between vector and exterior calculus, depending on what suits best.

2.4.2 Quaternionized De Rham Cohomology

The central idea in DEC is the replacement of vector fields by differential forms. Discretization errors can be better identified than in vector calculus and the approximation of the field quantities is done in a more natural way. The cohomology where the cochains are differential forms is called de Rham cohomology [192]. As a starting point, [239] describes the de Rham cohomology as it measures precisely the extent to which the fundamental theorem of calculus fails in higher dimensions and on general manifolds. An associated aspect is the point that a unique description of an EM field using potentials is only possible if no undefined regions are enclosed in Ω .

A suitable way for presenting the relations of the used differential forms in the continuous setting and in a discretized manner is a specific commutative diagram, called the DEC-de Rham diagram in Fig. 2.18. See [203] for a previous version.

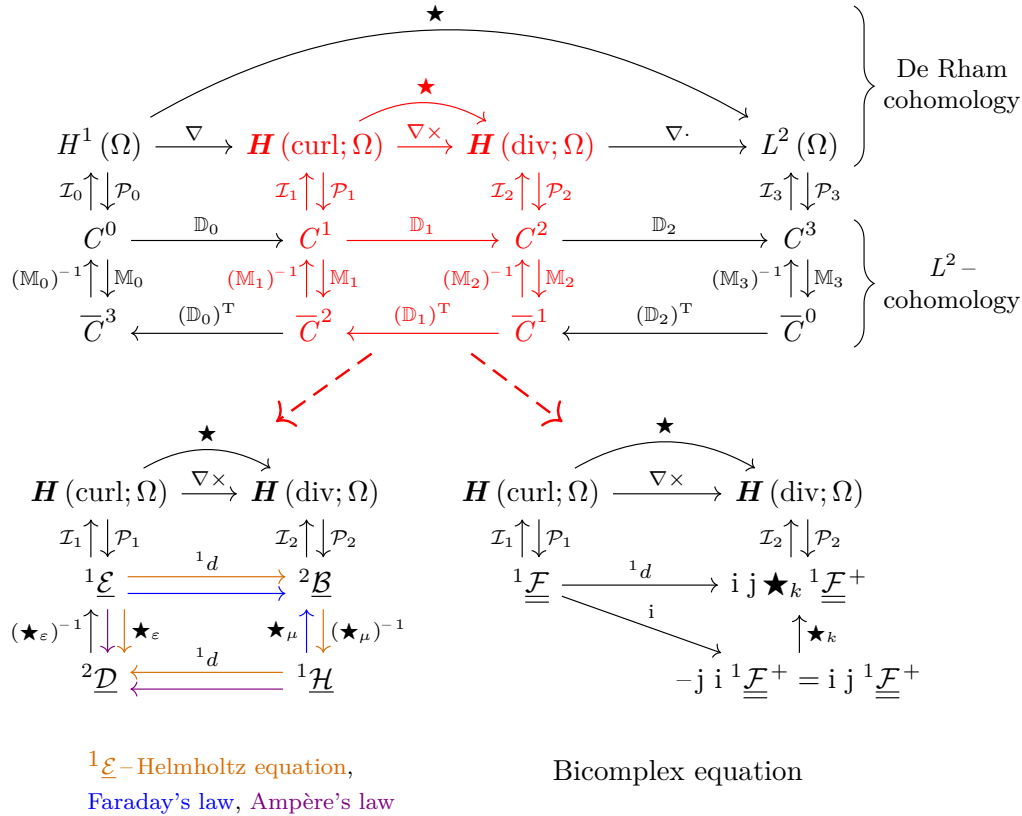


Figure 2.18 The DEC-de Rham diagram for contractible domains in \mathbb{R}^3 is drawn on the top, where the relevant part is marked in red. After elimination of the constitutive equations on the bottom left, the blue lines depict Faraday's law, whereas the violet lines show Ampère's law. The orange lines indicate the Helmholtz equation for the electric field. The bicomplex-valued Pseudo-Helmholtz equation is drawn on the bottom right, which is called "quaternionized de Rham cohomology" throughout this thesis, since the p -forms are bicomplex- instead of complex-valued.

This diagram considers the primal and the dual mesh²⁶ (the dual mesh is an auxiliary construction to geometrically incorporate transformations). On the top of Fig. 2.18, the de Rham diagram of the de Rham cohomology is shown, where the continuous Hodge operator \star maps between inner product spaces. For the discrete setting shown on the middle and the bottom row, the L^2 -cohomology is used, respectively. This is a subcomplex of the de Rham complex, which uses square-integrable differential forms [65]. A formal introduction of the L^2 -cohomology is given e.g. in [65]. For further reading, several subcomplexes of the de Rham complex concerning finite element spaces for three-dimensional manifolds are discussed e.g. in [180]. The discretized primal C^p and dual \bar{C}^p cochain²⁷ spaces are given on the middle and the bottom, respectively. They are visualized later on in section 2.4.4. Following [13], the discrete finite element spaces C^p and \bar{C}^p of p -cochains are finite-dimensional subspaces of the continuous Hilbert spaces $H^1(\Omega)$, $\mathbf{H}(\text{curl}; \Omega)$, $\mathbf{H}(\text{div}; \Omega)$ and $L^2(\Omega)$ of square-integrable scalar and vector fields, respectively. The projection and interpolation maps \mathcal{P}_p and \mathcal{I}_p transform between the de Rham and the L^2 -cohomology, respectively. For an example of primal and dual brick mesh, see Fig. 2.25 in section 2.4.4. In [188], a generalization of the top of Fig. 2.18 – which considers also discrete dual p -cochains – is presented. Discretized operators are $\star \xrightarrow{\sim} \mathbb{M}_p$ and ${}^p d \xrightarrow{\sim} \mathbb{D}_p$. The matrices \mathbb{M}_p and \mathbb{D}_p are exemplarily discussed e.g. in [28]. Table 2.2 shows an overview of the wording used for the discrete setting.

Table 2.2 Wording of the discrete p -dimensional setting in DEC.

Mathematical concept	Quantity	Discrete setting
Cohomology	Single objects	p -forms
	Connectivity of objects	p -cochains
Homology	Single objects	p -entities
	Connectivity of objects	p -chains

It should be noted again that cohomology handles functions in the cotangential space, which is defined on the tangential space handled by homology. For a discussion of connectivity exemplified on a three-dimensional FEM mesh, see e.g. [106].

Before eliminating the constitutive equations (2.43) (see later on in this section), Faraday’s law lies on the middle line and Ampère’s law lies on the bottom left in Fig. 2.18. The de Rham projection map \mathcal{P}_p transforms smooth vector fields to differential p -cochains, the Whitney interpolation map \mathcal{I}_p performs the inverse transformation (see the subsequently shown Fig. 2.19). For a formal definition of \mathcal{P}_p and \mathcal{I}_p , see e.g. [19]. Note that these two maps are different to the musical operators due to their projection / interpolation property. The musical operators only map between p -forms from exterior calculus and tangential vectors from vector calculus, which will be discussed later on in section 2.4.4.

In Fig. 2.19, the transformation behavior of the mimetic operators is exemplified in principle on a brick element. If \mathcal{P}_1 is applied on a smooth vector field on the left (which is defined with reference to a line), the discretized 1-cochain on the right includes only the function values on the

²⁶Following [188], the dual mesh incorporates in the context of the de Rham cohomology the duality between p -forms and $(3 - p)$ -forms, which is a property shared with the Hodge operator discussed later in this section. In [188], the dual mesh is explained regarding p -forms.

²⁷As reported in [188], a p -cochain assigns a physical value to a geometric object, whereas the value which corresponds to a p -chain is assigned to the geometric object as a whole.

four colored edges as nonzero entries. Contrary, the function values on the other eight edges are zero. Since this projection is done on edges instead on zero-dimensional points and therewith preserves the 1-dimensional nature of the vector field, \mathcal{P}_p is called mimetic. Since mimetic methods mimic the continuous level operators [2], the presented FEM approach is a mimetic one. The two maps \mathcal{P}_p and \mathcal{I}_p , which are structures for mimetic discretization of PDEs, are detailed investigated in [28]. In [2], a mimetic finite element framework for Maxwell's equations is discussed by the use of a mixed FEM (there are DOFs assigned to nodes, edges and faces).

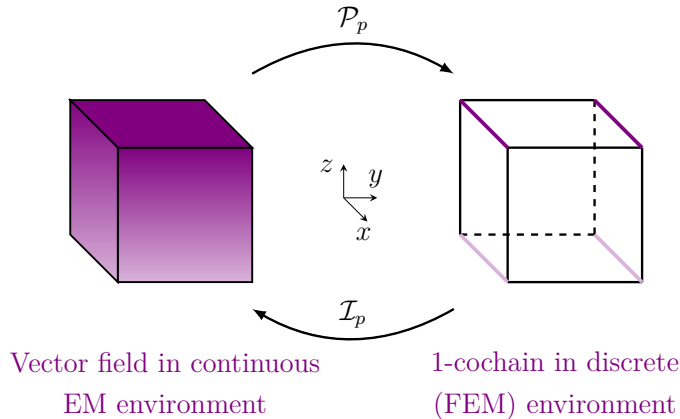


Figure 2.19 Principle of the mimetic operators \mathcal{P}_p and \mathcal{I}_p demonstrated on a brick element. They transform between the continuous and discrete setting. On the continuous left side, the color gradient indicates the intensity of an x -oriented vectorial function with reference to a line, which varies over z . On the discretized right side, only the four nonzero edge values are highlighted.

According to [117], the Maxwell system (2.7a–2.7d) discussed in section 2.2.2 in source-free, three-dimensional space can be alternatively expressed by the use of differential forms as

$$\begin{aligned} {}^1d^1\underline{\mathcal{E}} &= -j\omega^2\underline{\mathcal{B}}, & {}^2d^2\underline{\mathcal{B}} &= 0, \\ {}^1d^1\underline{\mathcal{H}} &= j\omega^2\underline{\mathcal{D}}, & {}^2d^2\underline{\mathcal{D}} &= 0. \end{aligned} \quad (2.42)$$

These equations do not depend on the metric of the underlying manifold. Here, the exterior derivative operator pd acts on 1-forms (the electric and magnetic field intensity ${}^1\underline{\mathcal{E}}$ and ${}^1\underline{\mathcal{H}}$) and 2-forms (the electric and magnetic flux density ${}^2\underline{\mathcal{D}}$ and ${}^2\underline{\mathcal{B}}$) and increases the rank of the form by one. This satisfies the generalized Stokes' theorem (2.34), see section 2.4. The discretized counterpart of pd is the coboundary operator whose adjoint is the boundary operator. In the context of de Rham cohomology, the Hodge Star \star is an isomorphism between p -forms and $(3-p)$ -forms for $p = 0, 1, 2, 3$ [190], which contains the material properties according to [52] as

$$\begin{aligned} {}^2\underline{\mathcal{D}} &= \star_\epsilon {}^1\underline{\mathcal{E}} & \text{or} & & {}^1\underline{\mathcal{E}} &= \star_\epsilon^{-1} {}^2\underline{\mathcal{D}} \\ {}^2\underline{\mathcal{B}} &= \star_\mu {}^1\underline{\mathcal{H}} & \text{or} & & {}^1\underline{\mathcal{H}} &= \star_\mu^{-1} {}^2\underline{\mathcal{B}}, \end{aligned} \quad (2.43)$$

where \star_ϵ includes the permittivity and \star_μ includes the permeability. Equations (2.43) involve the metric in the Hodge operator. By discretizing the Maxwell's equations, only at this point a discretization error is made. The discrete Hodge operator is mathematically discussed, for instance, in [124] and [125]. See e.g. [35] for a discrete Hodge operator for EM wave propagation.

The action of the Hodge star can be intuitively explained by the duality between primal edges and dual faces. For a regular brick mesh, the discrete Hodge star maps the dual forms exactly without an error. If other finite elements are used or the mesh is irregular, an error is introduced by this map. Therefore, discrete Hodge operators are an open topic of research. In order to clarify the geometrical meaning, important connections are depicted in Fig. 2.20.

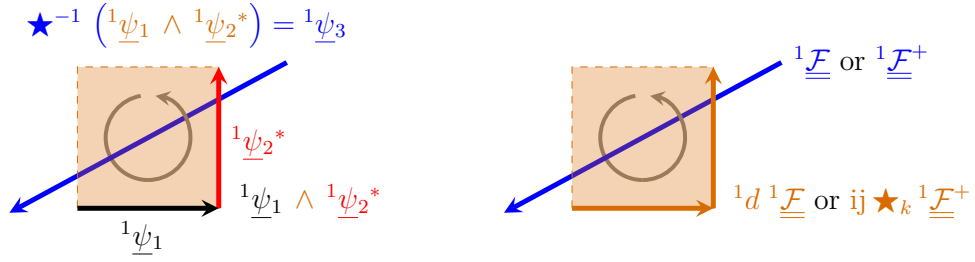


Figure 2.20 Geometric relations of several important operators and operations. Left side: correlation of the Hodge operator to the wedge product. Right side: transformation of the differential bicomplex EM field (drawn in blue) by the exterior derivative and the Hodge operator in accordance to the bottom right of Fig. 2.18.

On the left in Fig. 2.20, the two 1-forms ${}^1\underline{\psi}_1$ (drawn in black) and ${}^1\underline{\psi}_2^*$ (depicted in red) are connected through the wedge product (\wedge) to produce a 2-form (plotted in orange). The inverse Hodge operator acts on this 2-form, which leads to the 1-form ${}^1\underline{\psi}_3$ (drawn in blue). In gray, the orientation of the 2-form is given, which is in accordance to the geometrical meaning of Faraday's and Ampère's law in vector calculus when applying $\nabla \times$ to the (blue colored) line in three spatial dimensions. The right side of Fig. 2.20 shows the geometrical interpretation of the bottom right of Fig. 2.18. Both the exterior derivative 1d and the Hodge operator \star_k transform the differential bicomplex EM field ${}^1\underline{\mathcal{F}}$ (or its outer conjugate) to a 2-form, which fulfills the Pseudo-Helmholtz equation (2.46) presented later on in section 2.4.4.

The Hodge operator \star (compare to Fig. 2.18 and Fig. 2.20) defines an inner product through a metric, which is given for 1-forms by the vectorial Hilbert space \mathbf{H} ($\text{curl}; \Omega$), as

$$\langle {}^1\underline{\psi}_w, {}^1\underline{\psi}_u \rangle = \int_{\Omega} {}^1\underline{\psi}_w \wedge \star {}^1\underline{\psi}_u^* \, d\Omega = \int_{\Omega} {}^1\underline{\psi}_w {}^1\underline{\psi}_u^* \, d\Omega, \quad (2.44)$$

which is valid for a complex-valued 1-form ${}^1\underline{\psi}$. For a possible adaptation of (2.44) to bicomplex-valued 1-forms, see (2.28) in section 2.3.2. The derivation from the second expression in (2.44) – which connects the 1-form via the wedge operator (and considers the Hodge star) to the last expression – can be found e.g. in [181]. This equality means that the conformal approximation of the respective form through a mass matrix in FEM leads to the so-called Whitney Hodge operator. The discrete Whitney Hodge operator used in this thesis concerning general FEM implementation is further discussed, for instance, in [19], where it is called Galerkin Hodge operator. For examples of geometrically defined discrete Hodge operators, see e.g. [18] or [177]. Once the inner product is defined by (2.44), it is possible to introduce various Hilbert spaces on it [15]. When the wedge product connects two forms, a parallelepiped is build as shown for the 2D case in Fig. 2.20 and the resulting form's degree is equal to the sum of both form's degrees. By connecting two 1-forms, an oriented surface (a 2-form) is created. Following [256], this is shown below in (2.45), where the definition of the Poynting vector in DEC ${}^2\underline{\mathcal{S}}$ is given as

$${}^2\underline{\mathcal{S}} = {}^1\underline{\mathcal{E}} \wedge {}^1\underline{\mathcal{H}}. \quad (2.45)$$

The formulation in vector calculus (see later on section 2.6.2) – which uses the cross product (\times) – is a special case of (2.45) and is defined only for 2D and 3D spaces. According to [16] and [252], the wedge product in the field of GA has the advantage that it is applicable to spaces of any dimension, whereas the cross product fails on this task. If $\wedge \star$ acts on a p -form, it does not change the rank, see the conversion from the second to the third expression in (2.44).

It is important to note that the application of the Hodge operator to a field quantity does not change the shape of it, only the form on which that quantity is defined on is changed, which will be of special interest for the Hodge decomposition discussed later on in section 2.4.7.

2.4.3 Whitney Forms and Spurious Solutions

The utilized mimetic finite elements, called Whitney forms, will be introduced now. Since the bicomplex-formulated EM field needs merely the primal mesh for conformal discretization (see Fig. 2.18 in section 2.4.2), no dual mesh is needed at all. Following [19], the approximation of continuous vector fields is done by Whitney p -forms. The possible p -forms which can be defined on a three-dimensional manifold (here the brick element) are shown below in Fig. 2.21.

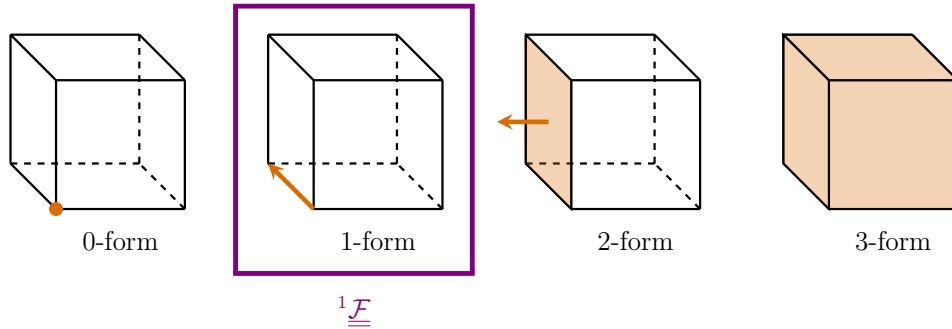


Figure 2.21 Possible p -forms defined on a three-dimensional manifold. For oriented p -forms, an arrow indicates the orientation.

Both the 1-forms and 2-forms depicted in Fig. 2.21 are oriented, whereas 0-forms and 3-forms are not. The 1-form (framed in violet) is important for conformal discretization of the differential bicomplex-valued EM field $\underline{\underline{1\mathcal{F}}}$, which will be discussed in the following sections. Note that the manifold assumed here is three-dimensional, compared to the two-dimensional one presented in Fig. 2.13, see section 2.4. Analogous, the tangential space on the brick element is defined on the boundary, therefore it is two-dimensional. Therewith, possible solutions of a FEM formulation are restricted to be two-dimensional instead of three-dimensional as the manifold. By continuing this idea, the 1-form which allows only values on an edge itself, restricts the solution space to be one-dimensional. This explains the suppression of spurious modes, done by the use of Whitney elements instead of vectorial nodal elements. For conformal discretization of EM wave propagation on a primal grid, edge elements are used. Therefore, a deeper investigation of their properties is convenient.

In Fig. 2.22, the tangential continuity of a normalized field intensity using Whitney edge elements on two brick elements is shown.

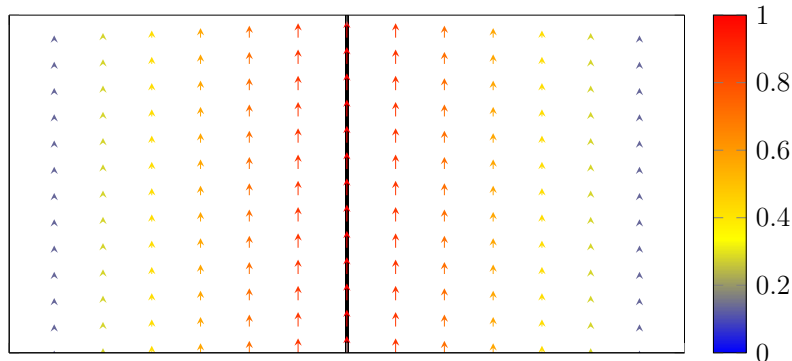


Figure 2.22 Principle of tangential continuity of a normalized field intensity using Whitney edge DOFs (1-forms, compare to the second illustration from the left in Fig. 2.21) on brick elements. See Fig. 2.23 below for the three-dimensional behavior of one edge-based shape function's normalized field intensity.

On the middle of Fig. 2.22, where the element transition is placed, the tangential field shows a continuous behavior. Merely the shared edge on the transition has got a nonzero value. Therewith, a conformal approximation of 1-forms (or in vector calculus: vectors) is possible. Furthermore, the used brick elements are free of divergence, which fulfills Gauss's law for magnetism (2.7c) and its counterpart for electricity (2.7d) – discussed in section 2.2.2 – implicitly. Note that for a general finite element, these divergence equations have to be explicitly fulfilled, since neglecting of them is a possible origin of spurious solutions [123]. Regarding a general discussion concerning spurious solutions in terms of computational electromagnetics, see e.g. [141].

The interpolated normalized field intensity of a sample Whitney edge-based shape function is depicted below in Fig. 2.23.

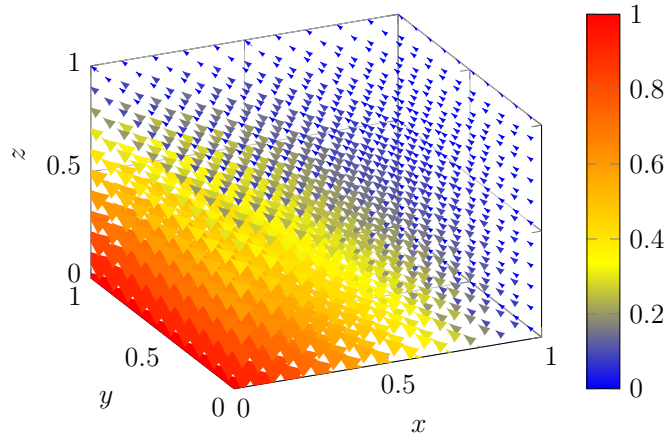


Figure 2.23 Exemplary normalized field intensity of a Whitney edge-based shape function in the unit cell of the brick element. It shows the 3D alternative of Fig. 2.22 on one finite element.

A constant field can be observed along the edge depicted on the bottom left of Fig. 2.23, where the y -directed field intensity decreases radially perpendicular to this edge. By combining different edge values, several field pattern can be constructed. Note that merely particular field variations can be represented exactly. Therefore, the tetrahedral finite element has got shortcomings when applying the bicomplex FEM. For graphical illustration of other shape functions defined on the brick element than the one presented in Fig. 2.23, see e.g. [269]. To clarify further the difference to commonly used scalar 0-forms, Fig. 2.24 shows the normalized field intensity of a sample nodal-based shape function.

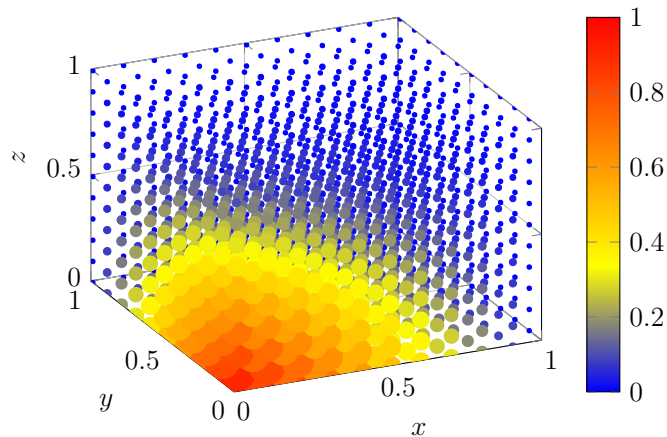


Figure 2.24 Exemplary normalized field intensity of a Whitney nodal-based shape function in the unit cell of a brick element.

The field decays from the brick's corner on the bottom left in Fig. 2.24 radially in every direction. One can imagine that the approximation through 0-forms has got other merits and shortcomings. Since nodal vector-valued shape function might have independent values for their components, spurious modes may arise in a higher amount than for edge-based shape functions. Roughly said, the FEM have got a larger solution space and, therefore, more possibilities to fail. According to [234], spurious modes arise in the solution of the vector wave equation, if the wrong differential form is used to approximate the electric field vector. This means, for instance, the standard nodal finite elements presented above in Fig. 2.24. In [234], it is further stated that the true cause of spurious modes is the incorrect approximation of the null space of the curl operator. This is discussed in detail later on in section 2.4.6.

2.4.4 Generalized Conformal Discretization of the Pseudo-Helmholtz Equation

This section clarifies profoundly the proposed metric-free definition of the bicomplex EM field. The term "generalized" in the heading refers to a metric-free definition of the bicomplex PDE. In the context of DEC, it is a common practice to discretize Faraday's and Ampère's law on separate grids [19, 211]. Exemplary for a brick mesh, the primal and dual mesh constructed by brick elements is illustrated below in Fig. 2.25.

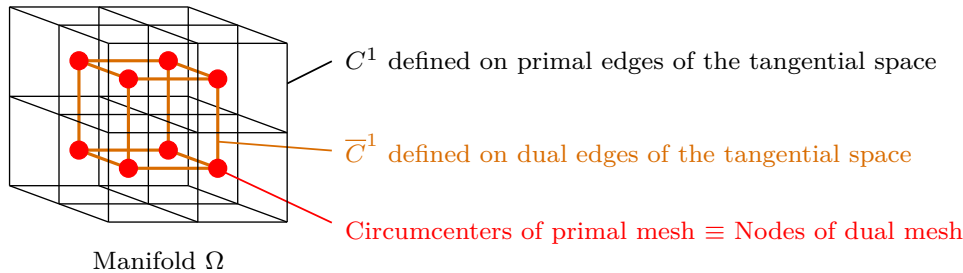


Figure 2.25 Primal and dual brick mesh. The circumcenters of the primal mesh are used as nodes for the dual mesh. For relations between the discretized primal C^1 and dual \bar{C}^1 cochain spaces, see Fig. 2.18 in section 2.4.2.

Note that merely eight elements of the primal mesh (black cubes) and one element of the dual mesh (orange cube) are shown, respectively, to reveal the mesh construction. Contrary for a tetrahedral mesh, the dual mesh is not unique, several possibilities are, among others, the Voronoi dual and the barycentric dual [177]. A widely known problem which arises when using both meshes is the truncation of the dual mesh at the boundary of the manifold $\partial\Omega$.

Contrary to the approach of using two meshes mentioned above, the differential bicomplex-valued field intensity ${}^1\underline{\mathcal{F}}$ is discretized merely on the primal mesh (see Fig. 2.18 in section 2.4.2 for details). Based on the derivation of (2.6) (presented in section 2.2.2) in [202], the Pseudo-Helmholtz equation in the context of DEC is

$${}^1d {}^1\underline{\mathcal{F}} = ij \star_k {}^1\underline{\mathcal{F}}^+, \quad \text{where } \star_k = \omega \sqrt{\star_\mu \star_\varepsilon}. \quad (2.46)$$

By assuming lossless media, the wavenumber Whitney Hodge operator \star_k is real-valued. Edge elements yield a conformal approximation in the quaternionized de Rham cohomology, see Fig. 2.18. Contrary to biquaternions, where the pseudoscalar²⁸ maps a p -form like the Hodge operator to

²⁸The pseudoscalar is build by the product of all basis vectors as shown in Fig. 2.9 (see section 2.1.2), see e.g. [252] for further reading.

the orthogonal complement [213], the pseudoscalar / imaginary unit i used throughout this thesis is a map from ${}^1\mathcal{H}$ to ${}^1\mathcal{E}$ and, therefore, a map between dual 1-forms and primal 1-forms as for the RHS of (2.46). As an inverse map, $i^{-1} = -i$ projects ${}^1\underline{\mathcal{F}}^+$, which exists like ${}^1\mathcal{E}$ on the primal mesh, from the primal to the dual mesh. Then, \star_k acts on ${}^1\underline{\mathcal{F}}^+$, which results in a primal 2-form. The LHS of (2.46) is transformed by 1d from a primal 1-form to a primal 2-form, as ordinarily done for Faraday's law (see Fig. 2.18).

When setting up the inner product in (2.44) (see section 2.4.2), the field problem becomes non-self-adjoint because of the first term of (2.32), see section 2.3.2. Therefore, a suitable stabilization technique has to be applied. For three-dimensional examples discussed in this thesis, instable cases are avoided by special discretization. Multidimensional stabilization is examined e.g. in [207]. A short overview on stabilization techniques for the type of the bicomplex PDE is given in appendix E. Furthermore, appendix F shows a sketch to stabilize (2.32) for the 1D-case.

Since this thesis aims at a conformal discretization of the bicomplex EM field, also the curl operator ($\nabla \times$) of vector calculus needs a conformal discrete version in addition to the EM field $\underline{\mathbf{F}}$ itself. For this, it is appropriate to further investigate the two musical operators, which were introduced in section 2.4 as mappings from p -vectors to p -covectors (done by flat \flat) and from p -covectors to p -vectors (done by sharp \sharp), respectively. In other words, they transform between the tangential and cotangential space. According to [198], their effect is equivalent to that of the covariant metric tensor g_{pq} presented in (2.38) of section 2.4.1. In accordance to the notation of [105], this yields for the bicomplex EM field the two transformation rules

$${}^1\underline{\mathcal{F}} = \underline{\mathbf{F}}^\flat \quad \text{and} \quad \underline{\mathbf{F}} = {}^1\underline{\mathcal{F}}^\sharp. \quad (2.47)$$

Note that these expressions are rather based on interpretation than on mathematical equality, since the coordinate differential ds has to be included in ${}^1\underline{\mathcal{F}}$ compared to $\underline{\mathbf{F}}$ (see Fig. 2.26 below).

Next, it is appropriate to present an adequate level of detail and show a concept of the integral kernel of (2.36) (see section 2.4.1), which is also valid in general relativity (GR). In order to achieve this, (2.35) of section 2.4.1 is illustrated in more detail regarding both definitions of the bicomplex EM field for vector calculus and exterior calculus below in Fig. 2.26.

Vector calculus: contravariant vector components with covariant \mathbf{e}_p -base

$${}^1\underline{\mathcal{F}} = \left(\sum_{q=1}^K \underbrace{(g^{pq} \underline{F}_p)}_{\underline{F}^q} \mathbf{e}_q \right) \cdot \left(\sum_{p=1}^K dx^p \mathbf{e}_p \right) \xrightarrow{\mathbb{R}^3} \begin{pmatrix} \underline{F}^1 \mathbf{e}_1 \\ \underline{F}^2 \mathbf{e}_2 \\ \underline{F}^3 \mathbf{e}_3 \end{pmatrix} \cdot \begin{pmatrix} dx^1 \mathbf{e}_1 \\ dx^2 \mathbf{e}_2 \\ dx^3 \mathbf{e}_3 \end{pmatrix} = \underline{F}_1 dx^1 + \underline{F}_2 dx^2 + \underline{F}_3 dx^3$$

Exterior calculus: covariant vector components with contravariant dx^p -base

Figure 2.26 Connection of the bicomplex-valued EM field between vector calculus and exterior calculus by the use of the metric tensor, valid for generalized coordinates in GR. Contravariant quantities are illustrated in orange, whereas covariant quantities are depicted in blue. Invariant quantities as well as operations are drawn in black. The explicit contravariant metric tensor is marked in violet, whereas the implicit covariant metric tensor is encoded in the scalar product of the covariant base vectors. Regarding the effect of the musical operators, see Fig. 2.27.

For the vector calculus representation shown in Fig. 2.26, the metric is included to the field components and coordinate differentials by means of the metric tensor or its inverse, respectively. As in (2.37) and (2.38) in section 2.4.1, K represents the number of dimensions which are spanning the vector space. If the covariant bicomplex-valued EM field components \underline{F}_p are multiplied by the inverse metric tensor g^{pq} in the first bracket, contravariant field components \underline{F}^q are received after

application of the index cancellation rule shown in (2.40) of section 2.4.1. Following [228] and using the commutative property of the two arguments of the scalar product, the elements of the metric tensor (implicitly expressed through the scalar product, see Fig. 2.26) can be derived as

$$g_{pq} = \mathbf{e}_p \cdot \mathbf{e}_q = \mathbf{e}_q \cdot \mathbf{e}_p. \quad (2.48)$$

It is obvious now that one entry of the metric tensor is another formulation of the inner product of two elements which belong to the same covector space. The covariant metric tensor for the second bracket of Fig. 2.26, which builds ds , is expressed through the scalar product of that covariant base vectors, where \mathbf{e}_q is placed in the first bracket and \mathbf{e}_p is placed in the second bracket. After usage of (2.48), a multiplication of $[g^{pq}]$ by $[g_{pq}]$ yields the identity matrix. The dot product of $\underline{\mathbf{F}}$ and ds gives finally the differential form ${}^1\underline{\mathcal{F}}$, which is independent of metric (invariant under base change). This shows that only the representation is changed when a musical operator is applied. Despite the fact that the vectorial $\underline{\mathbf{F}}$ and the differential ${}^1\underline{\mathcal{F}}$ are invariant quantities, the vector components \underline{F}^q of $\underline{\mathbf{F}}$ have to compensate the changed \mathbf{e}_q if a base change occurs. However, for the components of ${}^1\underline{\mathcal{F}}$, no variations arise, since ${}^1\underline{\mathcal{F}}$ is independent of the metric. Note that the numerical values of the covariant bicomplex-valued EM field components \underline{F}_p act as scaling factors for the differentials, as obvious on the right of Fig. 2.26.

For clarity, Fig. 2.27 shows the mappings between the tangential and the cotangential space induced by the musical operators \flat and \sharp , respectively.

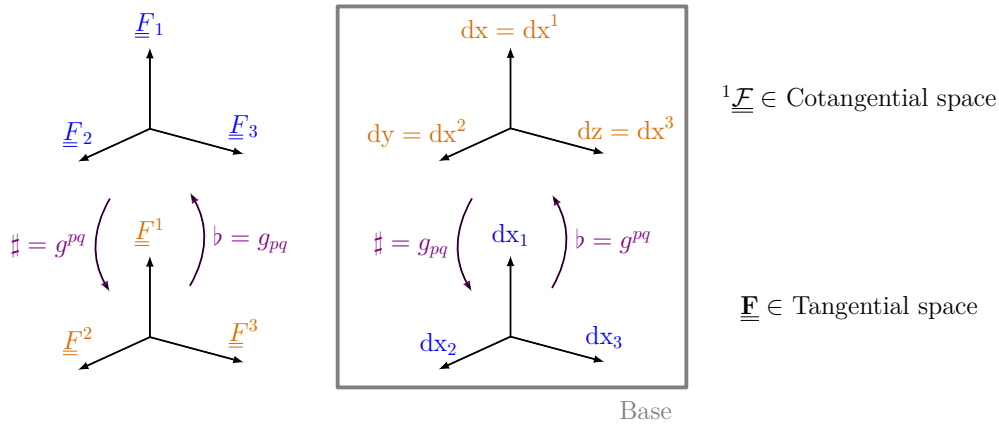


Figure 2.27 The musical operators (drawn in violet) map as isomorphisms between the cotangential space (placed on the top) and the tangential space (placed on the bottom). Applied to the bicomplex-formulated EM field components on the left, they map between co- and contravariant vector field components, respectively. On the right, they map between contra- and covariant coordinate differentials, respectively. For an overview of the used quantities, see Fig. 2.26.

The cotangential space (drawn on the top of Fig. 2.27) includes metric-independent covariant differential forms ${}^1\underline{\mathcal{F}}$, which are defined with respect to the contravariant coordinate differentials. Contrary, the tangential space (drawn on the bottom of Fig. 2.27) includes metric-dependent contravariant tangential EM fields $\underline{\mathbf{F}}$, which are defined regarding covariant coordinate differentials. In accordance to the definition of ordinary vector field quantities e.g. in [105] or [127], it follows

$$\nabla \times \underline{\mathbf{F}} = \left(\star {}^1d \underline{\mathbf{F}}^\flat \right)^\sharp = \left(\star {}^1d {}^1\underline{\mathcal{F}} \right)^\sharp. \quad (2.49)$$

Note the additional Hodge operator \star in front of 1d , which arises not on the LHS of the bicomplex PDE of exterior calculus (2.46). Here, \star maps back from a 2-form to a 1-form, since in vector calculus, all vectors correspond to 1-forms. The expression ${}^1d {}^1\underline{\mathcal{F}}$ is conformally discretized in FEM by the use of a convection matrix based on Whitney edge DOFs, see e.g. (3.13) defined later in section 3.5 for brick elements.

2.4.5 Generalized Conformal Discretization of the Helmholtz Equation

This section shows an interpretation of ordinary Helmholtz equations in the framework of DEC to model EM wave propagation as a comparison to the presented bicomplex concept. In order to distinguish the first from the latter, the solution spaces of both PDEs are discussed. At the end of this section, the FEM implementation of the DEC-Helmholtz equations is explained.

The vector Helmholtz equations of vector calculus (2.13a, 2.13b) discussed in section 2.3.1 are rewritten (see e.g. [51]) by combining the first and third term, respectively, to

$$\begin{aligned}\nabla \times \left(\frac{1}{\mu} \nabla \times \underline{\mathbf{E}} \right) &= \omega^2 \varepsilon \underline{\mathbf{E}} \\ \nabla \times \left(\frac{1}{\varepsilon} \nabla \times \underline{\mathbf{H}} \right) &= \omega^2 \mu \underline{\mathbf{H}}.\end{aligned}\quad (2.50)$$

The following equations are oriented on [117] and contain possible conformal Whitney Hodge operators for an interpretation of the ordinary Helmholtz equations of vector calculus in DEC. In the context of DEC, (2.50) are converted by use of (2.42) and (2.43) of section 2.4.2 to

$$\begin{aligned}{}^1d \star_{\mu}^{-1} {}^1d {}^1\underline{\mathcal{E}} &= \omega^2 \star_{\varepsilon} {}^1\underline{\mathcal{E}} \\ {}^1d \star_{\varepsilon}^{-1} {}^1d {}^1\underline{\mathcal{H}} &= \omega^2 \star_{\mu} {}^1\underline{\mathcal{H}}.\end{aligned}\quad (2.51)$$

As in vector calculus, two independent Helmholtz equations (2.51) are available in exterior calculus²⁹. Similar to the limitation of possible solutions achieved by Whitney elements discussed in section 2.4.3, Fig. 2.28 shows a further limitation of the solution space of the bicomplex PDE compared to Helmholtz PDEs, where $k = \omega \sqrt{\mu \varepsilon}$.

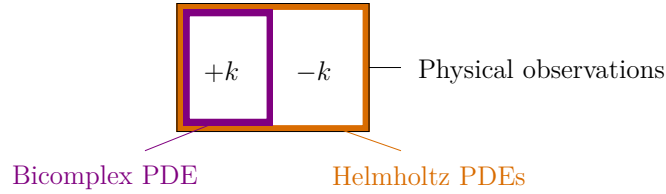


Figure 2.28 Solution spaces of the two used kinds of PDEs.

As shown in Fig. 2.28, the Helmholtz PDEs (depicted in orange) cover both possible physical solutions (indicated in black), which are the two directions of propagation based on the positive and negative wavenumber k with its associated EM field components. Contrary, the bicomplex PDE (2.46) discussed in section 2.4.4 includes only one direction of propagation (see the violet frame in Fig. 2.28), which will be discussed in detail later on in section 2.7. The expression ${}^1d \star_{\mu}^{-1} {}^1d {}^1\underline{\mathcal{E}}$ used in (2.51) is in general a stiffness matrix in the Whitney FEM³⁰. For a detailed discussion of FEM implementation, see later on Chapter 3. By the use of Whitney edge elements for expressing ${}^1d \star_{\mu}^{-1} {}^1d {}^1\underline{\mathcal{E}}$ and ${}^1d \star_{\varepsilon}^{-1} {}^1d {}^1\underline{\mathcal{H}}$ as a stiffness matrix, respectively, and $\star_{\varepsilon} {}^1\underline{\mathcal{E}}$ and $\star_{\mu} {}^1\underline{\mathcal{H}}$ as a mass matrix, respectively, both ${}^1\underline{\mathcal{E}}$ and ${}^1\underline{\mathcal{H}}$ are conformally approximated. For an implementation of this technique, see e.g. [9]. In [34], Whitney elements are considered regarding variational formulations. For further reading, variational formulations of EM problems in the context of differential geometry are discussed in [44]. An additional important difference regarding FEM implementation of (2.51) compared to the bicomplex PDE (2.46) presented in section 2.4.4 is that another kind of boundary conditions is suitable (see later on section 3.6 for details).

²⁹Other formulations are also possible, see e.g. [117] for an alternative dual wave equation.

³⁰The Whitney FEM uses DOFs on p -forms (Whitney forms) rather than only on nodes.

2.4.6 Topological Concept

This section shows a possible topological concept of the bicomplex-formulated Maxwell system by a quaternionization of the de Rham cohomology. To avoid an in-depth mathematical investigation, merely those quantities and relations which are important here will be discussed. For a detailed discussion of differential forms from a topological perspective, see e.g. [214]. A mathematical introduction to algebraic topology can be found, for instance, in [208]. For a broader description, see e.g. [145]. There, simplicial complexes, function spaces and differential forms are presented regarding cohomology. Topological aspects of EM problems from the perspective of the FEM are investigated e.g. in [14] or [192]. The manifolds addressed in this thesis represent simple connected spaces. Applications of (co)homology computation in low frequency electrodynamics can be found for example in [83]. Eddy current problems are discussed e.g. in [82]. Another important application of computational homology is digital image processing, see e.g. [145]. By the use of differential forms ${}^p\psi$ and the exterior derivative pd in the de Rham cohomology of a smooth manifold Ω , non-trivial topologies can be studied, which is outside the scope of this thesis. For problems of this kind, like holes or tunnels, a practice-oriented discussion of induction heating is presented in [192]. The concept of homology is used to detect holes in a manifold's geometry, whereas the cohomology is used to study functions which are defined on this manifold in calculus. A hole in the homology corresponds to a discontinuity of a function located in this hole (cohomology), which results e.g. in invalidity of integral theorems as for the generalized Stokes' theorem (see (2.34) in section 2.4).

A general overview of the topological relationships between the cochain complex (or: de Rham complex) and the chain complex is sketched below in Fig. 2.29.

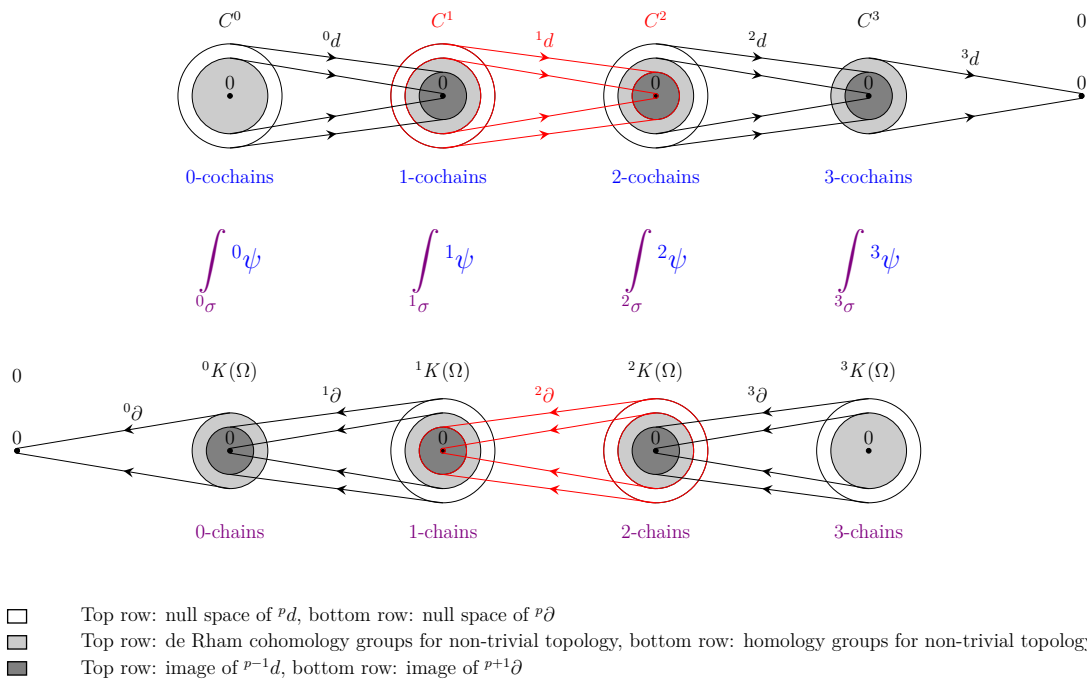


Figure 2.29 Duality in different spaces: Cochain and chain complex on the manifold Ω . The generalized Stokes' theorem (2.34) further shows this duality between cohomology and homology.

Figure 2.29 is oriented on [138] and [154], the consideration of conformal integration related to Stokes' theorem (2.34) – shown on the middle row of Fig. 2.29 – is inspired by [149]. As discussed at the beginning of section 2.4, vector spaces of p -forms C^p used for FEM handling are defined on Ω . These Hilbert spaces, which limit the underlying cotangential space to certain values (e.g.

edge values in the case of C^1 , which suppress spurious modes in FEM, see especially section 2.4.3), are elaborately examined in [31]. They are isomorphic to the equivalence class of p -forms. The top row of Fig. 2.29 shows the de Rham complex, where the spaces of arbitrary complex differential forms ${}^p\psi$ are placed. They mimic the vector fields of the EM field quantities. The circles represent distinct subsets of the respective p -form or p -chain. On the bottom, the chain complex – where the boundary operator ${}^p\partial$ act on – is placed. The p -chains form the manifold Ω in a spatial sense and represent the underlying tangential space (which corresponds in the FEM framework to the mesh). The operator ${}^p\partial$ acts on the boundary of the space of p -chains ${}^pK(\Omega)$, or – in the context of FEM – on the entities of the mesh. It is obvious from the transformation behavior that when applying pd (or ${}^p\partial$) twice, the result is in every case zero. This yields several vector identities known from vector calculus. A general rule for applying the respective differential operator (homomorphism) to a p -form or p -chain on simply connected domains is

$$\text{null space}({}^pd) = \text{image}({}^{p-1}d) \quad \text{and} \quad \text{null space}({}^{p-1}\partial) = \text{image}({}^p\partial), \quad (2.52)$$

respectively, where the operators pd and ${}^p\partial$ act on the generalized Hilbert space of p -forms C^p on the top row and on the generalized space of p -chains ${}^pK(\Omega)$ on the bottom row, respectively. In words, the first equation of (2.52) means that the null space³¹ of pd is identical to the image³² of ${}^{p-1}d$ in the upper sequence of Fig. 2.29. The null space of an operator is also known in literature as the space of closed p -forms, whereas the image of an operator is also known as the space of exact p -forms. Following [93], the p -th de Rham cohomology group for a general topology H_{dR}^p is then the finite-dimensional quotient space³³

$$H_{\text{dR}}^p = \frac{\text{null space}({}^pd)}{\text{image}({}^{p-1}d)} = \frac{\text{closed } p\text{-forms}}{\text{exact } p\text{-forms}}. \quad (2.53)$$

However, by handling homology as a quotient group, the homology group of Ω captures the interaction between p -cycles in Ω that come from looking at dimension $p - 1$ and p -boundaries in Ω , that come from looking at dimension $p + 1$ [214]. If the space of the denominator is equal to the space of the numerator, the dimension of H_{dR}^p is zero. Exemplary for vector spaces which are different in one dimension, the dimension of H_{dR}^p is one, and so forth. Note that if one handles a homology group instead of a cohomology group, the denominator is changed to $\text{image}({}^{p+1}\partial)$ and the numerator is changed to ${}^p\partial$. This counterpart to (2.53) for homology instead of cohomology is reported e.g. in [145]. According to the Poincaré-Lemma [144] for the de Rham cohomology, the null space of ${}^pd \equiv \text{image of } {}^{p-1}d$ holds for trivial topology.

The de Rham cohomology groups H_{dR}^p are included in Fig. 2.29 (depicted in gray), where one can see that they do not transform with a differential operator. Non-trivial topologies arise e.g. in eddy current formulations which are based on the magnetic scalar potential [81]. There, conductive regions form holes (which corresponds to the Betti number $b_2(\Omega) \neq 0$) in Ω . In [206], loop fields³⁴ are discussed as a further example. A common practice is to insert spatial cuts into Ω to make the topology of Ω simply connected (\equiv trivial), as done, for instance, in [81–83] or [106]. If one determines the Betti numbers (see later on in (2.54)) of a meshed manifold, it is clear whether these cuts are necessary or not to receive a simply connected domain. The space of

³¹Informally, the null space (or: kernel) of an operator contains all objects which are mapped to the zero vector when applying that operator to these objects.

³²The image of an operator is appropriately understood as the nonzero output of that operator.

³³For a quotient space, the space in the denominator is a subspace of the numerator's space. Note that the fraction line is not meant algebraically as for numbers, it is rather formalistic to express inequality of two spaces.

³⁴Loop fields are curl-free vector fields which cannot be expressed as the gradient of any single-valued scalar potential.

2-forms which are curl-free and where the divergence vanishes is H_{dR}^2 , an example is an impressed current density inside a current-carrying wire loop. On the top row of Fig. 2.29, the red marked bicomplex formulation shares the properties of the de Rham cohomology and does not affect the relations there. Especially the curl operator is important, because only this operator is used in the bicomplex-valued differential equation (2.6), see section 2.2.2.

As previously discussed on Fig. 2.29, the duality of cohomology and homology leads to the idea that the embedding of the spatial quaternionization of a temporal complex EM field is possible on both the cohomology or the homology, which is shown below in Fig. 2.30.

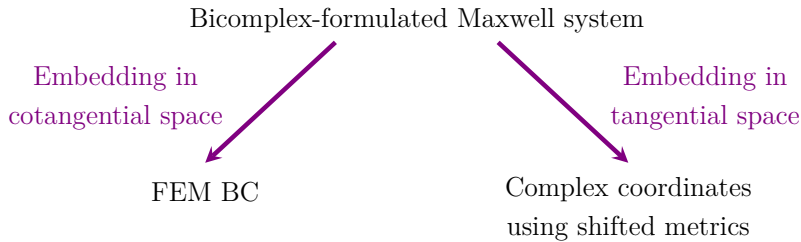


Figure 2.30 Possible embeddings of bicomplex EM wave field.

Based on the typical procedure in FEM of designing the function space (which is the cotangential space of the cohomology and lies spatially on the tangential space, see the top of Fig. 2.27 presented in section 2.4.4), the left way of Fig. 2.30 is chosen, called the cohomology concept. The embedding on the right, called the homology concept, covers the proposed approach presented in Fig. 2.8 (see section 2.1.2), where a shifted metric is used to embed the magnetic field. There, the cotangential space is simply temporal complex and the tangential space is spatially complex. Later on in section 2.8, the choice of cotangential space will be further justified.

As mentioned in section 2.4.3, the used brick and tetrahedral elements are free of divergence. Therefore, the image of the 2d -operator depicted in Fig. 2.29 is empty and on C^2 there is merely the de Rham cohomology group (which is also zero, since in this thesis only simply connected domains are used) and the image of the curl operator (which is for simply connected domains equivalent to the null space of the div operator) as 2-forms (electric and magnetic flux density).

The image of the 0d -operator is equivalent to the null space of the 1d -operator (1-forms electric and magnetic field), which exists on C^1 . Furthermore, 1-forms (which have got a nonzero curl) are members of this space. The de Rham cohomology groups are mapped to zero through ${}^p d$, whereas the homology groups are mapped to zero through ${}^p \partial$. The different integrations shown on the middle row of Fig. 2.29 connect the two complexes. Starting with the left formulation depicted in Fig. 2.29, the integration of scalar 0-forms is defined pointwise. Secondly, vectorial 1-forms have to be integrated along a path. Contrary to this, the integration of a vectorial 2-form is defined on areas. The right side is related to the integration of scalar 3-forms over volumes.

The existence of holes in the topology corresponds to the dimension of H_{dR}^p . This is expressed by the p -th Betti number (see e.g. [73], [106] or [214]) of the p 'th cohomology group, which counts the number of linearly independent p -forms on Ω as

$$b_p(\Omega) = \dim(H_{\text{dR}}^p). \quad (2.54)$$

The first Betti number $b_0(\Omega)$ is the number of connected components, the second one $b_1(\Omega)$ counts two-dimensional holes (or tunnels) and the third one $b_2(\Omega)$ represents the number of spherical holes. Higher Betti numbers are not intuitively accessible and furthermore not of interest in the electrodynamics considered in this thesis. Betti numbers regarding simple geometrical entities are discussed e.g. in [69], [93] or [254]. The analysis of the topologically invariant Betti numbers has got several technical applications, like data compression by identifying these key

topological features in [78] or pattern recognition through identification of deformed printed letters as discussed in [131]. According to [102], the cubical complex (which is in this thesis the manifold Ω , meshed with brick elements) is a class of cell complex³⁵. The cells of this complex are cubes of different dimensions. In [102], an algorithm which computes the Betti numbers of cubical complexes is presented. See e.g. [145] or [214] for further investigations on cubical complexes.

The Euler-Poincaré characteristic $\chi(\Omega)$ (see e.g. [102] or [247]) depicts a relation of the Betti numbers, which is also valid for cubical complexes as

$$\chi(\Omega) = b_0(\Omega) - b_1(\Omega) + b_2(\Omega). \quad (2.55)$$

As for the tetrahedral complex discussed in [69], the computation of $b_1(\Omega)$ for H_{dR}^1 is much more complicated than for both $b_0(\Omega)$ and $b_2(\Omega)$. The direct evaluation of $b_1(\Omega)$ by identifying all independent 1-cycles of the respective homology group can be circumvented by obtaining $b_1(\Omega)$ from (2.55) [102]. In this way, the value of $\chi(\Omega)$ might be obtained based on the respective number of p -entities contained in Ω through the Euler characteristic [247] as

$$\chi(\Omega) = n_0(\Omega) - n_1(\Omega) + n_2(\Omega) - n_3(\Omega), \quad (2.56)$$

where $n_0(\Omega)$ is the number of nodes (0-entities), $n_1(\Omega)$ is the number of edges (1-entities), $n_2(\Omega)$ is the number of faces (2-entities) and $n_3(\Omega)$ is the number of volumes (3-entities). Note that the value of $\chi(\Omega)$ in (2.55) is the same as that for $\chi(\Omega)$ in (2.56). Both (2.55) and (2.56) are described in a larger extend in [214].

In general, for entities of dimension three relevant in this thesis, a more intuitive concept is applicable to obtain $b_1(\Omega)$ for H_{dR}^1 . It is widely known (e.g. from network theory: Kirchhoff's circuit laws), that there are $N - 1$ independent equations, where N is the number of unknowns. This relation is also applicable for shape functions in FEM, imagine e.g. a prism, a tetrahedral or a brick element. For all of these entities, one shape function can be obtained by superposing the others. In more precise words, on the example of the brick element, the sixth 1-cycle (this means a loop composed by 4 edges respectively) can be expressed by superposing the five other 1-cycles, drawn in Fig. 2.31. There, a circulation is equivalent to the boundary of a square.

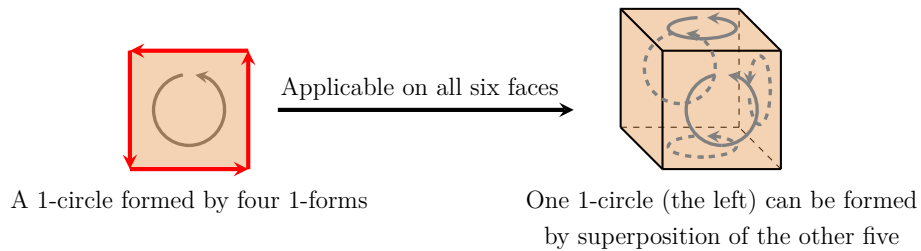


Figure 2.31 Intuitive process to determine the first Betti number $b_1(\Omega)$ for H_{dR}^1 . Since an arbitrary 1-circle overdetermines the system, it has to be subtracted as $b_1(\Omega) = 6 - 1 = 5$. This is summarized for various H_{dR}^p and two kinds of entities in Fig. 2.35, see later on section 2.4.7.

As shown for the Hodge operator in Fig. 2.20 (see section 2.4.2), the wedge product of two 1-forms yields a 2-form with a circulating orientation, which can be used here for describing two-dimensional holes. Intuitively, one would count these two-dimensional holes of the lattice formed by the edges, which would yield 6 corresponding to the number of faces. The possibility of superposition yields then a reduction by one for $b_1(\Omega)$. This is in accordance to [214], where it is reported and pictured out – in the context of topology of graphs – that the number of holes equals the number of linearly independent cycles. Note that this reduction of $b_1(\Omega)$ is only applicable for polygons without exclusions of p -entities (see [78] for a counterexample).

³⁵A cell complex is a broader classification of a chain complex.

2.4.7 Topological Study

The following topological study is valid for both the bicomplex EM field $\underline{\mathbf{F}}$ and the electric field $\underline{\mathbf{E}}$ / magnetic field $\underline{\mathbf{H}}$, respectively, since the bicomplex formulation is isomorphic to the Maxwell system, as discussed in connection with Fig. 2.4 (see section 2.1.1). From a practical view on EM fields, it is also of importance to investigate an extension of the de Rham complex: the Hodge decomposition. The Hodge decomposition theorem plays a significant role in the study of PDEs [36]. This section shows the principle of Hodge decomposition which splits the bicomplex EM field into mutually L^2 -orthogonal³⁶ subspaces \mathbf{X} (colored to improve the general view) to investigate the cohomology more in-depth. Additionally, as an example, a topological study of a given cubical or tetrahedral complex (brick or tetrahedral mesh) is done concerning the behavior of the cohomology based on homology, which may represents the handling of the bicomplex FEM.

The presented Hodge decomposition³⁷ is mainly oriented on [40] and [87]. Application of the Helmholtz-Hodge decomposition in the FEM environment to decompose Maxwell's equations into a divergence-free and a curl-free field is discussed e.g. in [179]. Helmholtz decomposition is addressed with respect to FEM e.g. in [184]. An approach for Hodge decomposition using DEC regarding computational modeling is shown for example in [73]. According to [40], the Hodge decomposition theorem states that an infinite-dimensional vector space $\text{VF}(\Omega)$ of all smooth vector fields $\mathbf{X} \in \underline{\mathbf{F}} / \underline{\mathbf{E}} / \underline{\mathbf{H}}$ in Ω , on which the L^2 -inner product is defined, is the direct sum³⁸ (denoted as \oplus). Note that in the following, all spaces and field quantities might be real, complex or bicomplex where appropriate. The Hodge decomposition theorem for trivial topology of Ω (see e.g. [40] or [191]) states a decomposition of $\text{VF}(\Omega)$ into a curl-free gradient space $\text{G}(\Omega)$ and a divergence-free curl space, called knots, $\text{K}(\Omega)$ as

$$\text{VF}(\Omega) = \text{G}(\Omega) \oplus \text{K}(\Omega). \quad (2.57)$$

The fields in (2.57) are defined according to [40] as

$$\text{G}(\Omega) = \text{null space}(\text{curl}) = \text{image}(\text{grad}) = (\mathbf{X} \in \text{VF}(\Omega) : \mathbf{X} = \nabla \phi) \quad (2.58a)$$

$$\text{K}(\Omega) = \text{null space}(\text{div}) = \text{image}(\text{curl}) = (\mathbf{X} \in \text{VF}(\Omega) : \nabla \cdot \mathbf{X} = 0, \mathbf{X} \cdot \mathbf{n} = 0). \quad (2.58b)$$

This is in accordance to the idea of H. Helmholtz in [121], that any vector field can be decomposed in an irrotational part $\text{G}(\Omega)$ and a rotational part $\text{K}(\Omega)$. In analogy to the 3D sphere taken as the manifold of interest in [40] and [191], the cuboidal manifolds used for FEM BC have a trivial topology. Following [5], a third possibility are fields which are both divergence-free and curl-free, called the harmonic components (as mentioned earlier in section 2.4.6, an example of such a field is H_{dR}^2). To further generalize the theory to a general Ω , the Hodge decomposition theorem for general topology (see again e.g. [40] or [191]) states a decomposition of $\text{VF}(\Omega)$ into five mutually orthogonal subspaces \mathbf{X} (which are introduced in the following, see especially Fig. 2.32) as

$$\text{VF}(\Omega) = \text{FK}(\Omega) \oplus \text{HK}(\Omega) \oplus \text{CG}(\Omega) \oplus \text{GG}(\Omega) \oplus \text{HG}(\Omega). \quad (2.59)$$

There, $\text{FK}(\Omega)$ stands for fluxless knots, $\text{HK}(\Omega)$ means harmonic knots, $\text{CG}(\Omega)$ are curly gradients, $\text{GG}(\Omega)$ implies grounded gradients and $\text{HG}(\Omega)$ represents harmonic gradients. It is important to note that this classification is not directly related to the conformal discretization of EM field

³⁶Similarly to the Euclidean scalar product, which equals zero between unit vectors, means L^2 -orthogonality a vanishing inner product between base vectors contained in a Lebesgue space.

³⁷The Hodge decomposition is a generalization of the Helmholtz decomposition from vector fields defined on \mathbb{R}^3 to differential forms defined on p -dimensional manifolds.

³⁸The direct sum is used to combine vector spaces which allows for the combination of their members, respectively. For details, see e.g. [151].

quantities, which is easily recognizable since $CG(\Omega)$ appears in both C^1 and C^2 in Fig. 2.32, where the field pattern of (2.59) are illustrated in a discrete sense on a block of 3x3 brick elements.

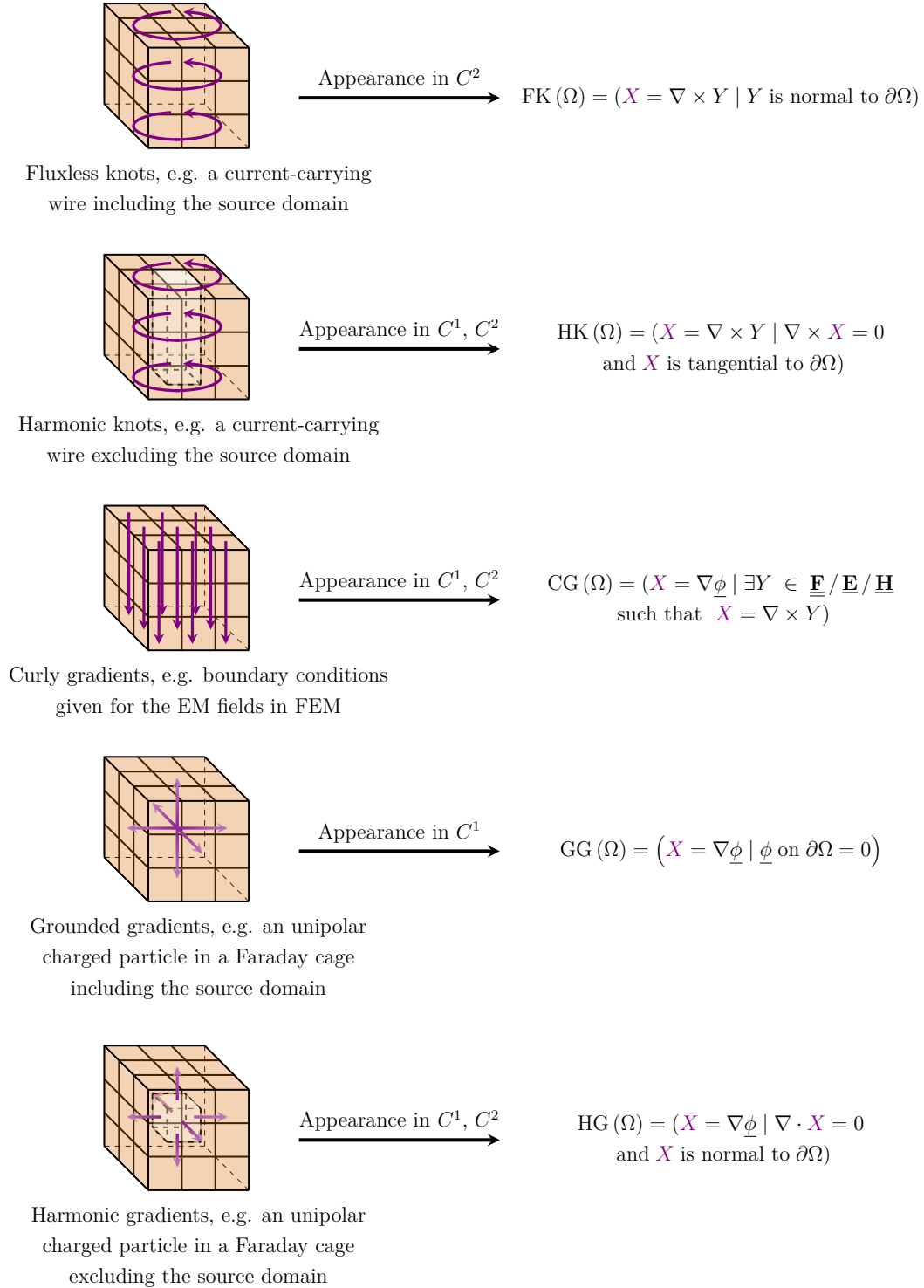


Figure 2.32 Visualization of the field pattern of the five mutually orthogonal subspaces presented in (2.59) which are the result of the Hodge decomposition theorem applied to an arbitrary vector field in 3D space. The definitions on the right are oriented on [87], where the fields are illustrated on the manifolds: torus, ball, or a ball with a three-dimensional hole in its center. Here, these manifolds are adapted to several brick meshes, which have the same topology, respectively.

A special field type, called fluxless knots $\text{FK}(\Omega)$, is depicted on the top of Fig. 2.32. There are closed loop fields defined on a trivial topology (topologically equivalent to a ball topology), which are only included in C^2 . Therefore, they can be conformally approximated by 2-forms. The origin of the term "fluxless" is explained in [40] as if the flux through every cross-sectional surface vanishes, then all interior fluxes are zero. For a torus topology (the three bricks on the middle are left out) shown next, harmonic knots $\text{HK}(\Omega)$ can exist. They are the analogon of $\text{FK}(\Omega)$ for non-trivial topology. In the middle of Fig. 2.32, curly gradients $\text{CG}(\Omega)$ are shown, which occur in both C^1 and C^2 . Following again [40], that name is derived from the circumstance that these are the only gradient vector fields that lie in the image of curl. Grounded gradients $\text{GG}(\Omega)$ are illustrated by field lines originating at some point in the trivial topology of Ω . They decay away from that point to zero at $\partial\Omega$. Also for that field type, a counterpart for non-trivial topologies exists, which is called harmonic gradients $\text{HG}(\Omega)$. Here, only the brick in the middle is left out (topologically equivalent to a ball topology with a three-dimensional hole in its center), the origin of the field lines is now located at the inner $\partial\Omega$. Practical examples of the shown field types are given below, respectively. An auxiliary quantity Y is introduced to represent the existence of another arbitrary complex field.

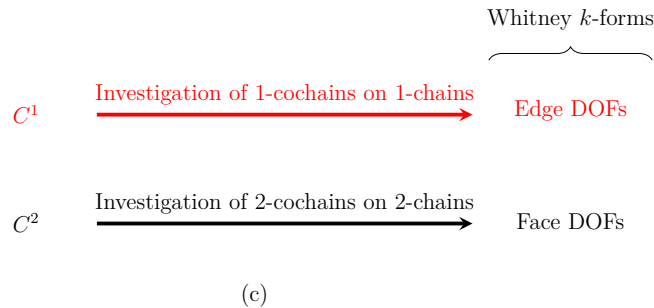
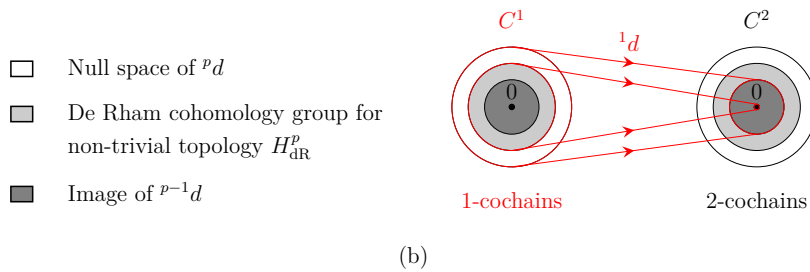
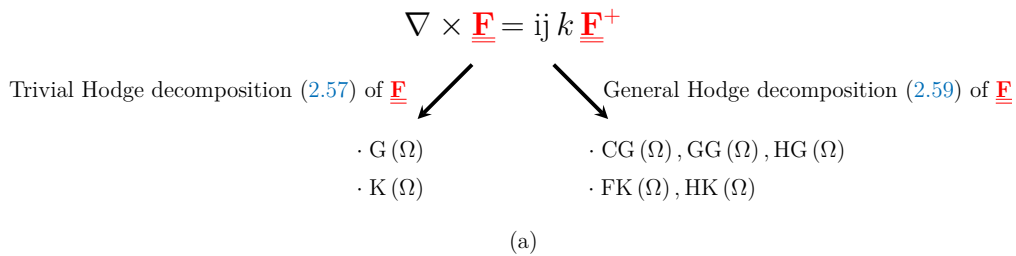


Figure 2.33 The two types of Hodge decomposition split an arbitrary three-dimensional vector field into two or five mutually orthogonal subspaces, respectively, which is shown on the top (a). Concerning the bicomplex PDE on the top, this allows for C^1 on the left and C^2 on the right in (b), respectively. C^1 and C^2 lead to conformal Whitney 1- and 2-forms, respectively, with associated DOFs in (c). Through the use of divergence-free brick elements, only C^1 is of interest.

In Fig. 2.33, the process of Hodge decomposition is implied and possible de Rham cohomology groups for the bicomplex Pseudo-Helmholtz equation (see (2.6) in section 2.2.2) defined on brick elements are shown. On the top (a), the vector fields which satisfy the bicomplex Pseudo-Helmholtz equation are decomposed into several field types through Hodge decomposition, by neglecting the fact that an exact decomposition is not possible in a discrete setting [184]. The bicomplex PDE is only conformally satisfied by the use of 1-forms. Therefore, C^1 is the right choice. Below in this section it will be shown that not only the direct occurrence of field types is relevant, rather their origin is important. Later on in section 2.5, a similar decomposition of fields is done by the use of the magnetic vector potential $\underline{\mathbf{A}}$ and the electric scalar potential $\underline{\phi}$. Volume fields are included in C^3 and scalar fields are contained in C^0 , which are not of direct interest and therefore not considered here. As shown in Fig. 2.32, several field types can be included in C^1 and C^2 , respectively. The application of $\nabla \times$ on $\underline{\mathbf{F}}$ and k on $\underline{\mathbf{F}}^+$ (or expressed regarding differential forms 1d on ${}^1\underline{\mathcal{F}}$ and \star_k on ${}^1\underline{\mathcal{F}}^+$) yields 2-forms, respectively, as explained earlier in section 2.4.4.

For analyzing the bicomplex EM field, the starting point is given by the five mutually orthogonal subspaces \mathbf{X} in (2.59) shown in Fig. 2.32. By neglecting the two harmonic components $\text{HK}(\Omega)$ and $\text{HG}(\Omega)$, there are $\text{FK}(\Omega)$, $\text{CG}(\Omega)$ and $\text{GG}(\Omega)$ left for trivial topologies discussed in this thesis. The $\text{GG}(\Omega)$ field does not match the behavior of the bicomplex EM field, since no sources are included in Ω and further no general requirement is assumed that the field components have to be zero at $\partial\Omega$. Only $\text{FK}(\Omega)$ and $\text{CG}(\Omega)$ are left to be the correct field types of the bicomplex PDE's solutions calculated by FEM.

As shown in Fig. 2.32, $\text{CG}(\Omega)$ can be derived from $\mathbf{X} = \nabla \underline{\phi}$ or $\mathbf{X} = \nabla \times \mathbf{Y}$, therefore it can be assigned to $\text{G}(\Omega)$ or $\text{K}(\Omega)$, respectively. If $\text{CG}(\Omega) \in \text{G}(\Omega)$ and therefore in C^1 (see 2.58a), then the bicomplex PDE is fulfilled. But there are two possible reasons to fulfill this, since $\text{CG}(\Omega)$ is a hybrid field type (it can be either a 1-form or a 2-form). When a boundary condition, which is interpreted as the gradient of a potential $\underline{\phi}$, is directly visualized as a FEM result, it can be seen as the gradient of a scalar function, so $\mathbf{X} = \nabla \underline{\phi}$. But the more appropriate one is that $\text{CG}(\Omega)$ is originating in the curl of another field \mathbf{Y} . This was shown on Fig. 2.10 (see section 2.2.2), where the electric field causes a magnetic field and vice versa. Regarding differential forms, the missing information is the effect of the Hodge operator. That means regarding vector calculus, that a conversion from a flux density to a field strength is necessary. Then, the curl-caused $\text{CG}(\Omega)$ which is derived from $\text{FK}(\Omega) \in C^2$ is also in C^1 , the same space as the gradient-caused $\text{CG}(\Omega)$ exists in. If this mapping from C^2 to C^1 would further be applied to $\text{FK}(\Omega)$, the field pattern of $\text{FK}(\Omega)$ would arise in C^1 . Note that the application of the Hodge operator maps only between vector spaces (so between the p -forms where the respective EM quantities are defined on) and does not change the pattern of the EM quantity, so the fields shown in Fig. 2.32 look still the same. With the field types obtained from Hodge decomposition, it is exemplarily possible to investigate the field relation in a waveguide for time-harmonic wave propagation, shown below in Fig. 2.34.

$$\begin{array}{ccc}
 \underline{\phi} \xrightarrow{\nabla} \mathbf{z}_1 \{ \underline{\mathbf{E}} \} \text{ or } \underline{\mathbf{E}} \text{ can be } \text{GG}(\Omega) \text{ or } \text{CG}(\Omega) & \xrightarrow{\nabla \times} & \underline{\mathbf{B}} \text{ can be } \text{FK}(\Omega) \text{ or } \text{CG}(\Omega) \\
 \uparrow \epsilon^{-1} & & \downarrow \mu^{-1} \\
 \underline{\mathbf{D}} \text{ can be } \text{FK}(\Omega) \text{ or } \text{CG}(\Omega) & \xleftarrow{\nabla \times} & \mathbf{z}_2 \{ \underline{\mathbf{F}} \} \text{ or } \underline{\mathbf{H}} \text{ can be } \text{GG}(\Omega) \text{ or } \text{CG}(\Omega)
 \end{array}$$

Figure 2.34 Process of wave propagation in a waveguide with assigned field types of Hodge decomposition by assuming a trivial topology of Ω . The EM field components which are included in the bicomplex PDE's solution space and the corresponding field types are marked in red. In blue, the two possibilities of generating the first bicomplex component (electric field) are indicated.

It is comprehensible that the electric field fulfills in the high-frequency regime the first possibility $\mathbf{X} = \nabla \underline{\phi}$ to generate $\text{CG}(\Omega)$, since the charge distribution in a hollow waveguide (see

e.g. [182]) leads to an electric scalar potential ϕ , which equals the electric field after applying the gradient, see the upper left side of Fig. 2.34. The second condition $\mathbf{X} = \nabla \times \mathbf{Y}$ is satisfied since the electric field can be derived e.g. from the magnetic field as shown in Fig. 2.10 (see section 2.2.2), or from the magnetic vector potential \mathbf{A} shown later on in (2.62), see section 2.5. Fluxless knots would be of interest if an EM problem is based e.g. on Gauss's law in (2.7c) or (2.7d) of section 2.2.2, since there a 2-form (a flux density) is the unknown quantity. Since the curl produces a 2-form, the definition of CG (Ω) in Fig. 2.32 for the language of differential forms is enhanced by the respective inverse Hodge operator defined in (2.43) (see section 2.4.2) and (2.46) (discussed in section 2.4.4) according to the transformation behavior shown in Fig. 2.18 (see section 2.4.2) as

$${}^1\mathcal{C}\mathcal{G}(\Omega) = ({}^1\mathcal{X} = {}^0d {}^0\phi \mid \exists {}^1\mathcal{Y} \in {}^1\underline{\mathcal{F}}/{}^1\underline{\mathcal{E}}/{}^1\underline{\mathcal{H}} \text{ such that } {}^1\mathcal{X} = \star_{k/\varepsilon/\mu}^{-1} ({}^1d {}^1\mathcal{Y})), \quad (2.60)$$

where ${}^1\mathcal{C}\mathcal{G}(\Omega)$ is the differential curly gradient space, ${}^1\mathcal{X}$ stands for an arbitrary complex differential subspace and ${}^1\mathcal{Y}$ represents an arbitrary complex differential auxiliary subspace. According to the three considered field quantities, the appropriate Hodge operator has to be used, see (2.43) in section 2.4.2 or (2.46) in section 2.4.4, respectively. The 2-form resulting from ${}^1d {}^1\mathcal{Y}$ has got the same orientation of its normal vector as the tangential vector of the 1-form produced by $\star_{k/\varepsilon/\mu}^{-1} ({}^1d {}^1\mathcal{Y})$, which is shown in Fig. 2.20 (see section 2.4.2) by consideration of Fig. 2.21 (see section 2.4.3). Furthermore, FK (Ω) is redefined for exterior calculus as

$${}^1\mathcal{F}\mathcal{K}(\Omega) = ({}^1\mathcal{X} = \star_{k/\varepsilon/\mu}^{-1} ({}^1d {}^1\mathcal{Y}) \mid {}^1\mathcal{Y} \in {}^1\underline{\mathcal{F}}/{}^1\underline{\mathcal{E}}/{}^1\underline{\mathcal{H}} \text{ and } {}^1\mathcal{Y} \text{ is normal to } \partial\Omega), \quad (2.61)$$

where ${}^1\mathcal{F}\mathcal{K}(\Omega)$ is the differential fluxless knot space. Note that ${}^1\mathcal{F}\mathcal{K}(\Omega)$ represents the field pattern of FK (Ω) in C^1 instead of C^2 , which is in contrast to the conventional definition. Therewith, the cohomology of the bicomplex EM field is classified in an appropriate manner. The Hodge decomposition into ${}^1\mathcal{C}\mathcal{G}(\Omega)$ and ${}^1\mathcal{F}\mathcal{K}(\Omega)$ will be exemplified on the numerical examples later on in section 4.2.5. It should be pointed out that the additional conversion between p -forms by the use of the respective Hodge operator is not necessary in vector calculus.

To examine the de Rham cohomology groups H_{dR}^p for the brick element, a separate handling of p -forms similar to the tetrahedron discussed in [69] is suitable. It has to be emphasized that the topology of interest here is not a solid brick itself, it is rather described by the respective p -chains which form the brick element. As recognizable in Fig. 2.21 (see section 2.4.3), the brick element has got 8 nodes, 12 edges, 6 faces and 1 volume. The 8 distinct nodes lead to $b_0(\Omega) = 8$, the possible independent two-dimensional holes (as discussed on Fig. 2.31 in section 2.4.6) enclosed by the 12 edges lead to $b_1(\Omega) = 5$ and the brick volume enclosed by the 6 faces to $b_2(\Omega) = 1$, respectively. As an interesting consequence of introducing Whitney elements for discretizing the continuous function behavior (defined on the continuous manifold Ω), the topology of Ω changes from trivial to non-trivial. This seems problematic, but this circumstance is eliminated by introducing the interpolation process of FEM after the DOFs are calculated. A further finding is the direct connection between discontinuities of functions and holes in the manifold, described by the topology. As mentioned above, since the used brick elements are free of divergence, C^1 includes all possible field quantities. To sum up, the topology of the continuous and discrete (after the interpolation procedure, see the last step of Fig. 3.5 discussed later on in section 3.4) manifold is trivial. An overview of Euler-Poincaré characteristics and related Betti numbers of the used tetrahedral and brick elements in the respective de Rham cohomology group is shown below in Fig. 2.35. The primal p -cochain space C^2 includes the transformed solutions of the bicomplex PDE through 1d and \star_k , which corresponds to the image of 1d . If face elements would be used, then H_{dR}^2 would be the suitable de Rham cohomology group for investigating the topology of Ω . As stated earlier, the interesting space for FEM BC is C^1 , where the solutions of the bicomplex PDE are included, which includes the null space of 1d . Suppose a certain unknown

(maybe relatively big) brick mesh (cubical complex). If $b_1(\Omega)$ of this mesh deviates from $b_1(\Omega)$ of a homogeneous brick mesh, one or more edges or its connection have to be different, which can be inferred by equating (2.55) and (2.56) presented in section 2.4.6. Note that the length and orientation of these edges is not of interest here, only the connectivity (which represents the topological structure) is relevant. Furthermore, the respective holes indicated by the Betti numbers of H_{dR}^1 confirm that function values are only defined on the edges and nowhere else in Ω .

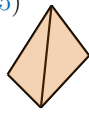
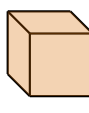
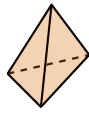
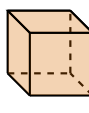




		Euler-Poincaré characteristic (2.55)		
H_{dR}^3	Tetrahedron	$\chi(\Omega) = 1 - 0 + 0 = 1$	$= 1$	
		$\chi(\Omega) = 4 - 6 + 4 - 1 = 1$	$= 1$	
		Euler characteristic (2.56)		
	Brick	$\chi(\Omega) = 1 - 0 + 0 = 1$	$= 1$	
		$\chi(\Omega) = 8 - 12 + 6 - 1 = 1$	$= 1$	
H_{dR}^2	Tetrahedron	$\chi(\Omega) = 1 - 0 + 1 = 2$	$= 2$	
		$\chi(\Omega) = 4 - 6 + 4 - 0 = 2$	$= 2$	
	Brick	$\chi(\Omega) = 1 - 0 + 1 = 2$	$= 2$	
		$\chi(\Omega) = 8 - 12 + 6 - 0 = 2$	$= 2$	
H_{dR}^1	Tetrahedron	$\chi(\Omega) = 1 - 3 + 0 = -2$	$= -2$	
		$\chi(\Omega) = 4 - 6 + 0 - 0 = -2$	$= -2$	
	Brick	$\chi(\Omega) = 1 - 5 + 0 = -4$	$= -4$	
		$\chi(\Omega) = 8 - 12 + 0 - 0 = -4$	$= -4$	
H_{dR}^0	Tetrahedron	$\chi(\Omega) = 4 - 0 + 0 = 4$	$= 4$	
		$\chi(\Omega) = 4 - 0 + 0 - 0 = 4$	$= 4$	
	Brick	$\chi(\Omega) = 8 - 0 + 0 = 8$	$= 8$	
		$\chi(\Omega) = 8 - 0 + 0 - 0 = 8$	$= 8$	

Figure 2.35 Euler / Euler-Poincaré characteristics and related Betti numbers of the tetrahedral and brick element in the respective de Rham cohomology group. On the first row, (2.55) is used and on the second row, (2.56) is utilized, respectively, which yield the same number.

This is in accordance to the statement in [131], that Betti numbers represent the underlying structure of datasets. Note that merely H_{dR}^3 shows according to its Betti numbers a trivial topology. If one studies H_{dR}^3 of a filled volume of arbitrary shape shown on the top of Fig. 2.35, all Betti numbers are equal to them of the Euclidean space \mathbb{R}^3 . For \mathbb{R}^3 , all quotient spaces $H_{\text{dR}}^{0,\dots,3}$ are zero, which makes \mathbb{R}^3 to a topologically simple space.

2.5 Relation to Potential Formulations

This section covers the relation of the bicomplex-formulated electromagnetism to ordinary potential formulations. As stated in [218], gauge symmetry means that the electric and magnetic fields are independent against gauge transformations of their potentials, so they are invariant under gauge transformations. For further reading, gauge symmetry in terms of particle physics, which can be understood as an extension or rather an adjustment of gauge symmetry concerning Maxwell's equations, is discussed e.g. in [218]. According to [158], no gauge condition was applied in the original derivation of the wave equation for the vector potential by J. C. Maxwell. As reported in [187], a rarely applied alternative to the commonly used potentials below are the electric and magnetic Hertz vectors / Hertz vector potentials, which are suitable if external sources are described by electric and magnetic polarization densities. This indicates that the choice of auxiliary quantities is arbitrary as stated at the beginning of Chapter 2 and should be oriented on the desired kind of EM problem. For an investigation of both the common potentials and the Hertz vectors in the language of differential forms, see e.g. [256].

The general principle of gauging is depicted below in Fig. 2.36 by considering relevant physical and mathematical quantities. Contrary to physical quantities, mathematical quantities are not directly measurable.

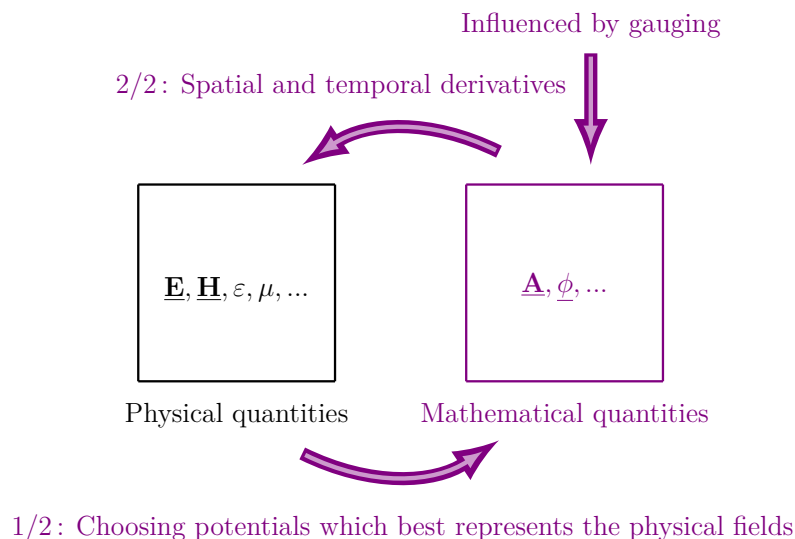


Figure 2.36 Principle of gauging potentials and relation of physical and mathematical field quantities as one possibility of designing mathematical representations of physical phenomena shown in Fig. 2.1, see Chapter 2. See Fig. 2.14 in section 2.4 for the connection of these quantities in the language of differential forms.

As a first step in Fig. 2.36, suitable scalar or vectorial potentials are chosen, which describe the physical quantities through derivatives of these potentials. After calculation of the respective potentials, the physical quantities are determined from them as a second step. By choosing a specific gauge, the calculation of these potentials might be beneficial influenced without changing the resulting physical quantities.

The connections of the non-observable magnetic vector potential $\underline{\mathbf{A}}$ and the electric scalar potential ϕ to the observable vector fields $\underline{\mathbf{E}}$ and $\underline{\mathbf{H}}$ in the international system of units (SI) –

after recasting the version of [170] – are

$$\begin{aligned}\underline{\mathbf{E}} &= -\nabla\phi - j\omega \underline{\mathbf{A}} \\ \underline{\mathbf{H}} &= \frac{1}{\mu} \nabla \times \underline{\mathbf{A}}.\end{aligned}\quad (2.62)$$

Applications of this conventional formulation with potentials are discussed e.g. in [6] or [109] and especially in the finite element environment in [22]. It would be further possible to introduce the magnetic scalar potential, which can be used to describe specific EM problems efficiently, see e.g. [62]. Caused by the non-existence of magnetic monopoles when describing the magnetic scalar potential analogous to the divergence of electric monopoles for the electric scalar potential ϕ , this quantity is not used throughout this thesis. In [62], another physical interpretation is done.

Since only wave fields with non-vanishing rotation are numerically calculated in this thesis, the electric scalar potential ϕ , which would yield gradient fields, can be neglected. By assuming a source-free domain, ϕ becomes zero and the fields depend only on the magnetic vector potential $\underline{\mathbf{A}}$. A substitution of the EM fields which describe homogeneous material distribution in (2.12) (see section 2.2.2) by (2.62) and usage of $k = \omega/c$ leads to

$$\nabla \times \left[\frac{1}{\sqrt{Z_0}} (-j\omega \underline{\mathbf{A}}) + i\sqrt{Z_0} \left(\frac{1}{\mu} \nabla \times \underline{\mathbf{A}} \right) \right] = ij \frac{\omega}{c} \left[\frac{1}{\sqrt{Z_0}} (-j\omega \underline{\mathbf{A}}) - i\sqrt{Z_0} \left(\frac{1}{\mu} \nabla \times \underline{\mathbf{A}} \right) \right]. \quad (2.63)$$

Using the linearity property of the Nabla operator and multiplying out the brackets yields

$$-\frac{j\omega}{\sqrt{Z_0}} \nabla \times \underline{\mathbf{A}} + i \nabla \times \frac{\sqrt{Z_0}}{\mu} (\nabla \times \underline{\mathbf{A}}) = i \frac{\omega^2}{\sqrt{Z_0} c} \underline{\mathbf{A}} - \frac{j\omega \sqrt{Z_0}}{\mu c} \nabla \times \underline{\mathbf{A}}. \quad (2.64)$$

To convert the time-harmonic Maxwell's equations into the bicomplex-valued counterpart in (2.8) (see section 2.2.2), a normalization was done by multiplying or dividing the respective equation by \sqrt{Z} assuming homogeneous material distribution. A renormalization and the use of $Z_0 / (\mu c) = 1$ let the first term on LHS and the second term on RHS cancel out and produce

$$i \nabla \times \frac{Z_0}{\mu} (\nabla \times \underline{\mathbf{A}}) = i \frac{\omega^2}{c} \underline{\mathbf{A}}. \quad (2.65)$$

This step shows that one of the two Maxwell's equations cancels out when using $\underline{\mathbf{A}}$ for expressing $\underline{\mathbf{E}}$ and $\underline{\mathbf{H}}$. With $Z = \mu c$, (2.65) turns out as

$$i \nabla \times (\nabla \times \underline{\mathbf{A}}) = i \frac{\omega^2}{c^2} \underline{\mathbf{A}}. \quad (2.66)$$

Applying the vector identity (B.1) reported in appendix B yields

$$i \nabla^2 \underline{\mathbf{A}} + i \frac{\omega^2}{c^2} \underline{\mathbf{A}} = i \nabla (\nabla \cdot \underline{\mathbf{A}}). \quad (2.67)$$

In summary, the relation of the bicomplex-formulated Maxwell system to the ordinary potential formulation is shown below in Fig. 2.37.

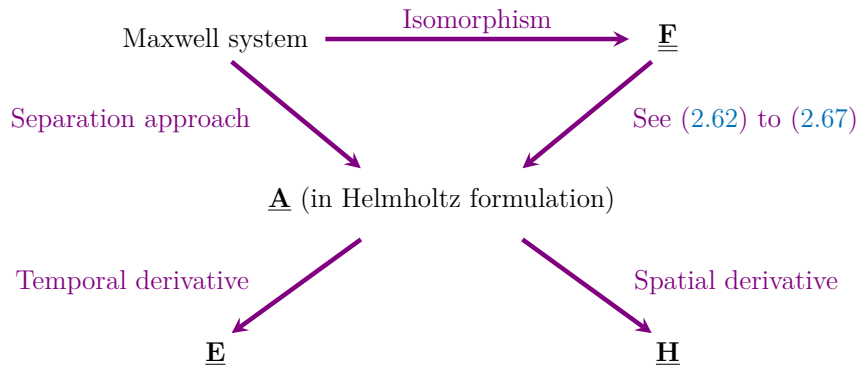


Figure 2.37 Relation of the bicomplex-formulated Maxwell system to the ordinary potential formulation.

As one can conclude from Fig. 2.37, the bicomplex-formulated Maxwell system is a clear alternative to potential formulations which use $\underline{\mathbf{A}}$. The common way of deriving $\underline{\mathbf{A}}$ from the Maxwell system using the separation approach is similar to the one described from (2.62) to (2.67). By introducing $\underline{\mathbf{A}}$, the bicomplex formulation is expendable, since one of Maxwell's equations (where one of them is discretized on the primal mesh and the other one on the dual mesh) cancels out.

The general potential formulations of Maxwell's equations in [263] is written in time-harmonic form for vacuum in the SI as

$$\begin{aligned} \nabla^2 \underline{\phi} + j\omega (\nabla \cdot \underline{\mathbf{A}}) &= -\frac{\rho}{\epsilon} \\ \nabla^2 \underline{\mathbf{A}} + \frac{\omega^2}{c^2} \underline{\mathbf{A}} &= -\mu \underline{\mathbf{J}} + \nabla \left(\nabla \cdot \underline{\mathbf{A}} + j \frac{\omega}{c^2} \underline{\phi} \right). \end{aligned} \quad (2.68)$$

Compared to (2.67), additional terms arise in the second equation of (2.68), since the assumption of a source-free domain is not done yet. To specify the potentials uniquely except of a gauge transformation, an appropriate gauge has to be applied. The Lorenz gauge (see e.g. [163] for an early reference), which is suitable for time-dependent EM fields, yields separate equations for $\underline{\phi}$ and $\underline{\mathbf{A}}$ based on (2.68). If a source-free vacuum domain is assumed and the Lorenz gauge condition $\nabla \cdot \underline{\mathbf{A}} = -j\omega/c^2 \underline{\phi}$ [251] is used, both right-hand sides of (2.67) and of the second equation in (2.68) become zero. The only difference between (2.67) and the second equation of (2.68) – which describes $\underline{\mathbf{A}}$ – is the assumed outer imaginary unit i . To produce (2.8), Ampère's law in (2.7b) (see section 2.2.2, respectively) was multiplied by the outer imaginary unit i . If this imaginary unit is removed, (2.67) equals the second equation of (2.68). They are in the same form as a Helmholtz equation of the complex-valued electric field (see e.g. (2.5) in section 2.2.1 after applying (B.1) from appendix B). The first equation in (2.62) confirms this as well for the bicomplex (2.67) as for the conventional (2.68) case.

This shows that also if one uses the potentials $\underline{\phi}$ and $\underline{\mathbf{A}}$, the bicomplex formulation yields correct results. It can be concluded that the assumption that the magnetic vector potential $\underline{\mathbf{A}}$ is spatially oriented as the electric field is correct. The bicomplex formulation of time-harmonic Maxwell's equations yields no contradiction to the use of potential formulations in this context. Due to the use of the Lorenz gauge, $\underline{\mathbf{A}}$ is Lorentz invariant. Therefore, the bicomplex (2.67) and the conventional (2.68) formulation – which are formulated in the language of vector calculus – may be used in special relativity. An introduction to general and special relativity is discussed e.g. in [24]. Based on [260], the Lorenz gauge condition in DEC becomes $\star^{-1} {}^2 d \star^1 \underline{\mathbf{A}} = -j\omega/c^2 {}^0 \underline{\phi}$ in the SI. As especially discussed for the differential bicomplex EM field ${}^1 \underline{\mathcal{F}}$ in section 2.4.4, the herein contained field quantities ${}^1 \underline{\mathbf{A}}$ and ${}^0 \underline{\phi}$ are defined independently of the metric. Therefore, the DEC version of the Lorenz gauge condition is valid for general relativity.

Several gauges of $\nabla \cdot \underline{\mathbf{A}}$ are reported, for instance, in [209] and [263], where [209] shows further analogies to fluid mechanics. Note that a specific gauge may yield incorrect results if not properly chosen. A concrete example is reported in [84], where contradicting solutions are obtained from the Lorenz gauge and the Coulomb gauge when calculating the EM field of a moving particle. In this case, the Hodge decomposition presented earlier in section 2.4.7 might be advantageous to analyze that problem. Further issues of decomposing a vector field into potential formulations are reported in [170].

In [200], gauge conditions concerning potential formulations of the EM field are discussed by the use of differential forms in the de Rham complex. This is not further discussed here, since the proposed bicomplex formulation is a direct formulation, as clarified throughout this section.

2.6 Derivation of Wave Quantities from the Bicomplex-valued Field

In this section, several important EM quantities are derived directly from the results of the bicomplex FEM. Both the homology concept and the cohomology concept of implementing the bicomplex EM field (see Fig. 2.30 in section 2.4.6) are considered here. Compared to the results of the complex FEM, the magnetic field of the homology concept is rotated to the electric field's orientation as presented in Fig. 2.8, see section 2.1.2. To interpret the magnetic field physically correct, it has to be inversely transformed to its original reference or considered in an appropriate manner. Remember that for EM problems in the language of vector calculus throughout this thesis, Cartesian coordinates are assumed.

An overview of some selected EM quantities derived from $\underline{\underline{\mathbf{F}}}$ is given below in Fig. 2.38.

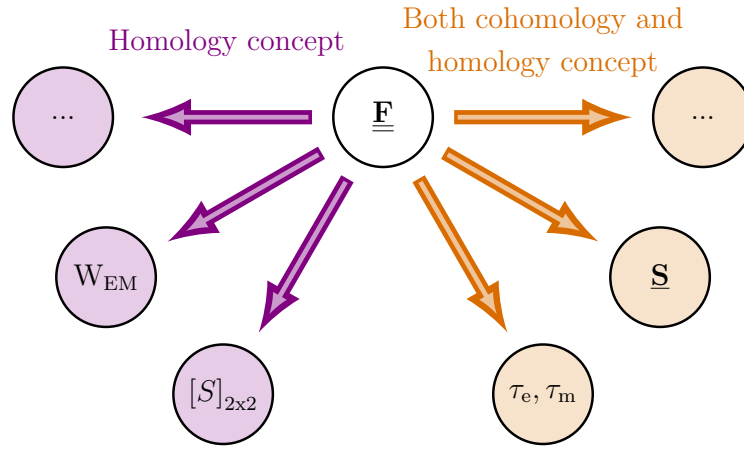


Figure 2.38 Several wave quantities derived from the bicomplex-valued field. The following definitions of the quantities on the left need the embedding of the bicomplex structure in the homology / tangential space (see the right side of Fig. 2.30), whereas the quantities on the right are valid for both the cohomology and the homology approach.

In Fig. 2.38, W_{EM} is the energy content of the EM wave, $\underline{\underline{\mathbf{S}}}$ is the Poynting vector, $[S]_{2 \times 2}$ is the scattering matrix for the case of 2 ports, τ_e is the electric part of the Maxwell stress tensor (MST) and τ_m is the magnetic part of the Maxwell stress tensor. Throughout this section, the magnetic field components are used directly, without an inverse transformation. The language of vector calculus is preferred over that of differential forms, since the base of the following derivations is the vectorial EM field generated by the FEM.

2.6.1 Energy Content

The following investigation of the EM fields' energy content is based on vector calculus, regarding a discussion of EM energy content in the language of differential forms, see e.g. [256].

To calculate the energy carried by an EM wave W_{EM} , the conventional way is to use

$$W_{EM} = \frac{\varepsilon}{2} |\underline{\underline{\mathbf{E}}}|_j^2 + \frac{\mu}{2} |\underline{\underline{\mathbf{H}}}|_j^2, \quad (2.69)$$

where $|\dots|_j$ is the common complex modulus defined in (2.29), see section 2.3.2. The derivation of the energy from the bicomplex-valued EM field in (2.2) (see section 2.1.1) calculated by FEM BC

can be done in a similar way. By taking the complex modulus of both the electric and magnetic subspaces, respectively, it follows

$$|\underline{\mathbf{F}}|_j = \frac{1}{\sqrt{Z}} |\underline{\mathbf{E}}|_j + i\sqrt{Z} |\underline{\mathbf{H}}|_j. \quad (2.70)$$

A further particular modulus of bicomplex numbers $|\dots|_i$ is defined in addition to (2.29) by following [164] as

$$|\underline{\mathbf{f}}|_i = \sqrt{\mathbf{e}^2 + \mathbf{h}^2} \quad \text{for } \underline{\mathbf{f}} = \mathbf{e} + i\mathbf{h}, \quad (2.71)$$

where \mathbf{e} and \mathbf{h} are generalized complex numbers and $\underline{\mathbf{f}}$ is a generalized bicomplex number. Compared to (2.29), where both the electric and magnetic subspaces are affected separately, (2.71) is related to the outer imaginary unit i . Application of (2.71) and squaring of (2.70) results in

$$|\underline{\mathbf{F}}|_j^2 = \frac{1}{Z} |\underline{\mathbf{E}}|_j^2 + Z |\underline{\mathbf{H}}|_j^2. \quad (2.72)$$

Expressing the wave impedance as $Z = \sqrt{\mu/\varepsilon}$ yields

$$|\underline{\mathbf{F}}|_j^2 = \frac{\sqrt{\varepsilon}}{\sqrt{\mu}} |\underline{\mathbf{E}}|_j^2 + \frac{\sqrt{\mu}}{\sqrt{\varepsilon}} |\underline{\mathbf{H}}|_j^2. \quad (2.73)$$

A multiplication of both sides by $\sqrt{\varepsilon\mu}/2$ gives

$$\frac{\sqrt{\varepsilon\mu}}{2} |\underline{\mathbf{F}}|_j^2 = \frac{\varepsilon}{2} |\underline{\mathbf{E}}|_j^2 + \frac{\mu}{2} |\underline{\mathbf{H}}|_j^2. \quad (2.74)$$

Apparently, the RHS of (2.74) equals the conventional expression for W_{EM} in (2.69). If the phase velocity v_{phase} is introduced as $v_{\text{phase}} = 1/\sqrt{\varepsilon\mu}$, a compact equation results as

$$W_{EM} = \frac{|\underline{\mathbf{F}}|_j^2}{2 v_{\text{phase}}}. \quad (2.75)$$

Compared to the conventional way of calculating W_{EM} in (2.69) which is based on two EM field variables, the alternative version (2.75) is based on merely one EM field variable.

2.6.2 Poynting Vector

The EM energy flux density in different media is given e.g. in [155] as the cross product between the electric field and the magnetic field in general. This is a purely spatial topological operation as indicated in Fig. 2.14 (see section 2.4). The wedge product is alternatively applied in (2.45) discussed in section 2.4.2 when differential forms are used. In three dimensions, the cross product is equivalent to quaternion multiplication with vanishing scalar part, see e.g. [23] for a contemporary investigation. A multiplication of two quaternions, which is also named Hamilton product, is easily done by multiplying each component of the first quaternion with each component of the second quaternion, respectively.

For time-harmonic EM vector field quantities, it is useful to employ the complex-valued Poynting vector $\underline{\mathbf{S}}$, which is defined in 3D as the cross product of the complex-valued electric field with the conjugate of the complex-valued magnetic field. In greater detail, $\underline{\mathbf{S}}_{\text{phy}}$ can be expressed by a determinant or by the difference of two Hadamard products³⁹ (indicated by the symbol \circ) as

$$\underline{\mathbf{S}}_{\text{phy}} = \frac{1}{2} (\underline{\mathbf{E}} \times \underline{\mathbf{H}}_{\text{phy}}^*) = \frac{1}{2} \begin{vmatrix} \mathbf{e}_x & \mathbf{e}_y & \mathbf{e}_z \\ E_x & E_y & E_z \\ H_x^* & H_y^* & H_z^* \end{vmatrix} = \frac{1}{2} \left[\begin{pmatrix} E_y \\ E_z \\ E_x \end{pmatrix} \circ \begin{pmatrix} H_z^* \\ H_x^* \\ H_y^* \end{pmatrix} - \begin{pmatrix} E_z \\ E_x \\ E_y \end{pmatrix} \circ \begin{pmatrix} H_y^* \\ H_z^* \\ H_x^* \end{pmatrix} \right]. \quad (2.76)$$

³⁹The Hadamard product is a component-wise matrix product for which no summation is applied after multiplication in contrast to the dot product. See e.g. [233] for details.

The transformation matrix in (2.4) discussed in 2.1.2 corresponds to the rotational effect of the imaginary unit i in the homology concept. After applying this matrix to the magnetic field, the Poynting vector directly generated from the bicomplex FEM results $\underline{\mathbf{S}}_{\text{BC}}$ is expressed as

$$\underline{\mathbf{S}}_{\text{BC}} = \frac{1}{2} (\underline{\mathbf{E}} \times \underline{\mathbf{H}}_{\text{BC}}^*) = \frac{1}{2} \begin{vmatrix} \mathbf{e}_x & \mathbf{e}_y & \mathbf{e}_z \\ \underline{E}_x & \underline{E}_y & \underline{E}_z \\ \underline{H}_y^* & \underline{H}_z^* & \underline{H}_x^* \end{vmatrix} = \frac{1}{2} \left[\begin{pmatrix} \underline{E}_y \\ \underline{E}_z \\ \underline{E}_x \end{pmatrix} \circ \begin{pmatrix} \underline{H}_y^* \\ \underline{H}_z^* \\ \underline{H}_x^* \end{pmatrix} - \begin{pmatrix} \underline{E}_z \\ \underline{E}_x \\ \underline{E}_y \end{pmatrix} \circ \begin{pmatrix} \underline{H}_x^* \\ \underline{H}_y^* \\ \underline{H}_z^* \end{pmatrix} \right]. \quad (2.77)$$

Compared to (2.76), the entries of the magnetic field in (2.77) are circularly shifted. For example, a TEM-wave in z -direction of Cartesian coordinates is assumed, where only two of six possible field components are given, which are \underline{E}_x and \underline{H}_y . The usual way would be the use of (2.76) and obtaining $\underline{\mathbf{S}}_{\text{phy}} = (\underline{E}_x \underline{H}_y^*) \mathbf{e}_z$. Contrary to this, the physical magnetic field \underline{H}_y is transformed by (2.4), which causes that this vector component lies on \mathbf{e}_x instead of \mathbf{e}_y . Therefore, it is named \underline{H}_x . This is visualized on the left one of the three colored coordinate systems in Fig. 2.8, see section 2.1.2. Application of (2.77) leads to $\underline{\mathbf{S}}_{\text{BC}} = (\underline{E}_x \underline{H}_x^*) \mathbf{e}_z$, which is equal to the Poynting vector calculated first from the physical orientation of the magnetic field in (2.76).

Note that no additional operations are necessary to consider the imaginary unit j , which describes the time-harmonic behavior of the field, because it is a scalar one. As an advantage of the direct procedure shown above, the inverse transformation of the magnetic field is omitted. The use of the bicomplex formulation leads in both the cohomology and the homology concept to a conformally approximated Poynting vector, since both $\underline{\mathbf{E}}$ and $\underline{\mathbf{H}}$ are conformally discretized.

2.6.3 Scattering Parameters

In high-frequency applications, scattering parameters (S-parameters) are usually used to describe the power flow of EM waves in a convenient manner. Since the spatial size of devices in high-frequency regime lies in the order of the wavelength, the voltage is not well-defined, rather it varies between different local positions. A more suitable description of wave propagation is made by the use of S-parameters based on the electric field. For a general introduction of S-parameters, see e.g. [197]. The following investigation is based on [60].

Regarding high-frequency 3D-applications of EM FEM, a 2D eigenmode analysis in the port plane is usually done in order to calculate the distribution of $\underline{\mathbf{E}}$. As an integral quantity, the power flow is constructed by the integration of all pointwise defined Poynting vectors in the respective port plane, followed by a normalization to a specific wave impedance. For all investigated examples in this thesis, the two-port matrix $[S]_{2 \times 2}$ is sufficient. Furthermore, only single-mode operation is assumed. Therefore, no superposition of modes is needed.

S-parameters can be divided into reflection parameters on the principal diagonal of $[S]_{2 \times 2}$ and transmission parameters apart from it. On the respectively excited port A_1 or A_2 , the computed electric field $\underline{\mathbf{E}}_c$ is expressed as the sum of the excited $\underline{\mathbf{E}}_1$ and the reflected field (denoted as $\underline{\mathbf{E}}_i$, which is scaled by the respective scattering parameter \underline{S}_{i1}) as

$$\underline{\mathbf{E}}_c = \underline{\mathbf{E}}_1 + \sum_{i=1}^2 \underline{S}_{i1} \underline{\mathbf{E}}_i, \quad (2.78)$$

where i denotes the port index. Non-excited ports (the respective other one in the case of a two-port model) are described with merely the reflected field through

$$\underline{\mathbf{E}}_c = \sum_{i=1}^2 \underline{S}_{i1} \underline{\mathbf{E}}_i. \quad (2.79)$$

By combining the implicit expressions for S-parameter (2.78) and (2.79) in matrix form and integrating over the respective port, they read as

$$[S]_{2 \times 2} = \begin{pmatrix} \underline{S}_{11} & \underline{S}_{12} \\ \underline{S}_{21} & \underline{S}_{22} \end{pmatrix} = \begin{pmatrix} \frac{\iint_{A_1} [(\underline{\mathbf{E}}_c - \underline{\mathbf{E}}_1) \cdot \underline{\mathbf{E}}_1^*] d\mathbf{A}_1}{\iint_{A_1} [\underline{\mathbf{E}}_1 \cdot \underline{\mathbf{E}}_1^*] d\mathbf{A}_1} & \frac{\iint_{A_1} [\underline{\mathbf{E}}_c \cdot \underline{\mathbf{E}}_1^*] d\mathbf{A}_1}{\iint_{A_1} [\underline{\mathbf{E}}_1 \cdot \underline{\mathbf{E}}_1^*] d\mathbf{A}_1} \\ \frac{\iint_{A_2} [\underline{\mathbf{E}}_c \cdot \underline{\mathbf{E}}_2^*] d\mathbf{A}_2}{\iint_{A_2} [\underline{\mathbf{E}}_2 \cdot \underline{\mathbf{E}}_2^*] d\mathbf{A}_2} & \frac{\iint_{A_2} [(\underline{\mathbf{E}}_c - \underline{\mathbf{E}}_2) \cdot \underline{\mathbf{E}}_2^*] d\mathbf{A}_2}{\iint_{A_2} [\underline{\mathbf{E}}_2 \cdot \underline{\mathbf{E}}_2^*] d\mathbf{A}_2} \end{pmatrix}. \quad (2.80)$$

Starting with $\underline{\mathbf{S}}_{\text{phy}} = 1/2 (\underline{\mathbf{E}} \times \underline{\mathbf{H}}_{\text{phy}}^*)$ in (2.76) of section 2.6.2 and using $\underline{\mathbf{H}}_{\text{phy}} = 1/Z (\mathbf{n} \times \underline{\mathbf{E}})$ for the investigated TEM and TE (transversal electric) waves gives $\underline{\mathbf{S}}_{\text{phy}} = 1/2 (\underline{\mathbf{E}} \times (1/Z (\mathbf{n} \times \underline{\mathbf{E}}))) = 1/(2Z) (\underline{\mathbf{E}} \cdot \underline{\mathbf{E}}^*)$. By assuming the same wave impedance for both ports, the S-parameters are expressed as the ratio of the respectively integrated $\underline{\mathbf{S}}_{\text{phy}}$ on the port. The port excitation is done on port 1 for the first column of $[S]_{2 \times 2}$ and on port 2 for the second column of $[S]_{2 \times 2}$.

Since $\underline{\mathbf{H}}$ is substituted by $\underline{\mathbf{E}}$ at the beginning, (2.80) is valid for the results of both FEM C and FEM BC. Therefore, no simplification is achieved for calculating S-parameter from the homology concept of FEM BC.

2.6.4 Maxwell Stress Tensor

For the conventionally formulated (indicated through the subscript "phy") MST in this section, see e.g. [250]. Contrary to the previously discussed Poynting vector (see section 2.6.2), the EM fields are used separately from each other to calculate of the electric and magnetic part of the MST, respectively. Especially the force action caused by the real-valued magnetic field (indicated in the following by omitting the underline) is of technical interest, which is ordinarily expressed as

$$\tau_{\text{m,phy}} = \mu \begin{pmatrix} \frac{1}{2} (H_x^2 - H_y^2 - H_z^2) & H_x H_y & H_x H_z \\ H_y H_x & \frac{1}{2} (H_y^2 - H_x^2 - H_z^2) & H_y H_z \\ H_z H_x & H_z H_y & \frac{1}{2} (H_z^2 - H_x^2 - H_y^2) \end{pmatrix}, \quad (2.81)$$

whereas the bicomplex-formulated version turns out as

$$\tau_{\text{m,BC}} = \mu \begin{pmatrix} \frac{1}{2} (H_y^2 - H_z^2 - H_x^2) & H_y H_z & H_y H_x \\ H_z H_y & \frac{1}{2} (H_z^2 - H_y^2 - H_x^2) & H_z H_x \\ H_x H_y & H_x H_z & \frac{1}{2} (H_x^2 - H_y^2 - H_z^2) \end{pmatrix}. \quad (2.82)$$

Note that all entries of the matrix $\tau_{\text{m,BC}}$ are present in $\tau_{\text{m,phy}}$, but in a reordered manner.

Regarding the real-valued electric part of the MST, both $\tau_{\text{e,BC}}$ and $\tau_{\text{e,phy}}$ are equivalent to each other, which reads similarly to $\tau_{\text{m,phy}}$ as

$$\tau_{\text{e,phy}} = \tau_{\text{e,BC}} = \varepsilon \begin{pmatrix} \frac{1}{2} (E_x^2 - E_y^2 - E_z^2) & E_x E_y & E_x E_z \\ E_y E_x & \frac{1}{2} (E_y^2 - E_x^2 - E_z^2) & E_y E_z \\ E_z E_x & E_z E_y & \frac{1}{2} (E_z^2 - E_x^2 - E_y^2) \end{pmatrix}. \quad (2.83)$$

After calculation of the divergence of the respective tensor followed by spatial integration as usual [250], the force is available. In case of the MST, the bicomplex-formulated EM field shows no additional merits nor shortcomings and leads to a similar calculation procedure. Again, the full EM field is conformally approximated, which makes FEM BC superior.

2.7 Wave Splitting of the Bicomplex-valued Field

The background of the wave splitting process (wave field decomposition through diagonalization of the system matrix [108]) shall be provided by symmetry considerations. In [108], different wave splitting techniques are investigated. For further reading on EM wave splitting, see e.g. [259].

As shown in section 2.2.2, the Pseudo-Helmholtz equation (2.6) describes one-way wave propagation. This is in contrast to the common Helmholtz equations (2.5) discussed in section 2.2.1, where both eigenvalues are included in its solution space, respectively. One-way wave propagation may be beneficial in numerically large problems [108], or if the second wave direction is not of interest [38]. Typical applications of one-way wave propagation modeling are seismo-acoustic problems considering many wavelengths [8, 90], which corresponds to the problem scale of the presented bicomplex FEM in the high-frequency regime. An important occurrence of wave splitting are absorbing boundary conditions (ABCs)⁴⁰, as shown in [232]. Further investigations on EM wave splitting in the context of ABCs are done in [119] and regarding the determination of material parameters in [118]. In [8], two categories of wave splitting are mentioned: a factorization of the wave equation and a factorization of the wave solution. Regarding FEM modeling, it is suitable to follow the first category by adjusting the wave equation, which is presented below.

According to [259], the forward and backward waves are uncoupled after the wave splitting process. This allows for a separate numerical implementation of the two waves. They are related by the transmission and the reflection coefficients, which will be shown below.

To apply ABCs to the Maxwell system, it is possible to use a discontinuous Galerkin FEM (DGFEM) [262], which will be discussed later on in section 4.2.2. A possible solution for continuous Galerkin FEM is the concept of diagonalization, see e.g. [232]. This technique aims at a separation of eigenvalues of the time-harmonic Maxwell system. Thus, it is an isomorphism to an equivalent system of two equations, where the first equation expresses incoming waves and the second one expresses outgoing waves. One has to note that the ordinary Helmholtz equation includes both possible wave directions. Therefore, a direct application of ABCs is possible there.

The bicomplex expressed Maxwell system inherently includes the process of diagonalization, which leads to the important fact that only one wave direction is expressed with one equation. For the previously investigated examples of homogeneous material distribution, one equation matches the requirements, because no reflected wave is generated. Based on (2.22) discussed in section 2.3.2 for inhomogeneous material distribution, one has to consider in addition a second equation for the FEM, which results in the following system of the bicomplex-expressed Maxwell system of the two possible wave directions $+z$ and $-z$:

$$\begin{aligned}\nabla \times \underline{\mathbf{F}}_+ + \frac{\nabla\sqrt{Z}}{\sqrt{Z}} \times \underline{\mathbf{F}}_+ &= ij k \underline{\mathbf{F}}_+, \\ \nabla \times \underline{\mathbf{F}}_- + \frac{\nabla\sqrt{Z}}{\sqrt{Z}} \times \underline{\mathbf{F}}_- &= ij k \underline{\mathbf{F}}_-, \end{aligned} \quad (2.84)$$

where $\underline{\mathbf{F}}_{+/-}$ is the EM field of a wave which travels in $+/-$ direction. Since the whole accompanying tripod⁴¹ is rotated to describe the second equation of (2.84) compared to the first one instead of inverting the wavenumber k , both equations look similar. Of course, the additional consideration

⁴⁰The purpose of absorbing boundary conditions is the truncation of a computational domain Ω with vanishing reflected wave parts.

⁴¹The accompanying tripod of a plane EM wave is build by the wave vector \mathbf{k} oriented in propagation direction and the transversal electric and magnetic field, respectively, by assuming a right-hand system. It can be understood as a moving local coordinate system and is illustrated on the top right of Fig. 2.2, see section 2.1.

of the second equation of (2.84) in FEM would lead to a system matrix of doubled size, which is a clearly drawback compared to the ordinary Helmholtz equation.

A locally exact wave splitting will be done next. More precisely, a one-dimensional wave splitting of the three-dimensional field problem in the possible wave directions $+z$ and $-z$ is suitable. Note that also multi-dimensional wave splittings are possible in general, as described e.g. in [108].

To express the two possible waves in a bicomplex manner, the energy-flux normalization described in [108] is modified to the impedance normalization (so-called in this thesis) as

$$\begin{pmatrix} \underline{\mathbf{F}}_+ \\ \underline{\mathbf{F}}_- \end{pmatrix} = \begin{pmatrix} \frac{1}{\sqrt{Z}} & i\sqrt{Z} \\ 1 & -i\sqrt{Z} \end{pmatrix} \begin{pmatrix} \underline{\mathbf{E}} \\ \underline{\mathbf{H}} \end{pmatrix}. \quad (2.85)$$

This transformation is isomorphic to the assumptions made in the first step of the derivation of the bicomplex equation (2.8), see section 2.2.2. The corresponding inverse transformation of (2.85) is then

$$\begin{pmatrix} \underline{\mathbf{E}} \\ \underline{\mathbf{H}} \end{pmatrix} = \begin{pmatrix} \sqrt{Z} \mathbf{z}_1 \{\dots\} & \sqrt{Z} \mathbf{z}_1 \{\dots\} \\ \frac{1}{\sqrt{Z}} \mathbf{z}_2 \{\dots\} & -\frac{1}{\sqrt{Z}} \mathbf{z}_2 \{\dots\} \end{pmatrix} \begin{pmatrix} \underline{\mathbf{F}}_+ \\ \underline{\mathbf{F}}_- \end{pmatrix}, \quad \text{where } \underline{\mathbf{F}}_{\pm} = \mathbf{z}_1 \pm i \mathbf{z}_2, \quad (2.86)$$

and $\mathbf{z}_{1/2} \{\dots\}$ means the outer real or imaginary part of $\underline{\mathbf{F}}_{\pm}$, respectively. To relate the forward and backward wave to each other, reflection and transmission coefficients are suitable. They will be introduced on a single material step by assuming an incidence angle perpendicular to the step next and applied later on in section 4.2.2 and section 4.2.4 on numerical examples. According to [250], the reflection coefficients for the electric and magnetic field r_e and r_m , respectively, are calculated as the ratio of the reflected part of the wave "ref" to the whole incident wave "inc" as

$$\begin{aligned} r_e &= \frac{|\underline{\mathbf{E}}_{\text{ref}}|}{|\underline{\mathbf{E}}_{\text{inc}}|} = \frac{Z_2 - Z_1}{Z_1 + Z_2}, \\ r_m &= \frac{|\underline{\mathbf{H}}_{\text{ref}}|}{|\underline{\mathbf{H}}_{\text{inc}}|} = \frac{Z_1 - Z_2}{Z_1 + Z_2}, \end{aligned} \quad (2.87)$$

where Z_1 is the wave impedance of material 1 and Z_2 is the one of material 2. Furthermore, transmission coefficients t_e and t_m are introduced as the ratio of the transmitted part of the wave "tra" to the whole incident wave as

$$\begin{aligned} t_e &= \frac{|\underline{\mathbf{E}}_{\text{tra}}|}{|\underline{\mathbf{E}}_{\text{inc}}|} = 1 + r_e = \frac{2Z_2}{Z_1 + Z_2}, \\ t_m &= \frac{|\underline{\mathbf{H}}_{\text{tra}}|}{|\underline{\mathbf{H}}_{\text{inc}}|} = 1 + r_m = \frac{2Z_1}{Z_1 + Z_2}. \end{aligned} \quad (2.88)$$

Using (2.87) and (2.88), the splitted bicomplex wave fields are related by

$$\begin{aligned} \begin{pmatrix} \underline{\mathbf{F}}_{\text{inc},+} \\ \underline{\mathbf{F}}_{\text{inc},-} \end{pmatrix} &= [t_{\text{bc}}] \begin{pmatrix} \underline{\mathbf{F}}_{\text{inc},+} \\ \underline{\mathbf{F}}_{\text{inc},-} \end{pmatrix} + [r_{\text{bc}}] \begin{pmatrix} \underline{\mathbf{F}}_{\text{inc},+} \\ \underline{\mathbf{F}}_{\text{inc},-} \end{pmatrix} \\ &= \begin{pmatrix} t_e \mathbf{z}_1 \{\dots\} & t_e \mathbf{z}_1 \{\dots\} \\ i t_m \mathbf{z}_2 \{\dots\} & i t_m \mathbf{z}_2 \{\dots\} \end{pmatrix} \begin{pmatrix} \underline{\mathbf{F}}_{\text{inc},+} \\ \underline{\mathbf{F}}_{\text{inc},-} \end{pmatrix} + \begin{pmatrix} r_e \mathbf{z}_1 \{\dots\} & r_e \mathbf{z}_1 \{\dots\} \\ i r_m \mathbf{z}_2 \{\dots\} & i r_m \mathbf{z}_2 \{\dots\} \end{pmatrix} \begin{pmatrix} \underline{\mathbf{F}}_{\text{inc},+} \\ \underline{\mathbf{F}}_{\text{inc},-} \end{pmatrix} \\ &= \begin{pmatrix} \underline{\mathbf{F}}_{\text{tra},+} \\ \underline{\mathbf{F}}_{\text{tra},-} \end{pmatrix} + \begin{pmatrix} \underline{\mathbf{F}}_{\text{ref},+} \\ \underline{\mathbf{F}}_{\text{ref},-} \end{pmatrix}, \end{aligned} \quad (2.89)$$

where $[t_{\text{bc}}]$ and $[r_{\text{bc}}]$ are matrices describing the reflection and transmission coefficient of the bicomplex wave field, respectively. If merely $\underline{\mathbf{F}}_{\text{inc},+}$ and no $\underline{\mathbf{F}}_{\text{inc},-}$ exists, (2.89) is simplified to

$$\begin{aligned} \underline{\mathbf{F}}_{\text{inc},+} &= \left(t_e \mathbf{z}_1 \left\{ \underline{\mathbf{F}}_{\text{inc},+} \right\} + i t_m \mathbf{z}_2 \left\{ \underline{\mathbf{F}}_{\text{inc},+} \right\} \right) + \left(r_e \mathbf{z}_1 \left\{ \underline{\mathbf{F}}_{\text{inc},+} \right\} + i r_m \mathbf{z}_2 \left\{ \underline{\mathbf{F}}_{\text{inc},+} \right\} \right) \\ &= \underline{\mathbf{F}}_{\text{tra},+} + \underline{\mathbf{F}}_{\text{ref},+}. \end{aligned} \quad (2.90)$$

The components of (2.89) are shown in Fig. 2.39, where the wave splitting appears at the step of material properties placed between material 1 (drawn in white) and 2 (colored in orange).

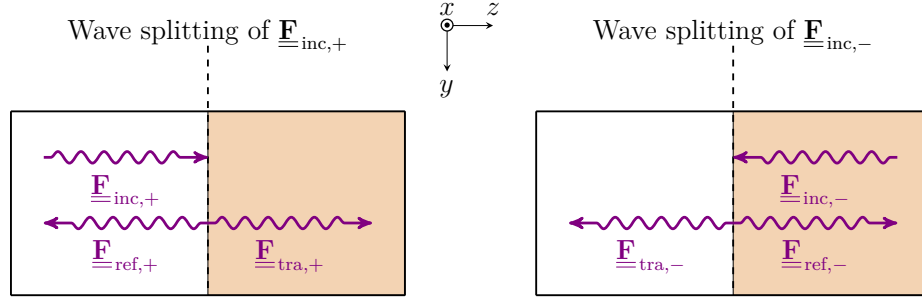


Figure 2.39 Bicomplex wave components of (2.89) for waves incoming from the positive and negative z -direction by assuming wave splitting at a step of material properties.

The incoming wave components $\underline{\mathbf{F}}_{\text{inc},+/-}$ are drawn on the top, respectively. On the material step, they are splitted into two wave parts $\underline{\mathbf{F}}_{\text{tra},+/-}$ and $\underline{\mathbf{F}}_{\text{ref},+/-}$, respectively, which travel in opposite directions. Later on in section 4.2.2 and 4.2.4, only the left case of Fig. 2.39 is considered. The above indicated isomorphism (see at the beginning of this section) between the bicomplex equation (discussed especially on Fig. 2.10 in section 2.2.2) and the process of diagonalization will be discussed now. In general, three steps may be distinguished, which are illustrated in Fig. 2.40.

Faraday's and Ampère's law's terms including $\underline{\mathbf{E}}$ are divided by $\sqrt{\underline{Z}}$
 " $\underline{\mathbf{H}}$ are multiplied by $\sqrt{\underline{Z}}$

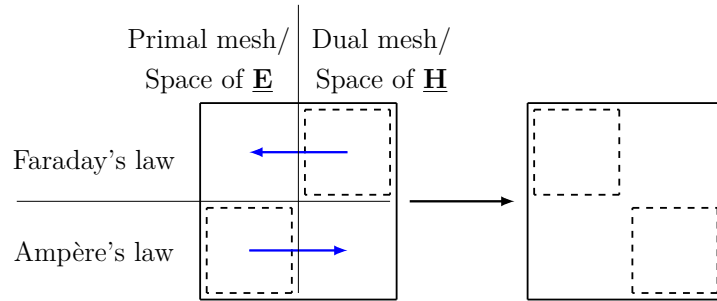
Impedance normalization without formatting

(a)

Faraday's law + i Ampère's law = Bicomplex equation

Formatting through the outer imaginary unit i

(b)



Diagonalization of temporal derivatives in the system matrix

(c)

Figure 2.40 Equivalence of derivation of the bicomplex equation (2.6) in section 2.2.2 and the process of wave splitting discussed here. (a) shows the impedance normalization without formatting, (b) the generation of the bicomplex format and (c) the diagonalization procedure.

First, both sides of Faraday’s and Ampère’s law are normalized by the wave impedance Z , see the top of Fig. 2.40. Second, both equations are rearranged into a bicomplex format by the outer imaginary unit i , shown on the middle. Third, i is factored out on the RHS (the temporal derivatives), as shown on the bottom of Fig. 2.40. As mentioned earlier, i maps between the primal and the dual mesh, or between the spaces of ${}^1\mathcal{E}$ and ${}^1\mathcal{H}$ (see e.g. Fig. 2.14 in section 2.4 or Fig. 2.18 in section 2.4.2). Note that (2.85) includes both steps (a) and (b) of Fig. 2.40.

To start next with the numerical implementation in FEM, a further condition has to be defined in addition to boundary values to ensure the uniqueness of the solutions of the Pseudo-Helmholtz equation for solving exterior boundary value problems. As for the Helmholtz equation, the Sommerfeld radiation condition (SRC) [219] has to be fulfilled at infinity in all spatial directions of the problem domain Ω in order to obtain physically reasonable radiated / outgoing waves. This condition was first mentioned in [229] and exhaustively outlined there. The SRC limits the solution space to outgoing waves and excludes incoming waves originating at infinity.

A graphical representation of a proposed bicomplex SRC is given below in Fig. 2.41.

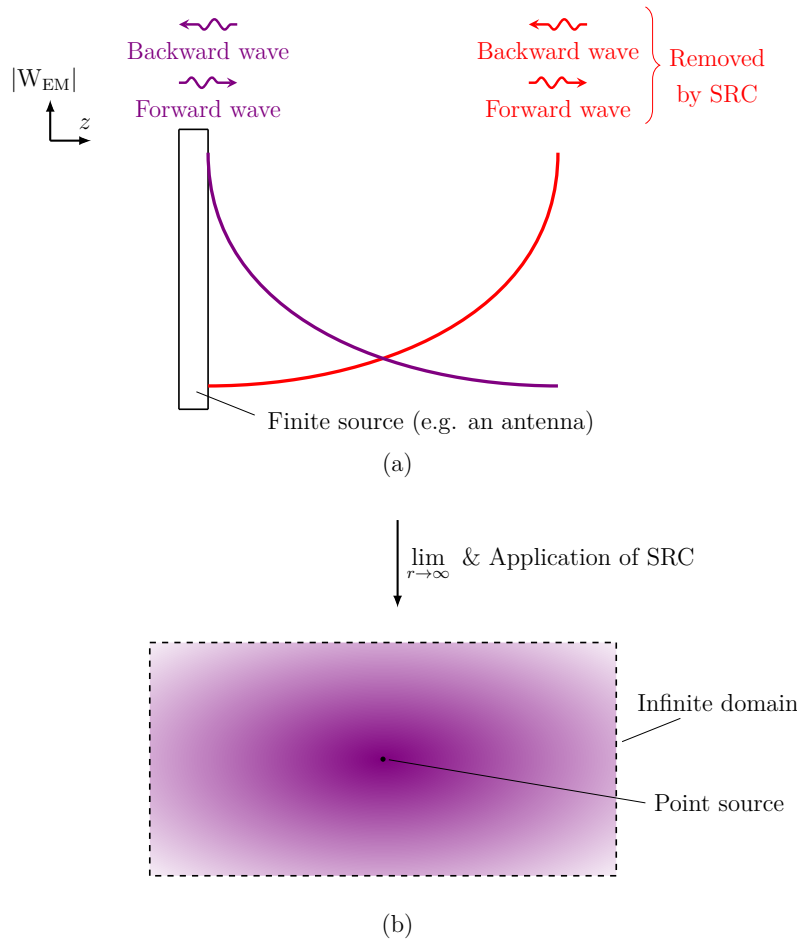


Figure 2.41 Principle of a bicomplex SRC (2.91) concerning the qualitative energy content W_{EM} of incoming and outgoing waves generated by finite sources. (a) shows the two possible asymptotical behaviors of waves, and (b) describes the situation after the application of the SRC in an infinite domain, a radially asymptotic decrease of the EM field strength is obvious.

On the top (a) of Fig. 2.41, the two possible behaviors of waves are shown, which are an asymptotical increase or decrease of their energy content W_{EM} (see (2.75) discussed in section 2.6.1), respectively. The bicomplex SRC removes the ones which increase by going away from the source (drawn in red). By shrinking additionally the finite source to one point in order to observe

the relations at infinity, the domain on the bottom (b) follows. Only forward and backward waves with a decreasing energy content by going away from the source (colored in violet) are now mathematically allowed since they are physically reasonable. Note regarding FEM implementation that the SRC applies at infinity, whereas boundary conditions apply at the boundary of Ω . The derivation of the bicomplex SRC is similar to the ordinary one and therefore not represented here.

For a three-dimensional domain, the SRC can be reformulated in a bicomplex sense as

$$\lim_{r \rightarrow \infty} r \left[\frac{\partial}{\partial r} \underline{\mathbf{F}} \mp ij k \underline{\mathbf{F}}^+ \right] = 0, \quad (2.91)$$

where r is the distance from the source to a point expressed in spherical coordinates. Since every object with finite dimensions might be contracted to a point compared to infinity, spherical coordinates are valid for an arbitrary shaped source and problem domain. The " \mp " in (2.91) means "-" or "+" for the bicomplex forward and backward wave equation (2.84), respectively, discussed in section 2.7. In (2.84), it is furthermore obvious that for the forward wave (which travels in $+z$ -direction), a "-" applies for the temporal derivative. Since the identity $ij = -ji$ is used in the derivation of (2.84), the signs are changed in (2.91), compared to [229].

2.8 Conjecture Regarding Gravitational Waves

At first, it has to be clarified that the approach proposed in this section merely aims to describe a conformal generalization of FEM BC defined on Ω (which is assumed to be a subspace of \mathbb{R}^3) to consider gravitational waves using a (co)homology approach. It is assumed further that a gravitational wave periodically deforms the homology of Ω . This approach is more problem-specific and observation-oriented than GR, which will be clarified below. All assumptions presented here are for massless relations. This is in contrast to the subject of gravito-electromagnetism, where mass is considered (see e.g. [72] or [237]). As widely known, gravity affects the propagation of light waves, for instance, by bending them. According to [26], in the absence of matter, both EM and gravitational waves are transverse and propagate at the speed of light. As discussed in [175], specific types of gravitational waves cause metric perturbations of the Minkowski space-time. It is further reported in [175], that one can consider the possibility of existing coupled states of EM and gravitational waves for which the metric perturbations are nonzero.

This gives rise to building a coupled system of EM and gravitational waves. As especially shown in section 2.4.1, it is usual in FEM to define EM wave quantities on the cotangential space as separate or combined variables, which might not correctly represent the physical phenomena in a conformal sense. Regarding observations, EM waves are directly measurable and do not affect the metric, whereas gravitational waves are not directly measurable and deform the metric.

The Minkowski space-time is an elegant framework to describe relativistic effects, where four dimensions (three spatial and one temporal) are embedded in the tangential space (homology). Changes on a spatial dimension affect the temporal dimension and vice versa, which is represented by the corresponding norm. Contrary to this, for the proposed generalization of the bicomplex system (cohomology approach), the temporal dimension is eliminated by using temporal complex vector amplitudes in the cotangential space (cohomology), as done throughout this thesis. Concerning this case the three spatial dimensions are embedded in the tangential space (homology), as usual. For the generalized version, changed dimensions of Ω can be implemented by changed absolute coordinates. This would change the length components instead of the base vectors itself as shown on the bottom right of Fig. 2.15 in section 2.4.1. A change of basis through a manipulation of the metric coefficients g_{pq} would be further possible, as shown on the bottom left of Fig. 2.15. As a covariant theory, homology can represent metric perturbations by a manipulation of the

chain complex. On the other hand, the contravariant cohomology theory perfectly matches the behavior of the EM field, as seen especially in section 2.4.1. Following section 2.4.6, the use of the duality of cohomology and homology (both possibilities of Fig. 2.30 together, see section 2.4.6) yields the proposed structure below in Fig. 2.42.

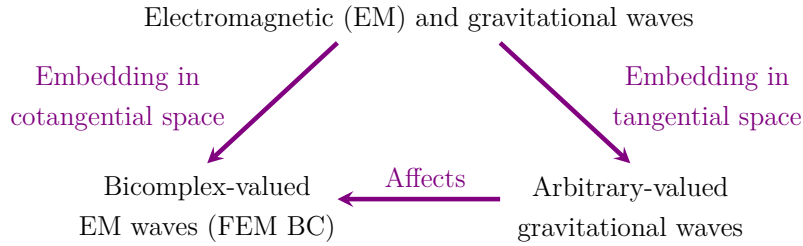


Figure 2.42 Proposed topological concept of both electromagnetic and gravitational waves. The chain complex (defined on the tangential space) is the observer’s reference frame.

On the left of Fig. 2.42, the contravariant cohomology approach presented throughout this thesis is placed. At the right side, the covariant homology approach is used for embedding curvature of space caused by gravitational waves, see the bottom right of Fig. 2.15 discussed in section 2.4.1. The format of gravitational waves is not specified here and should be in accordance to the chosen gravitational field variables. See e.g. [26] for an investigation of gravitational waves analogous to EM waves, where a second vector potential similar to the magnetic vector potential $\underline{\mathbf{A}}$ is introduced to describe plane gravitational waves by satisfying a wave equation. Naturally, the proposed structure considers that changes on function spaces (cohomology) do not affect the chain complex (homology) where they are defined on, since the differential bicomplex EM field ${}^1\underline{\mathcal{F}}$ is assumed to be massless. Contrary, a changed metric described by a locally varying metric tensor in (2.38) of section 2.4.1 affects the cohomology from the perspective of the observer, since the chain complex is the observer’s reference frame. A varying metric tensor is indicated by non-vanishing Christoffel symbols [228], which describe these variations through spatial derivatives of the base vectors⁴² in a compact manner. As shown later on in sections 4.2.3 and 4.2.4, the existing components of the EM field do not have to be necessarily symmetric. Hence, pure EM waves or pure gravitational waves are included in the proposed model.

The relative change in length caused by a gravitational wave is usually expressed by the dimensionless parameter strain h [150] as

$$h \approx \frac{\Delta L}{L}, \tag{2.92}$$

where ΔL is the absolute change of length of an object and L is the length of that object. According to [150], an exemplary magnitude of a gravitational wave is $h \approx 10^{-21}$. Therewith, the size of the metric perturbation caused by gravitational waves could cause problems concerning the finite element environment when adding mesh cells in this region, which would be extremely small compared to other mesh cells. A possible solution is to use mesh deformation⁴³ instead of remeshing Ω . Probably a much greater problem than the numerical accuracy is the accuracy of the shape functions, which especially determines the accuracy of the FEM solution.

⁴²In flat space (which can be described by an Euclidean metric in contrast to curved space), the covariant derivative [228] (a generalization of the ordinary derivative in a way that both the vector components and the base vectors are differentiated using the product rule) is equal to the ordinary derivative since the base vectors are the same everywhere in that space.

⁴³Examples of mesh deformation using curvilinear coordinates are presented e.g. in [188]. There it is reported that a mesh deformation changes only the FEM mass matrix, which is based on the Hodge operator (as previously discussed in section 2.4.2).

Within this chapter, the cohomology concept of the bicomplex-formulated EM wave propagation (see the left side of Fig. 2.30 presented in section 2.4.6) is used to design a suitable finite element framework, where mainly special features will be discussed in detail. Contrary to numerical forward methods such as the Transmission Line Matrix Method [210], the FEM covers inverse boundary value problems (BVPs), such as electrodynamics in frequency domain. As an alternative in high-frequency regime, the solution of Maxwell's equations might also be obtained from the ray tracing method [264], which is based on ray optics. In Fig. 3.1, the principle of handling BVPs in FEM is illustrated using a brick mesh.

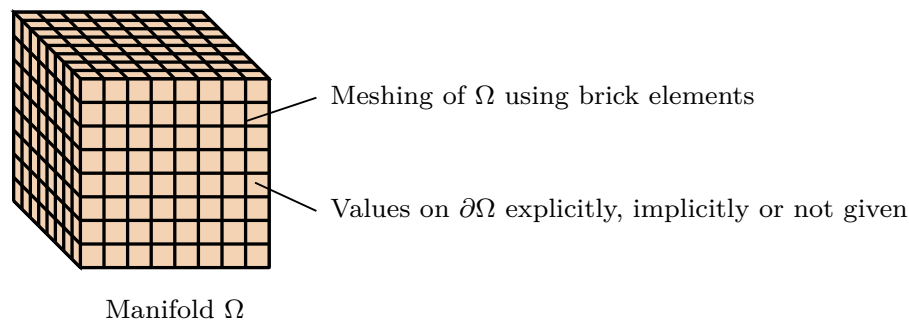


Figure 3.1 Principle of handling BVPs defined on the manifold Ω using brick finite elements.

On the spatial boundary $\partial\Omega$, function values can be given explicitly by enforcing several boundary conditions, implicitly by fulfilling e.g. Neumann boundary conditions deducible from Green's identities (see appendix A) or left open. In general, different combinations of boundary conditions are possible to satisfy a PDE. This provides a certain degree of freedom, for instance, one can specify function values of a PDE's solution on $\partial\Omega$ (Dirichlet boundary conditions) or instead spatial derivatives (Neumann boundary conditions). A transformation between these two kinds of boundary conditions can be done using a Dirichlet-to-Neumann operator, for a profound investigation regarding time-harmonic Maxwell's equations, see e.g. [42].

A meshing of the problem domain / manifold Ω makes it possible to use vector spaces for approximating continuous function values (continuous FEM) defined on Ω . For basic investigations on vector spaces, see e.g. [156]. Also quadratic forms on real and complex vector spaces, which are the results of the tensor product between the sets of basis and test functions, are discussed there on an introductory level. Fundamentals on computational handling of functions, as e.g. numerical integration, can be found for example in [183], [215] or [231]. An advantage of FEM is the sparsity of the system matrix [142]. Only a few nontrivial values, the neighboring nodes, need to be stored.

This leads to a drastic reduction in computer storage demand. Furthermore, efficient algorithms might reduce the computation time. There are e.g. LU decomposition methods, frontal and multifrontal methods and conjugate gradient / Krylov subspace methods. The reader is invited to explore e.g. [251] for details of these algorithms. Therefore, the FEM is well-suited for large-scale EM problems and in this regard superior to integral equation methods or full-matrix based numerical methods. Differently to the Method of Moments (MoM), the FEM solves differential equations, whereas the MoM is based on integral equations [143].

In this chapter, the modeling concept of FEM will be shown first in section 3.1. Secondly, a short insight into the state-of-the-art of FEM is presented in section 3.2. Thirdly, edge-based variational formulations are discussed in section 3.3. This is followed by implementation specifics of the proposed bicomplex FEM in section 3.4. The discretization of topological spaces using meshes will be considered next in section 3.5. Finally, three-dimensional bicomplex absorbing boundary conditions are discussed in section 3.6, since they differ from the ordinary version used in FEM. The generation of the matrices is a well-known standard procedure in FEM.

3.1 Concept of Finite Element Modeling

In this section, the problem class of the bicomplex FEM is deduced and the corresponding linear equation system is introduced. A classification of the used three-dimensional FEM methods is done by a progressive deduction presented below in Fig. 3.2.

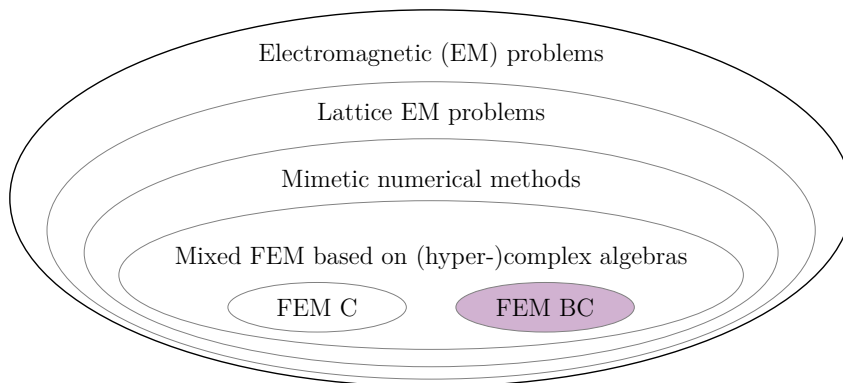


Figure 3.2 Progressive deduction of the used three-dimensional FEM variants.

The most general category depicted on the top of Fig. 3.2 includes electromagnetic problems in general, which can be defined on continuous or discretized domains Ω (where Ω is meshed by the use of finite elements, see Fig. 3.1). Also analytical investigations of EM wave propagation problems is included there, see e.g. [178]. By excluding continuous domains, discretized or lattice EM problems remain, where Ω is only defined on certain geometric entities. A next step on deduction are mimetic numerical methods which imitate specific properties of the continuum problem (as discussed earlier in section 2.4). The FEM is one possibility to solve lattice (using a mesh) EM problems, another one is the use of finite differences (see e.g. [241]). Both the common complex-valued FEM C and the proposed bicomplex-valued FEM BC can be assigned to mixed FEM methods, since Whitney edge elements are used. As shown throughout Chapter 2, the two FEM approaches are based on different algebras.

It is common to formulate one of Maxwell's equations ((2.7a, 2.7b), see section 2.2.2) combined with the corresponding divergence condition ((2.7c, 2.7d), see also section 2.2.2) as a saddlepoint problem, see e.g. [51]. By assuming a source-free domain, the electric field and the magnetic field

can be assigned as DOFs. In contrast to these mixed formulations, which are based on several evenly fulfilled quantities, the bicomplex FEM relies on merely one field variable. Furthermore, since only divergence-free finite elements are used and no sources are considered, the two divergence conditions are fulfilled inherently. Throughout this thesis, first order shape functions are used in general. For higher-order Whitney forms concerning different finite elements, see e.g. [103] or [142]. The hierarchical version is especially discussed e.g. in [257].

Following [188], the differential p -forms are approximated by the use of piecewise polynomial expansions on the respective elements by using tensor products. For differential forms, this is done in a similar manner as for the definition of the tensor product regarding vector calculus in (2.3) of section 2.1.2 and the definitions of the inner products of the Hilbert space $H^1(\Omega)$ shown earlier in (2.17) of section 2.3.1 and $\mathbf{H}(\text{curl}; \Omega)$ introduced later on in (3.4), see section 3.3.

Since the number format is affected by the bicomplex FEM as elaborately discussed throughout Chapter 2, several possibilities of arbitrary-valued linear equation systems are shown in Fig. 3.3.

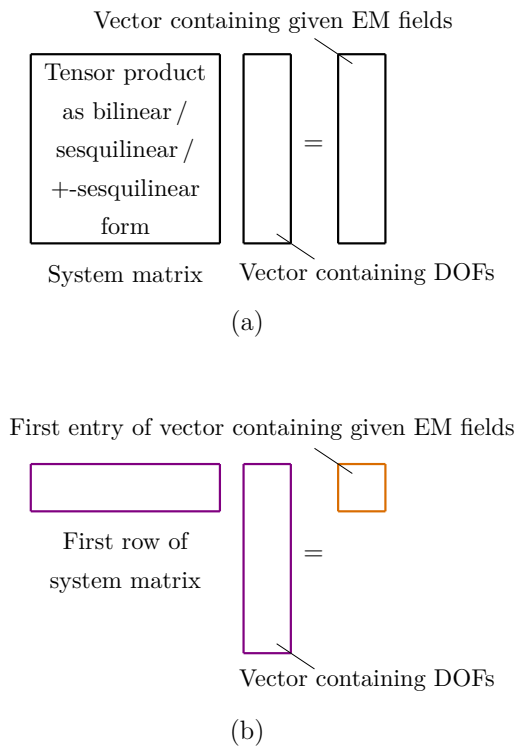


Figure 3.3 Intuitive interpretation of FEM linear equation system. In (a), the full linear equation system is shown. For both FEM C and FEM BC, it is represented by real numbers, see later on Fig. 3.4 in section 3.4. Below in (b), the integration procedure building the real-valued first entry of the RHS vector (drawn in orange) is implemented by matrix multiplication of the first row of the real-valued system matrix and the real-valued vector containing the DOFs (drawn in violet).

The system matrix on the top left of Fig. 3.3 can be real-valued (bilinear form), complex-valued (sesquilinear form) or bicomplex-valued (+-sesquilinear form). It contains all possible combinations of arbitrary-valued shape functions which are represented as a real-valued bilinear form, respectively, see later on Fig. 3.4 in section 3.4. Single entries of this system matrix represent the results of integrations over one distinct inner product of shape functions, respectively. Integration over the full domain Ω , which is indicated e.g. later on by (3.5) or (3.6) presented in section 3.3, is incorporated by the matrix multiplication in (a) of Fig. 3.3. Contrary, the matrix product shown in (b) represents the subsystem of the first equation of the FEM linear equation system depicted on the top.

3.2 State-of-the-Art in the Finite Element Method

In the here presented short sketch of fundamental strategies concerning certain steps of the FEM process, merely a few aspects are covered. The FEM has been established extensively in various topics of physics over the last decades. Beginning with the origin of this method, the recently published article [160] provides a historical overview of FEM, which covers the last eighty years. Some areas of application are mechanical problems discussed e.g. in [268] or electromagnetic problems which are discussed for example in [196]. General usage of the FEM regarding EM problems can be found, for instance, in [212]. Different kinds of wave propagation are further areas of application, as e.g. mechanical wave propagation [112]. Concerning this thesis, EM wave propagation is of interest, since there the electric and magnetic field are naturally coupled as several types of modes. An introduction to EM wave propagation is given, for instance, in [249]. Various EM wave propagation examples including scattering problems in the context of 3D FEM are discussed e.g. in [142], [143] or [193]. Furthermore, various EM wave propagation problems viewed in the classical vector calculus are reported in [146], [197] or [223]. A discussion of difficulties concerning time-harmonic wave propagation problems is presented in [29]. Despite the fact that many approaches and numerical techniques are available to handle EM wave propagation problems in FEM, 3D finite element application is still an open area in research [134].

As shown by Fig. 2.21 in section 2.4.3, the use of Whitney p -forms allows the assignment of DOFs to several geometric objects instead of solely to nodes. Following [217], Whitney edge functions are available in commercial FEM software as e.g. MAXWELL™ of ANSYS® Electronics Desktop™ [10] or CST Studio Suite® [63]. This context will be addressed by the use of edge DOFs on brick elements concerning all three-dimensional examples later on discussed in section 4.2. Regarding techniques for calculating the inverse of the system matrix, iterative methods¹ are often the preferred choice over direct methods to improve the computational efficiency. In this thesis, only direct methods which are available in the standard MATLAB environment are used, which will be adequately addressed in section 4.1.1.

Multiphysics coupling is state-of-the-art in commercial FEM softwares as well, especially in COMSOL Multiphysics® [61]. This topic is beyond the scope of this thesis, it should be noted that the bicomplex concept does not limit multiphysics coupling. Suitable isomorphisms between number systems might be rather advantageous than using the same number format for all physics.

A further common practice is a combination of FEM with the Boundary Element Method (BEM)². FEM-BEM coupling is superior to classical FEM in terms of efficiency regarding certain problem classes, as e.g. exterior problems (all EM sources and the material distribution are contained in Ω / enclosed by $\partial\Omega$). See e.g. [126] for an investigation of this technique regarding EM scattering. Also this topic is outside the scope of this thesis. It is assumed that there is no limitation in terms of coupling FEM BC to an appropriate kind of BEM.

To the best of the author's knowledge, all available FEM softwares on the market as the packages MAXWELL or HFSS™ of ANSYS Electronics Desktop [10], CST Studio Suite [63], COMSOL Multiphysics [61] or deal.II [12] do not allow a number format outside of the common real and complex numbers. Therefore, all presented numerical results are generated by an implementation in MATLAB without the use of any additional software package.

The following sections cover further differences to standard FEM in a broader manner.

¹Iterative methods for solving a linear system of equations generate the vector containing DOFs instead of direct matrix inversion by specific algorithms, details can be found e.g. in [142] or [193].

²Compared to FEM, where volumes of objects are discretized in the three-dimensional case, in BEM only surfaces of these objects are discretized.

3.3 Variational Formulations for 3D-FEM

Regarding implementation purposes of the proposed bicomplex cohomology concept (FEM BC), the imaginary unit i keeps the field components separately. In the context of DEC, a conversion of the PDE of continuous vector fields into discretized p -cochains is necessary, which is done by the de Rham projection map \mathcal{P}_p (see Fig. 2.19 in section 2.4.2). Concerning edge elements, this context will be discussed later on in detail, see Fig. 3.6 in section 3.4. Discretization of the vectorial $\underline{\mathbf{E}}$ using vectorial shape functions $\underline{\varphi}$ yields (exemplary for basis functions $\underline{\varphi}_u$)

$$\underline{\mathbf{E}} \xrightarrow[\text{using } \mathcal{P}_p]{\text{Discretization}} \tilde{\underline{\mathbf{E}}} = \sum_{u=1}^U E_u \underline{\varphi}_u, \quad (3.1)$$

where E_u contains the unknown edge coefficients and $\tilde{\underline{\mathbf{E}}} \in \mathbf{H}(\text{curl}; \Omega)$ is the approximated vector field. The vectorial Sobolev space $\mathbf{H}(\text{curl}; \Omega)$ for edge approximation [86] is

$$\mathbf{H}(\text{curl}; \Omega) = \{ \underline{\varphi} \in \mathbf{L}^2(\Omega); \text{curl } \underline{\varphi} \in \mathbf{L}^2(\Omega) \}, \quad (3.2)$$

where \mathbf{L}^2 denotes the vector-valued Lebesgue space of square-integrable functions (not to be confused with its scalar counterpart (2.16), see section 2.3.1)

$$\mathbf{L}^2(\Omega) = \left\{ \underline{\varphi} : \int_{\Omega} |\underline{\varphi}|^2 \, d\Omega < \infty \right\}. \quad (3.3)$$

The magnitude of the norm in (3.3) leads to the error norm (4.2) discussed later on in section 4.1.1. By introducing a scalar product on the Sobolev space $\mathbf{H}(\text{curl}; \Omega)$, it becomes a Hilbert space endowed with a metric. The solutions of the field problem are approximated in this space as the tensor product of test $\tilde{\underline{\mathbf{E}}}_w$ and basis $\tilde{\underline{\mathbf{E}}}_u$ functions, which is a bilinear, a sesquilinear or a $+$ -sesquilinear (for the bicomplex case) form in FEM, respectively. The inner product of the finite-dimensional complex-valued Hilbert space $\mathbf{H}(\text{curl}; \Omega)$ is defined as

$$\langle \tilde{\underline{\mathbf{E}}}_w, \tilde{\underline{\mathbf{E}}}_u \rangle = \int_{\Omega} \tilde{\underline{\mathbf{E}}}_w \cdot \tilde{\underline{\mathbf{E}}}_u^* \, d\Omega, \quad (3.4)$$

where $\tilde{\underline{\mathbf{E}}}_w, \tilde{\underline{\mathbf{E}}}_u \in \mathbf{H}(\text{curl}; \Omega)$ and $*$ means the ordinary complex conjugate of the argument. Note again that (3.4) represents one entry of the tensor product shown in (2.3), see section 2.1.2. The weak form of (2.51) (discussed in section 2.4.5) in the language of vector calculus is received by multiplying it by $\tilde{\underline{\mathbf{E}}}_w$ and integration by parts through the use of (A.1) from appendix A as

$$F(\tilde{\underline{\mathbf{E}}}) = \iiint_{\Omega} \left[(\nabla \times \tilde{\underline{\mathbf{E}}}_w) \cdot (\nabla \times \tilde{\underline{\mathbf{E}}}_u^*) - \nabla \cdot (\tilde{\underline{\mathbf{E}}}_w \times (\nabla \times \tilde{\underline{\mathbf{E}}}_u^*)) - k^2 \tilde{\underline{\mathbf{E}}}_w \cdot \tilde{\underline{\mathbf{E}}}_u^* \right] d\Omega = 0, \quad (3.5)$$

where the first term is self-adjoint. The second term is generated by integration and contains boundary integrals. In the case of Dirichlet boundary conditions, this term is translated to given field values on the RHS after applying Gauss' theorem (B.5) from appendix B. This approach leads to the same result as the tensor product in Galerkin FEM by neglecting discretization errors, where the basis functions and test functions lie in the same function space.

The weak form of (2.46) – presented in section 2.4.4 – expressed in vector calculus is received in a similar manner as (3.5), which reads as

$$F(\tilde{\underline{\mathbf{F}}}) = \iiint_{\Omega} \left[(\nabla \times \tilde{\underline{\mathbf{F}}}_w) \cdot \tilde{\underline{\mathbf{F}}}_u^+ - \nabla \cdot (\tilde{\underline{\mathbf{F}}}_w \times \tilde{\underline{\mathbf{F}}}_u^+) - ij k \tilde{\underline{\mathbf{F}}}_w^+ \cdot \tilde{\underline{\mathbf{F}}}_u^+ \right] \Big|_j \, d\Omega = 0, \quad (3.6)$$

where the first term is non-self-adjoint. Therefore, the usage of a suitable stabilization technique is recommended. For the benchmark problems discussed later on in section 4.2, no instable cases appear. The second term of (3.6) is handled in a similar manner as in (3.5). In section 3.6, the implementation of both second terms of (3.5) and (3.6) will be discussed by the use of ABCs.

3.4 Implementation Specifics of Bicomplex p D-FEM

This section covers implementation specifics of FEM BC valid for arbitrary dimension p . Generally, the generation of the mass and convection matrix required in FEM is realized according to the well-known standard procedure of FEM, see for example [196]. Later on in section 3.5, these issues will be discussed in detail and appropriate FEM matrix formulations will be given. After the assembling process of the elements of the two mentioned matrices, they are put in a bicomplex number format in form of (2.12) (see section 2.2.2) by the use of the MATLAB keyword `classdef`. Merely one bicomplex operation has to be defined, the subtraction. After subtracting the RHS of (2.12) from its LHS, the bicomplex system matrix is constructed.

This matrix is reformulated with real numbers, which is mathematically described in [270] for matrices with complex entries and in a straightforward manner in [164] for matrices with bicomplex entries. For example, the complex matrix is reformulated by placing its real part on the upper left and lower right place, see the red colored part of Fig. 3.4 below. The imaginary part is placed on the lower left position and with a minus sign on the upper right position. For the bicomplex case, the structure is presented in Fig. 3.4 (depicted in black).

Real matrix representation of complex system matrix

$$\begin{pmatrix} [\mathbf{E}_{\text{re}}] & -[\mathbf{E}_{\text{im}}] & -[\mathbf{H}_{\text{re}}] & [\mathbf{H}_{\text{im}}] \\ [\mathbf{E}_{\text{im}}] & [\mathbf{E}_{\text{re}}] & -[\mathbf{H}_{\text{im}}] & -[\mathbf{H}_{\text{re}}] \\ [\mathbf{H}_{\text{re}}] & -[\mathbf{H}_{\text{im}}] & [\mathbf{E}_{\text{re}}] & -[\mathbf{E}_{\text{im}}] \\ [\mathbf{H}_{\text{im}}] & [\mathbf{H}_{\text{re}}] & [\mathbf{E}_{\text{im}}] & [\mathbf{E}_{\text{re}}] \end{pmatrix}$$

Figure 3.4 Real matrix representation of the bicomplex system matrix, which is included in the FEM linear equation system in Fig. 3.3, see section 3.1.

The process indicated in Fig. 3.4 leads to a complex system matrix of double size compared to the real case, consequently, the size of the bicomplex one is doubled twice. After calculating the inverse of the real-formulated bicomplex system matrix, the computed coefficients for electric and magnetic fields are available according to (2.12).

In Fig. 3.5, the workflow of bicomplex FEM is illustrated. There, the steps in a continuous setting are drawn in violet. The first step in FEM is the meshing of Ω . From this, the homology can be created. Based on this, the cohomology is defined, where the coboundary operator (exterior derivative ${}^p d$) transforms between the equivalence classes of p -forms. Because only the primal mesh is needed for FEM BC, the problem domain is discretized as usual with tetrahedral or brick finite elements. According to the connectivity, the element matrices are built and assembled as global versions of the mass (MASS) matrix and the convection (CONV) matrix, which is also an ordinary process. Regarding the respective occurrence of the imaginary unit i on the RHS of (2.6) (see section 2.2.2), the global matrices are appropriately reordered. The imaginary unit j is handled as in common FEM C. After applying the real matrix representation shown in Fig. 3.4, the equation system is solved by matrix inversion. With the resulting DOFs, the EM field is

interpolated. For this, an algorithm detects the finite element, in which the point of interest lies. After adding the desired point to the set of the element nodes, a deformation of the convex hull³ is evaluated if the point lies not in the finite element.

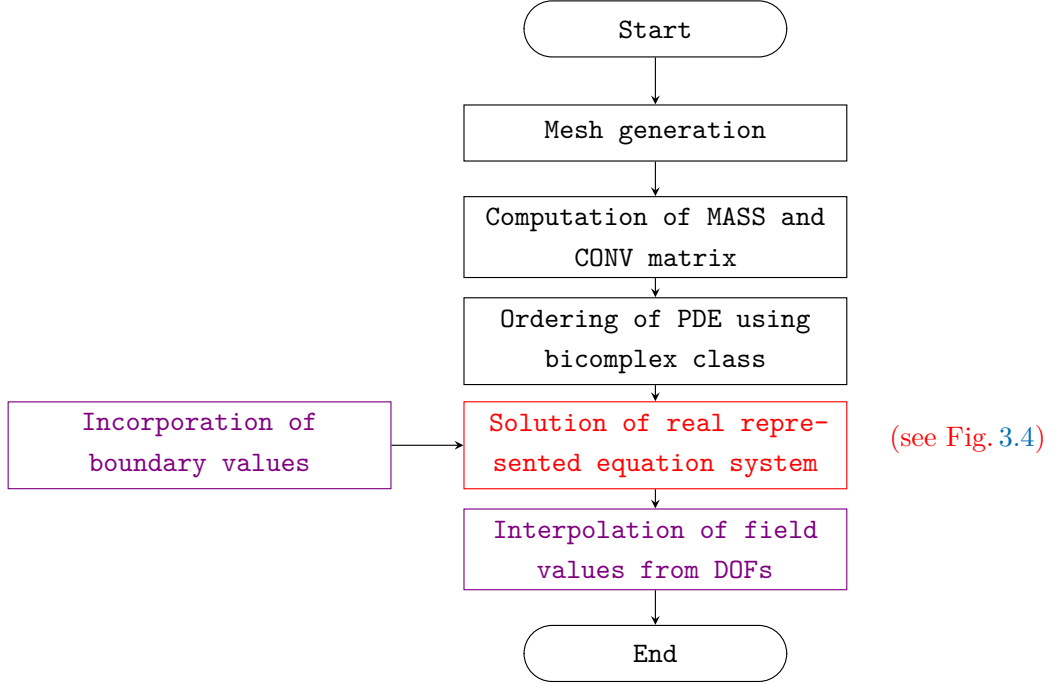


Figure 3.5 Workflow of bicomplex FEM.

To create a connection to the DEC-de Rham diagram presented earlier in Fig. 2.18 (see section 2.4.2), a clear distinction of the continuous setting expressed by vectors to the discrete setting expressed by differential p -forms is indicated in Fig. 3.6.

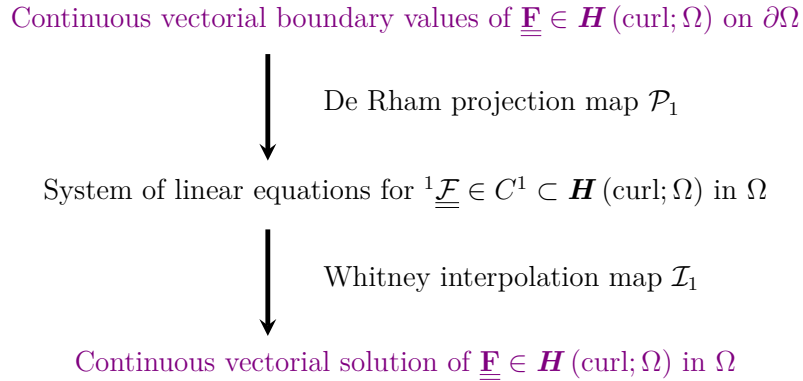


Figure 3.6 Relation of three-dimensional bicomplex FEM to the de Rham complex presented in Fig. 2.18 by consideration of the respective function spaces.

Remind that the principle of the de Rham projection map \mathcal{P}_1 and the Whitney interpolation

³The convex hull of a point set in three dimensions can be thought as the surface of a cloth of rubber which is spanned around that point set. According to [25], a convex polygon is spanned by its convex hull, which means that every straight line between two arbitrary points of that hull lie completely in the polygon. Details can be found e.g. in [25] or [152].

map⁴ \mathcal{I}_1 , which was discussed on Fig. 2.19 in section 2.4.2, is the conversion between the continuous and the discrete setting. On the top and the bottom of Fig. 3.6 the two continuous settings are drawn in violet to indicate the relation to the workflow of the bicomplex FEM depicted in Fig. 3.5. The system of linear equations presented on the middle of Fig. 3.6 is based on discrete differential p -forms. Note that the use of differential p -forms instead of vectors in the discrete FEM setting is preferred in order to suppress spurious modes. The used discretized primal 1-cochain space C^1 – which represents ${}^1\underline{\mathcal{F}}$ – is a proper subset (\subset) of the Hilbert space $\mathbf{H}(\text{curl}; \Omega)$.

3.5 Associated Matrices for Elements in 3D-FEM

The choice of shape functions, which span the discrete finite element spaces as presented in Fig. 2.18 (see section 2.4.2), is essential for the accuracy of the FEM. For different polynomial spaces, see e.g. [13]. In this section, the finite elements used for mesh construction are described in detail. Since the structure of the used brick meshes is simple regarding its regular arrangement and connectivity, no specific mesh generator is needed, as e.g. Gmsh [95]. Using the concept of DEC introduced in section 2.4 (see especially Fig. 2.11), the atlas used for both types of elements defined on the real spatial space \mathbb{R}^3 is shown below in Fig. 3.7.

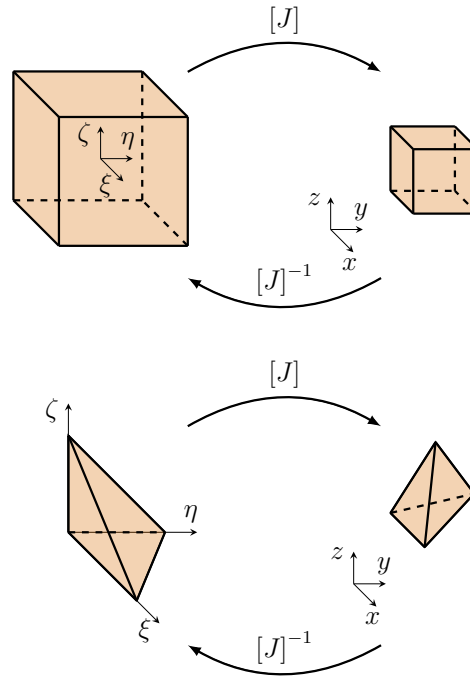


Figure 3.7 Atlas of two types of finite elements defined on the real spatial space \mathbb{R}^3 .

The local coordinate systems are depicted on the left (here, the elemental matrix description applies), whereas the global coordinate systems are shown on the right (here, the global matrix description is suitable). As an example of change of basis vectors shown on the bottom left of Fig. 2.15 in section 2.4.1, the Jacobian matrix⁵ $[J]$ maps between the local (ξ, η, ζ) and global

⁴Note that this interpolation process is rather a calculation, since the values between the DOFs depend on the shape functions.

⁵The Jacobian matrix includes all first order spatial derivatives of the base vectors of one coordinate system with respect to the base vectors of another coordinate system, see e.g. [228] for a discussion regarding tensor calculus. For the use in FEM covering EM problems, see e.g. [142].

(x, y, z) coordinate system, respectively. Note that for brick elements drawn on the top, $[J]$ is only nonzero at the principal diagonal, because only angle-preserving scalings of the reference brick are done. Contrary for tetrahedral elements drawn on the bottom, rotations and changes of angle ratios are possible in addition. On both element types, edge DOFs are used. For an application of face DOFs, see e.g. [258].

According to [228], the connection of $[J]$ to the metric tensor $[g_{pq}]$ is given by

$$[J]^T [J] = [g_{pq}], \quad (3.7)$$

where $[J]$ represents the transformation between Cartesian and generalized coordinates. Hence, $[J]$ (or its corresponding transpose $[J]^T$) includes the metric of the desired coordinate system in a comparable manner as $[g_{pq}]$ does. The difference is that $[J]$ transforms coordinates linearly, whereas $[g_{pq}]$ transforms differential line elements quadratically (see (2.38) in section 2.4.1). Since elements of the metric tensor g_{pq} represent – according to (2.48) (see section 2.4.4) – the inner product, the full metric tensor $[g_{pq}]$ represents the tensor product of base vectors. This is analogous to the MASS matrix of shape functions in FEM.

In the following, the eight-node version of the brick element is used. It is also known as linear order by means of one DOF per edge. The construction of the element matrices presented below is following the approach outlined in [269]. In Fig. 3.8, the normalized brick finite element is shown, where the scheme for edge and node numbering is depicted.

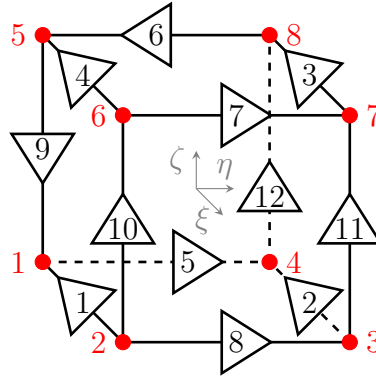


Figure 3.8 DOF numbering of the brick element where edges (drawn in black) and nodes (highlighted in red) are considered.

Compared to the generalized hexahedral element (see e.g. [134]), the local axes ξ, η, ζ are assumed to be parallel to the global axes x, y, z . The local coordinates can vary from -1 to $+1$ for the brick element shown in Fig. 3.8. Nodal DOFs are drawn in red on the corners and oriented DOFs on edges are illustrated in black. The local coordinates can be calculated from the global ones by

$$(\xi, \eta, \zeta) = \left(\frac{2}{l_x}(x - x_m), \frac{2}{l_y}(y - y_m), \frac{2}{l_z}(z - z_m) \right), \quad (3.8)$$

where x_m, y_m, z_m are the global center coordinates of the considered element and l_x, l_y, l_z are the corresponding lengths. In the given case, these lengths are equivalent to the respective 4 parallel edges. With the auxiliary parameters

$$\begin{aligned} \alpha_{1x} &= \frac{1}{2}(1 - \xi), & \alpha_{2x} &= \frac{1}{2}(1 + \xi), \\ \alpha_{1y} &= \frac{1}{2}(1 - \eta), & \alpha_{2y} &= \frac{1}{2}(1 + \eta), \\ \alpha_{1z} &= \frac{1}{2}(1 - \zeta), & \alpha_{2z} &= \frac{1}{2}(1 + \zeta), \end{aligned} \quad (3.9)$$

the 3D edge shape functions for the brick finite element are defined as

$$\begin{aligned}
 N_1^e &= \alpha_{1y}\alpha_{1z}, & N_2^e &= \alpha_{2y}\alpha_{1z}, \\
 N_3^e &= \alpha_{2y}\alpha_{2z}, & N_4^e &= \alpha_{1y}\alpha_{2z}, \\
 N_5^e &= \alpha_{1x}\alpha_{1z}, & N_6^e &= \alpha_{1x}\alpha_{2z}, \\
 N_7^e &= \alpha_{2x}\alpha_{2z}, & N_8^e &= \alpha_{2x}\alpha_{1z}, \\
 N_9^e &= \alpha_{1x}\alpha_{1y}, & N_{10}^e &= \alpha_{2x}\alpha_{1y}, \\
 N_{11}^e &= \alpha_{2x}\alpha_{2y}, & N_{12}^e &= \alpha_{1x}\alpha_{2y}.
 \end{aligned} \tag{3.10}$$

In (3.10), the superscript "e" implies numbering regarding the considered element (local coordinate system, see the left side of Fig. 3.7) instead of using global edge indices (global coordinate system, see the right side of Fig. 3.7). To evaluate the elemental CONV and stiffness (STIFF) matrix, the spatial derivatives of the shape functions in (3.10) are needed. They can be evaluated by applying the 3D-curl on this shape functions. Analytical integration of all possible combinations of two shape functions over the respective domain leads to the MASS matrix. Similarly, the integration of two derivatives leads to the STIFF matrix and that of one derivative and one function leads to the CONV matrix. For higher accuracy, numerical integration is avoided here and replaced by analytical integration. Alternatively, it is possible to apply the exterior derivative $^p d$ to the MASS matrix, which would produce the same STIFF or CONV matrix. The STIFF and MASS elemental matrices – used here for first order brick elements – are constructed in the same manner as in [269] and adjusted in the case of the CONV matrix.

In Fig. 3.9, the relation of the single terms of the variational formulations (3.5) and (3.6) (see section 3.3 for both equations) to FEM matrices is depicted.

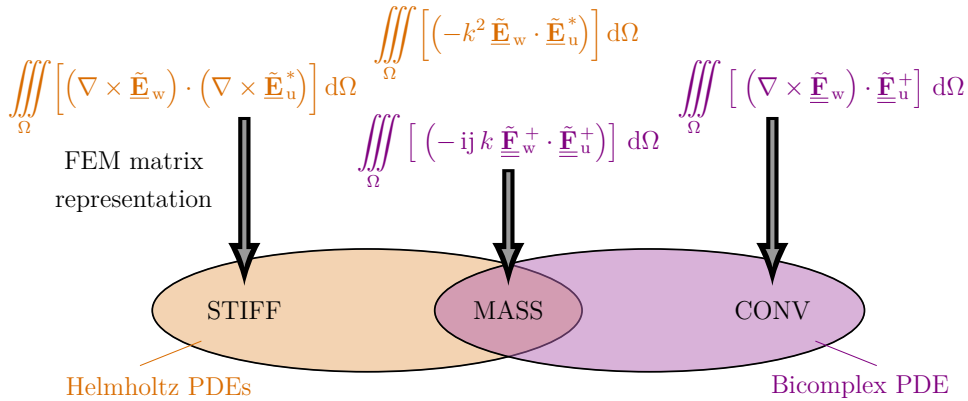


Figure 3.9 Relation of the terms of the variational formulations / weak form of the bicomplex PDE (3.6) and the Helmholtz PDEs (3.5) to their matrix representation in FEM based on Whitney edge DOFs.

Only the first and third terms of (3.5) and (3.6) are considered in Fig. 3.9, respectively, since the second terms are transformed to consider boundary conditions (see later on section 3.6). Note that in terms of the desired real-valued integral kernel for the bicomplex PDE (3.6) (see the discussion of (2.29) and (2.30) in section 2.3.2), the modulus of bicomplex numbers $|\dots|_j$, which is left out in Fig. 3.9 for illustration purposes, has to be applied after adding the CONV and the MASS matrices together.

The following elemental matrices (3.11), (3.12) and (3.13) are all the required expressions for first order brick elements (compare to Fig. 3.9). For the derivation of tetrahedral shape functions, see appendix C. As obvious from the middle of Fig. 3.9, the following elemental MASS matrix based on the first order brick element is used for both formulations, the complex-valued and the bicomplex-valued PDE

$$\text{MASS}_{\text{Brick}} = \frac{l_x l_y l_z}{36} \begin{pmatrix} [A]_{4 \times 4} & [0]_{4 \times 4} & [0]_{4 \times 4} \\ [0]_{4 \times 4} & [A]_{4 \times 4} & [0]_{4 \times 4} \\ [0]_{4 \times 4} & [0]_{4 \times 4} & [A]_{4 \times 4} \end{pmatrix},$$

$$\text{where } [A]_{4 \times 4} = \begin{pmatrix} 4 & 2 & 1 & 2 \\ 2 & 4 & 2 & 1 \\ 1 & 2 & 4 & 2 \\ 2 & 1 & 2 & 4 \end{pmatrix}. \quad (3.11)$$

For the Helmholtz equation, the STIFF matrix in (3.12) is needed (see the left of Fig. 3.9)

$$\text{STIFF}_{\text{Brick}} = \begin{pmatrix} \frac{l_x l_z}{6 l_y} [B] + \frac{l_x l_y}{6 l_z} [C] & -\frac{l_z}{6} [D] & -\frac{l_y}{6} [D]^T \\ -\frac{l_z}{6} [D]^T & \frac{l_x l_y}{6 l_z} [B] + \frac{l_y l_z}{6 l_x} [C] & -\frac{l_x}{6} [D] \\ -\frac{l_y}{6} [D] & -\frac{l_x}{6} [D]^T & \frac{l_y l_z}{6 l_x} [B] + \frac{l_x l_z}{6 l_y} [C] \end{pmatrix},$$

$$\text{where } [B] = \begin{pmatrix} 2 & -2 & -1 & 1 \\ -2 & 2 & 1 & -1 \\ -1 & 1 & 2 & -2 \\ 1 & -1 & -2 & 2 \end{pmatrix},$$

$$\text{and } [C] = \begin{pmatrix} 2 & 1 & -1 & -2 \\ 1 & 2 & -2 & -1 \\ -1 & -2 & 2 & 1 \\ -2 & -1 & 1 & 2 \end{pmatrix},$$

$$\text{and } [D] = \begin{pmatrix} 2 & 1 & -1 & -2 \\ -2 & -1 & 1 & 2 \\ -1 & -2 & 2 & 1 \\ 1 & 2 & -2 & -1 \end{pmatrix}. \quad (3.12)$$

The transpose of a submatrix is denoted by \dots^T and the size of the submatrices 4×4 is omitted. For the bicomplex PDE, the CONV matrix in (3.13) is required (see the right of Fig. 3.9)

$$\text{CONV}_{\text{Brick}} = \frac{1}{8} \begin{pmatrix} \begin{bmatrix} 0 \end{bmatrix}_{4 \times 4} & \begin{bmatrix} -l_x l_y \\ l_x l_y \end{bmatrix}_{2 \times 4} & \begin{bmatrix} l_x l_z \\ -l_x l_z \\ l_x l_z \end{bmatrix}_{1 \times 4} \\ \begin{bmatrix} l_x l_y \\ -l_x l_y \\ l_x l_y \end{bmatrix}_{1 \times 4} & \begin{bmatrix} 0 \end{bmatrix}_{4 \times 4} & \begin{bmatrix} -l_y l_z \\ l_y l_z \end{bmatrix}_{2 \times 4} \\ \begin{bmatrix} -l_x l_z \\ l_x l_z \end{bmatrix}_{2 \times 4} & \begin{bmatrix} l_y l_z \\ -l_y l_z \\ l_y l_z \end{bmatrix}_{1 \times 4} & \begin{bmatrix} 0 \end{bmatrix}_{4 \times 4} \end{pmatrix}. \quad (3.13)$$

3.6 Absorbing Boundary Conditions for 3D-FEM

To solve boundary value problems in calculating wave propagation, absorbing boundary conditions are often an appropriate choice to model the surfaces of the truncated domain Ω . In the FEM literature, it is not widely described how to do this in detail. Merely the boundary terms derived from a variational formulation are often given. Therefore, a thorough investigation follows, which covers conventional ABCs for the Helmholtz equation and furthermore ABCs for the bicomplex formulation of the Maxwell system within the frequency domain.

In order to obtain suitable ABCs for the benchmark wave field problems, the starting point are one kind of the Silver-Müller absorbing boundary conditions [17], given by

$$(\underline{\mathbf{E}} - Z \underline{\mathbf{H}} \times \mathbf{n}) \times \mathbf{n} = \underline{\mathbf{E}}_0 \times \mathbf{n} \quad \text{or} \quad (Z \underline{\mathbf{H}} + \underline{\mathbf{E}} \times \mathbf{n}) \times \mathbf{n} = Z \underline{\mathbf{H}}_0 \times \mathbf{n} \quad \text{on } \partial\Omega, \quad (3.14)$$

where $\underline{\mathbf{E}}_0$ and $\underline{\mathbf{H}}_0$ are given fields which are defined on the two-dimensional tangential space of the manifold's boundary $\partial\Omega = A$, Z is the wave impedance, \mathbf{n} is the surface normal and $\underline{\mathbf{E}}$ and $\underline{\mathbf{H}}$ are unknown fields. In [262], (3.14) are called impedance boundary conditions. A comprehensive investigation of ABCs for the time-dependent Maxwell system is presented in [88]. For the derivation of (3.14), see e.g. [178]. Since the bicomplex-formulated Maxwell system only supports one-way wave propagation, the boundary where the excitation is placed contains no reflected wave and is therefore handled as a Dirichlet boundary condition. To enable a better comparability to problems based on the Helmholtz equation, the same assumption is made there. Because the ABCs are only assigned to passive ports (no excitation), a reduction of (3.14) and rearranging yields

$$\underline{\mathbf{E}} \times \mathbf{n} = (Z \underline{\mathbf{H}} \times \mathbf{n}) \times \mathbf{n} \quad \text{or} \quad Z \underline{\mathbf{H}} \times \mathbf{n} = -(\underline{\mathbf{E}} \times \mathbf{n}) \times \mathbf{n} \quad \text{on } \partial\Omega, \quad (3.15)$$

which is suitable for the bicomplex-formulated time-harmonic Maxwell system. In [88], similar formulations are called zeroth order absorbing boundary conditions. Following [17], a differentiation of the right equation⁶ in (3.15) and substitution of Faraday's law (2.7a) (see section 2.2.2) gives another kind of Silver-Müller absorbing boundary conditions as

$$(\nabla \times \underline{\mathbf{E}}) \times \mathbf{n} = j k (\underline{\mathbf{E}} \times \mathbf{n}) \times \mathbf{n} \quad \text{on } \partial\Omega. \quad (3.16)$$

Contrary, the usage of Ampère's law (2.7b) (see section 2.2.2) would produce a similar formulation for the magnetic field $\underline{\mathbf{H}}$. Similar formulations of (3.16) in [88] are called first order absorbing boundary conditions. For problems based on the Helmholtz equation, (3.16) is suitable. A derivation of both (3.15) and (3.16) with application to waveguide problems can be found e.g. in [248]. Further applications of ABCs for the Helmholtz equation using edge elements are discussed e.g. in [143] or [189]. Based on the second term of (3.5) and (3.6) (see section 3.3 for both equations), the respective contribution of the ABCs to the variational formulations will be described next in more detail.

In the following, the curvilinear integral of the whole manifold's boundary is understood as a surface integral concerning the port plane A .

⁶The consideration of the right equation is here arbitrarily chosen, the left one would yield similar results.

Starting with the second term of (3.5) from section 3.3 and consideration of (A.3) from appendix A gives

$$\iint_{\partial\Omega=A} \left[- \left(\tilde{\mathbf{E}}_w \times \left(\nabla \times \tilde{\mathbf{E}}_u^* \right) \right) \right] \cdot d\mathbf{A} = 0, \quad (3.17)$$

where A is oriented by its corresponding differential surface element $d\mathbf{A}$. Insertion of the ABC presented in (3.16) into (3.17) leads to

$$\iint_{\partial\Omega=A} \left[j k \tilde{\mathbf{E}}_w \times \left(\tilde{\mathbf{E}}_u^* \times \mathbf{n} \right) \right] \cdot d\mathbf{A} = 0. \quad (3.18)$$

Application of (B.3) (see appendix B) yields the contribution to the variational formulation as

$$\iint_{\partial\Omega=A} \left[-j k \tilde{\mathbf{E}}_w \cdot \tilde{\mathbf{E}}_u^* \right] \mathbf{n} \cdot d\mathbf{A} = 0. \quad (3.19)$$

The term (3.19) has to be added to the third term of (3.5) from section 3.3 on those edges which lie in the port plane. A similar formulation for the Helmholtz equation based on the magnetic field can be established and is not explicitly given here.

Contrary, the derivation of the bicomplex case (see section 3.3) starts with the second term of the variational formulation (3.6) and (B.5) from appendix B, where again the curvilinear integral of the whole manifold's boundary is here understood as a surface integral concerning the port plane A , as

$$\iint_{\partial\Omega=A} \left[- \left(\tilde{\mathbf{E}}_w \times \tilde{\mathbf{E}}_u^+ \right) \right] \cdot d\mathbf{A} = 0. \quad (3.20)$$

By applying the left equation of (3.15) and $\mathbf{H} \times \mathbf{n} = 0$ (see also [262]), only a contribution to the mass matrix of the magnetic field MASS_H is nonzero, namely

$$\iint_{\partial\Omega=A} \left[\tilde{\mathbf{H}}_w \times \left(\tilde{\mathbf{H}}_u^* \times \mathbf{n} \right) \right] \cdot d\mathbf{A} = 0. \quad (3.21)$$

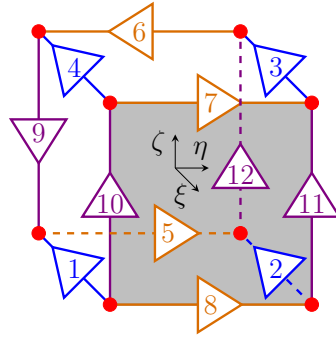
As done for the derivation of (3.19), application of (B.3) to (3.21) yields finally

$$\iint_{\partial\Omega=A} \left[-\tilde{\mathbf{H}}_w \cdot \tilde{\mathbf{H}}_u^* \right] \mathbf{n} \cdot d\mathbf{A} = 0. \quad (3.22)$$

In (3.22), no impedance Z is included as in (3.15), since the electric and magnetic fields are normalized (see (2.2) in section 2.1.1).

With respect to edge elements, the general idea how to implement wave reflections on material transitions in FEM is to manipulate the MASS matrix on those edges which are lying in the port plane as discussed above. To do this, two ways are common. First, by expressing the port plane using a two-dimensional quadrilateral mesh and adding the related integral expressions to them of the three-dimensional brick mesh. The examples discussed in [142] or [143] follow this way. Second, a direct manipulation of the three-dimensional formulation is possible, which is shown below. For the used brick elements, the local axes ξ, η, ζ are parallel to the global axes x, y, z . In the following, the direction of wave propagation is ξ (or x in the global sense).

In Fig. 3.10, the procedure of applying ABCs on a port plane A is shown.



$$\text{MASS}_{\text{Brick}} = \frac{l_x l_y l_z}{36} \begin{pmatrix} [A]_{4 \times 4} & [0]_{4 \times 4} & [0]_{4 \times 4} \\ [0]_{4 \times 4} & [A]_{4 \times 4} & [0]_{4 \times 4} \\ [0]_{4 \times 4} & [0]_{4 \times 4} & [A]_{4 \times 4} \end{pmatrix}$$

↓

$$\text{Manipulating 4 entries : } [A]_{4 \times 4} = \begin{pmatrix} - & - & - & - \\ - & \times & \times & - \\ - & \times & \times & - \\ - & - & - & - \end{pmatrix}$$

Figure 3.10 Direct manipulation of the 3D MASS matrix instead of a separate 2D handling of the port plane (the gray face in front) to consider ABCs for FEM BC and FEM C. To implement the reflecting wave portion, the part of the tensor product which involves edges 10 and 11 in the gray drawn port plane A is manipulated.

By assuming a field quantity oriented in positive ζ -direction to be considered for occurring wave reflections, the port is placed in the $\zeta\eta$ -plane on the front of the brick element (see the top of Fig. 3.10). For convenience, the whole computational domain Ω is assumed to be built up using merely one element, whereas for real meshes, this process has to be applied for every brick element which touches the gray drawn port plane A . Depending on whether FEM BC or FEM C is used, the value applied to the four marked entries is different.

The two ABCs (3.19) and (3.22) are sufficient if only transversal EM field components exist, e.g. for a TEM-wave. Contrary for a TE_{10} -wave, appropriate ABCs should be derived from the analytical solution of that wave, which – following [250] – reads for Cartesian coordinates as

$$\begin{aligned} \underline{E}_y &= -\underline{E}_0 e^{-j\beta z} \sin\left(\frac{\pi}{a} x\right) \\ \underline{H}_x &= \frac{\underline{E}_0}{Z} e^{-j\beta z} \sin\left(\frac{\pi}{a} x\right) \\ \underline{H}_z &= \frac{-j}{\beta} \frac{\pi}{a} \frac{\underline{E}_0}{Z} e^{-j\beta z} \cos\left(\frac{\pi}{a} x\right), \end{aligned} \quad (3.23)$$

where \underline{E}_0 is a given field value, β is the wavenumber in propagation direction, ω is the angular frequency and a is the width of the rectangular waveguide. According to [250], β of a TE_{10} -wave guided by a rectangular waveguide is calculated as

$$\beta = \sqrt{\omega^2 \varepsilon \mu - \frac{\pi^2}{a^2}}. \quad (3.24)$$

In order to obtain absorbing boundary conditions in the port plane A , only waves traveling in

z -direction are of interest. Therefore, the trigonometric expressions \sin and \cos over x defined in (3.23) are neglected. Given field values \underline{E}_0 are moved to the RHS of the FEM equation system. Therefore, they are not considered in the respective MASS matrix.

By further neglecting the time-harmonic term in (3.23) represented by the exponential function, the ABC for bicomplex wave field problems becomes complex-valued in contrast to the real-valued contribution to MASS_H presented in (3.22) as

$$\iint_{\partial\Omega=A} \left[\left(\frac{j}{\beta} \frac{\pi}{a} - 1 \right) \tilde{\mathbf{H}}_w \cdot \tilde{\mathbf{H}}_u^* \right] \mathbf{n} \cdot d\mathbf{A} = 0. \quad (3.25)$$

Note that as for (3.22), Z is dropped out in (3.25) caused by the impedance normalization.

As seen previously e.g. in (3.16), Helmholtz problems usually use first order derivatives of the EM field to incorporate ABCs. A derivation of the transversal field components \underline{E}_y and \underline{H}_x regarding z and a derivation with respect to x of the longitudinal field component \underline{H}_z based on (3.23) yields

$$\begin{aligned} \frac{\partial}{\partial z} \underline{E}_y &= j\beta \underline{E}_0 e^{-j\beta z} \sin\left(\frac{\pi}{a}x\right) \\ \frac{\partial}{\partial z} \underline{H}_x &= -j\beta \frac{\underline{E}_0}{Z} e^{-j\beta z} \sin\left(\frac{\pi}{a}x\right) \\ \frac{\partial}{\partial x} \underline{H}_z &= \frac{-j}{\beta} \frac{\pi^2}{a^2} \frac{\underline{E}_0}{Z} e^{-j\beta z} \cos\left(\frac{\pi}{a}x\right). \end{aligned} \quad (3.26)$$

In the same way as for (3.23) in order to obtain ABCs in the port plane A , the trigonometric expressions \sin and \cos over x and the time-harmonic term represented by the exponential function are neglected. Furthermore, given field values \underline{E}_0 are moved to the right of the FEM equation system. Both magnetic field components in (3.26) are imaginary and yield together

$$\iint_{\partial\Omega=A} \left[-j \left(\beta + \frac{1}{\beta} \frac{\pi^2}{a^2} \right) \tilde{\mathbf{H}}_w \cdot \tilde{\mathbf{H}}_u^* \right] \mathbf{n} \cdot d\mathbf{A} = 0. \quad (3.27)$$

The ABC for the electric case can be easily obtained in a similar way from the first equation of (3.26).

All used kinds of ABCs (3.19), (3.22), (3.25) and (3.27) of the benchmark problems (discussed later on in section 4.2) are presented below in Table 3.1.

Table 3.1 ABCs for the benchmark problems investigated in section 4.2. For both versions of FEM BC, an additional factor is necessary, which is described subsequently.

Type of wave	Type of ABC	ABC for FEM BC	ABC for FEM C
TEM	transversal	-1 , see (3.22)	$-jk$, see (3.19)
TE ₁₀	transversal and longitudinal	$\left(\frac{j}{\beta} \frac{\pi}{a} - 1 \right)$, see (3.25)	$-j \left(\beta + \frac{1}{\beta} \frac{\pi^2}{a^2} \right)$, see (3.27)

Both ABCs of FEM C shown in Table 3.1 can be directly applied to the mass matrix, since through the spatial derivation with respect to the propagation direction done in (3.16), the ABC is located in the port plane A .

Note that in the following explanation, wave propagation is assumed in the ξ - (or x -) direction (as done on Fig. 3.10) instead of the z -direction as done for the analytical expressions of the waveguide's EM field in (3.23) and (3.26). To apply the two ABCs of FEM BC listed in Table

3.1, an additional factor is necessary. For a good comprehensibility, the derivation of the eleventh entry of (3.11) (see section 3.5) which lies on the principal diagonal is done by

$$\text{MASS}_{\text{Brick}, 11} = \int_{x_1}^{x_2} \int_{y_1}^{y_2} \int_{z_1}^{z_2} [N_{11}^e \cdot N_{11}^e] dz dy dx. \quad (3.28)$$

Note that for convenience, the subscript "11" of $\text{MASS}_{\text{Brick}, 11}$ in (3.28) is equivalent to the ordinary numbering of a matrix (11,11), where the first number indicates the row and the second one stands for the column. Insertion of integration limits and consideration of (3.8), (3.9) and (3.10) from section 3.5 yields the following only one nonzero ζ -oriented component as

$$\text{MASS}_{\text{Brick}, 11} = \int_{-1}^1 \int_{-1}^1 \int_{-1}^1 \left[\left(\frac{1}{4} (1 + \xi) (1 + \eta) \right) \cdot \left(\frac{1}{4} (1 + \xi) (1 + \eta) \right) \right] \frac{l_x l_y l_z}{8} d\zeta d\eta d\xi. \quad (3.29)$$

After rearrangement, it follows that

$$\text{MASS}_{\text{Brick}, 11} = \frac{l_x l_y l_z}{128} \int_{-1}^1 \int_{-1}^1 \int_{-1}^1 [(1 + \xi)^2 (1 + \eta)^2] d\zeta d\eta d\xi. \quad (3.30)$$

Integration and simplification leads to

$$\text{MASS}_{\text{Brick}, 11} = \frac{l_x l_y l_z}{128} \frac{8}{3} \frac{8}{3} 2 = \frac{l_x l_y l_z}{36} 4, \quad (3.31)$$

which is finally the eleventh entry of (3.11) on the principal diagonal, see section 3.5. To obtain the additional factor to $\text{MASS}_{\text{Brick}, 11}$, called $\text{MASS}_{\text{Brick}, 11'}$, a similar two-dimensional integration procedure in the port plane follows, where the ξ - (or x -) dependence of (3.28) or (3.29) vanishes as

$$\text{MASS}_{\text{Brick}, 11'} = \int_{-1}^1 \int_{-1}^1 \left[\left(\frac{1}{2} (1 + \eta) \right) \cdot \left(\frac{1}{2} (1 + \eta) \right) \right] \frac{l_x l_y}{4} d\zeta d\eta. \quad (3.32)$$

After rearranging this expression, the counterpart to (3.30) is

$$\text{MASS}_{\text{Brick}, 11'} = \frac{l_x l_y}{16} \int_{-1}^1 \int_{-1}^1 [(1 + \eta)^2] d\zeta d\eta. \quad (3.33)$$

As done in (3.31), integration and simplification yields

$$\text{MASS}_{\text{Brick}, 11'} = \frac{l_x l_y}{16} \frac{8}{3} 2 = \frac{l_x l_y}{36} 12. \quad (3.34)$$

The last step is to divide $\text{MASS}_{\text{Brick}, 11}$ presented in (3.31) by $\text{MASS}_{\text{Brick}, 11'}$ expressed in (3.34), which finally gives the additional factor $l_z/3$. Since the contribution of the ABC to the mass matrix is directly applied to the element-based formulation of the tensor product, this factor is used for all four marked entries on the top of Fig. 3.10. Contrary, if a two-dimensional quadrilateral element-based formulation is constructed by the use of (3.32), the relations between diagonal and off-diagonal are different from those given in (3.11) (see section 3.5), since there are less interactions between parallel edges.

The implementation of ABCs for both the complex and the bicomplex problem class shown above represents only one of several possibilities. A different approach is chosen in [235], where vector one-way ABCs are derived from a one-way wave equation. Higher-order ABCs are examined e.g. in [17] or [88].

This chapter shows a numerical investigation of an introductory one- and various three-dimensional EM wave propagation problems to benchmark the bicomplex formulation in the FEM environment using MATLAB R2018b. All calculations are processed on an x64 Intel® Core™ i7-8700K central processing unit (CPU) @ 3.70 GHz, equipped with 64 GB random access memory (RAM). Generally, numerical results of the proposed bicomplex concept are compared to them of conventionally expressed Helmholtz formulations. Sparse matrix techniques¹ are used in MATLAB by the keyword `sparse` to improve the efficiency of execution. In the one-dimensional example, nodal-based finite elements of linear order are used. Other numerical interpolation procedures are examined e.g. in [1]. Contrary, for all three-dimensional examples, edge-based brick finite elements of linear order (see section 3.5 for details) are used.

For convenience, the analytical solution – and therefore the exact values on the boundaries – are known for all considered numerical examples. Dirichlet boundary conditions are utilized for the examples with homogeneous material distribution. Contrary, for inhomogeneous material distribution, ABCs which are derived in section 3.6 are used. Note that the bicomplex ABCs from section 3.6 are built using a similar strategy as for the mixed Maxwell system². A DGFEM³ of that mixed Maxwell system including ABCs is presented e.g. in [262].

Starting with the 1D case in section 4.1, TEM-wave propagation for homogeneous material distribution is presented as an introductory example. This is followed by several 3D examples, which are discussed in section 4.2 in order to show the applicability to practical EM wave propagation problems, involving plane waves and waveguide modes. To enhance the perspective on the numerically calculated EM fields, a qualitative Hodge decomposition is discussed subsequently. The transition to the two-dimensional approach towards the three-dimensional one is trivial and is therefore not examined. For further reading, especially two-dimensional electromagnetic FEM problems in the language of DEC are reviewed e.g. in [122]. At the end in section 4.3, important findings which were identified by the simulation studies are summarized and discussed.

¹The use of sparse matrix techniques can be advantageous regarding memory requirement, since only nonzero elements are stored. Furthermore, computations can be beneficially modified. Concerning this matter, see for example [67] and [97] regarding MATLAB implementation, or [195] in terms of FEM in general.

²In the mixed Maxwell system, the electric and the magnetic field are handled as single variables, respectively.

³The main difference to the continuous FEM is that the DGFEM does not ensure continuity on the element interfaces, see e.g. [262] for details. According to [173], DGFEM offers more flexibility, for example the possibility to use different discretization spaces of neighboring elements.

4.1 One-dimensional Finite Element Method

This section describes an introducing one-dimensional example of TEM-wave propagation in free space using a regular mesh. Note that in this example, the interpolated points lie direct on the nodal values, so on the DOFs. Wave propagation is assumed to take place in free space in one direction along the Cartesian coordinate z . For FEM modeling, the unit region Ω is discretized using evenly spaced nodal finite elements. The spatial resolution is controlled by a discretization parameter n and the extension of a finite element h_{ele} (expressed in the unit m) is defined by

$$h_{\text{ele}} = \frac{1}{2^n}. \quad (4.1)$$

Dirichlet boundary conditions are assumed at the start and at the end of the unit interval. Without loss of generality, the number value of the magnitude of $\underline{\mathbf{E}}$ has been chosen arbitrarily as the square root of the free space impedance Z_0 , which results in $|\underline{\mathbf{E}}| = E_{\text{re}} \approx 19.41 \text{ V/m}$. The one-dimensional TEM-wave is assumed as a cosine for the real part of $\underline{\mathbf{E}}$ with an arbitrarily chosen wavenumber $k = 8 \text{ m}^{-1}$, which corresponds to a frequency of approximately 382 MHz.

4.1.1 Discussion of the Same Discretization Parameter n

For this section, a comparison of different FEM approaches is presented by assuming the same discretization parameter n . In Fig. 4.1, the results of E_{re} for $n = 3$ using the standard complex FEM C (drawn in cyan) and the bicomplex FEM BC (depicted in green) compared to the analytical (ANA) solution (colored in red) are shown.

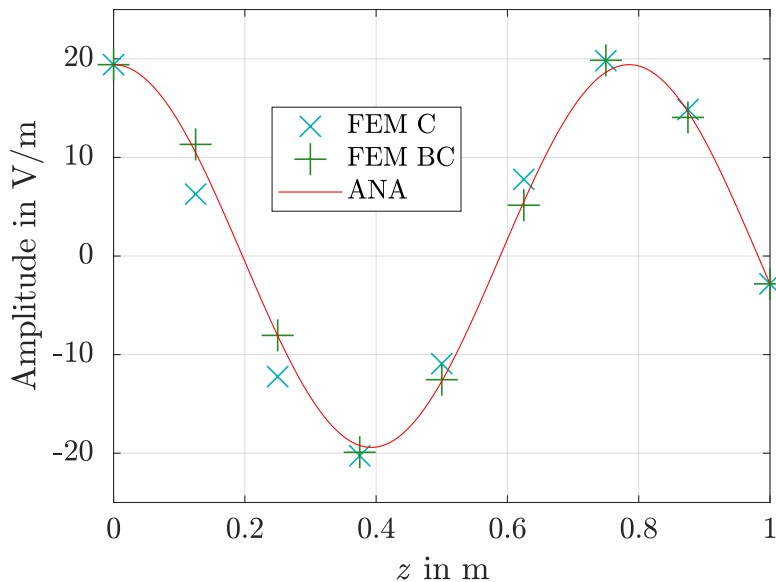


Figure 4.1 Electric field E_{re} distribution calculated by means of various methods, where $n = 3$ is used in FEM.

The complex-valued case FEM C is based on the Helmholtz equation (2.5), see section 2.2.1. Contrary, FEM BC is based on (2.6) discussed in section 2.2.2, where a much better agreement with the analytical reference solution ANA is achieved. A quantification of the numerical solutions is done next by consideration of two different error definitions.

The first one is the Forward Normalized root mean square error (Forward NRMSE) $\|e\|_{\text{FWD}}^{\%}$. With respect to the real part of the electric field it follows that in accordance to the L^2 -norm defined in (2.16) of section 2.3.1

$$\|e\|_{\text{FWD}}^{\%} = \frac{\sqrt{\frac{1}{M} \sum_{m=1}^M (E_{\text{re, FEM}}^m - E_{\text{re, ANA}}^m)^2}}{\max(E_{\text{re, ANA}}) - \min(E_{\text{re, ANA}})} \cdot 100\%. \quad (4.2)$$

In (4.2), M is the number of interpolated points, which corresponds to the nodal values contained in Ω . Based on FEM C and FEM BC, the Forward NRMSEs for selected values for n are depicted below in Fig. 4.2.

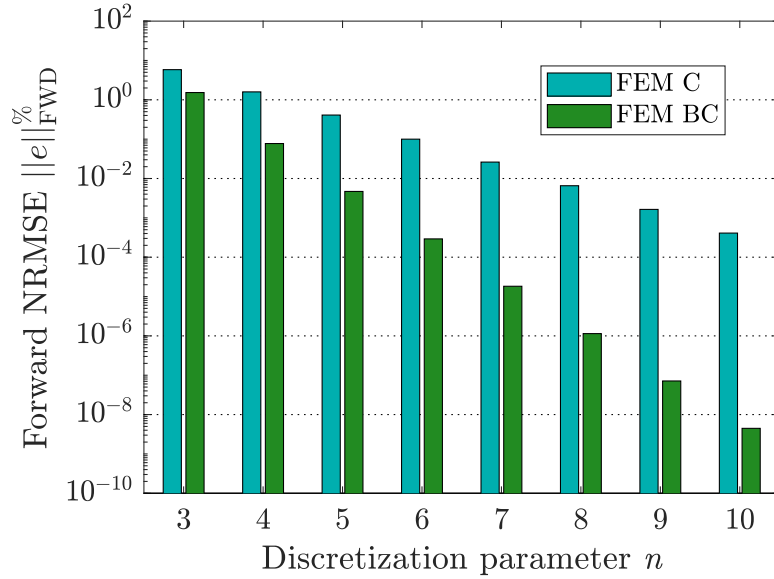


Figure 4.2 Forward NRMSE $\|e\|_{\text{FWD}}^{\%}$ for selected values of the discretization parameter n .

In accordance to (4.1) reported in section 4.1, the extension of a finite element h_{ele} is halved when n is increased by 1. As intuitively expectable for mesh refinement, the error $\|e\|_{\text{FWD}}^{\%}$ decreases for higher values of n in every case. The accuracy of FEM BC exhibits a very pronounced progressive increase with the discretization parameter n when observing $E_{\text{re, FEM}}$ directly on the DOFs. Expressed in numerical values, it reaches a value of $\|e\|_{\text{FWD}}^{\%} \approx 5 \cdot 10^{-9} \%$ for $n = 10$ instead of $\|e\|_{\text{FWD}}^{\%} \approx 5 \cdot 10^{-4} \%$ for FEM C. A further examination of FEM BC is justified by this results.

The second type of error is the Backward NRMSE $\|e\|_{\text{BWD}}^{\%}$, which reads as

$$\|e\|_{\text{BWD}}^{\%} = \frac{\sqrt{\frac{1}{M} \sum_{m=1}^M (b_{\text{re, FEM}}^m - b_{\text{re, ANA}}^m)^2}}{\max(b_{\text{re, ANA}}) - \min(b_{\text{re, ANA}})} \cdot 100\%, \quad (4.3)$$

where b_{re} is the RHS vector of the global FEM equation system (see Fig. 3.3 in section 3.1), which contains given boundary values. Below in Fig. 4.3, the Backward NRMSEs for selected values of n are shown. For FEM C, there are higher values for $\|e\|_{\text{BWD}}^{\%}$ than that of FEM BC, caused by the use of another solver in order to obtain the inverse of the system matrix. The unsymmetric-pattern multifrontal solver [68] is applied for FEM BC, caused by the matrix structure described in Fig. 3.4 (see section 3.4). Contrary for FEM C, the banded solver for tridiagonal matrices is used. Regarding solving strategies for linear systems, see e.g. [50] or [101].

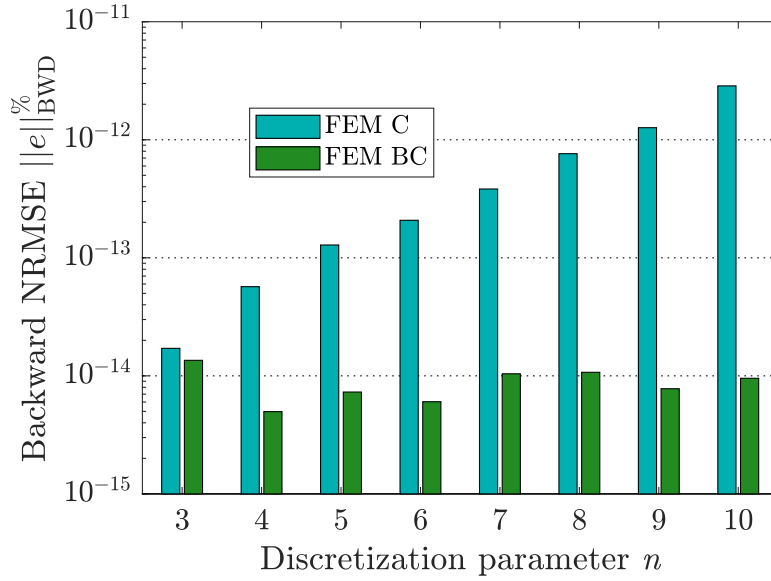


Figure 4.3 Backward NRMSE $\|e\|_{\text{BWD}}^{\%}$ for selected values of the discretization parameter n .

The Backward NRMSE depicted in Fig. 4.3 lies between $\|e\|_{\text{BWD}}^{\%} \approx 5 \cdot 10^{-15} \%$ and $\|e\|_{\text{BWD}}^{\%} \approx 5 \cdot 10^{-12} \%$ in all cases, which makes this error negligible in comparison to the Forward NRMSE examined before in Fig. 4.2. To estimate the performance of both FEM approaches, the calculation time T_{CPU} is presented in Fig. 4.4 as a function of n .

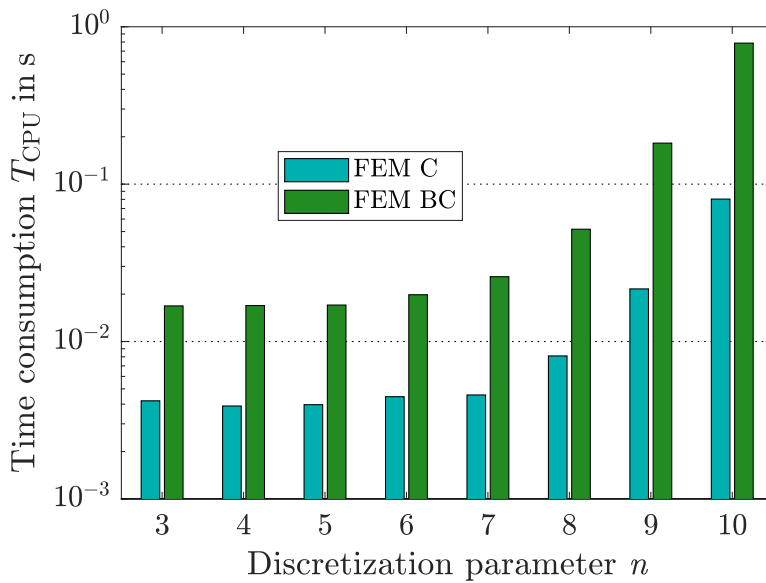


Figure 4.4 Calculation time T_{CPU} for selected values of the discretization parameter n .

Compared to FEM C, some additional operations have to be applied for FEM BC, for instance the generation of the bicomplex class (see Fig. 3.5 in section 3.4). As mentioned previously, another solver is used for the calculation of the inverse of the system matrix. These circumstances and a doubled size of the system matrix leads to a ratio of about 5 in comparison to T_{CPU} of FEM C.

As a second performance parameter, the memory requirements are compared in Table 4.1 for two specific values of n , which were obtained by evaluation of the size of the workspace in MATLAB.

Table 4.1 Memory requirements for two specific values of the discretization parameter n .

	$n = 6$ (65 Nodes)	$n = 10$ (1025 Nodes)
FEM C	0.27 MByte	67 MByte
FEM BC	1.56 MByte	387 MByte

The relation of the memory requirements shown in Table 4.1 is similar to that of the calculation time, the ratio between FEM BC and FEM C is about 5. This factor of about 5 for both performance parameters sound not satisfactorily at the moment. Therefore, a combined argumentation on an example aiming at a similar precision is done next, concerning FEM BC and FEM C. Note that the used algorithms are not optimized with respect to calculation time and memory requirement.

4.1.2 Discussion of the Same Accuracy of L^2 -norm

In contrast to section 4.1.1, where FEM BC and FEM C are compared in terms of equivalent discretization parameters, here the same accuracy of the L^2 -norm for both FEM approaches is assumed. By taking for FEM C $n = 10$ (1025 Nodes) and for FEM BC $n = 6$ (65 Nodes), Fig. 4.2 (presented in section 4.1.1) shows a Forward NRMSE of $\|e\|_{\text{FWD}}^{\%} \approx 4 \cdot 10^{-4} \%$ for both cases. This is illustrated below in Fig. 4.5, which shows a selected section of Fig. 4.2.

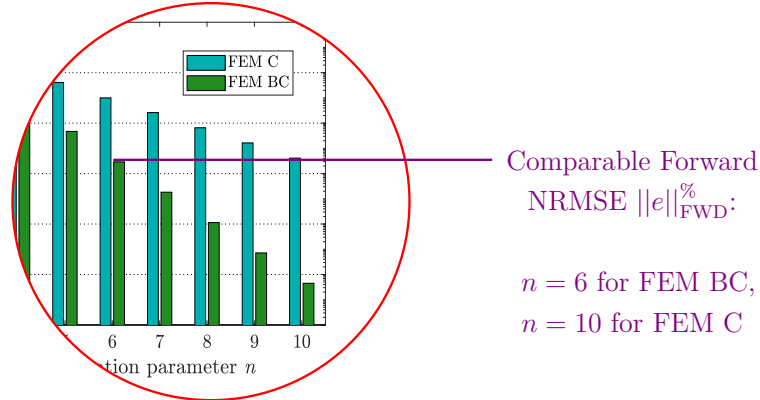


Figure 4.5 Detail of Fig. 4.2 (see section 4.1.1) to indicate a comparable accuracy of L^2 -norm for the two distinct bicomplex and complex FEM models.

The calculation time shown in Fig. 4.4 (see section 4.1.1) is $T_{\text{CPU}} \approx 8 \cdot 10^{-2}$ s for FEM C and about $2 \cdot 10^{-2}$ s for FEM BC. For memory requirements, Table 4.1 (presented in section 4.1.1) shows a value of about 67 MByte for FEM C and about 1.56 MByte for FEM BC, respectively. Therewith, already with the non-optimized algorithm, the calculation time using FEM BC is shortened to one fourth and the memory requirement is reduced to about 2.5 % for the same amount of L^2 -norm in terms of Forward NRMSE $\|e\|_{\text{FWD}}^{\%}$. A high amount of 1025 nodes is used for meshing Ω for FEM C, whereas only 65 nodes are necessary in the case of FEM BC.

The major reason for the significant improvement of accuracy concerning the L^2 -norm is the order of PDEs on which FEM C and FEM BC are based on, respectively. This will be further examined in the following section 4.2 regarding three-dimensional electromagnetic wave propagation problems.

4.2 Three-dimensional Finite Element Method

To benchmark the proposed bicomplex FEM with the conventional Helmholtz FEM regarding practical 3D field problems, convenient examples with known analytical solutions are selected, which are based on simple geometric settings. An exemplary high-frequency application based on a more complicated geometry, which couples the EM field between a coaxial and a dielectric waveguide, can be found e.g. in [261]. As shown in section 2.4.7, the calculated bicomplex EM field and hence the complex EM fields consist – from a topological point of view – of curly gradient or fluxless knot field patterns, respectively, which are conformally approximated using Whitney edge elements. An overview of the field problems presented here is sketched below in Fig. 4.6.

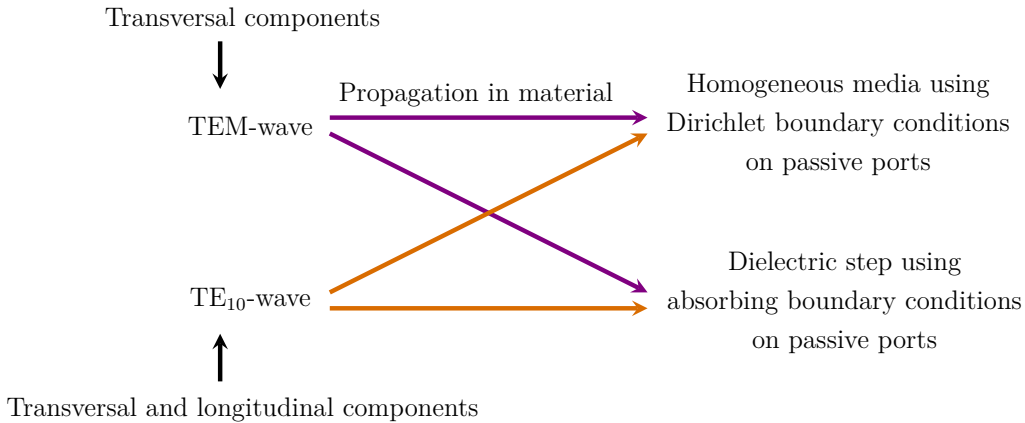


Figure 4.6 Investigated numerical examples using the three-dimensional bicomplex FEM.

On all excitation ports, Dirichlet boundary conditions are used to ensure a consistent proceeding. This is possible since all analytical solutions are known. Both benchmark problems of the TE₁₀-wave (see the orange arrows in Fig. 4.6) are placed in a hollow waveguide, which transversally limits the field problem. Contrary, for the TEM-wave examples (indicated by the violet arrows in Fig. 4.6), the EM fields are constant in the transversal plane. These examples cover a wide range of practical problems which arise in high-frequency engineering. The generalization to higher-order modes, permeable transitions and various geometric settings of the problem domain Ω is assumed to be straightforward.

The TEM-wave example in homogeneous media uses a real-valued wavenumber of $k = 1 \text{ m}^{-1}$ where the wave vector is oriented in z -direction. This corresponds to a frequency of about 48 MHz⁴, since $300 \text{ MHz} / (2\pi) \approx 48 \text{ MHz}$. For TEM-wave propagation through the dielectric step, a different frequency of 800 MHz is chosen. This fits better to the chosen size of the computational domain Ω . Since the transversal dimensions of the waveguide determine its behavior to guide modes, or – in other words – which modes are evanescent or able to propagate, the frequency is chosen to 5 GHz for both the hollow and the partially dielectric-filled waveguide, which yields single-mode propagation of the TE₁₀-wave.

4.2.1 TEM-wave in Free Space

In this section, the investigations of [203] are enhanced. The field components \underline{H}_x and \underline{E}_y are oriented perpendicular to the direction of propagation z with the wavenumber $k = 1 \text{ m}^{-1}$, or approximately 48 MHz in the domain Ω . Using Dirichlet boundary conditions, the phase starts at

⁴The frequency is calculated by $f = ck / (2\pi)$, where c is the speed of light.

0° and ends up at about 57° , or – otherwise expressed – 16% of a wavelength. The analytical solution of the real part of \underline{E}_y is drawn in Fig. 4.7.

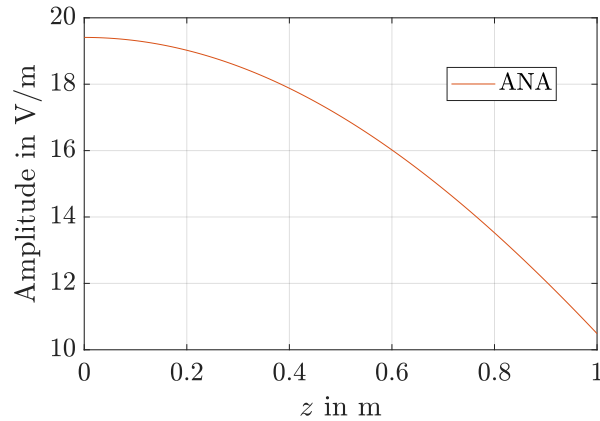


Figure 4.7 Analytical solution of the real electric field concerning TEM-wave propagation.

As usual in FEM (see also Fig. 3.5 in section 3.4), first the edge values (DOFs) are calculated. Then, the field is interpolated at equidistant points shown in Fig. 4.8, which are the same for all following FEM meshes as $(11 \times 11 \times 21) = 2541$.

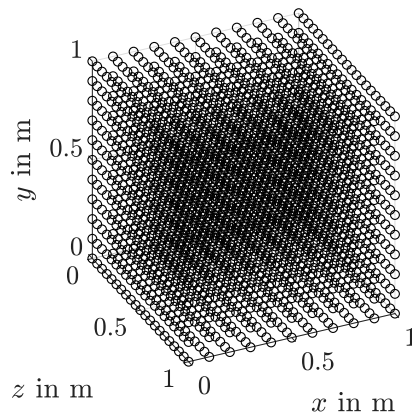


Figure 4.8 Field evaluation points $(11 \times 11 \times 21)$ for TEM-wave propagation in Ω .

Note that the density of points depicted in Fig. 4.8 in z -direction is higher to ensure a sufficient resolution in propagation direction.

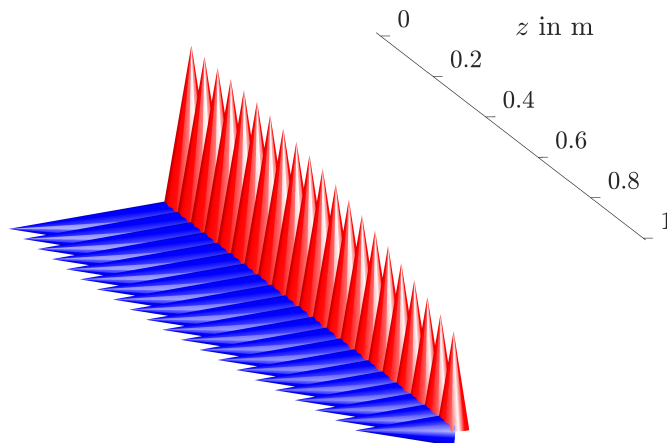


Figure 4.9 Field pattern of TEM-wave propagating over z , arbitrary placed in the xy -plane.

Since the field pattern of the TEM-wave is constant in the xy -plane, merely the center line is plotted in Fig. 4.9. As done for Fig. 4.7, only the real part of the EM field at an arbitrary position in the xy -plane is shown there. Contrary to Fig. 2.2 depicted in section 2.1, the electric field in Fig. 4.9 (drawn in red) is oriented in y -direction, whereas the magnetic field (drawn in blue) is oriented in x -direction. Both field quantities follow the cosine shape shown in Fig. 4.7.

The first kind of investigated meshes is the regular mesh, where three modifications are depicted in Fig. 4.10.

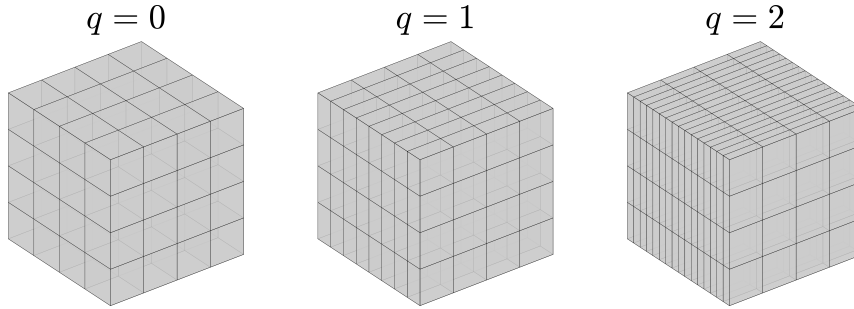


Figure 4.10 q -times refined regular brick meshes of Ω with a length of 1 m.

The initial mesh, which is shown on the left, consists of $(4 \times 4 \times 4) = 64$ brick elements. It is refined in propagation direction twice, where q is the discretization parameter which specifies the number of splitting one brick element in z -direction similar to the one-dimensional case (4.1) in section 4.1. This results in the extension of a brick element in z -direction h_{ele} as

$$h_{\text{ele}} = \frac{1}{2^q}. \quad (4.4)$$

Note that the choice of q refines the mesh in a similar way to n (which is used in (4.1) for the one-dimensional case) in one direction.

As investigated in section 4.1, Fig. 4.11 shows a comparison of $\|e\|_{\text{FWD}}^{\%}$ concerning the real part of the electric field.

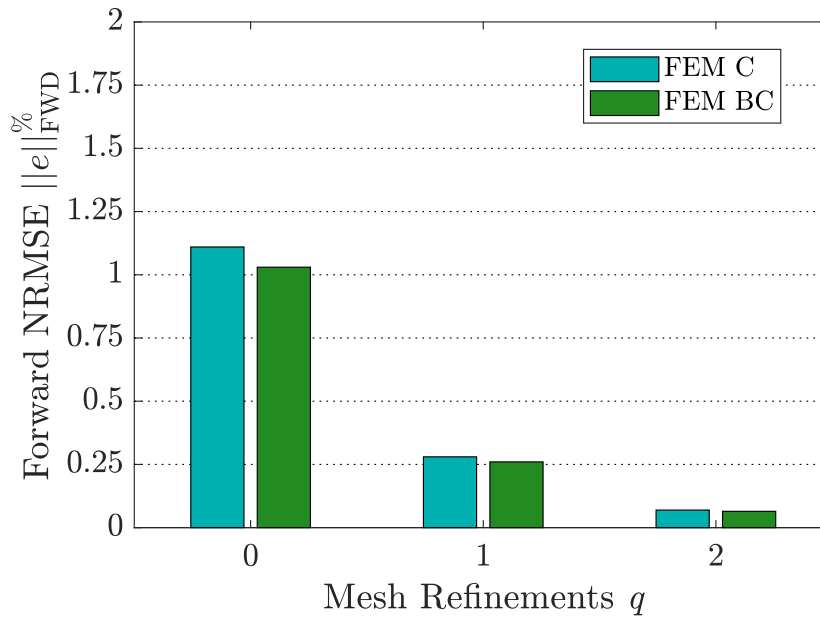


Figure 4.11 $\|e\|_{\text{FWD}}^{\%}$ of $E_{\text{re},\text{FEM}}$ for wave propagation on the meshes in Fig. 4.10, calculated at the points shown in Fig. 4.8.

A slightly higher accuracy of FEM BC compared to FEM C is achieved for all refinement steps of the regular brick mesh depicted in Fig. 4.11. The improvement can be estimated as about 7% in every refinement.

The second kind of investigated meshes are the irregular versions shown in Fig. 4.12.

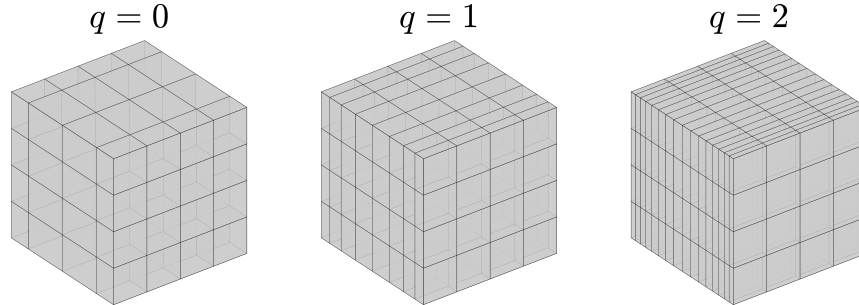


Figure 4.12 q -times refined irregular brick meshes of Ω with a length of 1 m.

As for the regular mesh, the first mesh on the left consists of $(4 \times 4 \times 4) = 64$ brick elements and is refined in a similar manner using (4.4) by keeping the mesh aspect ratio⁵ of 2 constant. A comparison of $\|e\|_{\text{FWD}}^{\%}$ regarding the real part of the electric field is presented in Fig. 4.13.

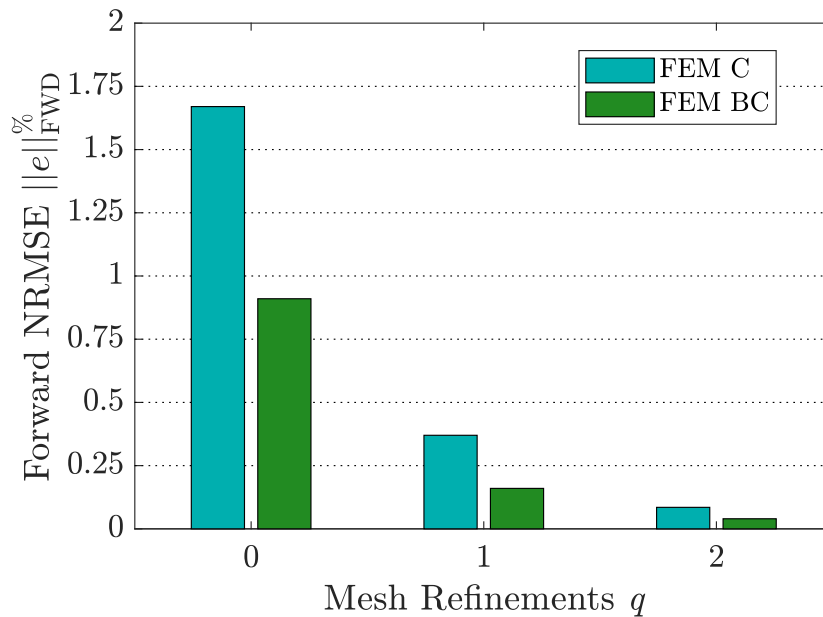


Figure 4.13 $\|e\|_{\text{FWD}}^{\%}$ of $E_{\text{re}, \text{FEM}}$ for wave propagation on the meshes in Fig. 4.12, calculated on the points shown in Fig. 4.8.

A significantly higher accuracy of FEM BC compared to FEM C for irregular brick meshes is obvious in Fig. 4.13, where a reduction of $\|e\|_{\text{FWD}}^{\%}$ to about 50% is representative, or – in other words – a factor of 2 is achieved.

Since the number of bricks and associated edges are similar for both regular and irregular meshes, they are jointly represented in Table 4.2.

⁵The mesh aspect ratio means here the quotient of the longest extension of a finite element in z -direction and the shortest one.

Table 4.2 Mesh Properties for regular / irregular meshes.

Mesh refinements q	Number of Elements	Number of Edges
0	4x4x4	300
1	4x4x8	560
2	4x4x16	1080

A refinement in z -direction doubles the number of elements, whereas the number of edges (DOFs) do not rise that much (as indicated on the right of 4.2) since global edges are shared by several local edges of single brick elements, respectively. The time consumption including the interpolation procedure after calculating the edge values (see the workflow of FEM BC in Fig. 3.5, reported in section 3.4) is given in Table 4.3.

Table 4.3 Time consumption for regular / irregular meshes.

Mesh refinements q	FEM BC in s	FEM C (<u>E</u> or <u>H</u>) in s
0	1.55	1.03
1	1.67	1.06
2	2.09	1.12

A comparison of the times for $q = 2$ reveals a seemingly disadvantageous factor of about 2 for FEM BC, since the needed time is roughly doubled. However, this is acceptable, because FEM BC yields both E and H.

Lastly, memory requirements of the system matrix are given below in Table 4.4.

Table 4.4 Memory requirements for regular / irregular meshes.

Mesh refinements q	FEM BC in MByte	FEM C (<u>E</u> or <u>H</u>) in MByte
0	0.73	0.15
1	1.41	0.32
2	2.77	0.67

In general, a factor of about 4 describes the ratio between FEM BC and FEM C (depicted in Table 4.4) well, caused by a changed size of the system matrix. The square system matrix is 4 times larger in total for FEM BC, see the real matrix representation of the bicomplex system matrix in Fig. 3.4, which was illustrated in section 3.4.

It has to be further noted, that less essential boundary conditions⁶ are needed for FEM BC, because the combined solution of the EM field lowers the possibilities of joint solutions. This means that TEM-waves calculated by FEM C require zero-Dirichlet boundary conditions on the transversal boundaries which are oriented perpendicular to the field direction in the transversal plane. For FEM BC they do not have to be explicitly enforced.

⁶Essential boundary conditions have to be enforced explicitly.

4.2.2 TEM-wave Passing a Dielectric Step

Here, the TEM-wave is assumed as a cosine for the real part of the electric field E_{re} over the z -direction with a frequency of 800 MHz. In contrast to the previous section 4.2.1, Dirichlet boundary conditions are only used for the excitation port of the EM field, whereas ABCs cover the opposing port, respectively. The field problem – mapped in the computational domain Ω – is sketched below in Fig. 4.14.

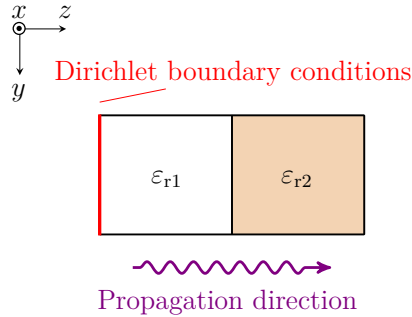


Figure 4.14 Longitudinal cross section of the dielectric step.

The left half space depicted in Fig. 4.14, which is called region 1, consists of air with the relative permittivity $\varepsilon_{r1} = 1$. A material with $\varepsilon_{r2} = 10$ is assumed for the right half space, called region 2. For both FEM BC and FEM C, Dirichlet boundary conditions are applied on the left (indicated in red, see Fig. 4.14). For FEM C, an absorbing boundary condition is implemented on the right. This combination is also used for the consecutive bicomplex FEM shown later on in Fig. 4.16. Since FEM BC involves no direct wave reflection in its solution space (one-way wave equation, see (2.84) in section 2.7), mixed boundary conditions⁷ are avoided to achieve a better comparability. All discussed examples of TEM- and TE_{10} -waves in this thesis are monochromatic, however the following procedure is also applicable to arbitrary waveforms using a Fourier decomposition⁸ to produce several monochromatic subproblems. Depending on the relation of the wave impedances in both media, the incident wave is splitted into a transmitted and a reflected part. This principle is shown below in Fig. 4.15. The incident wave enters Ω through the left boundary.

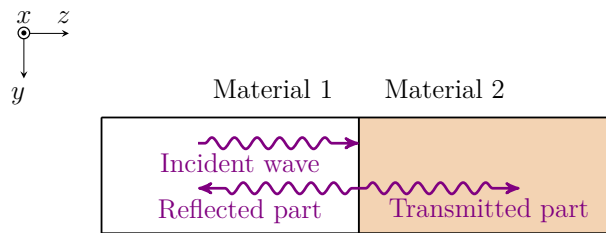


Figure 4.15 Wave behavior on a dielectric / permeable interface.

It is widely known in optics that a light wave which passes a step from air to glass is not affected by a phase change, whereas a light wave which is reflected on this step changes its phase

⁷Mixed boundary conditions are a combination of several contributions on a boundary, e.g. a combination of absorbing and Neumann boundary conditions.

⁸An arbitrary shaped time signal can be transformed to the frequency domain and decomposed into discrete frequencies using the Fourier decomposition, see e.g. [139].

by 180° . Therefore, the sign of the reflected part is inverted and the superposition of the incident wave with its reflected part generates a cumulative wave, which is shifted in amplitude and phase, in general. The PDE system (2.84) discussed in section 2.7 is able to cover inhomogeneous material distributions using the second term, respectively. Since the continuous FEM is not able to handle jumps of function values between neighboring elements, as pictured out later on for the forward wave in Fig. 4.18, a semi-analytical approach is used here. For the FEM implementation of (2.84), a DGFEM would be suitable, which is outside the scope of this thesis. See for example [262], where the DGFEM is used to model the 1st-order Maxwell system, or [173], where different DGFEM approaches are applied to the 2nd-order Maxwell system (Helmholtz equations). Note also that if the DGFEM is utilized, a separate handling of the forward and backward wave is necessary. The implementation of a bicomplex-formulated DGFEM is assumed to be straightforward.

A numerical example of a consecutive bicomplex continuous FEM using a one-side excited forward wave through nonzero Dirichlet boundary conditions is compared in the following to another model. This model uses standard Helmholtz equations with left-sided nonzero Dirichlet boundary conditions and right-sided ABCs, where the same forward wave is excited on the left. The process of consecutive bicomplex FEM is sketched below in Fig. 4.16.

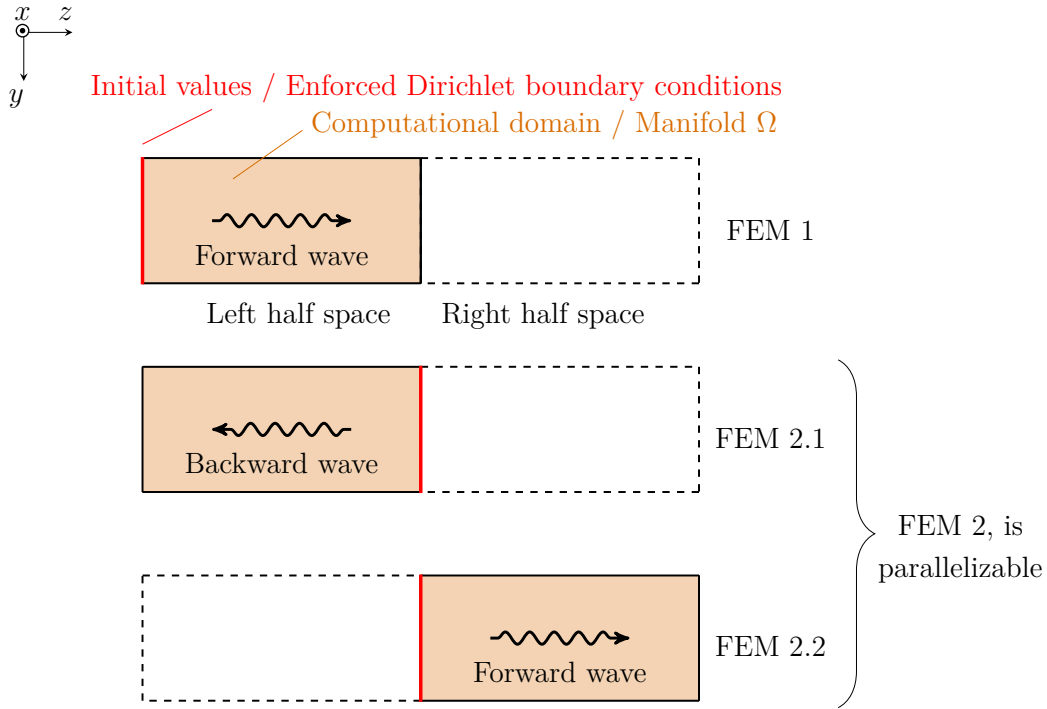


Figure 4.16 Process of consecutive bicomplex FEM depicted on the half space TEM-wave problem. On the material step, the wave splitting occurs. FEM 1 calculates the initial Dirichlet boundary conditions of FEM 2, whereas on the respective other side of Ω , ABCs are invoked.

Due to the independence of FEM 2.1 and FEM 2.2 (see Fig. 4.16), they are parallelizable, which is not considered in the presented numerical examples. In the case of DGFEM, FEM 1 and FEM 2.2 can be combined to calculate the forward wave in one step. To handle different wave impedances than Z_0 in (2.12) (see section 2.2.2), as e.g. for a TEM-wave which propagates in a dielectric material or a TE_{10} -wave in general, an appropriate impedance normalization is necessary.

In the following, the process presented in Fig. 4.16 is explained in more detail for the partially dielectric-filled rectangular waveguide (see later on section 4.2.4). The special handling of the three FEM steps depicted in Fig. 4.16 is shown in Fig. 4.17. Note that for a TEM-wave, some simplifications apply.

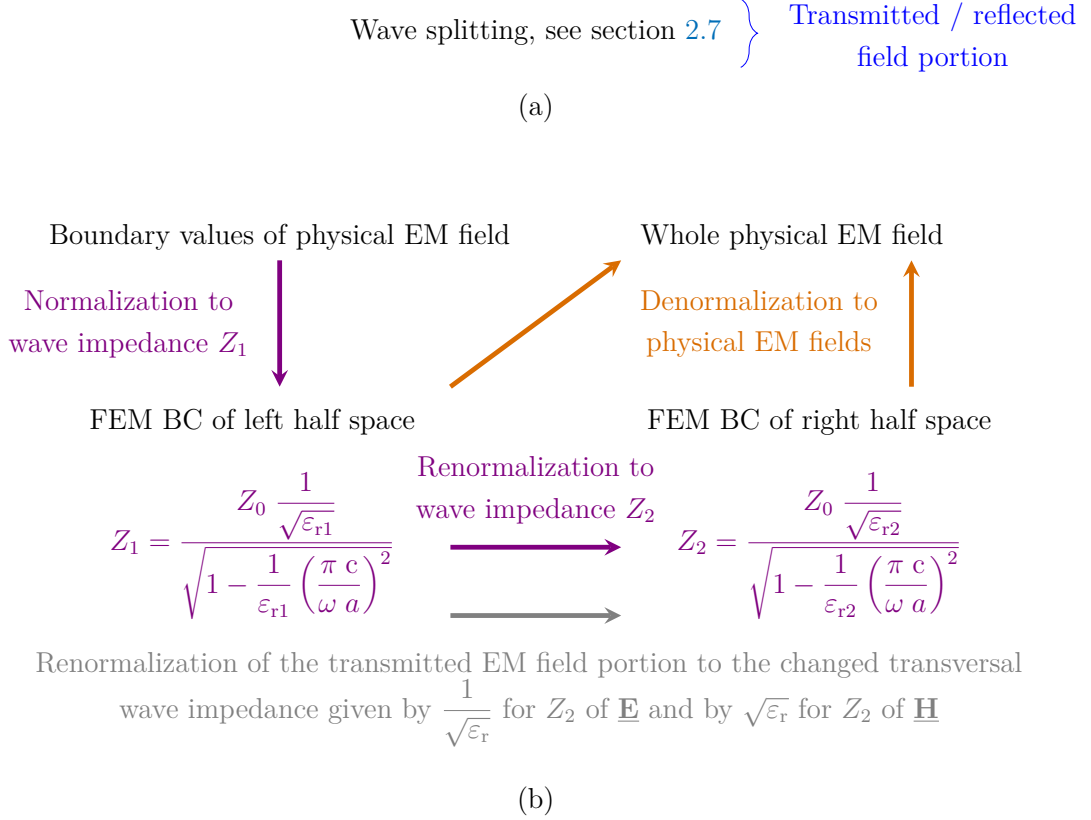


Figure 4.17 Handling of the interface at the dielectric step among the process of consecutive bicomplex FEM shown in Fig. 4.16 exemplified on a TE_{10} -wave guided by a rectangular waveguide. In [250], the presented impedance relations are derived in detail.

In Fig. 4.17, a is the width of a rectangular waveguide (see the explanations to Fig. 4.28 later on in section 4.2.4) as used in the following sections 4.2.3 and 4.2.4, c is the speed of light, ω is the angular frequency and the permittivities of the two half spaces are ϵ_{r1} and ϵ_{r2} , respectively. For FEM 2.1, the same impedance normalization as for FEM 1 is applied, which is Z_0 for free space in the case of TEM-wave, and Z_1 in the case of TE_{10} -wave, respectively, as shown on the left of Fig. 4.17. Therefore, only the wave splitting (a) and the normalization indicated in violet on the bottom left of (b) in Fig. 4.17 takes place for both FEM 1 and FEM 2.1. Since the wave impedance of the right half space Z_2 differs from Z_1 of the left half space, another impedance normalization is applied for FEM 2.2, as indicated in violet on the bottom right of (b) in Fig. 4.17. Furthermore, an additional renormalization as shown on the bottom of (b) in gray has to be applied to the transmitted field portion of (a). It is important to note that this renormalization refers to the transversal wave impedance, since only transversal field components are numerically delivered from the left half space to the right half space. For the TEM-wave, the transversal wave impedance is equal to the (general) wave impedance. This equivalence does not hold for a TE_{10} -wave, where also a longitudinal magnetic field component exists and, therefore, the wave impedance differs from the transversal one. After FEM calculations, the results are denormalized, as indicated in orange, and added together to form the whole EM field.

It is convenient now to analyze the analytical TEM-wave field solution (see especially (2.87) and (2.88) in section 2.7), since its propagation behavior is more complicated than that of the undisturbed TEM-wave in free space discussed before in section 4.2.1. Figure 4.18 shows both the electric and magnetic field's real and imaginary part at an arbitrary line in the transversal xy -plane over z . The material step is placed at $z = 0.5$ m.

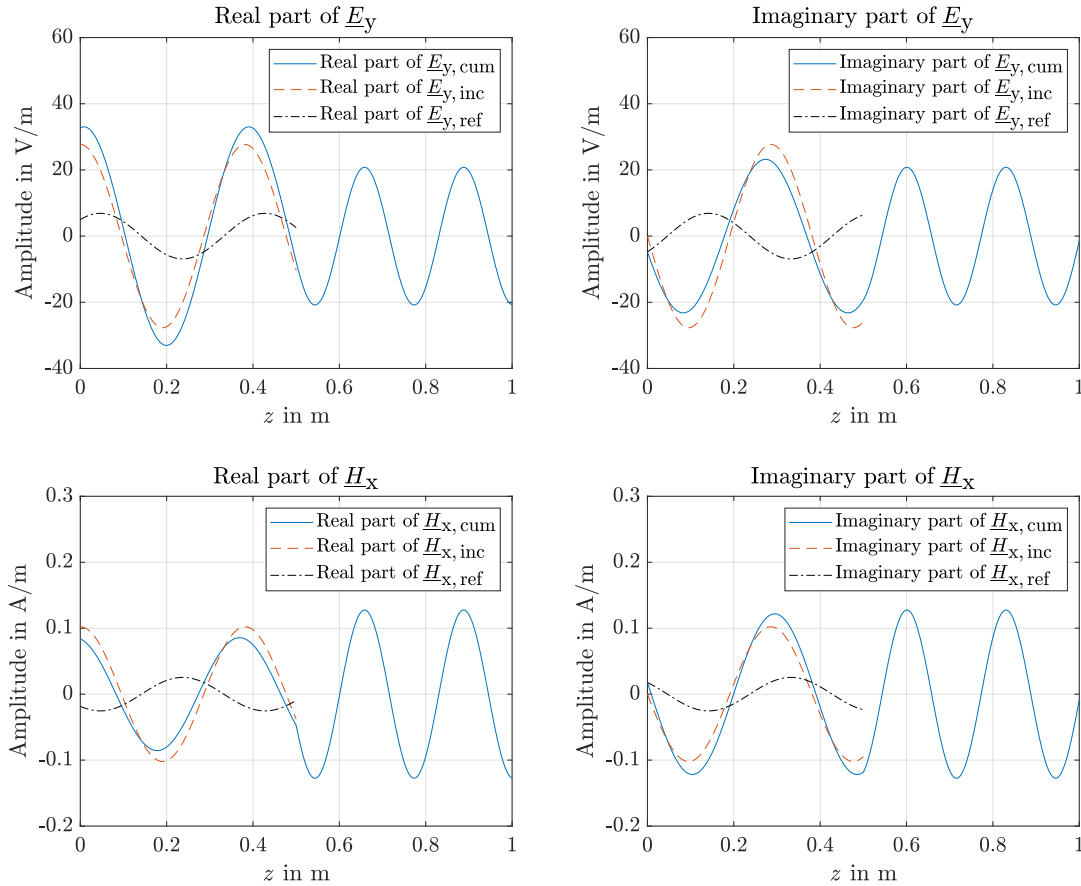


Figure 4.18 Propagation behavior of the transversal field intensities of the TEM-wave which passes a material step.

In Fig. 4.18, the subscript "cum" means the resulting – or cumulative – wave, which is equal to the transmitted part in the right half space. The incident wave is indicated by the subscript "inc" and the reflected wave by the subscript "ref", respectively. As indicated in Fig. 4.18, the tangential field intensities of the resulting wave (drawn in blue) are continuous on the material step, which is the case for all shown transversal field components. It is well-known that the ratio of the transmitted to the reflected parts is determined by the ratio of the wave impedances, see especially (2.87) and (2.88) in section 2.7. Note that for the reflected portion of the electric field, a sign inversion (phase shift of 180°) occurs, whereas the phase of the reflected magnetic field's part is unchanged.

To discretize the computational domain Ω , the regular brick mesh shown in Fig. 4.10 (see section 4.2.1) is chosen. The discretization parameter is varied in the range $q = 3..6$, which corresponds to 32...256 elements in z -direction, respectively. At first, the behavior of FEM C is plotted at the middle line ($x = y = 0.5$ m) of Ω over z in Fig. 4.19 to get an insight of the behavior of the EM field for $q = 3$. For q lower than 3, the numerical results are not meaningful, because of too less elements per wavelength. In high-frequency engineering it is a widespread rule of thumb to use 6 (see [165]) to 10 (see [267]) elements per wavelength for the meshing of Ω .

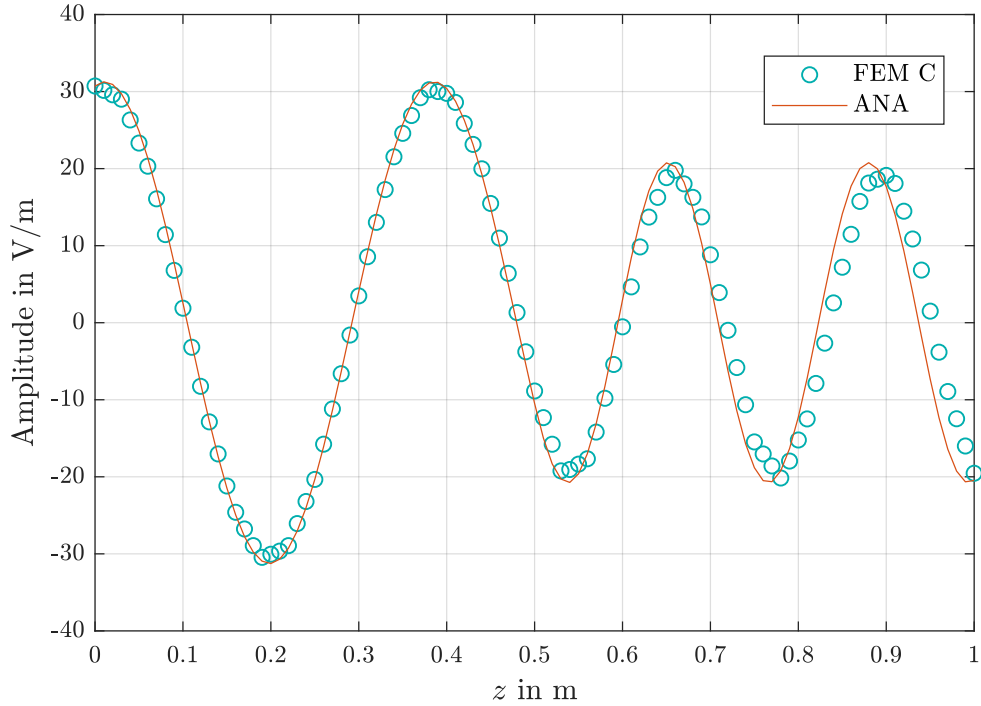


Figure 4.19 Real \underline{E}_y of FEM C for inhomogeneous material distribution and $q = 3$, numerical dispersion is evident on the right.

The numerical results of FEM BC are shown in Fig. 4.20, again on the middle line of Ω .

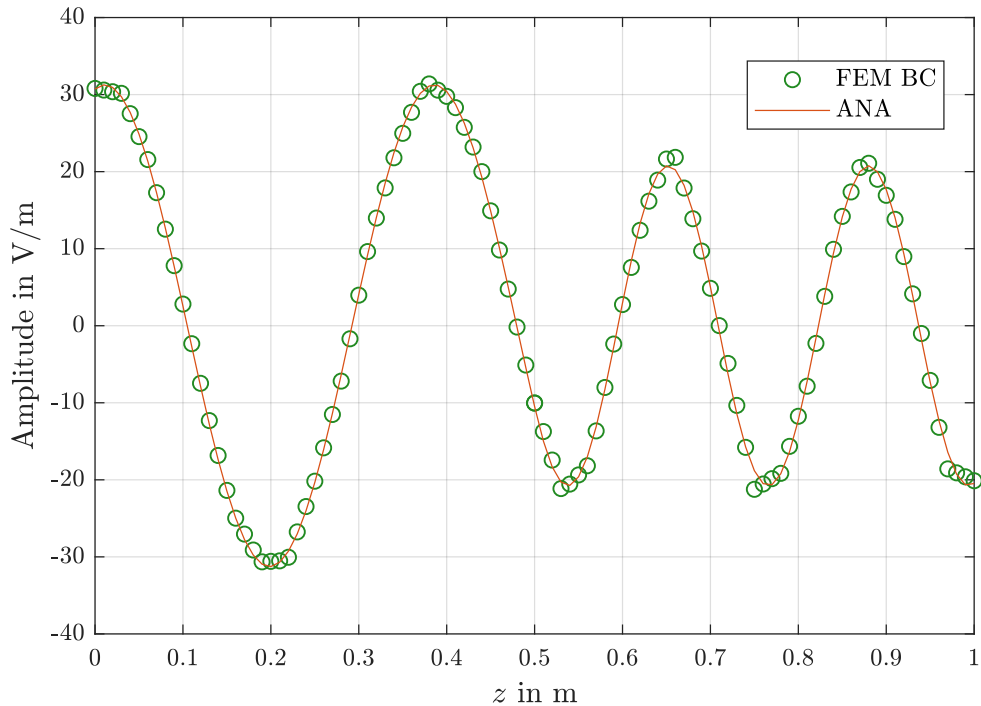


Figure 4.20 Real \underline{E}_y of consecutive FEM BC for inhomogeneous material distribution and $q = 3$, no numerical dispersion is apparent.

Mainly in the right half space of Fig. 4.19, numerical dispersion is obvious, which is not the case for FEM BC in Fig. 4.20. This detrimental effect is also called pollution effect, see e.g. [21].

An error comparison of $\|e\|_{\text{FWD}}^{\%}$ regarding the real part of the electric field for several values of q is shown below in Fig. 4.21.

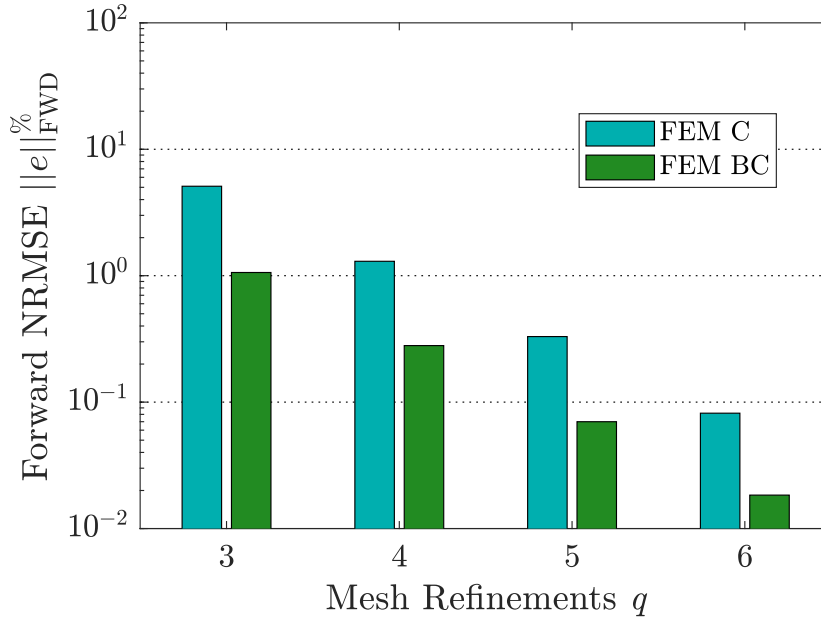


Figure 4.21 $\|e\|_{\text{FWD}}^{\%}$ of $E_{\text{re},\text{FEM}}$ for wave propagation on regular brick meshes based on Fig. 4.10, calculated at the interpolation points (11x11x101).

Note that up to the observed numerical accuracy, an error evaluation on the middle line ($x = y = 0.5$ m) over z of Ω would yield the same results as an error evaluation at an arbitrary line in the xy -plane over z . For the waveguide examples discussed later on, the error resulting from the choice of the position will differ. In Fig. 4.21, FEM BC yields for every q slightly better results than FEM C for $q + 1$. A direct comparison for the same q reveals a drastic improvement of about 350 %. Note that the process of consecutive FEM shown in Fig. 4.16 used for FEM BC calculates three homogeneous regions, respectively, which are superposed at the end. Contrary, FEM C handles the inhomogeneous region directly with one step.

The time consumption is listed below in Table 4.5, where the interpolation procedure after calculating the edge values is included there, as done in the previous section 4.2.1.

Table 4.5 Time consumption regarding several values of q for inhomogeneous material distribution.

Mesh refinements q	FEM BC in s	FEM C ($\underline{\mathbf{E}}$ or $\underline{\mathbf{H}}$) in s
3	2.25	0.99
4	3.94	1.27
5	9.17	2.31
6	26.46	5.32

A direct comparison of the calculation times listed in Table 4.5 for the same q reveals a rising difference in percent when q gets higher. As is recognizable from Fig. 4.21, the error of FEM BC for q is comparable to FEM C for $q + 1$. By comparing the calculation times this way, FEM BC needs about 70 % more time. However, FEM BC is slightly more accurate and the whole EM

field is present. Note that FEM BC might be faster through parallelization, as discussed earlier in this section concerning the explanations of Fig. 4.16.

A direct comparison of memory requirements is omitted here, because of the different approaches used for FEM BC and FEM C, respectively. Through the consecutive process for FEM BC presented in Fig. 4.16, the element number of FEM BC is halved compared to FEM C. This leads to an about two times smaller number of DOFs and therewith a quartered matrix size. Since the system matrix of FEM BC has got four times more entries than that of FEM C (see e.g. Fig. 3.4 discussed in section 3.4), the sizes of the system matrices are comparable. Roughly spoken, the memory requirements are therefore in a similar scale.

It turned out that an additional implementation of ABCs for the passive ports of FEM BC (as discussed in section 3.6) shows merely a small improvement of the numerical results compared to no explicit consideration of boundary conditions at these ports.

4.2.3 TE_{10} -wave in a Hollow Rectangular Waveguide

This section extends the investigations presented in [203]. Concerning TE_{10} -wave propagation, a hollow rectangular waveguide exhibits both transversal and longitudinal field components. This dominant mode is observed at 5 GHz in single mode operation. The problem is sketched below in Fig. 4.22, where wave propagation is assumed in the positive z -direction.

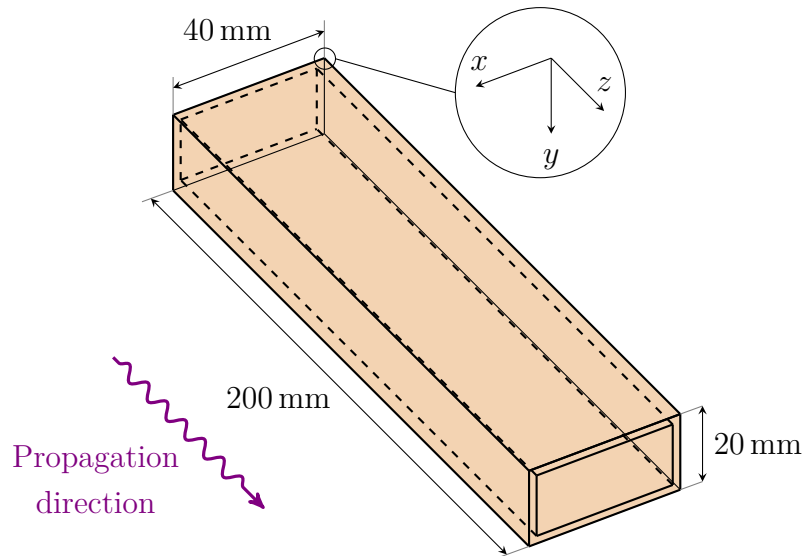


Figure 4.22 Sketch of the hollow rectangular waveguide.

Inner dimensions of the waveguide region Ω depicted in Fig. 4.22 are $(x, y, z) = (40, 20, 200)$ mm. Again, edge DOFs on brick elements are used to discretize Ω . Additionally to the previous investigations on TEM-waves, FEM BC needs zero-Dirichlet boundary conditions concerning the tangential field components merely at $x = 0$ mm and $x = 40$ mm for $\underline{\mathbf{E}}$, whereas FEM C needs them in addition at $y = 0$ mm and $y = 20$ mm for $\underline{\mathbf{E}}$. Since the field problem is two-dimensional in the xz -plane, only one element is taken in y -direction. The number of elements is 1024 and the number of edges is 5362. After calculation of the DOFs, the field is interpolated at $(33 \times 3 \times 81)$ equidistant points. The analytical solution at the center line $(x, y, z) = (20 \text{ mm}, 10 \text{ mm}, z)$ of Ω is drawn below in Fig. 4.23.

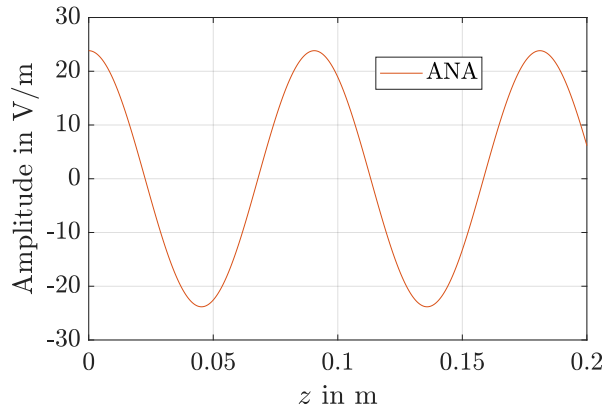


Figure 4.23 Analytical solution of the real electric field concerning TE_{10} -mode propagation evaluated at the center line of Ω .

The used mesh is depicted in Fig. 4.24. Figure 4.25 shows a few vectorial values of the real part of $\underline{\mathbf{E}}$ in red and $\underline{\mathbf{H}}$ in blue, respectively, located on the middle slice (indicated in green) of Fig. 4.24. Note that the field pattern of $\underline{\mathbf{E}}$ in Fig. 4.25 is inverted in comparison to Fig. 4.23, since the y -axis is reversed in Fig. 4.25.

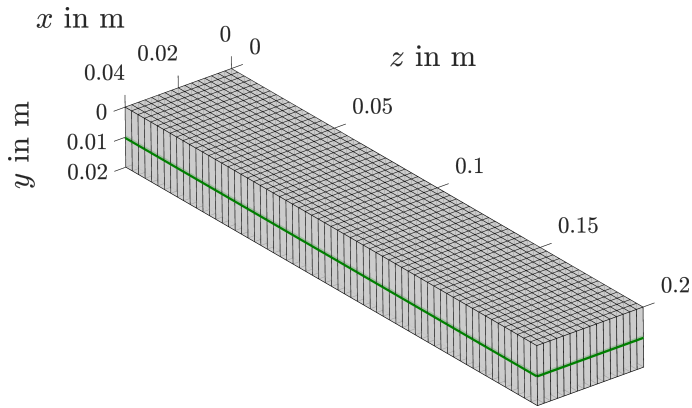


Figure 4.24 Mesh for TE_{10} -mode propagation in Ω .

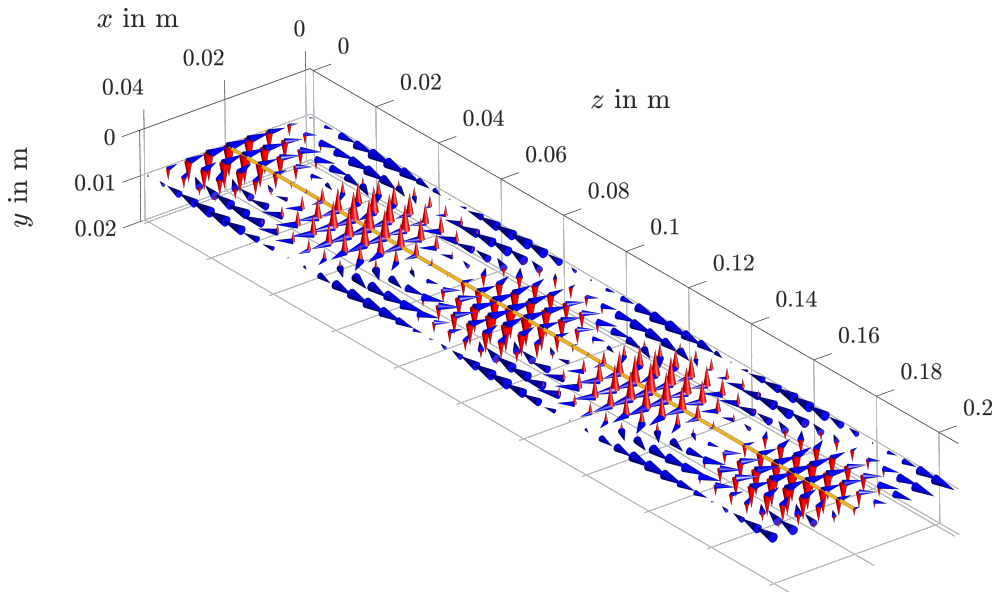


Figure 4.25 Field pattern for TE_{10} -mode propagation in Ω .

In Fig. 4.26, the real \underline{E}_y calculated by FEM C is shown at the center line of Ω , which is drawn in orange in Fig. 4.25.

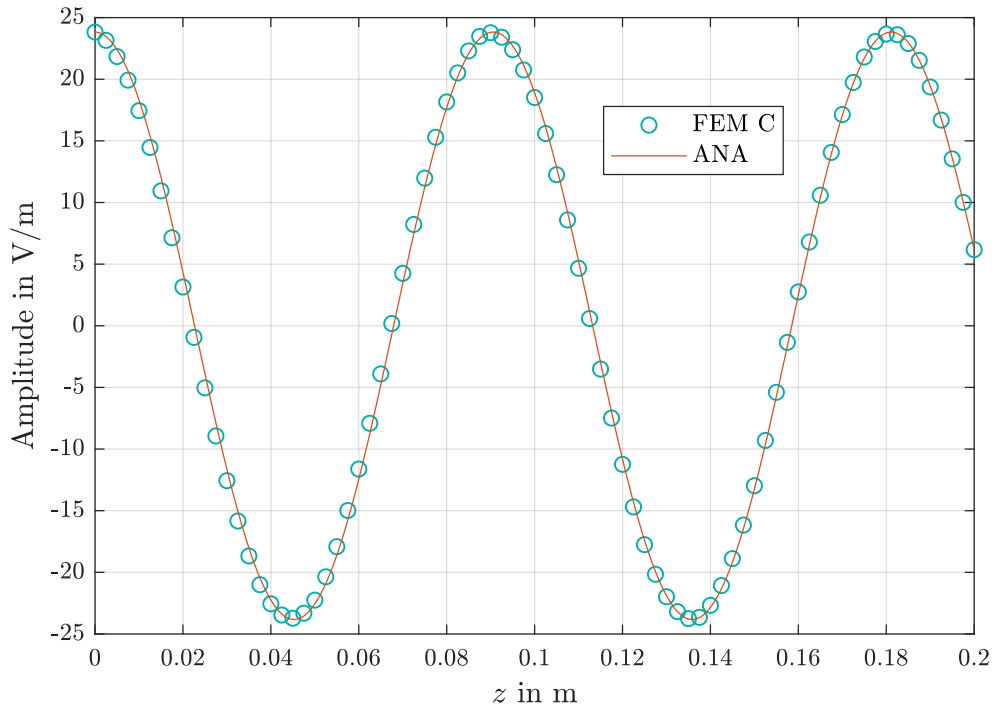


Figure 4.26 Real part of \underline{E}_y calculated by FEM C, numerical dispersion is evident (displacement at the left side).

Analogously, Fig. 4.27 reveals the real \underline{E}_y calculated by FEM BC in a similar manner.

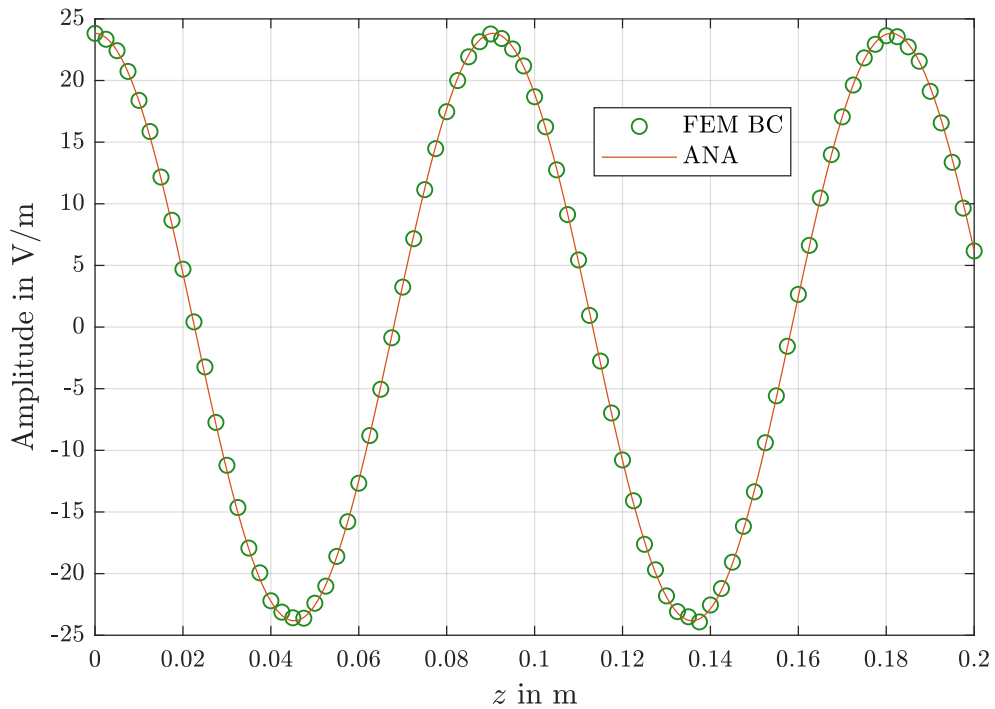


Figure 4.27 Real part of \underline{E}_y calculated by FEM BC, no numerical dispersion is apparent.

By using the Helmholtz equation in FEM C for calculating wave propagation, especially for high wave numbers, a phase error occurs. Especially on the first quarter period in Fig. 4.26, a left-sided displacement occurs. FEM BC in Fig. 4.27 does not show this effect. Note that previously in section 4.2.2 (see especially Fig. 4.19), numerical dispersion was also observed for FEM C concerning the example of a TEM-wave which passes a dielectric step.

An error comparison for the real part (indicated by the omitted underscore) of all field components of the TE₁₀-mode is presented in Table 4.6.

Table 4.6 Error Comparison of $\|e\|_{\text{FWD}}^{\%}$ regarding the respective real field component of the TE₁₀-mode.

Field component	FEM BC in %	FEM C in %
Transversal E_y	0.42	0.81
Transversal H_x	1.89	1.99
Longitudinal H_z	1.71	2.10

In Table 4.6, FEM BC shows an about halved error for E_y . Also the magnetic field components are calculated more accurately. Both transversal and the one longitudinal field component show improved results when using FEM BC instead of FEM C. A deviation in the achieved accuracy for the electric field towards the magnetic field is remarkable. The purely transversal nature of the electric field fits well with the also purely transversal boundary conditions, which are used to truncate the computational domain Ω . Contrary for the magnetic field (which consists of both a transversal and a longitudinal component), the longitudinal oriented DOFs are not covered by boundary conditions, rather they are floating.

As considered in the previous sections 4.2.1 and 4.2.2, time consumption and memory requirements are of interest in this case, too. They are presented below in Table 4.7.

Table 4.7 Time / Memory requirements for TE₁₀-mode.

Field component	FEM BC in s / MByte	FEM C in s / MByte
<u>E</u>	12.62 / 12.51	2.77 / 1.17
<u>H</u>		2.66 / 3.61

Regarding calculation time reported in Table 4.7, a factor of 5 might be concluded for FEM BC. The small-scale first example (see Table 4.4 in section 4.2.1) has shown a factor 2. In terms of memory requirements, the factor of 4 from the first example (see Table 4.4 in section 4.2.1) can be confirmed for the magnetic field listed in Table 4.7. Because of the additional zero-Dirichlet boundary conditions used for E in FEM C, the amount of memory usage for the sparse system matrix of FEM C is significantly smaller than that of FEM BC.

This section has shown that also for the fundamental TE₁₀-mode guided by the hollow rectangular waveguide, FEM BC provides more accurate results concerning both the electric and the magnetic field components. Again, numerical dispersion arises for FEM C as observed in section 4.2.2. In the following section 4.2.4, the waveguide model of this section is enhanced with a dielectric material placed in one half, worked out in a similar manner as in section 4.2.2 for the plane TEM-wave.

4.2.4 TE₁₀-wave in a Partially Dielectric-filled Rectangular Waveguide

For the waveguide considered in the previous section 4.2.3 and drawn in Fig. 4.22, one half of vacuum and one half filled with a lossless dielectric material. An effective permittivity of $\epsilon_r = 2.7$ is assumed for the latter one. The material step is placed at $z = 100$ mm. Again, the propagation direction is the positive z -direction, the frequency is 5 GHz and single mode operation is assumed. In accordance to section 4.2.2, the process of consecutive FEM BC is used, see Fig. 4.16 and Fig. 4.17 in section 4.2.2 for details. In Fig. 4.28, the field problem is sketched.

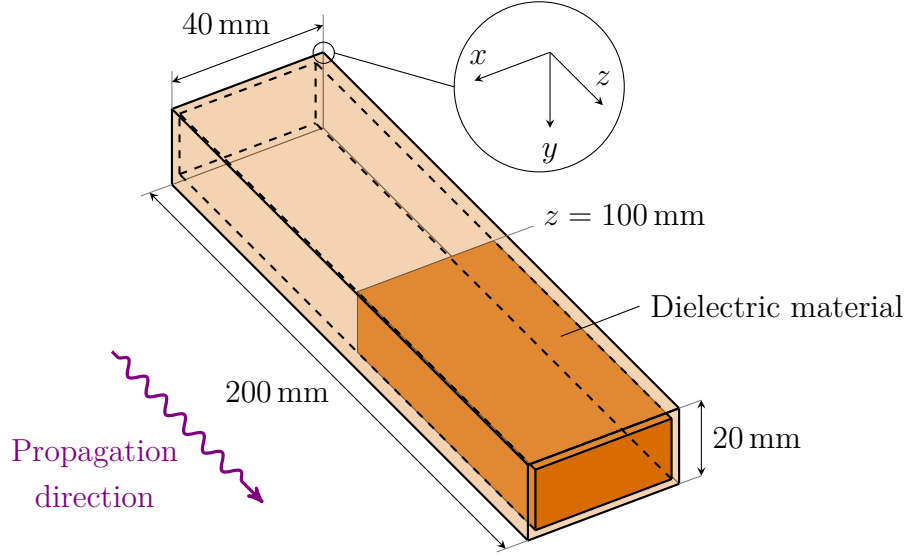


Figure 4.28 Sketch of the partially dielectric-filled rectangular waveguide.

The electric field's magnitude of the incident wave $\underline{\mathbf{E}}_{\text{inc}}$ is calculated in accordance to [250] as

$$|\underline{\mathbf{E}}_{\text{inc}}| = \sqrt{\frac{4PZ_1}{ab}}. \quad (4.5)$$

In (4.5), Z_1 is the wave impedance of the left half space, P is the port excitation power, which is assumed as $P = 1$ W and the port dimensions are – as previously chosen – the width and the height of the rectangular waveguide, $a = 40$ mm and $b = 20$ mm, respectively.

Contrary to the hollow waveguide discussed in section 4.2.3, where in the transversal x -direction merely 16 elements are used as shown in Fig. 4.24, here 128 elements are used. This high resolution is essential here, since the EM field at the end of the left half space at $z = 100$ mm, which is calculated by the first step of the consecutive FEM (see Fig. 4.16), has to be sufficiently precise to build the initial field for FEM 2.1 and FEM 2.2, respectively. The resolution in the y -direction is again 1 element and that of the z -direction is again 64 elements.

As discussed for the dielectric step passed by a TEM-wave in section 4.2.2, Fig. 4.29 shows the behavior of the transversal electric and magnetic field's real and imaginary part, respectively, which is analytically calculated based on (2.87) and (2.88), see section 2.7. Note that the EM field is calculated at the center line of the waveguide over the z -direction, see later on the orange line in Fig. 4.33. In Fig. 4.30, the analytical solution for the longitudinal field component of the magnetic field is presented. The field is plotted again over z , but in difference to Fig. 4.29 at $x = 0$ mm instead at $x = 20$ mm (see the green line in Fig. 4.33), since the longitudinal magnetic field component of the TE₁₀-wave vanishes on the center line of the waveguide. Note that contrary

to the magnetic field shown on the bottom of Fig. 4.29, the phase of the reflected longitudinal magnetic wave component is inverted (phase shift of 180°), as for \underline{E}_y on the top of Fig. 4.29.

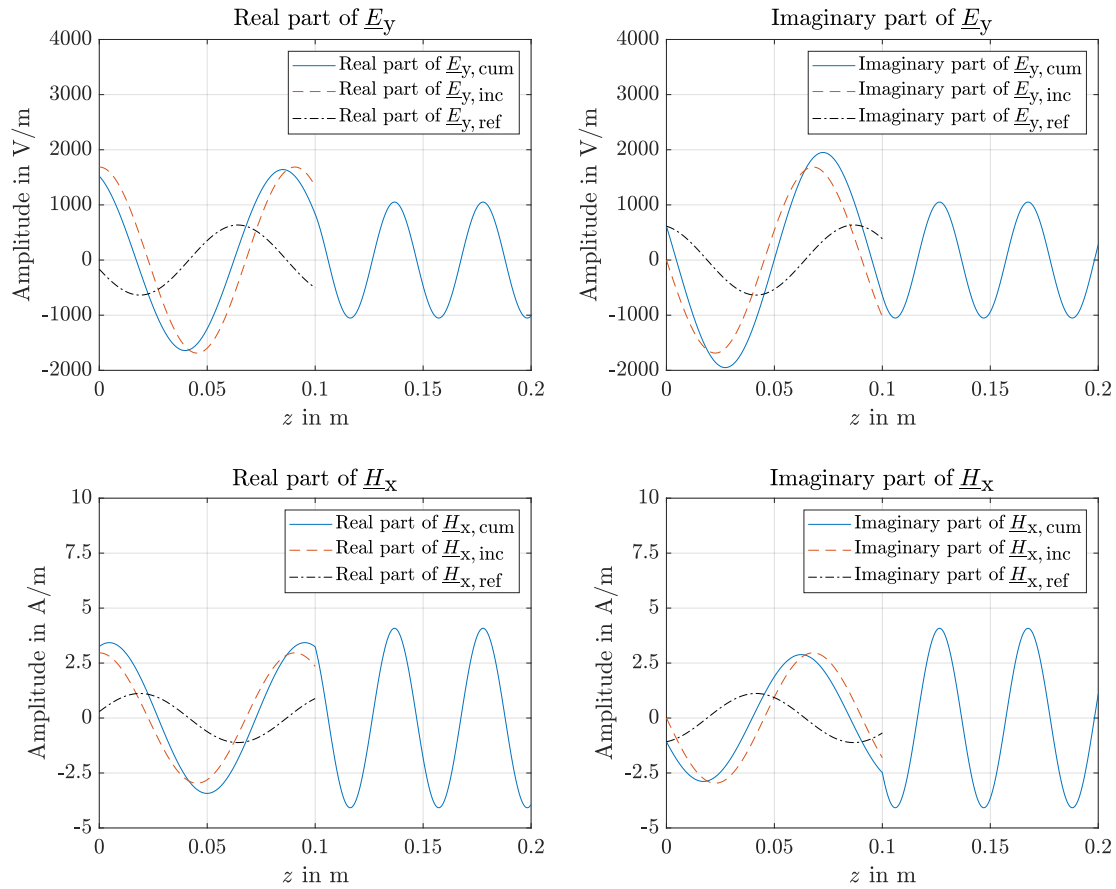


Figure 4.29 Propagation behavior of transversal field intensities of the partially dielectric-filled waveguide.

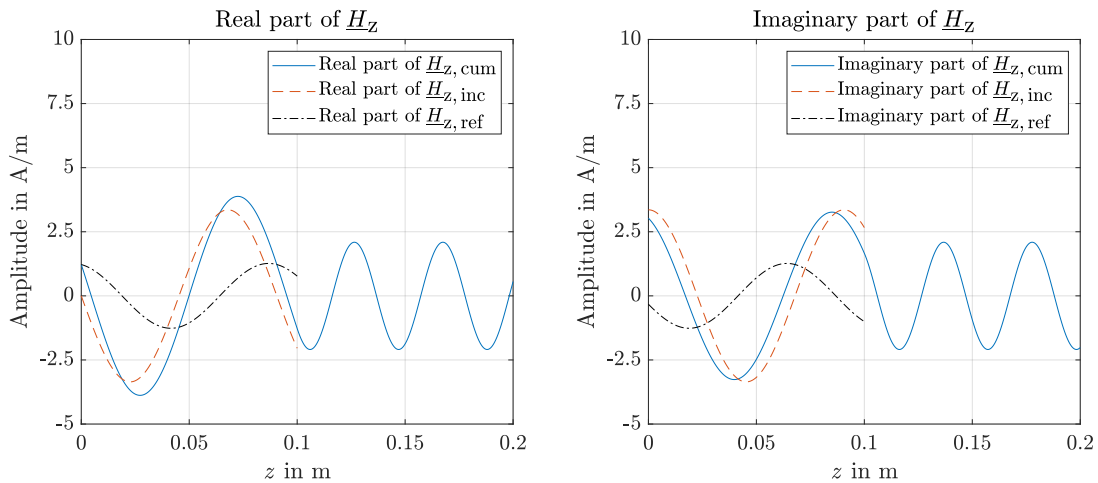


Figure 4.30 Propagation behavior of the longitudinal field intensity of the partially dielectric-filled waveguide.

The results of the real electric field \underline{E}_y calculated by FEM C are visualized below in Fig. 4.31. As for the TEM-wave passing a dielectric step discussed in section 4.2.2 and for the TE_{10} -wave which propagates in a hollow rectangular waveguide presented in section 4.2.3, a slight numerical dispersion can be observed in the right half space of Fig. 4.31.

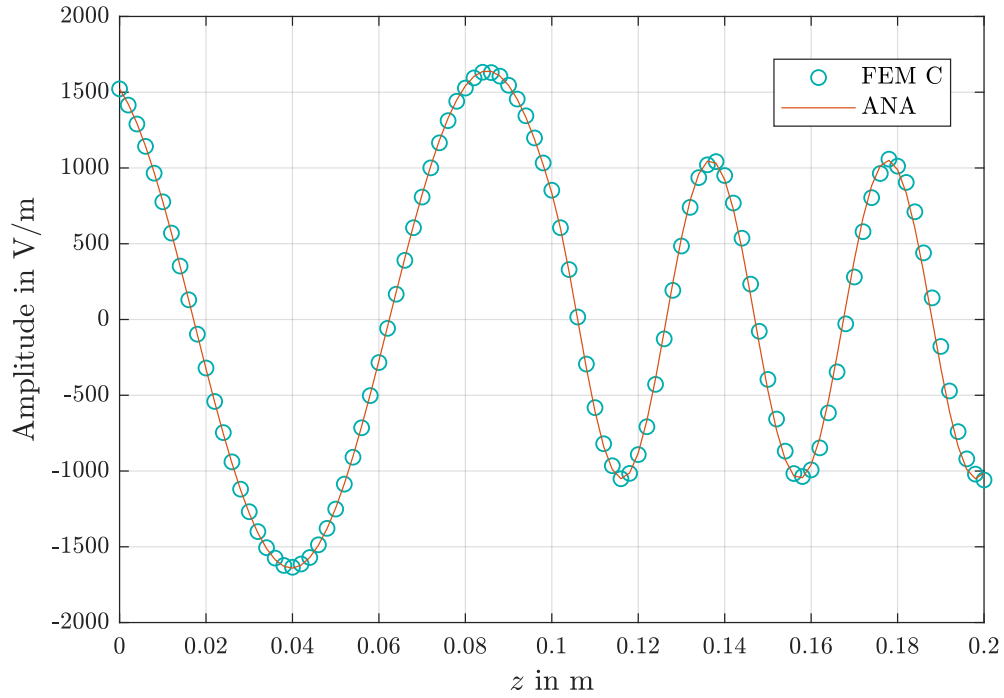


Figure 4.31 Real \underline{E}_y of the partially filled waveguide, calculated by FEM C.

In Fig. 4.31 and Fig. 4.32, the real \underline{E}_y is shown at the center line of Ω , drawn in orange in Fig. 4.33. Obviously, the results of FEM BC are in better agreement with ANA than those of FEM C shown in Fig. 4.31.

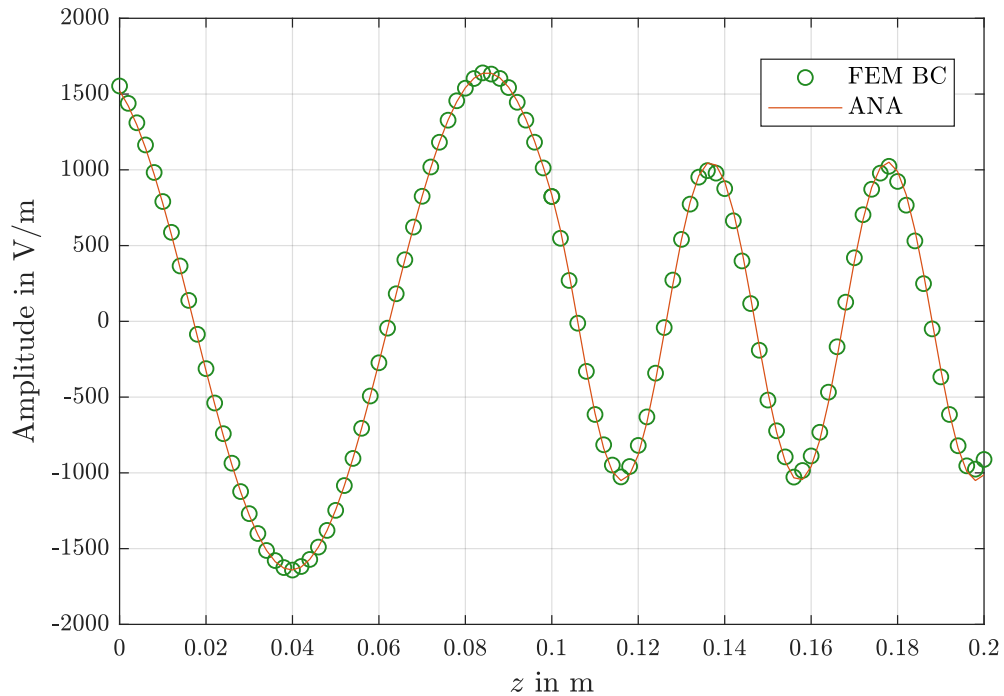


Figure 4.32 Real \underline{E}_y of the partially filled waveguide, calculated by FEM BC.

As done in section 4.2.3, the EM field is interpolated at $(33 \times 33 \times 81)$ equidistant points. In Fig. 4.33, a few vectorial values of both the real part of $\underline{\mathbf{E}}$ (depicted in red) and that of $\underline{\mathbf{H}}$ (colored in blue) are plotted, located on the middle slice (indicated in green) of Fig. 4.24 (see section 4.2.3).

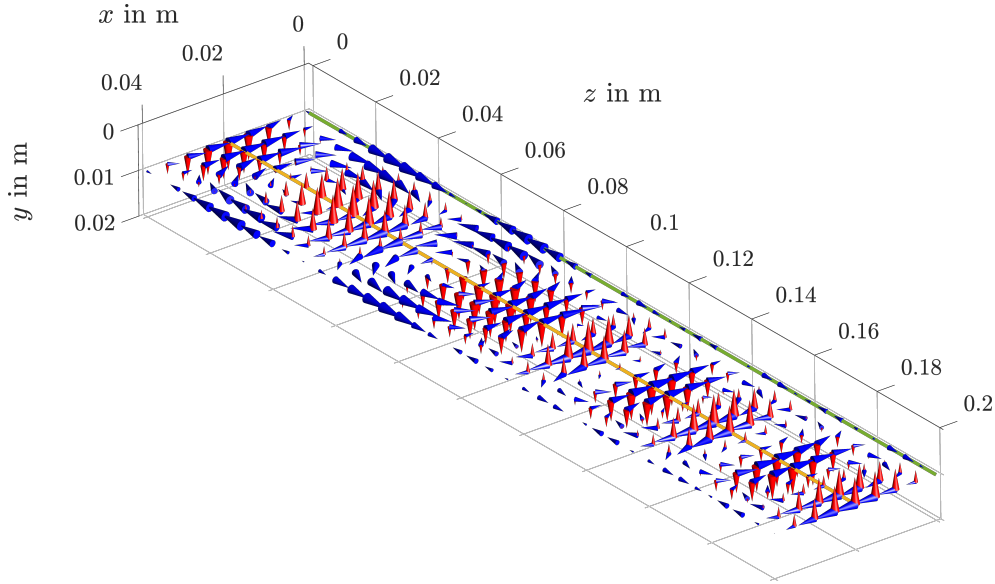


Figure 4.33 Field pattern for TE_{10} -wave propagation in Ω of the partially filled waveguide.

Table 4.8 Error Comparison of $\|e\|_{FWD}^{\%}$ regarding the respective real field component of TE_{10} -mode in partially filled waveguide.

Field component	FEM BC in %	FEM C in %
Transversal E_y	0.67	1.00
Transversal H_x	1.30	1.62
Longitudinal H_z	1.99	2.63

An error comparison for the real part of all field components of the TE_{10} -wave is presented in Table 4.8. As concluded in section 4.2.3, the results for the longitudinal magnetic field component H_z are less accurate in general, since the boundary conditions consider only DOFs in the port plane⁹. This leads to a small discontinuity of H_z at $z = 0.1$ m among other deviations in the field pattern. In general, FEM BC is more accurate than FEM C for all calculated field components with an approximated factor of one third. Time consumption and memory requirements are presented in Table 4.9. As in section 4.2.3, the memory requirement for the sparse system matrix is significantly smaller for FEM C because of the additional zero-Dirichlet boundary conditions used for $\underline{\mathbf{E}}$. In contrast to section 4.2.3, the consecutive FEM BC discussed in section 4.2.2 is used here, which yields further deviations regarding time consumption and memory requirements.

Table 4.9 Time / Memory requirements for TE_{10} -wave in partially filled waveguide.

Field component	FEM BC in s / GByte	FEM C in s / GByte
$\underline{\mathbf{E}}$	70.53 / 17.80	12.45 / 0.09
$\underline{\mathbf{H}}$		5.83 / 0.12

⁹According to the bottom of Table 3.1 in section 3.6, the ABCs for the TE_{10} -wave consider longitudinal field components, but they are only applied to edge DOFs which lie in the port plane.

4.2.5 Qualitative Hodge Decomposition

This section contains a short discussion on Hodge decomposition of the EM fields calculated by FEM BC and FEM C, respectively. For the sake of brevity, no quantitative numerical decomposition will be investigated here.

In section 2.4.7, it was shown that EM fields – which fulfill the bicomplex PDE – can be decomposed into several field types ${}^1\mathcal{CG}(\Omega)$ defined in (2.60) and ${}^1\mathcal{FK}(\Omega)$ defined in (2.61), respectively, valid for the discussed trivial topologies of Ω . Since ${}^1\mathcal{CG}(\Omega)$ and ${}^1\mathcal{FK}(\Omega)$ are defined in the language of differential forms to show the conformal discretization of wave quantities in an appropriate manner, the vector fields calculated by FEM are interpreted as corresponding differential forms. It is important to note that the Hodge decomposition into five mutually orthogonal subspaces based on (2.59) (see section 2.4.7 for details) – which is used here – is only one possibility to decompose an EM vector field in 3D. An alternative would be e.g. the decomposition for a trivial topology presented in (2.57) into two mutually orthogonal subspaces, called the curl-free gradient space $G(\Omega)$ and the divergence-free curl space $K(\Omega)$ (see also section 2.4.7). Further possibilities are e.g. the Helicity decomposition or the Bohren decomposition, which can be advantageous for the investigation of EM waves' polarization as discussed in [64].

Because the fields calculated by FEM BC and FEM C look similar, no distinction will be made here between them. In Table 4.10, a decomposition of all smooth vector fields $X \in \underline{\mathbf{F}} / \underline{\mathbf{E}} / \underline{\mathbf{H}} \xrightarrow{\mathcal{P}_1} {}^1\mathcal{X} \in {}^1\underline{\mathcal{F}} / {}^1\underline{\mathcal{E}} / {}^1\underline{\mathcal{H}}$ contained in Ω is shown. This transformation is in accordance to the definitions of ${}^1\mathcal{CG}(\Omega)$ and ${}^1\mathcal{FK}(\Omega)$, respectively. As mentioned in section 2.4.7, the additional application of the Hodge operator can be neglected for vector calculus, which leads to the definitions of $\mathcal{CG}(\Omega)$ and $\mathcal{FK}(\Omega)$ in Fig. 2.32 (see section 2.4.7), respectively.

Table 4.10 Qualitative Hodge decomposition of the EM fields (calculated in the 3D topologically trivial numerical examples) into curly gradients and fluxless knots, respectively.

Investigated in	Calculated EM vector field	Hodge decomposition including mapping to differential p -forms
Section 4.2.1 and 4.2.2	$\underline{\mathbf{F}} / \underline{\mathbf{E}}$ and $\underline{\mathbf{H}}$ of TEM-mode	${}^1\mathcal{CG}(\Omega)$
Section 4.2.3 and 4.2.4	$\underline{\mathbf{z}}_1 \{ \underline{\mathbf{F}} \} / \underline{\mathbf{E}}$ of TE ₁₀ -mode	${}^1\mathcal{CG}(\Omega)$
	$\underline{\mathbf{z}}_2 \{ \underline{\mathbf{F}} \} / \underline{\mathbf{H}}$ of TE ₁₀ -mode	${}^1\mathcal{FK}(\Omega)$

Since the electric and magnetic fields of both examples of the TEM-wave – in free space (see section 4.2.1) and through a dielectric transition (see section 4.2.2) – show only straight field lines which are perpendicular to each other (depicted in Fig. 4.9, see section 4.2.1), they can be directly recognized as ${}^1\mathcal{CG}(\Omega)$, respectively. Obviously, a variation of the intensity of the EM field over the z -direction occurs, which does not affect the type of field pattern, see the definition of ${}^1\mathcal{CG}(\Omega)$ in (2.60) of section 2.4.7. The field pattern of the waveguide's TE₁₀-mode depicted in Fig. 4.25 (see section 4.2.3) and Fig. 4.33 (see section 4.2.4) shows for the electric field only straight field lines as for the TEM-mode, where the intensity of these field lines vary in the transversal x -direction. Contrary for the magnetic field, closed loop fields can be identified (see e.g. Fig. 4.25 or Fig. 4.33). This is in accordance with the discussed process of wave propagation shown in Fig. 2.34 (see section 2.4.7), which indicates that wave propagation is an alternating process between two different field patterns ${}^1\mathcal{CG}(\Omega)$ and ${}^1\mathcal{FK}(\Omega)$. Note that the TEM-wave is a special case of this process, since the boundary conditions in the far-field deform the magnetic field in a way that a conversion from fluxless knots to curly gradients (or, in other words: from

closed field loops to straight field lines) takes place. Then, an alternating process between the same field pattern ${}^1\mathcal{CG}(\Omega)$ is present, which can be recognized in Fig. 2.34. This is illustrated below in Fig. 4.34, where the two field patterns ${}^1\mathcal{CG}(\Omega)$ and ${}^1\mathcal{FK}(\Omega)$ presented in Fig. 2.32 can be clearly identified in the respective computational domain Ω .

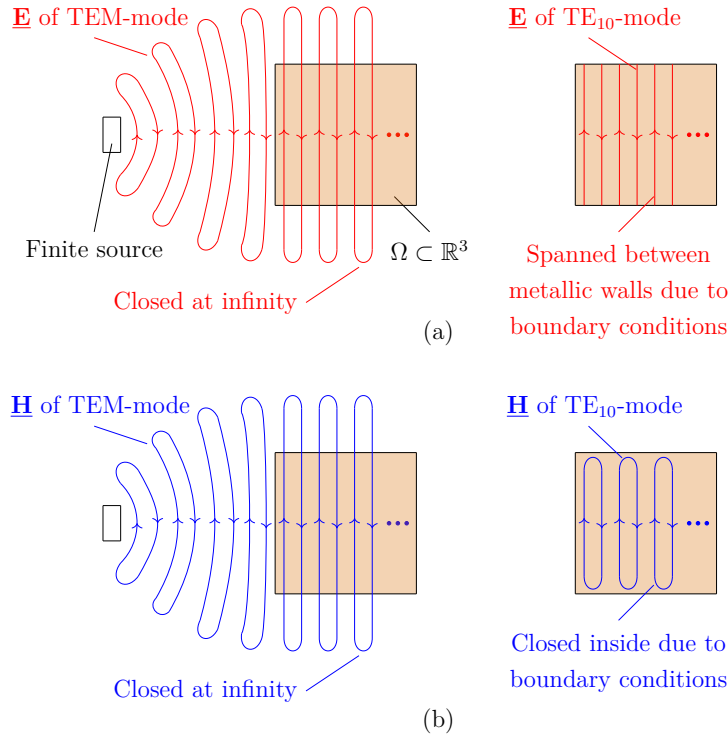


Figure 4.34 Qualitative EM field pattern of the fundamental modes in free space on the left and in a rectangular waveguide on the right, respectively. In (a), the electric field is illustrated, (b) shows the magnetic field. The decrease of EM field intensity over the distance is not visualized.

On the left of Fig. 4.34, the far-field of an EM wave in free space is considered to be in Ω . Contrary on the right, the wave is guided inside a rectangular waveguide. The electric field contained in Ω of both considered modes in (a) indicate a behavior of $\mathcal{CG}(\Omega)$, which is also satisfied due to boundary conditions by the magnetic field of the TEM-wave on the left of (b). In contrast, the magnetic field of the TE_{10} -mode on the right of (b) shows closed field lines, which corresponds to $\mathcal{FK}(\Omega)$. Higher-order modes¹⁰ – as e.g. the TM_{11} -mode (transversal magnetic) of the rectangular waveguide – show also closed \underline{H} -loops, whereas \underline{E} is spanned between the metallic surfaces inside the waveguide in various ways. There might be also closed loops inside the waveguide for \underline{E} , as for the TM_{21} -mode. In this case, also \underline{E} consists partially of $\mathcal{FK}(\Omega)$. A deduction regarding differential forms is, that the arbitrary complex differential auxiliary subspace ${}^1\mathcal{Y}$ whose spatial derivative generates ${}^1\mathcal{CG}(\Omega)$ (see (2.60) in section 2.4.7), can be now identified as ${}^1\mathcal{FK}(\Omega)$ or ${}^1\mathcal{CG}(\Omega)$, which depends on the field pattern.

Furthermore, it can be concluded, that the field patterns received from Hodge decomposition of \underline{F} are not necessarily the same for both the electric and magnetic part, rather they depend on boundary conditions. Therefore, a unique determination is only possible for the electric part $\mathbf{z}_1\{\underline{F}\} = \underline{E}$ and the magnetic part $\mathbf{z}_2\{\underline{F}\} = \underline{H}$ in a separate manner, or if the boundary conditions are based on the same geometrical setting (as for the TEM-wave), respectively.

¹⁰At higher frequencies, modes with field pattern different than the fundamental mode might be able to propagate, depending on the waveguide geometry. Graphical representations of some of these modes (e.g. TE or TM) inside the rectangular waveguide can be found e.g. in [199] or [266].

grade of determination induced by the purely transversal boundary conditions. In the first TEM example (see section 4.2.1), a very coarse mesh is used. There, FEM BC shows only a small error improvement of about 8 %, which demonstrates that a sufficient discretization per wavelength is important. The remarkable improvement of about 381 % for the TEM-mode which passes a dielectric step (see section 4.2.2) is justified further by the semianalytical approach of the consecutive FEM BC. In the first example of TE₁₀-mode propagation in homogeneous media discussed in section 4.2.3, the error improvement is significant with about 93 %. Compared to the first TEM-mode example with only 8 % error improvement, the mesh is here fine enough for an even higher improvement of accuracy. Contrary, the example of the TE₁₀-mode, which propagates in a partially dielectric-filled rectangular waveguide (see section 4.2.4), shows a lesser improvement of about 49 %, which can be explained by the accuracy limitation through the use of ABCs instead of Dirichlet boundary conditions.

Besides the improvement of error, further interesting relationships are recapitulated below. As discussed in section 4.2.2, the consecutive bicomplex FEM can be parallelized, which would further reduce the calculation time. Alternatively, when using a DGFEM, the forward wave can be computed in one step. It was shown in sections 4.2.2, 4.2.3 and, to a lesser extent, in section 4.2.3, that the numerical dispersion is reduced when using FEM BC instead of FEM C. The drastic error improvement for FEM BC achieved in section 4.2.2 is based on the process of consecutive FEM, which calculates three homogeneous regions, respectively, instead of one inhomogeneous region for FEM C. Furthermore, it should be noted that an additional implementation of ABCs for FEM BC on the non-excited port yields merely a small error improvement of the numerical results compared to no explicit manipulation of boundary conditions on the passive port.

4.3.2 Discussion of the Poynting Vector Field's Real Part

Another possibility to interpret the error improvement of FEM BC is to calculate the Poynting vector field, which includes both the full complex-valued electric and magnetic field, instead of only the electric field's real part as done before. It is assumed that generally a higher error occurs compared to the separate evaluation of the electric or magnetic field, since here, the product of both fields is calculated. This yields also a multiplication of those fields' errors. To observe the practically relevant active power transfer, the real part of the complex-valued Poynting vector field $\underline{\mathbf{S}}$ is of interest, which is based on the complex-valued transversal field components of the EM field. By assuming only the existence of \underline{E}_y and \underline{H}_x , based on (2.76) from section 2.6.2 follows

$$\underline{\mathbf{S}} = \frac{1}{2} (\underline{E}_y \underline{H}_x^*) \mathbf{e}_z. \quad (4.6)$$

Note that the product in (4.6) yields – due to numerical errors – not exactly a real-valued Poynting vector field $\underline{\mathbf{S}}$. Therefore, only the real part of this product is compared to the exact real-valued analytically calculated Poynting vector field. For error evaluation regarding the real-valued Poynting vector, (4.2) from section 4.1.1 is redefined in order to avoid zero denominators as

$$\|e\|_{\text{FWD}}^{\%} = \frac{\sqrt{\frac{1}{M} \sum_{m=1}^M (S_{\text{re, FEM}}^m - S_{\text{re, ANA}}^m)^2}}{\max(S_{\text{re, ANA}})} \cdot 100 \%, \quad (4.7)$$

where all quantities in (4.7) adopted for $\underline{\mathbf{S}}$ are similar to (4.2). For the TEM-wave problems discussed in section 4.2.1 and 4.2.2, the denominator of (4.7) would be zero if the form of the denominator in (4.2) would be used because $\underline{\mathbf{S}}$ is constant in Ω . The waveguide examples discussed after in section 4.2.3 and 4.2.4 are covered in an appropriate manner with this approach, since there, $\underline{\mathbf{S}}$ varies in the transversal plane between its maximum on the center of the x -expansion and zero on the walls of the waveguides (see e.g. Fig. 4.22 in section 4.2.3 or Fig. 4.28 in section 4.2.4).

The second transversal field quantity \underline{H}_x is evaluated at the same points used for \underline{E}_y , see the previous sections for details. For the first TEM-mode example discussed in section 4.2.1, the homogeneous mesh (see the left one in Fig. 4.10) and $q = 0$ is assumed. In the second TEM-mode example (see section 4.2.2), also the homogeneous mesh and $q = 3$ (see (4.4) in section 4.2.1, one refinement more than the right one of Fig. 4.10) is chosen. For TE₁₀-mode propagation, only one discretization is shown in both sections 4.2.3 and 4.2.4, which is used for the evaluation of \mathbf{S} .

An overview of the numerical accuracy of FEM C (numerator) and FEM BC (denominator) with the corresponding improvement of $\|e\|_{\text{FWD}}^{\%}$ regarding \mathbf{S} is given below in Table 4.12.

Table 4.12 Error improvements of FEM BC concerning the real Poynting vector field \mathbf{S} .

Investigated in	Propagating mode	Improvement of $\ e\ _{\text{FWD}}^{\%}$ regarding the real Poynting vector obtained by FEM BC
Section 4.2.1	TEM-mode	$\left(\frac{1.18\%}{1.11\%} - 1\right) \cdot 100\% \approx 6\%$
Section 4.2.2		$\left(\frac{19.68\%}{6.81\%} - 1\right) \cdot 100\% \approx 189\%$
Section 4.2.3	TE ₁₀ -mode	$\left(\frac{3.49\%}{3.06\%} - 1\right) \cdot 100\% \approx 14\%$
Section 4.2.4		$\left(\frac{6.59\%}{3.75\%} - 1\right) \cdot 100\% \approx 74\%$

Note that \underline{E}_y and \underline{H}_x of FEM C are separately calculated, based on Helmholtz equations (2.13a) and (2.13b), respectively, see section 2.3.1. In accordance to Table 4.11, every numerical example shows a higher accuracy achieved by FEM BC. It is noticeable, that the improvement in percent differs in every case between Table 4.11 and Table 4.12, since the full complex-valued EM field is considered in Table 4.12. As shown e.g. in Table 4.6 and Table 4.8 for the waveguide examples (see section 4.2.3 or section 4.2.4, respectively), \mathbf{H} is calculated with a lower accuracy than \mathbf{E} in both FEM BC and FEM C (due to the fact that \mathbf{H} consists of both a transversal and a longitudinal component, see Fig. 4.34 in section 4.2.5). Therefore, $\|e\|_{\text{FWD}}^{\%}$ for the real part of \mathbf{S} in Table 4.12 is assumed to be higher than $\|e\|_{\text{FWD}}^{\%}$ for the real part of $\underline{\mathbf{E}}$ reported in Table 4.11, which is correct in every case (not to be confused with the improvement of $\|e\|_{\text{FWD}}^{\%}$).

Overall, the tendencies are comparable. Regarding the TEM-mode examples, the improvements achieved by FEM BC are smaller. For TE₁₀-modes, it is also smaller for the first example (see section 4.2.3) and higher for the second example (see section 4.2.4). Following the Hodge decomposition of the numerical examples presented in section 4.2.5, this is caused by the different field types of $\underline{\mathbf{E}}$ and $\underline{\mathbf{H}}$ in the case of TE₁₀-modes on the one side, and on the different kind of boundary conditions on the other side. A further tendency is that the numerical examples of inhomogeneous material distribution discussed in section 4.2.2 and 4.2.4 show – compared to those of homogeneous material distribution examined in section 4.2.1 and 4.2.3 – a higher $\|e\|_{\text{FWD}}^{\%}$ for \mathbf{S} (see the left percentages in the brackets of Table 4.12, respectively). This can be explained by the use of a different number of terms for the PDE concerning $\underline{\mathbf{E}}$ and $\underline{\mathbf{H}}$ (absence or presence of the third term in (2.13a) or (2.13b), see section 2.3.1) or that of $\underline{\mathbf{F}}$ (absence or presence of the second term on the LHS in (2.22), see section 2.3.2).

Generally, FEM BC provides numerical results with higher accuracy compared to FEM C, which is mainly caused by the lower order of the underlying partial differential equation. Besides this 1st-order nature of the bicomplex PDE for homogeneous material distribution, the additional term¹¹ for the variational formulation of inhomogeneous material distribution is also one order lower compared to that of the Helmholtz equations, which increases the accuracy further.

¹¹Compare the second term of (2.33) in section 2.3.2 to the last term of (2.21) in section 2.3.1.

5.1 Summary

In this work, the objective was set to be both practical as well as theoretical in order to achieve novel applicable procedures of EM wave field modeling in FEM. On the one side, a bicomplex-formulated one-way wave equation, which was applied to EM wave propagation problems, has been shown by the use of primal mimetic finite elements in MATLAB. As a motivation to break up ordinary handling of electromagnetism – by formulating and discretizing together what physically occurs together – this thesis discusses practical applications in high-frequency engineering.

Based on cohomology theory, the conformal discretization of the bicomplex EM field is profoundly described, which increases the value of the present thesis compared to heuristic approaches. The application of DEC has shown, that the reformulated time-harmonic Maxwell's equations for EM wave propagation in frequency domain are conformally approximated in a quaternionized de Rham cohomology without the use of a dual mesh, which leads to an increase of the accuracy at all. The theoretical contribution of this thesis to involve the effect of the outer imaginary unit i as a mapping from primal 1-forms to dual 1-forms in the de Rham cohomology should be further emphasized. This involvement allows to construct a conformal discretization of the EM field on merely the primal mesh. By interpreting geometrical relations in a different way, the process of wave splitting – to diagonalize the part of the time-harmonic Maxwell system which represents the temporal derivatives – is isomorphic to the derivation of the proposed bicomplex formulation. A further important outcome is the generalized bicomplex formulation expressed in the language of DEC, which is valid for arbitrarily desired coordinate systems through the use of the metric tensor. This formulation includes a novel continuous Hodge operator, which is appropriately discretized in FEM by the use of suitable proposed variational formulations.

The merits and shortcomings of the bicomplex FEM are identified on various basic 3D examples. For both regular and irregular element distribution as well as for homogeneous and inhomogeneous material distribution, the bicomplex FEM shows a fundamentally higher accuracy. In other words, it is possible to use less elements for discretizing the computational domain Ω in order to observe a similar accuracy. The comparison of the bicomplex FEM to the conventional FEM (which uses the Helmholtz equation with complex-valued numbers) based on several numerical benchmark examples reveals this fundamentally higher accuracy of the proposed method with respect to the L_2 -norm concerning the Forward NRMSE $\|e\|_{\text{FWD}}^{\%}$. This concerns both the electric and the magnetic field, which can be explained by the lower order of the underlying PDE. The whole EM field is calculated at the same location in Ω and with roughly similar accuracy (depending on the field type based on Hodge decomposition). These relations might be further improved when

optimizing the implementation of the calculations using iterative matrix inversion or parallelization techniques, as discussed for the consecutive FEM of inhomogeneous material distribution. In addition to calculate either the electric field or the magnetic field of Helmholtz equation-based problems, both field quantities are present using the bicomplex concept. So it is not necessary to calculate the other field with an additional FEM approach subsequently. The bicomplex FEM is a direct approach, so neither electric scalar potential nor magnetic vector potential is employed, which avoids further numerical errors. Also the relation to common potential formulations is covered in detail. To truncate Ω appropriately, ordinary ABCs are reformulated and implemented in a bicomplex manner. Possible field types of the 3D benchmark problems were analyzed by the use of the Hodge decomposition. In the bicomplex FEM, the occurrence of spurious solutions is significantly reduced by the use of Whitney edge-based finite elements.

To conclude the investigation, FEM BC is an advantageous alternative to conventional approaches, especially for one-way wave field simulations where the entire EM field is of interest.

5.2 Outlook and Future Work

As shown in this thesis, further EM quantities such as the field energy, the Poynting vector, scattering parameters or the Maxwell stress tensor can be derived directly from the reformulated bicomplex EM field. Thus, advantageous calculation procedures can be generated. Through the use of bicomplex analysis as an isomorphism, no restrictions on the temporal behavior of the Maxwell system have been made by the assumption of the time-harmonic case. If general time dependence is desired, the inner imaginary unit j is omitted. Nevertheless, the outer imaginary unit i might be used in a similar geometric manner to yield a conformal approximation of the whole EM field through the use of primal mimetic finite elements. Several selected possibilities to enhance the presented model are listed below.

- Other discontinuous material transitions different from the discussed half space problem, like resistive sheets may be also considered in a bicomplex formulation. The involvement of lossy and anisotropic materials as well as the generalization to higher-order finite elements are assumed to be straightforwardly implementable as in the conventional FEM.
- Consideration of other finite element types for meshing. Note that some of them might limit the solution accuracy caused by the interpolation behavior of the Whitney DOFs.
- Three-dimensional stabilization techniques for the diagonalized time-harmonic Maxwell system (received after the process of wave splitting) might reduce numerical errors.
- The revealed degree of freedom to design a number system with arbitrary structure offers the enhancement of the proposed bicomplex concept to include gravitational waves. Recent publications have shown that the speed of an EM wave is virtually the same as the speed of a gravitational wave, which gives rise to combine them in one gravito-electromagnetic wave quantity in an alternative number system using geometric algebra. Note that for this kind of problem, the FEM is maybe not the right choice, because the scale of relativistic effects may differs in a large scale from the size of the problem domain.
- In terms of special relativity, the subspaces which contain the complex-valued electric and magnetic field, respectively, might be reformulated as four-vectors.
- Multiphysics couplings are conceivable as extensions of the bicomplex concept in order to consider other physics or to build up hybrid methods.

By adjusting the proposed bicomplex structure in an appropriate way, other analytical approaches and numerical techniques might be reformulated with advantages as well.

Appendices

The appendices include auxiliary material regarding derivations of presented equations on the one side, and some enhancements of the discussed content on the other side. At first, appropriate Green's identities for consideration of boundary terms in FEM are introduced in appendix A. This is followed by vector identities and integral theorems in appendix B. To extend the presented discretization procedure based on brick elements, shape functions on tetrahedral elements of first order are discussed in appendix C. Afterwards, the bicomplex equation is classified based on the Maxwell system in appendix D. At last, the subject of stabilization is briefly addressed in appendix E and a guideline for stabilizing the bicomplex FEM is given in appendix F.

A Green's Identities

According to [143], there are five commonly used Green's theorems. Two of them are related to scalar quantities, further two consider vector quantities and one handles hybrid forms of both scalar and vector quantities.

Regarding variational formulations discussed in section 3.3, the first and second vector Green's theorems are convenient for the generation of the weak forms of the ordinary Helmholtz equations and the bicomplex-valued Pseudo-Helmholtz equation, respectively. They represent the operator switch to avoid double derivatives of the generalized vector quantities \mathbf{a} and \mathbf{b} . In general, this operator switch generates additional boundary terms, which are used for considering boundary terms in FEM.

The first vector Green's theorem reads as

$$\iiint_{\Omega} [(\nabla \times \mathbf{a}) \cdot (\nabla \times \mathbf{b}) - \mathbf{a} \cdot (\nabla \times \nabla \times \mathbf{b})] d\Omega = \oint_{\partial\Omega=A} [\mathbf{a} \times \nabla \times \mathbf{b}] \cdot d\mathbf{A}, \quad (\text{A.1})$$

where $\partial\Omega = A$ represents a general boundary of the manifold Ω . The second vector Green's theorem is

$$\iiint_{\Omega} [\mathbf{b} \cdot (\nabla \times \nabla \times \mathbf{a}) - \mathbf{a} \cdot (\nabla \times \nabla \times \mathbf{b})] d\Omega = \oint_{\partial\Omega=A} [\mathbf{a} \times \nabla \times \mathbf{b} - \mathbf{b} \times \nabla \times \mathbf{a}] \cdot d\mathbf{A}. \quad (\text{A.2})$$

Contrary to the first vector Green's theorem (A.1), both curl operators, which act on \mathbf{b} , are moved to \mathbf{a} . Both vector Green's theorems (A.1) and (A.2) can be derived from the generalized Stokes theorem (2.34) presented in section 2.4, by using the divergence theorem (B.5), see later on in appendix B. A substitution of $\mathbf{a} = \mathbf{b} \times \nabla \times \mathbf{c}$ in the divergence theorem (B.5) yields

$$\iiint_{\Omega} [\nabla \cdot (\mathbf{b} \times \nabla \times \mathbf{c})] d\Omega = \oint_{\partial\Omega=A} [\mathbf{b} \times \nabla \times \mathbf{c}] \cdot d\mathbf{A}. \quad (\text{A.3})$$

After applying the vector identity (B.2) of appendix B to the LHS, (A.1) follows.

If one applies (B.2) from appendix B again to the second term of the LHS in (A.1) and transfers one term by the use of (B.5) from appendix B to the RHS of (A.1), (A.2) is revealed.

B Vector Identities and Integral Theorems

The following four vector identities (see e.g. [142]) for three-dimensional Cartesian coordinates are presented by means of the generalized scalar quantity ψ and vector quantities \mathbf{a} , \mathbf{b} and \mathbf{c} as

$$\nabla \times (\nabla \times \mathbf{a}) = \nabla (\nabla \cdot \mathbf{a}) - \nabla^2 \mathbf{a}, \quad (\text{B.1})$$

$$\nabla \cdot (\mathbf{a} \times \mathbf{b}) = \mathbf{b} \cdot (\nabla \times \mathbf{a}) - \mathbf{a} \cdot (\nabla \times \mathbf{b}), \quad (\text{B.2})$$

$$\mathbf{a} \times (\mathbf{b} \times \mathbf{c}) = (\mathbf{a} \cdot \mathbf{c}) \mathbf{b} - (\mathbf{a} \cdot \mathbf{b}) \mathbf{c}, \quad (\text{B.3})$$

$$\nabla \times (\psi \mathbf{a}) = \psi (\nabla \times \mathbf{a}) + (\nabla \psi) \times \mathbf{a}. \quad (\text{B.4})$$

Several relevant integral theorems are listed below, which are all special cases of the generalized Stokes' theorem (2.34) discussed in section 2.4. By the use of the following three integral theorems, the behavior of a vector field, which is defined on a manifold Ω , can be expressed by the behavior of that vector field at the boundary of Ω (see also Fig. B1 below). It is assumed that Ω is a subset of \mathbb{R}^3 . The first one is the divergence (or: Gauss's [142]) theorem, which reads as

$$\iiint_{\Omega} [\nabla \cdot \mathbf{a}] d\Omega = \oiint_{\partial\Omega=A} \mathbf{a} \cdot d\mathbf{A}, \quad (\text{B.5})$$

where \mathbf{n} is the surface normal of the generalized boundary A and $d\mathbf{A}$ is the corresponding differential surface element. The second one is Stokes' theorem of vector calculus [143]

$$\iint_A [\nabla \times \mathbf{a}] \cdot d\mathbf{A} = \oint_{\partial A=s} \mathbf{a} \cdot ds, \quad (\text{B.6})$$

where s describes the generalized boundary contour of A and ds is the corresponding differential line element. Finally, the fundamental theorem of calculus [214], based on one coordinate x , is

$$\int_c^d q(x) dx = Q(d) - Q(c). \quad (\text{B.7})$$

It states that the difference of the antiderivatives $Q(d)$ and $Q(c)$ is equal to the value of the integral over the function $q(x)$ itself. Note that both (B.5) and (B.6) handle vector quantities, whereas (B.7) considers scalar quantities. These integral theorems are depicted below in Fig. B1.

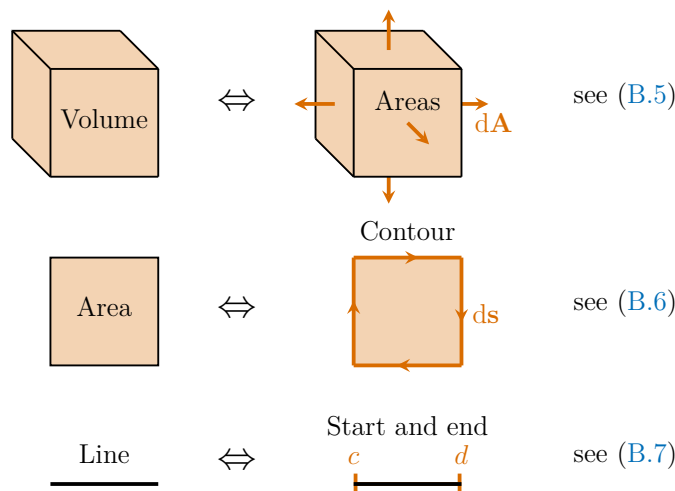


Figure B1 Visualization of integral theorems as important special cases of the generalized Stokes' theorem (2.34), see section 2.4. Note that on the top right, the orange-colored objects indicate the surface of the manifold $\partial\Omega$, whereas on the top left, the volume Ω is highlighted.

C Derivation of Tetrahedral Shape Functions

This appendix presents an extension of the discussion regarding the relation of the brick finite element in section 3.5 to the tetrahedral finite element. The construction of the element matrices is analytically done in accordance to [142]. Regarding the edge numbering, the convention in [9] is used. Here, the four-node version of the tetrahedral element is used, which is also known as linear order. The normalized tetrahedral finite element is shown below in Fig. C1.

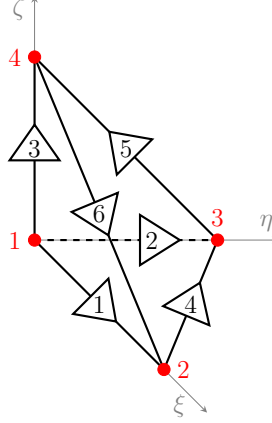


Figure C1 DOF numbering of tetrahedral element, where edges and nodes are considered.

Edge DOFs and their orientation are drawn in black, whereas nodal DOFs are red-marked. In contrast to the brick element, the transformation from global to local coordinates and vice versa is done by the use of the Jacobian matrix $[J]$ through the so-called Piola mappings. These mappings are done in a common way and will not be repeated here, details are given in [9]. As assumed in section 3.5, the global coordinates are x, y, z and the local coordinates are ξ, η, ζ . Following [9], the 3D edge shape functions for the tetrahedral finite element are defined as

$$\begin{aligned}
 N_1^e &= \begin{pmatrix} 1 - \zeta - \eta \\ \xi \\ \xi \end{pmatrix}, & N_2^e &= \begin{pmatrix} \eta \\ 1 - \zeta - \xi \\ \eta \end{pmatrix}, \\
 N_3^e &= \begin{pmatrix} \zeta \\ \zeta \\ 1 - \eta - \xi \end{pmatrix}, & N_4^e &= \begin{pmatrix} -\eta \\ \xi \\ 0 \end{pmatrix}, \\
 N_5^e &= \begin{pmatrix} 0 \\ -\zeta \\ \eta \end{pmatrix}, & N_6^e &= \begin{pmatrix} \zeta \\ 0 \\ -\xi \end{pmatrix}.
 \end{aligned} \tag{C.1}$$

In order to evaluate the elemental MASS matrix, the STIFF matrix and the CONV matrix for the tetrahedral finite element, the topological derivatives of the shape functions in (C.1) are suitable. Again, they can be evaluated by applying the 3D-curl on this shape functions, see e.g. [9] or [142]. In order to achieve a higher accuracy compared to the brick elements, an analytical integration is applied here. The elemental matrices for first order tetrahedral elements are oriented on [142] for the MASS matrix and the STIFF matrix, and adapted in the case of the CONV matrix. In a similar use to (3.11) in section 3.5, the elemental MASS matrix is used for both FEM formulations, the complex-valued Helmholtz equation (3.5) and the bicomplex-valued Pseudo-Helmholtz equation (3.6), see section 3.3 for both equations. All matrix entries can be derived straightforwardly in accordance to the procedure reported in [142]. Below, all necessary elemental matrices for the first order tetrahedral element are shown. At first, $\text{MASS}_{\text{Tetra}}$ reads as

$$\text{MASS}_{\text{Tetra}} = \frac{1}{120 \det([J])} \cdot \begin{pmatrix} M_{11} & M_{12} & M_{13} & M_{14} & M_{15} & M_{16} \\ & M_{22} & M_{23} & M_{24} & M_{25} & M_{26} \\ & & M_{33} & M_{34} & M_{35} & M_{36} \\ & & & M_{44} & M_{45} & M_{46} \\ & \text{symm.} & & & M_{55} & M_{56} \\ & & & & & M_{66} \end{pmatrix},$$

where

$$M_{11} = (l_1^e)^2 \quad (2 f_{22} - 2 f_{12} + 2 f_{11}),$$

$$M_{12} = (l_1^e) (l_2^e) \text{sign}_1 \text{sign}_2 \quad (2 f_{23} - f_{21} - f_{13} + f_{11}),$$

$$M_{13} = (l_1^e) (l_3^e) \text{sign}_1 \text{sign}_3 \quad (2 f_{24} - f_{21} - f_{14} + f_{11}),$$

$$M_{14} = (l_1^e) (l_4^e) \text{sign}_1 \text{sign}_4 \quad (f_{23} - f_{22} - 2 f_{13} + f_{12}),$$

$$M_{15} = (l_1^e) (l_5^e) \text{sign}_1 \text{sign}_5 \quad (f_{24} - f_{23} - f_{14} + f_{13}),$$

$$M_{16} = (l_1^e) (l_6^e) \text{sign}_1 \text{sign}_6 \quad (f_{22} - f_{24} - f_{12} + 2 f_{14}),$$

$$M_{22} = (l_2^e)^2 \quad (2 f_{33} - 2 f_{13} + 2 f_{11}),$$

$$M_{23} = (l_2^e) (l_3^e) \text{sign}_2 \text{sign}_3 \quad (2 f_{34} - f_{13} - f_{14} + f_{11}),$$

$$M_{24} = (l_2^e) (l_4^e) \text{sign}_2 \text{sign}_4 \quad (f_{33} - f_{23} - f_{13} + 2 f_{12}),$$

$$M_{25} = (l_2^e) (l_5^e) \text{sign}_2 \text{sign}_5 \quad (f_{34} - f_{33} - 2 f_{14} + f_{13}),$$

$$M_{26} = (l_2^e) (l_6^e) \text{sign}_2 \text{sign}_6 \quad (f_{32} - f_{34} - f_{12} + f_{14}),$$

$$M_{33} = (l_3^e)^2 \quad (2 f_{44} - 2 f_{14} + 2 f_{11}),$$

$$M_{34} = (l_3^e) (l_4^e) \text{sign}_3 \text{sign}_4 \quad (f_{34} - f_{24} - f_{13} + f_{12}),$$

$$M_{35} = (l_3^e) (l_5^e) \text{sign}_3 \text{sign}_5 \quad (f_{44} - f_{43} - f_{14} + 2 f_{13}),$$

$$M_{36} = (l_3^e) (l_6^e) \text{sign}_3 \text{sign}_6 (f_{42} - f_{44} - 2 f_{12} + f_{14}),$$

$$M_{44} = (l_4^e)^2 (2 f_{33} - 2 f_{23} + 2 f_{22}),$$

$$M_{45} = (l_4^e) (l_5^e) \text{sign}_4 \text{sign}_5 (f_{34} - f_{33} - 2 f_{24} + f_{23}),$$

$$M_{46} = (l_4^e) (l_6^e) \text{sign}_4 \text{sign}_6 (f_{32} - 2 f_{34} - f_{22} + f_{24}),$$

$$M_{55} = (l_5^e)^2 (2 f_{44} - 2 f_{43} + 2 f_{33}),$$

$$M_{56} = (l_5^e) (l_6^e) \text{sign}_5 \text{sign}_6 (f_{42} - f_{44} - 2 f_{32} + f_{34}),$$

$$M_{66} = (l_6^e)^2 (2 f_{22} - 2 f_{42} + 2 f_{44}). \tag{C.2}$$

The Jacobian matrix is denoted by $[J]$ and sign_p stands for the local sign of the edge p , see again [9] for details. Here, the auxiliary parameters f_{ij} and b_i^e, c_i^e, d_i^e are used, which are defined according to [142] with respect to the global coordinates x_i^e, y_i^e, z_i^e as

$$f_{ij} = b_i^e b_j^e + c_i^e c_j^e + d_i^e d_j^e,$$

where

$$b_1^e = y_2^e (z_4^e - z_3^e) - y_3^e (z_4^e - z_2^e) + y_4^e (z_3^e - z_2^e),$$

$$b_2^e = -y_1^e (z_4^e - z_3^e) + y_3^e (z_4^e - z_1^e) - y_4^e (z_3^e - z_1^e),$$

$$b_3^e = y_1^e (z_4^e - z_2^e) - y_2^e (z_4^e - z_1^e) + y_4^e (z_2^e - z_1^e),$$

$$b_4^e = -y_1^e (z_3^e - z_2^e) + y_2^e (z_3^e - z_1^e) - y_3^e (z_2^e - z_1^e),$$

$$c_1^e = -x_2^e (z_4^e - z_3^e) + x_3^e (z_4^e - z_2^e) - x_4^e (z_3^e - z_2^e),$$

$$c_2^e = x_1^e (z_4^e - z_3^e) - x_3^e (z_4^e - z_1^e) + x_4^e (z_3^e - z_1^e),$$

$$c_3^e = -x_1^e (z_4^e - z_2^e) + x_2^e (z_4^e - z_1^e) - x_4^e (z_2^e - z_1^e),$$

$$c_4^e = x_1^e (z_3^e - z_2^e) - x_2^e (z_3^e - z_1^e) + x_3^e (z_2^e - z_1^e),$$

$$\begin{aligned}
d_1^e &= x_2^e (y_4^e - y_3^e) - x_3^e (y_4^e - y_2^e) + x_4^e (y_3^e - y_2^e), \\
d_2^e &= -x_1^e (y_4^e - y_3^e) + x_3^e (y_4^e - y_1^e) - x_4^e (y_3^e - y_1^e), \\
d_3^e &= x_1^e (y_4^e - y_2^e) - x_2^e (y_4^e - y_1^e) + x_4^e (y_2^e - y_1^e), \\
d_4^e &= -x_1^e (y_3^e - y_2^e) + x_2^e (y_3^e - y_1^e) - x_3^e (y_2^e - y_1^e).
\end{aligned} \tag{C.3}$$

As discussed in section 3.5 (see especially Fig. 3.9), the STIFF matrix represents the first term of the Helmholtz equation (3.5) shown in section 3.3. The counterpart to (3.12), discussed in section 3.5 and valid for tetrahedral elements (see [142] for details), is

$$\text{STIFF}_{\text{Tetra}} = \frac{2}{3 (\det([J]))^3} \cdot \begin{pmatrix} S_{11} & S_{12} & S_{13} & S_{14} & S_{15} & S_{16} \\ & S_{22} & S_{23} & S_{24} & S_{25} & S_{26} \\ & & S_{33} & S_{34} & S_{35} & S_{36} \\ & & & S_{44} & S_{45} & S_{46} \\ \text{symm.} & & & & S_{55} & S_{56} \\ & & & & & S_{66} \end{pmatrix},$$

where

$$\begin{aligned}
S_{ij} &= (l_i^e) (l_j^e) \text{sign}_i \text{sign}_j \left[(c_{i1}^e d_{i2}^e - d_{i1}^e c_{i2}^e) (c_{j1}^e d_{j2}^e - d_{j1}^e c_{j2}^e) + \right. \\
&\quad \left. (d_{i1}^e b_{i2}^e - b_{i1}^e d_{i2}^e) (d_{j1}^e b_{j2}^e - b_{j1}^e d_{j2}^e) + (b_{i1}^e c_{i2}^e - c_{i1}^e b_{i2}^e) (b_{j1}^e c_{j2}^e - c_{j1}^e b_{j2}^e) \right].
\end{aligned} \tag{C.4}$$

In this context, the first index denotes the local edge number, whereas the second index implies the (first or second) node of this edge. Lastly, the CONV matrix is needed for the Pseudo-Helmholtz equation (3.6), see section 3.3. The corresponding matrix to (3.13) (see section 3.5) is

$$\text{CONV}_{\text{Tetra}} = \frac{1}{12 (\det([J]))^2} \cdot \begin{pmatrix} C_{11} & C_{12} & C_{13} & C_{14} & C_{15} & C_{16} \\ & C_{22} & C_{23} & C_{24} & C_{25} & C_{26} \\ & & C_{33} & C_{34} & C_{35} & C_{36} \\ \text{anti-} & & & C_{44} & C_{45} & C_{46} \\ \text{symm.} & & & & C_{55} & C_{56} \\ & & & & & C_{66} \end{pmatrix},$$

where

$$\begin{aligned}
C_{ij} &= (l_i^e) (l_j^e) \text{sign}_i \text{sign}_j \left[(c_{i1}^e d_{i2}^e - d_{i1}^e c_{i2}^e) (b_{j1}^e - b_{j2}^e) + \right. \\
&\quad \left. (d_{i1}^e b_{i2}^e - b_{i1}^e d_{i2}^e) (c_{j1}^e - c_{j2}^e) + (b_{i1}^e c_{i2}^e - c_{i1}^e b_{i2}^e) (d_{j1}^e - d_{j2}^e) \right].
\end{aligned} \tag{C.5}$$

D Classification of Pseudo-Helmholtz Equation

According to [37], the general system of Vekua equations is

$$\begin{aligned} u'_x - v'_y &= a(x, y)u + b(x, y)v + f(x, y) \\ u'_y + v'_x &= c(x, y)u + d(x, y)v + g(x, y), \end{aligned} \tag{D.1}$$

where the superscript "′" indicates a derivative with respect to the subscript. The mathematical classification of the first two equations of the Maxwell system (2.7a, 2.7b) (see section 2.2.2) by assuming general time dependency into the Vekua equation system (D.1) allows for an analytical investigation of possible solutions of this system. Despite the fact that this thesis focuses rather on the construction of the bicomplex concept as well as its numerical implementation in FEM than on the aforementioned task, this classification is only mentioned briefly in this appendix.

Since the bicomplex-valued Pseudo-Helmholtz equation is isomorphic to the Maxwell system, it is a Vekua-type equation system (see e.g. [70] or [153] for details). By neglecting the RHS of (D.1), the appropriate system of Vekua equations (D.1) for the bicomplex Pseudo-Helmholtz equation (2.6) of section 2.2.2 is

$$\begin{aligned} u'_x - v'_y &= 0 \\ u'_y + v'_x &= 0, \end{aligned} \tag{D.2}$$

which is valid for the absence of current densities and space charge densities. With the use of Maxwell's equations (2.7a, 2.7b) for general time dependency by using the nomenclature of (D.2), (2.7a, 2.7b) are rewritten to

$$\begin{aligned} \varepsilon E'_t - H'_x &= 0 \\ E'_x + \mu H'_t &= 0, \end{aligned} \tag{D.3}$$

where the subscript "x" intends a spatial derivative of generalized dimension (i.e. the curl operator in (2.7a, 2.7b), see section 2.2.2) and the subscript "t" indicates a temporal derivative, which is one-dimensional as a timeline. The system (D.3) is nearly the same as the time-harmonic Maxwell system (2.7a, 2.7b) presented in section 2.2.2, but with general time dependency, since no complex vector amplitudes are used. According to [37], the solutions of (D.2) are analytic functions¹, which is obvious since the derivatives in (D.2) have to be applicable in every point. The corresponding weak form covered by FEM do not need this global property of differentiability, rather only single finite elements have to fulfill it (this explains why the FEM can handle problems of general topology, see the topological discussions in sections 2.4.6 and 2.4.7). Note that the complex vector amplitudes – in order to express the time derivative as in Maxwell's equations (2.7a, 2.7b) – are not introduced until now.

In contrast, the consideration of current densities and electric flux densities would lead to generalized analytic functions as solutions. Following [37], the Pseudo-Helmholtz equation is quadrature-solvable, which means it is finite-integrable (see also the definition of the Lebesgue space of square-integrable functions (2.16) in section 2.3.1). Therefore, the field quantities might be expressed through the integral of a tensor product, which allows the use of the FEM.

As an alternative to the presented bicomplex approach, a continuative time-dependent quaternionic reformulation of Maxwell's equations in terms of inhomogeneous material distribution is reported in [153]. There, current densities and electric flux densities are considered. In this case, the solutions are not finite-integrable, so the bicomplex FEM would have to be modified in a suitable manner. The consideration of this case is outside the scope of this thesis. For further reading on the subject of Vekua equations in terms of the Maxwell system, see e.g. [70] or [148].

¹Analytic functions are real differentiable at every point.

E Stabilization Technique for Bicomplex-valued Convection-Reaction Equation

Caused by the 1st-order spatial derivative, the Pseudo-Helmholtz equation (2.6) presented in section 2.2.2 and certainly as well its inhomogeneous counterpart (2.22) discussed in section 2.3.2 contain a convective term, which contributes to the FEM system matrix. When this term is dominant compared to the reactive term for one or more elements, the system matrix is no longer positive definite². In the context of variational formulations, this problem is known as non-self-adjoint. The solution is obtained by seeking in general a stationary point instead of a minimum of the corresponding functional. Thereby, the property of superconvergence is not given and – as a consequence – no error bounds can be estimated.

To handle also material combinations where this phenomenon arises, a suitable stabilization technique can provide a solution. According to [107], the symmetry of a linear operator is related to a bilinear form. A problem which is non-self-adjoint can be symmetrized by transforming the problem into another one with the same solutions, or by changing the corresponding bilinear form (or similar form). By following the second approach, the FEM test functions are modified by adding an appropriate amount of numerical diffusion to them, which leads to an approximated symmetrization of the problem [176]. According to [92], there are many different ways to do this, such as Streamline Upwind Petrov Galerkin (SUPG), Galerkin / Least-Squares (GaLS) or Unusual Stabilized Finite Element Method (USFEM).

A mixed time-harmonic formulation of Maxwell's equations with GaLS stabilization is reported in [85]. A further reference to linear stabilization of first order PDEs in the topic of heat transfer is e.g. [130].

F Guideline to Stabilize the Bicomplex FEM

As mentioned in section 2.3.2, a direct implementation of a material inhomogeneity is not possible for the bicomplex-formulated continuous FEM. Therefore, only a guideline is described in this appendix, which is assumed to be applicable in a discontinuous FEM environment. In section 2.3.2, (2.32) was derived:

$$\int_{\Omega} \left| \left[\nabla \underline{\varphi}_w \cdot \underline{\varphi}_u^+ - \frac{\nabla \sqrt{Z}}{\sqrt{Z}} \underline{\varphi}_w^+ \cdot \underline{\varphi}_u^+ - \text{ij} k \underline{\varphi}_w^+ \cdot \underline{\varphi}_u^+ \right] \right|_{\text{j}} d\Omega = 0.$$

The implementation of the second term of the LHS is assumed as follows. Note that this procedure considers smooth as well as sharp changes of the permittivity. The gradient of the square root of the wave impedance Z is calculated as the numerical derivative, which is multiplied by an ordinary MASS matrix after normalization. An alternative way to numerically consider sharp steps with the use of Heaviside step functions is presented in [194]. For the analytical handling of material step discontinuities, see e.g. [238].

Next, the SUPG stabilization technique mentioned previously in appendix E is intended to be applied. At least one additional term – which acts as a numerical diffusion – has to be added to (2.32) in general.

²The definiteness of a square matrix is necessary for the uniqueness of the solution. Non-definiteness leads to spurious oscillations, the solution becomes numerically unstable.

By enhancing the space of test functions to the whole equation (which leads to i-conjugation) as similarly done in [85], the SUPG-stabilized weak form of (2.22) by using nodal finite elements for the 1D-case is constructed as

$$\begin{aligned} & \int_{\Omega} \left| \left[\nabla \underline{\varphi}_u \cdot \underline{\varphi}_w^+ - \frac{\nabla \sqrt{Z}}{\sqrt{Z}} \underline{\varphi}_u^+ \cdot \underline{\varphi}_w^+ - \text{ij} k \underline{\varphi}_u^+ \cdot \underline{\varphi}_w^+ \right] \right. \\ & + \tau_{\text{STAB}} \left[\nabla \underline{\varphi}_u \cdot \nabla \underline{\varphi}_w^+ + \left(\frac{\nabla \sqrt{Z}}{\sqrt{Z}} \right)^2 \underline{\varphi}_u^+ \cdot \underline{\varphi}_w^+ \right. \\ & \left. \left. + k^2 \underline{\varphi}_u^+ \cdot \underline{\varphi}_w^+ \right] \right|_{\text{j}} d\Omega = 0. \end{aligned} \quad (\text{F.1})$$

As assumed in section 2.3.2, $\underline{\varphi}_u$ are bicomplex-valued basis functions and $\underline{\varphi}_w$ are bicomplex-valued test functions. In (F.1), the three stabilization terms are multiplied by an appropriate element size-depending stabilization factor τ_{STAB} , which is usually constructed by weighting the element size in 1D (or equivalently the characteristic length in 2D and 3D), see e.g. [242]. Another example is discussed in [71], where a stabilization factor for a mixed electro- and magnetostatic formulation is derived.

Note that the construction of τ_{STAB} is in general heuristic. Only for specific examples, it is possible to derive it from the analytical solution, as e.g. for the coth-function in [94].

The classification into stable and unstable finite elements is done by evaluating the Damköhler number D_a (see e.g. [129]), which is defined as the ratio of the modulus of reactive terms to convective terms, multiplied by the element size h_{ele} . Based on (2.32) from section 2.3.2, this results in

$$D_a = \frac{\int_{\Omega} \left| -\frac{\nabla \sqrt{Z}}{\sqrt{Z}} \underline{\varphi}_u^+ \cdot \underline{\varphi}_w^+ - \text{ij} k \underline{\varphi}_u^+ \cdot \underline{\varphi}_w^+ \right|_{\text{j}} d\Omega}{\int_{\Omega} \left| \nabla \underline{\varphi}_u \cdot \underline{\varphi}_w^+ \right|_{\text{j}} d\Omega} h_{\text{ele}}. \quad (\text{F.2})$$

The consideration of D_a is appropriate for FEM BC, since (2.32) includes only convective and reactive terms. In the case of complex-valued Helmholtz FEM in (2.20) (see section 2.3.1), the decision if a finite element is stable or not is more complicated, because of the additional diffusive term (first term on the LHS).

Bibliography

- [1] M. Abramowitz and I. A. Stegun, *Handbook of Mathematical Functions: With Formulas, Graphs, and Mathematical Tables*. Washington D.C., USA: National Bureau of Standards, Applied Mathematics Series 55, 10th Printing, 1972.
(Page 77).
- [2] J. H. Adler, C. Cavanaugh, X. Hu, and L. T. Zikatanov, “A Finite-Element Framework for a Mimetic Finite-Difference Discretization of Maxwell’s Equations,” *SIAM Journal on Scientific Computing*, vol. 43, no. 4, pp. A2638–A2659, 2021.
(Page 30, 30).
- [3] R. Agarwal, M. Goswami, and R. P. Agarwal, “Sumudu Transform in Bicomplex Space and its Applications,” *Annals of Applied Mathematics (AAM)*, vol. 33, no. 3, pp. 239–253, 2017.
(Page 6).
- [4] R. Agarwal, M. Goswami, R. P. Agarwal, K. Kesa, V. Kamma, and D. Baleanu, “Solution of Maxwell’s Wave Equations in Bicomplex Space,” *Romanian Journal of Physics*, vol. 62, no. 5, Art. No. 115, 2017.
(Pages 6, 15).
- [5] E. Ahusborde, M. Azaiez, J.-P. Caltagirone, M. Gerritsma, and A. Lemoine, “Discrete Hodge Helmholtz Decomposition,” *Monografías Matemáticas García de Galdeano*, vol. 39, pp. 1–10, 2014.
(Page 42).
- [6] C. Amrouche, C. Bernardi, M. Dauge, and V. Girault, “Vector Potentials in Three-dimensional Non-smooth Domains,” *Mathematical Methods in the Applied Sciences*, vol. 21, no. 9, pp. 823–864, 1998.
(Page 49).
- [7] H. Anastassiou, P. E. Atlamazoglou, and D. Kaklamani, “Application of Bicomplex (Quaternion) Algebra to Fundamental Electromagnetics: A Lower Order Alternative to the Helmholtz Equation,” *IEEE Transactions on Antennas and Propagation*, vol. 51, no. 8, pp. 2130–2136, 2003.
(Pages 1, 6, 6, 10, 12, 13, 14, 15, 15, 18).
- [8] D. A. Angus, “The One-Way Wave Equation: A Full-Waveform Tool for Modeling Seismic Body Wave Phenomena,” *Surveys in Geophysics*, vol. 35, no. 2, pp. 359–393, 2014.
(Page 55, 55).
- [9] I. Anjam and J. Valdman, “Fast MATLAB assembly of FEM matrices in 2D and 3D: Edge elements,” *Applied Mathematics and Computation*, vol. 267, pp. 252–263, 2015.
(Pages 37, 111, 111, 111, 111, 113).
- [10] ANSYS® Electronics Desktop™, *Software*. Canonsburg, Pennsylvania, USA: ANSYS, Inc., 2020.
(Page 64, 64).
- [11] P. L. Arlett, A. K. Bahrani, and O. C. Zienkiewicz, “Application of finite elements to the solution of Helmholtz’s equation,” *Proceedings of the Institution of Electrical Engineers*, vol. 115, no. 12, pp. 1762–1766, 1968.
(Page 15).
- [12] D. Arndt, W. Bangerth, B. Blais, M. Fehling, R. Gassmüller, T. Heister, L. Heltai, U. Köcher, M. Kronbichler, M. Maier, P. Munch, J.-P. Pelteret, S. Proell, K. Simon, B. Turcksin, D. Wells, and J. Zhang, “The deal.II Library, Version 9.3,” *Journal of Numerical Mathematics*, vol. 29, no. 3, pp. 171–186, 2021.
(Page 64).
- [13] D. N. Arnold, *Analysis and Numerics of Partial Differential Equations*, 1st ed. F. Brezzi, P. C. Franzone, U. Gianazza, and G. Gilardi (Eds.), Milano, Italy: Springer-Verlag Italia, Springer INdAM Series 4, Ch. Spaces of Finite Element Differential Forms, 2013.
(Pages 29, 68).

- [14] D. N. Arnold, R. S. Falk, and R. Winther, “Finite element exterior calculus, homological techniques, and applications,” *Acta Numerica*, Cambridge University Press, vol. 15, pp. 1–155, 2006.
(Page 38).
- [15] D. N. Arnold, R. S. Falk, and R. Winther, “Finite element exterior calculus: From Hodge theory to numerical stability,” *Bulletin of the American Mathematical Society*, vol. 47, no. 2, pp. 281–354, 2010.
(Page 31).
- [16] J. W. Arthur, *Understanding Geometric Algebra for Electromagnetic Theory*. Hoboken, New Jersey, USA: John Wiley & Sons, IEEE Press Series on Electromagnetic Wave Theory, 2011.
(Pages 13, 31).
- [17] F. Assous and E. Sonnendrücker, “Joly–Mercier boundary condition for the finite element solution of 3D Maxwell equations,” *Mathematical and Computer Modelling*, vol. 51, no. 7, pp. 935–943, 2010.
(Pages 72, 72, 76).
- [18] B. Auchmann and S. Kurz, “A Geometrically Defined Discrete Hodge Operator on Simplicial Cells,” *IEEE Transactions on Magnetics*, vol. 42, no. 4, pp. 643–646, 2006.
(Page 31).
- [19] B. Auchmann and S. Kurz, “De Rham currents in discrete electromagnetism,” *COMPEL - The International Journal for Computation and Mathematics in Electrical and Electronic Engineering*, vol. 26, no. 3, pp. 743–757, 2007.
(Pages 29, 31, 32, 34).
- [20] S. Axler, *Linear Algebra Done Right*, 3rd ed. Cham, Switzerland: Springer International Publishing AG, Undergraduate Texts in Mathematics, 2015.
(Page 7).
- [21] I. M. Babuška and S. A. Sauter, “Is the Pollution Effect of the FEM Avoidable for the Helmholtz Equation Considering High Wave Numbers?” *SIAM Journal on Matrix Analysis and Applications*, vol. 34, no. 6, pp. 2392–2423, 1997.
(Page 91).
- [22] E. A. Badea, M. E. Everettz, G. A. Newman, and O. Biro, “Finite-element analysis of controlled-source electromagnetic induction using Coulomb-gauged potentials,” *Geophysics*, vol. 66, no. 3, pp. 786–799, 2001.
(Page 49).
- [23] J. Baek, H. Jeon, G. Kim, and S. Han, “Visualizing Quaternion Multiplication,” *IEEE Access*, vol. 5, pp. 8948–8955, 2017.
(Page 52).
- [24] C. Bambi, *Introduction to General Relativity: A Course for Undergraduate Students of Physics*. Singapore, Singapore: Springer Nature Singapore Pte Ltd., Undergraduate Lecture Notes in Physics (ULNP), 2018.
(Page 50).
- [25] L. Barba, M. Hoffmann, M. Korman, and A. Pilz, “Convex Hulls in Polygonal Domains,” in *16th Scandinavian Symposium and Workshops on Algorithm Theory (SWAT 2018)*, D. Eppstein, Ed., vol. 101, Malmö, Sweden, pp. 8:1–8:13, 2018.
(Page 67, 67).
- [26] S. M. Barnett, “Maxwellian theory of gravitational waves and their mechanical properties,” *New Journal of Physics*, vol. 16, no. 2, Art. No. 023027, 2014.
(Pages 59, 60).
- [27] H. Beriot and M. Tournour, “A Review of Stabilized FEM for Helmholtz Equation,” in *Conference Noise and Vibration: Emerging methods (NOVEM 2009)*, Oxford, UK, Art. No. 85, pp. 1–12, 2009.
(Page 13).
- [28] P. B. Bochev and J. M. Hyman, *Compatible Spatial Discretizations*, 1st ed. D. N. Arnold, P. B. Bochev, R. B. Lehoucq, R. A. Nicolaides, and M. Shashkov (Eds.), New York, USA: Springer-Verlag New York, The IMA Volumes in Mathematics and its Applications (IMA, volume 142), Ch. Principles of Mimetic Discretizations of Differential Operators, 2006.
(Pages 20, 29, 30).
- [29] N. Bootland, V. Dolean, P. Jolivet, F. Nataf, S. Operto, and P.-H. Tournier, “Several ways to achieve robustness when solving wave propagation problems,” arXiv:2103.06025v2, Numerical Analysis, 2021, Accessed: 04.07.2022. [Online]. Available: <https://arxiv.org/pdf/2103.06025.pdf>
(Page 64).

- [30] D. Borthwick, *Introduction to Partial Differential Equations*. Cham, Switzerland: Springer International Publishing AG, Universitext, 2018.
(Page 13).
- [31] A. Bossavit, “Magnetostatic problems in multiply connected regions: some properties of the curl operator,” *IEE Proceedings A (Physical Science, Measurement and Instrumentation, Management and Education, Reviews)*, vol. 135, no. 3, pp. 179–187, 1988.
(Page 39).
- [32] A. Bossavit, “Whitney forms: a class of finite elements for three-dimensional computations in electromagnetism,” *IEE Proceedings A (Physical Science, Measurement and Instrumentation, Management and Education, Reviews)*, vol. 135, no. 8, pp. 493–500, 1988.
(Page 5).
- [33] A. Bossavit, “Differential geometry for the student of numerical methods in electromagnetism,” Clamart, France: Électricité de France, Études et Recherches, 1991, Accessed: 04.07.2022. [Online]. Available: <https://www.researchgate.net/publication/200018385>
(Page 23).
- [34] A. Bossavit, *Computational Electromagnetism. Variational Formulation, Complementarity, Edge Elements*. San Diego, California, USA: Vol. 2 of Electromagnetism Series, Academic Press, 1998.
(Page 37).
- [35] A. Bossavit, “The Discrete Hodge Operator in Electromagnetic Wave Propagation Problems,” *5th International Conference on Mathematical and Numerical Aspects of Wave Propagation, SIAM*, pp. 753–759, 2000.
(Page 30).
- [36] P. Bracken, “Some results for the Hodge decomposition theorem in Euclidean three-space,” *International Journal of Contemporary Mathematical Sciences*, vol. 11, no. 4, pp. 155–164, 2016.
(Page 42).
- [37] S. Brsakoska and B. Ilievski, *Two Theorems for the Vekua Equation*. Mathematica Balkanica, New Series vol. 26, fasc. 3–4, 2012.
(Page 115, 115, 115).
- [38] O. Bschorr and H.-J. Raida, “One-Way Wave Equation Derived from Impedance Theorem,” *Acoustics*, vol. 2, no. 1, pp. 164–170, 2020.
(Page 55).
- [39] F. E. Burstall, *Spectral Theory and Geometry*. E. B. Davies and Y. Safarov (Eds.), Cambridge, UK: Cambridge University Press, London Mathematical Society Lecture Note Series (volume 273), Ch. Basic Riemannian geometry, 1999.
(Page 21).
- [40] J. Cantarella, D. DeTurck, and H. Gluck, “Vector Calculus and the Topology of Domains in 3-Space,” *The American Mathematical Monthly*, vol. 109, no. 5, pp. 409–442, 2002.
(Pages 42, 42, 42, 42, 42, 44, 44).
- [41] H. Cartan, *Differential Forms*. Mineola, New York, USA: Dover Publications, 2006.
(Page 22, 22).
- [42] M. Cassier, A. Welters, and G. W. Milton, *Extending the Theory of Composites to Other Areas of Science*. G. W. Milton (Ed.), Salt Lake City, Utah, USA: Milton-Patton Publishers, vol. 1, Ch. 4 - Analyticity of the Dirichlet-to-Neumann map for the time-harmonic Maxwell’s equations, 2016.
(Page 61).
- [43] A. Cayley, “Desiderata and Suggestions: No. 2. The Theory of Groups: Graphical Representation,” *American Journal of Mathematics*, vol. 1, no. 2, pp. 174–176, 1878.
(Page 8).
- [44] M. Cessenat, *Mathematical Methods in Electromagnetism - Linear Theory and Applications*. Singapore, Singapore: World Scientific Publishing Co. Pte. Ltd., Series on Advances in Mathematics for Applied Sciences: Volume 41, 1996.
(Page 37).
- [45] B. C. Chanyal, “Sedenion unified theory of gravi-electromagnetism,” *Indian Journal of Physics*, vol. 88, pp. 1197–1205, 2014.
(Page 10).

- [46] B. C. Chanyal, V. K. Sharma, and O. P. S. Negi, "Octonionic Gravi-Electromagnetism and Dark Matter," *International Journal of Theoretical Physics*, vol. 54, pp. 3516–3532, 2015.
(Page 10).
- [47] J. M. Chappell, S. P. Drake, C. L. Seidel, L. J. Gunn, A. Iqbal, A. Allison, and D. Abbott, "Geometric Algebra for Electrical and Electronic Engineers," *Proceedings of the IEEE*, vol. 102, no. 9, Art. No. 6876131, 2014.
(Page 13).
- [48] C.-H. Chen and Y.-W. Kiang, "A Variational Theory for Wave Propagation in a One-Dimensional Inhomogeneous Medium," *IEEE Transactions on Antennas and Propagation*, vol. 28, no. 6, pp. 762–769, 1980.
(Page 16).
- [49] C. H. Chen and C.-D. Lien, "The Variational Principle for Non-Self-Adjoint Electromagnetic Problems," *IEEE Transactions on Microwave Theory and Techniques*, vol. 28, no. 8, pp. 878–886, 1980.
(Page 17).
- [50] K. Chen, *Matrix Preconditioning Techniques and Applications*. Cambridge, UK: Cambridge University Press, Cambridge Monographs on Applied and Computational Mathematics, 2005.
(Page 79).
- [51] L. Chen, "Finite Element Methods for Maxwell Equations," Irvine, California, USA: Department of Mathematics, University of California, 2020, Accessed: 04.07.2022. [Online]. Available: <https://www.math.uci.edu/~chenlong/226/FEMMaxwell.pdf>
(Pages 37, 62).
- [52] S. C. Chen and W. C. Chew, "Electromagnetic Theory with Discrete Exterior Calculus," *Progress in Electromagnetics Research*, vol. 159, pp. 59–78, 2017.
(Page 30).
- [53] M. V. Cheremisin, "Riemann-Silberstein representation of the complete Maxwell equations set," in *20th General Conference of the Condensed Matter Division (CMD) of the European Physical Society (EPS)*, Prague, Czech Republic, 2004.
(Page 13).
- [54] W. K. Clifford, "Applications of Grassmann's Extensive Algebra," *American Journal of Mathematics*, vol. 1, no. 4, pp. 350–358, 1878.
(Page 8).
- [55] S. R. Cloude, "Lie Groups in Electromagnetic Wave Propagation and Scattering," *Journal of Electromagnetic Waves and Applications*, vol. 6, no. 8, pp. 947–974, 1992.
(Page 12).
- [56] J. Cockle, "On Systems of Quadruple Algebra," *Mechanics' Magazine, Robertson and Co., London, UK*, vol. LI, pp. 197–199, 1849.
(Page 9).
- [57] G. C. Cohen, *Higher-Order Numerical Methods for Transient Wave Equations*, 1st ed. Germany: Springer-Verlag Berlin Heidelberg, Scientific Computation (SCIENTCOMP), 2002.
(Page 17).
- [58] I. Colombaro, J. Font-Segura, and A. Martinez, "Generalized Maxwell equations for exterior-algebra multivectors in (k, n) space-time dimensions," *The European Physical Journal Plus*, vol. 135, Art. No. 305, 2020.
(Page 20).
- [59] G. Comini, S. D. Giudice, and C. Nonino, *Finite Element Analysis In Heat Transfer: Basic Formulation & Linear Problems*. Washington D.C., USA: Taylor & Francis, 1994.
(Page 17).
- [60] COMSOL Multiphysics® Documentation v. 5.5, *S-Parameter Calculations*, COMSOL AB, Stockholm, Sweden, 2019.
(Page 53).
- [61] COMSOL Multiphysics® v. 5.4, *Software*. Stockholm, Sweden: COMSOL AB, 2020.
(Page 64, 64).
- [62] C. B. Crawford, "The physical meaning of the magnetic scalar potential and its use in the design of hermetic electromagnetic coils," *Review of Scientific Instruments*, vol. 92, no. 12, Art. No. 124703, 2021.
(Page 49, 49).

- [63] CST Studio Suite[®], *Software*. Vélizy-Villacoublay, France: Dassault Systèmes, 2020.
(Page 64, 64).
- [64] M. F. Dahl, “Geometric Properties of Electromagnetic Waves,” Ph.D. dissertation, Helsinki University of Technology, Helsinki, Finland, 2007.
(Page 101).
- [65] X. Dai, *Topology of Stratified Spaces*. G. Friedman, E. Hunsicker, A. Libgober, and L. Maxim (Eds.), New York, USA: Cambridge University Press, Ch. An introduction to L^2 cohomology, 2011.
(Page 29, 29).
- [66] P. Daly and J. D. Helps, “Exact finite element solutions to the Helmholtz equation,” *International Journal for Numerical Methods in Engineering*, vol. 6, no. 4, pp. 529–542, 1973.
(Page 15).
- [67] T. Davis, S. Rajamanickam, and W. Sid-Lakhdar, “A survey of direct methods for sparse linear systems,” *Acta Numerica*, vol. 25, pp. 383–566, 2016.
(Page 77).
- [68] T. A. Davis, “Algorithm 832: UMFPACK V4.3 - An Unsymmetric-Pattern Multifrontal Method,” *ACM Transactions on Mathematical Software (TOMS)*, vol. 30, no. 2, pp. 196–199, 2004.
(Page 79).
- [69] C. J. A. Delfinado and H. Edelsbrunner, “An incremental algorithm for Betti numbers of simplicial complexes on the 3-sphere,” *Computer Aided Geometric Design*, vol. 12, no. 7, pp. 771–784, 1995.
(Pages 40, 41, 46).
- [70] B. B. Delgado López, “Quaternionic Vekua Analysis in Domains in \mathbb{R}^3 with Application to Electromagnetic Systems of Equations,” Ph.D. dissertation, Center for Research and Advanced Studies of the National Polytechnic Institute, Mexico City, Mexico, 2018.
(Page 115, 115).
- [71] G. Deliège, E. Rosseel, and S. Vandewalle, “Iterative solvers and stabilisation for mixed electrostatic and magnetostatic formulations,” *Journal of Computational and Applied Mathematics*, vol. 215, no. 2, pp. 348–356, 2008.
(Page 117).
- [72] S. Demir and M. Taşlı, “A compact biquaternionic formulation of massive field equations in gravi-electromagnetism,” *The European Physical Journal Plus*, vol. 126, Art. No. 115, 2011.
(Pages 9, 10, 59).
- [73] M. Desbrun, E. Kanso, and Y. Tong, “Discrete Differential Forms for Computational Modeling,” in *Discrete Differential Geometry*, A. I. Bobenko, J. M. Sullivan, P. Schröder, and G. M. Ziegler, Eds. Basel, Switzerland: Birkhäuser Basel, Oberwolfach Seminars, vol. 38, pp. 287–323, 2008.
(Pages 20, 40, 42).
- [74] R. Descartes, D. E. Smith, and M. L. Latham, *The Geometry of René Descartes: With a Facsimile of the First Edition*. New York, USA: Dover Publications, Inc. New York, 1954.
(Page 9).
- [75] G. A. Deschamps, “Electromagnetics and differential forms,” *Proceedings of the IEEE*, vol. 69, no. 6, pp. 676–696, 1981.
(Pages 20, 21, 23).
- [76] C. Doran and A. Lasenby, *Geometric Algebra for Physicists*. Cambridge, UK: Cambridge University Press, 2003.
(Page 13).
- [77] J. Dressel, K. Y. Bliokh, and F. Nori, “Spacetime algebra as a powerful tool for electromagnetism,” *Physics Reports*, vol. 589, pp. 1–71, 2015.
(Page 13).
- [78] C. Du, C. Szul, A. Manawa, N. Rasekh, R. Guzman, and R. Davidson, “RGB image-based data analysis via discrete Morse theory and persistent homology,” arXiv:1801.09530v1, Computer Vision and Pattern Recognition, 2018, Accessed: 04.07.2022. [Online]. Available: <https://arxiv.org/pdf/1801.09530.pdf>
(Page 41, 41).
- [79] K. Dullemond and K. Peeters, *Introduction to Tensor Calculus*. Durham, UK: Kees Dullemond and Kasper Peeters, 2010.
(Page 9).

- [80] F. J. Dyson, “Feynman’s proof of the Maxwell equations,” *American Journal of Physics*, vol. 58, no. 3, pp. 209–211, 1990.
(Page 3).
- [81] P. Dłotko and R. Specogna, “Efficient Cohomology Computation for Electromagnetic Modeling,” *CMES - Computer Modeling in Engineering and Sciences*, vol. 60, no. 3, pp. 247–278, 2010.
(Page 39, 39).
- [82] P. Dłotko and R. Specogna, “Cohomology in 3D Magneto-Quasistatics Modeling,” *Communications in Computational Physics*, vol. 14, no. 1, pp. 48–76, 2013.
(Pages 38, 39).
- [83] P. Dłotko and R. Specogna, “Physics inspired algorithms for (co)homology computations of three-dimensional combinatorial manifolds with boundary,” *Computer Physics Communications*, vol. 184, no. 10, pp. 2257–2266, 2013.
(Pages 38, 39).
- [84] W. W. Engelhardt, “Gauge Invariance in Classical Electrodynamics,” *Annales de la Fondation Louis de Broglie*, vol. 30, no. 2, pp. 157–178, 2005.
(Page 50).
- [85] A. Ern and J.-L. Guermond, *Handbook of Numerical Methods for Hyperbolic Problems - Basic and Fundamental Issues*, 1st ed. R. Abgrall and C.-W. Shu (Eds.), Amsterdam, The Netherlands: Elsevier B. V., vol. 17, Ch. 11 - Linear Stabilization for First-Order PDEs, 2016.
(Pages 116, 117).
- [86] A. Ern and J.-L. Guermond, “Analysis of the edge finite element approximation of the Maxwell equations with low regularity solutions,” *Computers and Mathematics with Applications*, vol. 75, no. 3, pp. 918–932, 2018.
(Page 65).
- [87] F. H. Razafindrazaka and K. Poelke and K. Polthier and L. Goubergrits, “A Consistent Discrete 3D Hodge-type Decomposition: implementation and practical evaluation,” arXiv:1911.12173v2, Numerical Analysis, 2019, Accessed: 04.07.2022. [Online]. Available: <https://arxiv.org/pdf/1911.12173.pdf>
(Pages xxi, 42, 43).
- [88] X. Feng, “Absorbing boundary conditions for electromagnetic wave propagation,” *Mathematics of Computation*, vol. 68, no. 225, pp. 145–168, 1999.
(Pages 72, 72, 72, 76).
- [89] D. E. Fernandes, S. I. Maslovski, and M. G. Silveirinha, “Asymmetric Mushroom-Type Metamaterials,” *IEEE Transactions on Microwave Theory and Techniques*, vol. 62, no. 1, pp. 8–17, 2014.
(Page 1).
- [90] L. Fishman, “One-Way Wave Equation Modeling in Two-Way Wave Propagation Problems,” in *Mathematical Modelling of Wave Phenomena 2002, Mathematical Modelling in Physics, Engineering and Cognitive Sciences*, B. Nilsson and L. Fishman, Eds., vol. 7, Växjö University Press, Växjö, Sweden, pp. 91–111, 2004.
(Page 55).
- [91] H. Flanders, *Differential Forms with Applications to the Physical Sciences*. New York, USA: Dover Publications, 2017.
(Pages 12, 22, 22).
- [92] L. P. Franca, G. Hauke, and A. Masud, “Revisiting stabilized finite element methods for the advective–diffusive equation,” *Computer Methods in Applied Mechanics and Engineering*, vol. 195, no. 13, pp. 1560–1572, 2006.
(Page 116).
- [93] T. Frankel, *The Geometry of Physics: An Introduction*, 3rd ed. Cambridge, UK: Cambridge University Press, 2012.
(Pages 12, 20, 22, 26, 39, 40).
- [94] T. P. Fries and H. G. Matthies, “A Review of Petrov-Galerkin Stabilization Approaches and an Extension to Meshfree Methods,” Department of Computer Science, Technical University Braunschweig, vol. 2004-01, pp. 1–71, Braunschweig, Germany, Tech. Rep., 2004, Accessed: 04.07.2022. [Online]. Available: https://publikationsserver.tu-braunschweig.de/receive/dbbs_mods_00001549
(Page 117).

- [95] C. Geuzaine and J.-F. Remacle, “Gmsh: A 3-D finite element mesh generator with built-in pre- and post-processing facilities,” *International Journal for Numerical Methods in Engineering*, vol. 79, no. 11, pp. 1309–1331, 2009.
(Page 68).
- [96] S. Giardino, “Quaternionic Electrodynamics,” *Modern Physics Letters A*, vol. 35, no. 39, pp. 1–17, Art. No. 2050327, 2020.
(Page 9).
- [97] J. Gilbert, C. Moler, and R. Schreiber, “Sparse matrices in MATLAB: Design and implementation,” *SIAM Journal on Matrix Analysis and Applications*, vol. 13, no. 1, pp. 333–356, 1992.
(Page 77).
- [98] A. Gillette, “Notes on Discrete Exterior Calculus,” Texas, USA: University of Texas at Austin, 2009, Accessed: 04.07.2022. [Online]. Available: <https://www.math.arizona.edu/~agillette/research/decNotes.pdf>
(Page 20).
- [99] A. Gillette and C. Bajaj, “Dual Formulations of Mixed Finite Element Methods with Applications,” *Computer-Aided Design*, vol. 10, no. 43, pp. 1213–1221, 2011.
(Page 20).
- [100] F. D. Goes, A. Butts, and M. Desbrun, “Discrete Differential Operators on Polygonal Meshes,” *ACM Transactions on Graphics (TOG)*, vol. 39, no. 4, pp. 110:1–110:14, 2020.
(Page 22).
- [101] G. H. Golub and C. F. V. Loan, *Matrix Computations*, 3rd ed. Baltimore and London: The Johns Hopkins University Press, Johns Hopkins Studies in the Mathematical Sciences, 1996.
(Page 79).
- [102] A. Gonzalez-Lorenzo, M. Juda, A. Bac, J.-L. Mari, and P. Real, “Fast, Simple and Separable Computation of Betti Numbers on Three-dimensional Cubical Complexes,” in *CTIC 2016: 6th International Workshop on Computational Topology in Image Context (2016)*, A. Bac and J.-L. Mari, Eds. Cham, Switzerland: Springer International Publishing, pp. 130–139, 2016.
(Page 41, 41, 41, 41).
- [103] R. D. Graglia, D. R. Wilton, and A. F. Peterson, “Higher Order Interpolatory Vector Bases for Computational Electromagnetics,” *IEEE Transactions on Antennas and Propagation*, vol. 45, no. 3, pp. 329–342, 1997.
(Page 63).
- [104] B. Greene, “String Theory on Calabi-Yau Manifolds,” arXiv:hep-th/9702155v1, High Energy Physics - Theory, 1997, Accessed: 04.07.2022. [Online]. Available: <https://arxiv.org/pdf/hep-th/9702155.pdf>
(Page 12).
- [105] B. Gross and P. J. Atzberger, “Spectral Numerical Exterior Calculus Methods for Differential Equations on Radial Manifolds,” *Journal of Scientific Computing*, vol. 76, no. 1, pp. 145–165, 2018.
(Pages 35, 36).
- [106] P. W. Gross and P. R. Kotiuga, “Data Structures for Geometric and Topological Aspects of Finite Element Algorithms,” *Progress In Electromagnetics Research*, vol. 32, pp. 151–169, 2001.
(Pages 29, 39, 40).
- [107] A. S. Gupta, *Calculus of Variations with Applications*, 12th ed. Delhi, India: PHI Learning Private Limited, 2015.
(Page 116).
- [108] M. Gustafsson, “Wave Splitting in Direct and Inverse Scattering Problems,” Ph.D. dissertation, Lund University, Lund, Sweden, 2000.
(Pages 55, 55, 55, 56, 56).
- [109] E. Haber, U. M. Ascher, D. A. Aruliah, and D. W. Oldenburg, “Fast Simulation of 3D Electromagnetic Problems Using Potentials,” *Journal of Computational Physics*, vol. 163, no. 1, pp. 150–171, 2000.
(Page 49).
- [110] S. Halici, *Models and Theories in Social Systems*, 1st ed. C. Flaut, Š. Hošková-Mayerová, and D. Flaut (Eds.), Cham, Switzerland: Springer Nature Switzerland AG, Studies in Systems, Decision and Control (SSDC, volume 179), Ch. On Bicomplex Fibonacci Numbers and Their Generalization, 2019.
(Page 6).

- [111] P. R. Halmos, *A Hilbert Space Problem Book, Graduate Texts in Mathematics*, 2nd ed. New York, USA: Springer-Verlag New York Inc., Graduate Texts in Mathematics (GTM, volume 19), 1982. (Page 17).
- [112] S. Ham and K.-J. Bathe, “A finite element method enriched for wave propagation problems,” *Computers & Structures*, vol. 94-95, pp. 1–12, 2012. (Page 64).
- [113] W. R. Hamilton, “On Quaternions.” *Proceedings of the Royal Irish Academy*, vol. 3, pp. 1–16, 1847. (Pages 9, 10, 11).
- [114] R. F. Harrington, “Matrix Methods for Field Problems,” *Proceedings of the IEEE*, vol. 55, no. 2, Art. No. 1447363, 1967. (Page 17).
- [115] R. F. Harrington, *Time-Harmonic Electromagnetic Fields*. Piscataway, New Jersey, USA: IEEE-Press, 2001. (Page 13, 13).
- [116] V. Hart and H. Segerman, “The Quaternion Group as a Symmetry Group,” in *Proceedings of Bridges Seoul 2014: Mathematics, Music, Art, Architecture, Culture*, G. Greenfield, G. Hart, and R. Sarhang, Eds., Phoenix, Arizona, USA, pp. 143–150, 2014. (Page 8).
- [117] B. He and F. L. Teixeira, “Geometric Finite Element Discretization of Maxwell Equations in Primal and Dual Spaces,” *Physics Letters A*, vol. 349, no. 1–4, pp. 1–14, 2006. (Pages 20, 30, 37, 37).
- [118] S. He and V. H. Weston, “Determination of the permittivity and conductivity in R^3 using wave splitting of Maxwell’s equations,” *Journal of Mathematical Physics*, vol. 36, no. 4, pp. 1776–1789, 1995. (Page 55).
- [119] S. He and V. H. Weston, “Wave-splitting and absorbing boundary condition for Maxwell’s equations on a curved surface,” *Mathematics and Computers in Simulation (MATCOM)*, vol. 50, no. 5, pp. 435–455, 1999. (Page 55).
- [120] F. W. Hehl and Y. N. Obukhov, *Foundations of Classical Electrodynamics: Charge, Flux, and Metric*, 1st ed. Boston, Massachusetts, USA: Springer Science+Business Media New York, Birkhäuser Boston, Progress in Mathematical Physics (PMP, volume 33), 2003. (Page 22).
- [121] H. Helmholtz, “Über Integrale der hydrodynamischen Gleichungen, welche den Wirbelbewegungen entsprechen.” *Journal für die reine und angewandte Mathematik*, vol. 1858, no. 55, pp. 25–55, 1858. (Page 42).
- [122] R. Herrera, S. Botello, H. Esqueda, and M. Moreles, “A geometric description of Discrete Exterior Calculus for general triangulations,” *Revista Internacional de Métodos Numéricos para Cálculo y Diseño en Ingeniería*, vol. 35, no. 1, pp. 1–12, 2019. (Page 77).
- [123] P. Hillion, “Beware of Maxwell’s Divergence Equations,” *Journal of Computational Physics*, vol. 132, no. 1, pp. 154–155, 1997. (Page 33).
- [124] R. Hiptmair, “Discrete Hodge operators,” *Numerische Mathematik*, vol. 90, pp. 265–289, 2001. (Page 30).
- [125] R. Hiptmair, “Discrete Hodge-Operators: An Algebraic Perspective,” *Progress In Electromagnetics Research (PIER)*, vol. 32, pp. 247–269, 2001. (Page 30).
- [126] R. Hiptmair, “Coupling of Finite Elements and Boundary Elements in Electromagnetic Scattering,” *SIAM Journal on Numerical Analysis*, vol. 41, no. 3, pp. 919–944, 2003. (Page 64).
- [127] A. N. Hirani, “Discrete Exterior Calculus,” Ph.D. dissertation, California Institute of Technology, Pasadena, California, USA, 2003. (Pages 22, 36).

- [128] A. N. Hirani, K. B. Nakshatrala, and J. H. Chaudhry, “Numerical Method for Darcy Flow Derived Using Discrete Exterior Calculus,” *International Journal for Computational Methods in Engineering Science and Mechanics*, vol. 16, no. 3, pp. 151–169, 2015.
(Page 20).
- [129] P.-W. Hsieh and S.-Y. Yang, “A new stabilized linear finite element method for solving reaction-convection-diffusion equations,” *Computer Methods in Applied Mechanics and Engineering*, vol. 307, pp. 362–382, 2016.
(Page 117).
- [130] H.-C. Huang and A. S. Usmani, *Finite Element Analysis for Heat Transfer - Theory and Software*. London, UK: Springer-Verlag London Limited, 1994.
(Page 116).
- [131] H.-L. Huang, X.-L. Wang, P. P. Rohde, Y.-H. Luo, Y.-W. Zhao, C. Liu, L. Li, N.-L. Liu, C.-Y. Lu, and J.-W. Pan, “Demonstration of Topological Data Analysis on a Quantum Processor,” arXiv:1801.06316v2, Quantum Physics, 2019, Accessed: 04.07.2022. [Online]. Available: <https://arxiv.org/pdf/1801.06316.pdf>
(Pages 41, 47).
- [132] Z. Huang, R. Wang, S. Shan, and X. Chen, “Learning Euclidean-to-Riemannian Metric for Point-to-Set Classification,” in *2014 IEEE Conference on Computer Vision and Pattern Recognition (CVPR)*, L. O’Conner, Ed., Columbus, Ohio, USA, pp. 1677–1684, 2014.
(Page 21).
- [133] N. H. Ibragimov and R. N. Ibragimov, “Applications of Lie Group Analysis to Mathematical Modelling in Natural Sciences,” *Mathematical Modelling of Natural Phenomena*, vol. 7, no. 2, pp. 52–65, 2012.
(Page 12).
- [134] N. Ida and J. P. A. Bastos, *Electromagnetics and Calculation of Fields*, 2nd ed. New York, New York, USA: Springer-Verlag New York, Inc., 1997.
(Pages 64, 69).
- [135] F. Ihlenburg and I. Babuška, “Finite Element Solution of the Helmholtz Equation with High Wave Number Part I: The h -version of the FEM,” *Computers & Mathematics with Applications*, vol. 30, no. 9, pp. 9–37, 1995.
(Page 13).
- [136] F. Ihlenburg and I. Babuška, “Finite Element Solution of the Helmholtz Equation with High Wave Number Part II: The h - p -version of the FEM,” *SIAM Journal on Numerical Analysis*, vol. 34, no. 1, pp. 315–358, 1997.
(Page 13).
- [137] G. Iurato, “On the History of Differentiable Manifolds,” *International Mathematical Forum*, vol. 7, no. 10, pp. 477–514, 2012.
(Page 20).
- [138] V. G. Ivancevic and T. T. Ivancevic, “Undergraduate Lecture Notes in De Rham-Hodge Theory,” arXiv:0807.4991v4, Differential Geometry, 2011, Accessed: 04.07.2022. [Online]. Available: <https://arxiv.org/pdf/0807.4991.pdf>
(Page 38).
- [139] J. D. Jackson, *Classical Electrodynamics*, 3rd ed. New York, USA: John Wiley & Sons, Inc., 1999.
(Page 87).
- [140] G. Jeng and A. Wexler, “Self-Adjoint Variational Formulation of Problems Having Non-Self-Adjoint Operators,” *IEEE Transactions on Microwave Theory and Techniques*, vol. 26, no. 2, pp. 91–94, 1978.
(Page 17).
- [141] B.-N. Jiang, J. Wu, and L. A. Povinelli, “The Origin of Spurious Solutions in Computational Electromagnetics,” *Journal of Computational Physics*, vol. 125, no. 1, pp. 104–123, 1996.
(Page 33).
- [142] J.-M. Jin, *The Finite Element Method in Electromagnetics*, 3rd ed. New Jersey, USA: John Wiley & Sons, 2014.
(Pages 17, 61, 63, 64, 64, 68, 73, 110, 110, 111, 111, 111, 111, 113, 114).
- [143] J.-M. Jin, *Theory and Computation of Electromagnetic Fields*, 2nd ed. New Jersey, USA: John Wiley & Sons, 2015.
(Pages 62, 64, 72, 73, 109, 110).

- [144] K. Jänich, *Vector Analysis*. New York, USA: Springer Science+Business Media, LLC, Undergraduate Texts in Mathematics, 2001.
(Pages 20, 21, 22, 39).
- [145] T. Kaczynski, K. Mischaikow, and M. Mrozek, *Computational Homology*, 1st ed. New York, USA: Springer Science+Business Media New York, Applied Mathematical Sciences (AMS, volume 157), 2004.
(Pages 38, 38, 39, 41).
- [146] D. K. Kalluri, *Principles of Electromagnetic Waves and Materials*, 2nd ed. Boca Raton, Florida, USA: CRC Press, Taylor & Francis Group, 2018.
(Page 64).
- [147] L. Kettunen and T. Tarhasaari, “Geometry of Electromagnetism and its Implications in Field and Wave Analysis,” in *9th International Computational Accelerator Physics Conference (ICAP) 2006*, O. Boine-Frankenheim, S. Russenschuck, and F. Schmidt, Eds., Chamonix Mont-Blanc, France, 2006.
(Page 20).
- [148] K. V. Khmelnytskaya, V. V. Kravchenko, and S. M. Torba, “Modulated electromagnetic fields in inhomogeneous media, hyperbolic pseudoanalytic functions, and transmutations,” *Journal of Mathematical Physics*, vol. 57, no. 5, Art. No. 051503, 2016.
(Page 115).
- [149] C. Kißling, “Implementierung des Poynting-Theorems in die Finite-Elemente-Methode,” Master’s thesis, Technische Universität Ilmenau, Ilmenau, Germany, 2018.
(Page 38).
- [150] K. D. Kokkotas, *Encyclopedia of Physical Science and Technology*, 3rd ed. R. A. Meyers (Ed.), New York, New York, USA: Academic Press, Ch. Gravitational Wave Physics, 2003.
(Page 60, 60).
- [151] A. N. Kolmogorov and S. V. Fomin, *Measure, Lebesgue Integrals, and Hilbert Space*. New York, USA: Academic Press Inc., 2nd Printing, 1962.
(Pages 16, 16, 42).
- [152] V. Kovalevsky and H. Schulz, “Convex Hulls in a 3-Dimensional Space,” in *Combinatorial Image Analysis, 10th International Workshop, IWCIA 2004, Lecture Notes in Computer Science (LNCS, vol. 3322)*, R. Klette and J. Žunić, Eds. Auckland, New Zealand: Springer-Verlag Berlin Heidelberg, pp. 176–196, 2005.
(Page 67).
- [153] V. V. Kravchenko, “Quaternionic equation for electromagnetic fields in inhomogeneous media,” in *Progress In Analysis, Proceedings Of The 3rd International ISAAC Congress (In 2 Volumes)*, H. G. W. Begehr, R. P. Gilbert, and M. W. Wong, Eds., vol. 1, Berlin, Germany, pp. 361–366, 2003.
(Pages 19, 115, 115).
- [154] J. Kreeft, A. Palha, and M. Gerritsma, “Mimetic framework on curvilinear quadrilaterals of arbitrary order,” arXiv:1111.4304v1, Numerical Analysis, 2011, Accessed: 04.07.2022. [Online]. Available: <https://arxiv.org/pdf/1111.4304.pdf>
(Page 38).
- [155] L. D. Landau and E. M. Lifshitz, *Electrodynamics of Continuous Media*. Oxford, London, New York, Paris: Pergamon Press Ltd., Course of Theoretical Physics: Volume 8, 1960.
(Page 52).
- [156] G. Landi and A. Zampini, *Linear Algebra and Analytic Geometry for Physical Sciences*. Cham, Switzerland: Springer International Publishing AG, Undergraduate Lecture Notes in Physics, 2018.
(Page 61).
- [157] R. G. Lavoie, L. Marchildon, and D. Rochon, “Finite-Dimensional Bicomplex Hilbert Spaces,” *Advances in Applied Clifford Algebras*, vol. 21, pp. 561–581, 2011.
(Page 19).
- [158] P. Leung, “On Maxwell’s discovery of electromagnetic waves and the gauge condition,” *European Journal of Physics*, vol. 36, no. 2, Art. No. 025002, 2015.
(Page 48).
- [159] I. V. Lindell, *Differential Forms in Electromagnetics*. Hoboken, New Jersey, USA: John Wiley & Sons, IEEE Press Series on Electromagnetic Wave Theory, 2004.
(Page 22).

- [160] W. K. Liu, S. Li, and H. S. Park, “Eighty Years of the Finite Element Method: Birth, Evolution, and Future,” *Archives of Computational Methods in Engineering (2022)*, 2022.
(Page 64).
- [161] G. Livadiotis, “Complex Symmetric Formulation of Maxwell Equations for Fields and Potentials,” *Mathematics*, vol. 6, no. 7, Art. No. 114, 2018.
(Page 6).
- [162] J. D. Logan, *Applied Partial Differential Equations*, 3rd ed. Cham, Switzerland: Springer International Publishing Switzerland, Undergraduate Texts in Mathematics, 2015.
(Page 13).
- [163] L. Lorenz, “XXXVIII. On the Identity of the Vibrations of Light with Electrical Currents,” *The London, Edinburgh, and Dublin Philosophical Magazine and Journal of Science*, vol. 34, no. 230, pp. 287–301, 1867.
(Page 50).
- [164] M. E. Luna-Elizarrarás, M. Shapiro, D. C. Struppa, and A. Vajiac, *Bicomplex Holomorphic Functions - The Algebra, Geometry and Analysis of Bicomplex Numbers*, 1st ed. Cham, Switzerland: Springer International Publishing Switzerland, Frontiers in Mathematics (FM), 2015.
(Pages 6, 6, 14, 19, 52, 66).
- [165] S. Marburg, *Computational Acoustics of Noise Propagation in Fluids - Finite and Boundary Element Methods*, 1st ed. S. Marburg and B. Nolte (Eds.), Germany: Springer-Verlag Berlin Heidelberg, Ch. Discretization Requirements: How many Elements per Wavelength are Necessary?, 2008.
(Page 90).
- [166] MATLAB®, *Software 9.5.0.944444 (R2018b)*. Natick, Massachusetts, USA: The MathWorks Inc., 2018.
(Page 2).
- [167] J. C. Maxwell, *A Treatise on Electricity and Magnetism, Vol. I*, 1st ed. Oxford, UK: Clarendon Press, Clarendon Press Series, 1873.
(Pages 5, 9, 9).
- [168] J. C. Maxwell, *A Treatise on Electricity and Magnetism, Vol. II*, 3rd ed. New York, New York, USA: Dover Publications, Inc., Dover Books on Physics, Reprint Edition, 1954.
(Page 9).
- [169] S. H. Mazharimousavi, A. Roozbeh, and M. Halilsoy, “Electromagnetic wave propagation through inhomogeneous material layers,” *Journal of Electromagnetic Waves and Applications*, vol. 27, no. 16, pp. 2065–2074, 2013.
(Page 16).
- [170] K. T. McDonald, “The Helmholtz Decomposition and the Coulomb Gauge,” Princeton, New Jersey, USA: Joseph Henry Laboratories, Princeton University, 2020, Accessed: 04.07.2022. [Online]. Available: <http://kirkmcd.princeton.edu/examples/helmholtz.pdf>
(Pages 49, 50).
- [171] A. Menti, T. Zacharias, and J. Miliás-Argitis, “Geometric Algebra: A Powerful Tool for Representing Power Under Nonsinusoidal Conditions,” *IEEE Transactions on Circuits and Systems I: Regular Papers*, vol. 54, no. 3, pp. 601–609, 2007.
(Page 13).
- [172] T. Merz, “Geometric Interpretation of the Minkowski Metric,” ETH Zurich, Zurich, Switzerland: Preprints, Art. No. 2018090417, Version 3, 2019, Accessed: 04.07.2022. [Online]. Available: <https://www.preprints.org/manuscript/201809.0417/v3>
(Pages 2, 24, 26).
- [173] P. Monk and Y. Zhang, “Finite element methods for Maxwell’s equations,” in *Contemporary Mathematics: Symposium Celebrating 75 Years of Mathematics of Computation*, S. C. Brenner, I. Shparlinski, C.-W. Shu, and D. B. Szyld, Eds., vol. 754, Providence, Rhode Island, USA, pp. 159–176, 2020.
(Pages 77, 88).
- [174] P. Moon and D. E. Spencer, *Field Theory Handbook - Including Coordinate Systems, Differential Equations and Their Solutions*, 2nd ed. Germany: Springer-Verlag, Berlin, Heidelberg, 1988.
(Page 12).
- [175] A. N. Morozov, V. I. Pustovoi, and I. V. Fomin, “On the gravitational waves coupled with electromagnetic waves,” arXiv:2003.04104v1, General Relativity and Quantum Cosmology, 2020, Accessed: 04.07.2022. [Online]. Available: <https://arxiv.org/pdf/2003.04104.pdf>
(Page 59, 59).

- [176] K. W. Morton, *Topics in Numerical Analysis: Proceedings of the S.E.R.C. Summer School, Lancaster, July 19 - August 21, 1981*, 1st ed. P. R. Turner (Ed.), Germany: Springer-Verlag Berlin Heidelberg, Lecture Notes in Mathematics (LNM, volume 965), Ch. Finite Element Methods for Non-Self-Adjoint Problems, 1982.
(Page 116).
- [177] P. Mullen, P. Memari, F. Goes, and M. Desbrun, "HOT: Hodge-Optimized Triangulations," *ACM Transactions on Graphics (SIGGRAPH)*, vol. 30, no. 4, Art. No. 103, 2011.
(Pages 31, 34).
- [178] C. Müller, *Foundations of the Mathematical Theory of Electromagnetic Waves*. Germany: Springer-Verlag Berlin Heidelberg, Grundlehren der mathematischen Wissenschaften (GL, volume 155), 1969.
(Pages 62, 72).
- [179] Z. Nan, "Application of Helmholtz/Hodge Decomposition to Finite Element Methods for Two-Dimensional Maxwell's Equations," Ph.D. dissertation, Louisiana State University, Baton Rouge, Louisiana, USA, 2013.
(Page 42).
- [180] M. Neilan, "Discrete and conforming smooth de Rham complexes in three dimensions," *Mathematics of Computation*, vol. 84, no. 295, pp. 2059–2081, 2015.
(Page 29).
- [181] W. Neutsch, *Koordinaten - Theorie und Anwendungen*. Heidelberg, Berlin, Oxford: Spektrum Akademischer Verlag, 1995.
(Pages 11, 11, 26, 27, 31).
- [182] L. Nickelson, *Electromagnetic Theory and Plasmonics for Engineers*, 1st ed. L. Nickelson (Ed.), Singapore, Singapore: Springer Singapore, Ch. Rectangular Hollow Metallic Waveguides and Resonators, 2019.
(Page 46).
- [183] M. Oberguggenberger and A. Ostermann, *Analysis for Computer Scientists - Foundations, Methods, and Algorithms*, 2nd ed. Cham, Switzerland: Springer Nature Switzerland AG, Undergraduate Topics in Computer Science, 2018.
(Page 61).
- [184] S. O'Connor, Z. D. Crawford, O. H. Ramachandran, J. Luginsland, and B. Shanker, "Quasi-Helmholtz decomposition, Gauss' laws and charge conservation for finite element particle-in-cell," *Computer Physics Communications*, vol. 276, Art. No. 108345, 2022.
(Pages 42, 45).
- [185] P. J. Olver, *Introduction to Partial Differential Equations*. Cham, Switzerland: Springer International Publishing Switzerland, Undergraduate Texts in Mathematics (UTM), 2nd Printing, 2016.
(Page 13).
- [186] X. P. Orbán and J. Mira, "Dimensional scaffolding of electromagnetism using geometric algebra," *European Journal of Physics*, vol. 42, no. 1, Art. No. 015204, 2020.
(Pages 9, 13).
- [187] M. Ornigotti and A. Aiello, "The Hertz vector revisited: a simple physical picture," *Journal of Optics*, vol. 16, no. 10, Art. No. 105705, 2014.
(Page 48).
- [188] A. Palha, P. P. Rebelo, R. Hiemstra, J. Kreeft, and M. Gerritsma, "Physics-compatible discretization techniques on single and dual grids, with application to the Poisson equation of volume forms," *Journal of Computational Physics*, vol. 257, Part B, pp. 1394–1422, 2014.
(Pages 20, 21, 22, 24, 29, 29, 29, 29, 60, 63).
- [189] G. Pan, J. Tan, and B. K. Gilbert, "Full wave edge element based analysis of 3D metal-dielectric structures for high clock rate digital and microwave applications," *IEE Proceedings - Microwaves, Antennas and Propagation*, vol. 147, no. 5, pp. 391–397, 2000.
(Page 72).
- [190] P. S. Park, "Hodge theory," Cambridge, Massachusetts, USA: Department of Mathematics, Harvard University, 2018, Accessed: 04.07.2022. [Online]. Available: <https://scholar.harvard.edu/files/pspark/files/harvardminorthesis.pdf>
(Page 30).

- [191] J. Parsley, “The Biot-Savart operator and electrodynamics on subdomains of the three-sphere,” *Journal of Mathematical Physics*, vol. 53, no. 1, Art. No. 013102, 2012.
(Page 42, 42, 42).
- [192] M. Pellikka, S. Suuriniemi, L. Kettunen, and C. Geuzaine, “Homology and Cohomology Computation in Finite Element Modeling,” *SIAM Journal on Scientific Computing*, vol. 35, no. 5, pp. 1195–1214, 2013.
(Pages 21, 28, 38, 38).
- [193] G. Pelosi, R. Coccioli, and S. Selleri, *Quick Finite Elements for Electromagnetic Waves*, 2nd ed. Norwood, Massachusetts, USA: Artech House, 2009.
(Page 64, 64).
- [194] P. Petre, “The Weighted Residual Method for Wave Propagation in a One-Dimensional Inhomogeneous Medium,” *Periodica Polytechnica Electrical Engineering (Archives)*, vol. 31, no. 3-4, pp. 85–97, 1987.
(Pages 16, 116).
- [195] S. Pissanetsky, *Sparse Matrix Technology*, 1st ed. New York, USA: Academic Press, 1984.
(Page 77).
- [196] A. C. Polycarpou, *Introduction to the Finite Element Method in Electromagnetics*, 1st ed. Williston, Vermont, USA: Morgan & Claypool Publishers, Synthesis Lectures on Computational Electromagnetics (SLCE), 2006.
(Pages 64, 66).
- [197] D. M. Pozar, *Microwave Engineering*, 4th ed. Hoboken, New Jersey, USA: John Wiley & Sons, 2012.
(Pages 53, 64).
- [198] L. Ptackova, “Discrete Exterior Calculus: History, Theory and Applications,” Instituto Nacional de Matemática Pura e Aplicada, Laboratório VISGRAF, TR-15-06, Rio de Janeiro, Brazil, Tech. Rep., 2015, Accessed: 04.07.2022. [Online]. Available: https://www.visgraf.impa.br/Data/RefBib/PS_PDF/tr-06-2015/tr-06-2015.pdf
(Page 35).
- [199] S. Ramo, J. R. Whinnery, and T. V. Duzer, *Fields and Waves in Communication Electronics*, 3rd ed. Hoboken, New Jersey, USA: John Wiley & Sons, Inc., 1994.
(Page 102).
- [200] Z. Ren, “Application of Differential Forms in the Finite Element Formulation of Electromagnetic Problems,” *International Compumag Society (ICS) Newsletter*, vol. 7, no. 3, Art. No. ICS-00-07-3-Ren, 2000.
(Pages 16, 50).
- [201] T. Reum and H. Toepfer, “Introduction of the Bicomplex Analysis in the Finite Element Method Applied to Electromagnetic Far-Field Calculations,” in *19th International Symposium on Electromagnetic Fields in Mechatronics, Electrical and Electronic Engineering (ISEF)*, Nancy, France, 2019.
(Page 6).
- [202] T. Reum and H. Toepfer, “A bicomplex finite element method for wave propagation in homogeneous media,” *COMPEL - The International Journal for Computation and Mathematics in Electrical and Electronic Engineering*, vol. 39, no. 5, pp. 1031–1039, 2020.
(Pages 6, 11, 18, 18, 34).
- [203] T. Reum and H. Toepfer, “Investigation of Electromagnetic Wave Propagation in the Bicomplex 3D-FEM using a Wavenumber Whitney Hodge Operator,” *COMPEL - The International Journal for Computation and Mathematics in Electrical and Electronic Engineering*, vol. 41, no. 3, pp. 996–1010, 2022.
(Pages 11, 28, 82, 93).
- [204] D. Rochon and S. Tremblay, “Bicomplex Quantum Mechanics: I. The Generalized Schrödinger Equation,” *Advances in Applied Clifford Algebras*, vol. 14, no. 2, pp. 231–248, 2004.
(Page 6).
- [205] D. Rochon and S. Tremblay, “Bicomplex Quantum Mechanics: II. The Hilbert Space,” *Advances in Applied Clifford Algebras*, vol. 16, no. 2, pp. 135–157, 2006.
(Page 6).
- [206] A. Rodríguez, E. Bertolazzi, R. Ghiloni, and A. Valli, “Construction of a Finite Element Basis of the First de Rham Cohomology Group and Numerical Solution of 3D Magnetostatic Problems,” *SIAM Journal on Numerical Analysis*, vol. 51, no. 4, pp. 2380–2402, 2013.
(Page 39).

- [207] P. Roe, *Handbook of Numerical Analysis*. R. Abgrall and C.-W. Shu (Eds.), Amsterdam, The Netherlands: Elsevier Science B.V., Volume 18: Handbook of Numerical Methods for Hyperbolic Problems - Applied and Modern Issues, Ch. 3 - Multidimensional Upwinding, 2017.
(Page 35).
- [208] J. J. Rotman, *An Introduction to Algebraic Topology*. New York, USA: Springer-Verlag New York Inc., Graduate Texts in Mathematics (GTM, volume 119), 4th Printing, 1998.
(Page 38).
- [209] G. Rousseaux, “Galilean Covariance versus Gauge Invariance,” arXiv:0912.2360v1, Classical Physics, 2009, Accessed: 04.07.2022. [Online]. Available: <https://arxiv.org/pdf/0912.2360.pdf>
(Page 50, 50).
- [210] P. Russer, *Applied Computational Electromagnetics: State of the Art and Future Trends*, 1st ed. N. K. Uzunoglu, K. S. Nikita and D. I. Kaklamani (Eds.), Germany: Springer-Verlag Berlin Heidelberg, NATO ASI Subseries F: Computer and Systems Sciences (NATO ASI F, volume 171), Ch. The Transmission Line Matrix Method, 2000.
(Page 61).
- [211] J. Rabinä, “On a Numerical Solution of the Maxwell Equations by Discrete Exterior Calculus,” Ph.D. dissertation, University of Jyväskylä, Jyväskylä, Finland, 2014.
(Page 34).
- [212] M. N. O. Sadiku, *Numerical Techniques in Electromagnetics*, 2nd ed. Boca Raton, Florida, USA: CRC Press LLC, 2001.
(Page 64).
- [213] S. J. Sangwine, “Fundamental Representations and Algebraic Properties of Biquaternions or Complexified Quaternions,” *Advances in Applied Clifford Algebras*, vol. 21, no. 3, pp. 607–636, 2011.
(Page 35).
- [214] P. Saveliev, *Topology Illustrated*. Huntington, West Virginia, USA: Peter Saveliev, Department of Mathematics, Marshall University, 2016.
(Pages 16, 20, 38, 39, 40, 41, 41, 41, 110).
- [215] P. O. J. Scherer, *Computational Physics - Simulation of Classical and Quantum Systems*, 3rd ed. Cham, Switzerland: Springer International Publishing AG, Graduate Texts in Physics, 2017.
(Page 61).
- [216] E. Scholz, *History of Topology*, 1st ed. I. M. James (Ed.), Amsterdam, The Netherlands: Elsevier Science B.V., Ch. 2 - The Concept of Manifold, 1850-1950, 1999.
(Page 20).
- [217] S. Schoos and O. Schwanitz, “3D Electromagnetic Frequency Domain Simulation of a Filter Choke with a Multilayer Foil Winding,” in *Project: Electromagnetic CAD, Summer Term 2015*. Berlin, Germany: Chair Theoretische Elektrotechnik, Technische Universität Berlin, 2015.
(Pages 1, 64).
- [218] H. Schopper, *Particle Physics Reference Library, Volume 1: Theory and Experiments*, 1st ed. Cham, Switzerland: Springer Nature Switzerland AG, 2020.
(Page 48, 48).
- [219] S. H. Schot, “Eighty years of Sommerfeld’s radiation condition,” *Historia Mathematica*, vol. 19, no. 4, pp. 385–401, 1992.
(Page 58).
- [220] J. Schwichtenberg, *Physics from Symmetry*, 2nd ed. Cham, Switzerland: Springer International Publishing AG, Undergraduate Lecture Notes in Physics, 2018.
(Page 12, 12, 12).
- [221] A. Seagar, *Application of Geometric Algebra to Electromagnetic Scattering – the Clifford-Cauchy-Dirac Technique*, 1st ed. Singapore, Singapore: Springer Science+Business Media Singapore, 2016.
(Page 6).
- [222] C. Segre, “Le rappresentazioni reali delle forme complesse e gli enti iperalgebrici,” *Mathematische Annalen*, vol. 40, pp. 413–467, Leipzig, Germany, 1892.
(Pages 1, 9).

- [223] A. Shadowitz, *The Electromagnetic Field*. New York, USA: Dover Publications Inc., Dover Books on Physics, Reprint Edition, 1988.
(Page 64).
- [224] R. Sharipov, *Quick Introduction to Tensor Analysis*. Golden, Colorado, USA: Samizdat Press, Colorado School of Mines, 2004.
(Page 9, 9).
- [225] C. S. Sharma, “Complex structure on a real Hilbert space and symplectic structure on a complex Hilbert space,” *Journal of Mathematical Physics*, vol. 29, no. 5, pp. 1069–1078, 1988.
(Page 19).
- [226] L. Silberstein, “Elektromagnetische Grundgleichungen in bivectorieller Behandlung,” *Annalen der Physik*, vol. 327, pp. 579–586, 1907.
(Page 13).
- [227] L. Silberstein, “Nachtrag zur Abhandlung über ‘Elektromagnetische Grundgleichungen in bivectorieller Behandlung’,” *Annalen der Physik*, vol. 329, pp. 783–784, 1907.
(Page 13).
- [228] T. Sochi, “Tensor Calculus,” arXiv:1610.04347v1, History and Overview, 2016, Accessed: 04.07.2022. [Online]. Available: <https://arxiv.org/pdf/1610.04347.pdf>
(Pages 26, 26, 27, 27, 36, 60, 60, 68, 69).
- [229] A. Sommerfeld, “Die Greensche Funktion der Schwingungsgleichung,” *Jahresbericht der Deutschen Mathematiker-Vereinigung*, vol. 21, pp. 309–352, 1912.
(Pages 58, 59).
- [230] M. Spiegel and S. Lipschutz, *Vector Analysis and an Introduction to Tensor Analysis*, 2nd ed. New York, USA: The McGraw-Hill Companies, Inc., Schaum’s Outline Series, 2009.
(Pages 24, 24, 26, 26).
- [231] B. A. Stickler and E. Schachinger, *Basic Concepts in Computational Physics*, 2nd ed. Cham, Switzerland: Springer International Publishing Switzerland, 2016.
(Page 61).
- [232] A. Styahar, “Absorbing Boundary Conditions for Maxwell’s Equations,” Le Chesnay, Département Yvelines, France: Institut National de Recherche en Informatique et en Automatique (INRIA), 2009, Accessed: 04.07.2022. [Online]. Available: <http://www.mathmods.eu/resources/downloads/uns/finish/24-uns/94-styahar-report>
(Page 55, 55).
- [233] G. P. H. Styan, “Hadamard Products and Multivariate Statistical Analysis,” *Linear Algebra and its Applications*, vol. 6, pp. 217–240, 1973.
(Page 52).
- [234] D. Sun, J. Manges, X. Yuan, and Z. Cendes, “Spurious Modes in Finite-Element Methods,” *IEEE Antennas and Propagation Magazine*, vol. 37, no. 5, pp. 12–24, 1995.
(Page 34, 34).
- [235] W. Sun and C. A. Balanis, “Vector One-Way Wave Absorbing Boundary Conditions for FEM Applications,” *IEEE Transactions on Antennas and Propagation*, vol. 42, no. 6, pp. 872–878, 1994.
(Page 76).
- [236] P. G. Tait, *An Elementary Treatise on Quaternions*. Oxford, UK: Clarendon Press, Clarendon Press Series, 1867.
(Page 11).
- [237] M. Tanışli, M. E. Kansu, and D. Süleyman, “Reformulation of electromagnetic and gravito-electromagnetic equations for Lorentz system with octonion algebra,” *General Relativity and Gravitation*, vol. 46, no. 5, Art. No. 1739, 2014.
(Page 59).
- [238] J. Tao, J. Atechian, R. Ratovondrahanta, and H. Baudrand, “Transverse operator study of a large class of multidielectric waveguides,” *IEE Proceedings H - Microwaves, Antennas and Propagation*, vol. 137, no. 5, pp. 311–317, 1990.
(Page 116).

- [239] T. Tao, *The Princeton Companion to Mathematics*. T. Gowers, J. Barrow-Green, and I. Leader (Eds.), Princeton, New Jersey, USA: Princeton University Press, Ch. III.16 Differential Forms and Integration, 2008.
(Page 28).
- [240] F. L. Teixeira, “Geometric Aspects of the Simplicial Discretization of Maxwell’s Equations,” *Progress In Electromagnetics Research (PIER)*, vol. 32, pp. 171–188, 2001.
(Page 20).
- [241] F. L. Teixeira and W. C. Chew, “Lattice electromagnetic theory from a topological viewpoint,” *Journal of Mathematical Physics*, vol. 40, no. 1, pp. 169–187, 1999.
(Pages 20, 20, 20, 23, 62).
- [242] T. Tezduyar and S. Sathe, “Stabilization Parameters in SUPG and PSPG Formulations,” *Journal of Computational and Applied Mechanics*, vol. 4, no. 1, pp. 71–88, 2003.
(Page 117).
- [243] W. Thirring, *Lehrbuch der Mathematischen Physik, Band 2: Klassische Feldtheorie*, 2nd ed. Wien, Austria: Springer-Verlag, 1990.
(Page 16).
- [244] E. Tonti, “On the Geometrical Structure of Electromagnetism,” in *Gravitation, electromagnetism and geometrical structures*, G. Ferrarese, Ed. Bologna, Italy: Pitagora Editrice, pp. 281–308, 1995.
(Page 20).
- [245] E. Tonti, “Finite Formulation of the Electromagnetic Field,” *Progress In Electromagnetics Research (PIER)*, vol. 32, pp. 1–44, 2001.
(Page 20).
- [246] E. Tonti, *The Mathematical Structure of Classical and Relativistic Physics: A General Classification Diagram*, 1st ed. New York, USA: Springer Science+Business Media New York, Birkhäuser New York, Modeling and Simulation in Science, Engineering and Technology (MSSET), 2013.
(Page 23).
- [247] J. Toriwaki and T. Yonekura, “Euler Number and Connectivity Indexes of a Three Dimensional Digital Picture,” *Forma*, vol. 17, pp. 183–209, 2002.
(Page 41, 41).
- [248] O. Tsilipakos, E. E. Kriezis, and T. V. Yioultis, “Boundary condition for the efficient excitation and absorption of hybrid waveguide modes in finite element formulations,” *Microwave and Optical Technology Letters*, vol. 53, no. 11, pp. 2626–2631, 2011.
(Page 72).
- [249] F. T. Ulaby and U. Ravaioli, *Fundamentals of Applied Electromagnetics*, 7th ed. Upper Saddle River, New Jersey, USA: Pearson Education, Inc., 2015.
(Page 64).
- [250] A. v. Weiss, *Die elektromagnetischen Felder: Einführung in die Feldtheorie und ihre Anwendung*, 1st ed. Braunschweig and Wiesbaden, Germany: Friedrich Vieweg & Sohn, Nachrichtentechnik (XNT, volume 1), 1983.
(Pages xxiii, 54, 54, 56, 74, 74, 89, 97).
- [251] U. van Rienen, *Numerical Methods in Computational Electrodynamics - Linear Systems in Practical Applications*. Germany: Springer-Verlag Berlin Heidelberg, Lecture Notes in Computational Science and Engineering (LNCSE, volume 12), 2001.
(Pages 50, 62).
- [252] J. Vince, *Geometric Algebra: An Algebraic System for Computer Games and Animation*, 1st ed. London, UK: Springer-Verlag London Limited, 2009.
(Pages 9, 9, 13, 31, 34).
- [253] A. I. Vistnes, *Physics of Oscillations and Waves - With use of Matlab and Python*. Cham, Switzerland: Springer Nature Switzerland AG, Undergraduate Texts in Physics, 2018.
(Page 13).
- [254] B. Walker, “Using Persistent Homology to Recover Spatial Information from Encounter Traces,” in *Proceedings of the 9th ACM International Symposium on Mobile Ad Hoc Networking and Computing*, Hong Kong, China, pp. 371–380, 2008.
(Page 40).

- [255] K. F. Warnick, *Teaching Electromagnetics: Innovative Approaches and Pedagogical Strategies*, 1st ed. K. T. Selvan and K. F. Warnick (Eds.), Boca Raton, Florida, USA: CRC Press, Taylor & Francis Group, Ch. 7 Teaching Electromagnetic Field Theory Using Differential Forms, 2021. (Page 20, 20).
- [256] K. F. Warnick and P. Russer, “Differential Forms and Electromagnetic Field Theory,” *Progress in Electromagnetics Research*, vol. 148, pp. 83–112, 2014. (Pages 24, 31, 48, 51).
- [257] J. P. Webb, “Hierarchical Vector Basis Functions of Arbitrary Order for Triangular and Tetrahedral Finite Elements,” *IEEE Transactions on Antennas and Propagation*, vol. 47, no. 8, pp. 1244–1253, 1999. (Page 63).
- [258] T. Weinberg, “Fast Implementation of mixed RT0 finite elements in MATLAB,” *Society for Industrial and Applied Mathematics (SIAM) Undergraduate Research Online*, vol. 12, pp. 246–256, 2019. (Page 69).
- [259] V. H. Weston, “Time-domain wave splitting of Maxwell’s equations,” *Journal of Mathematical Physics*, vol. 34, no. 4, pp. 1370–1392, 1993. (Page 55, 55).
- [260] N. Wheeler, “Electrodynamical applications of the exterior calculus,” Portland, Oregon, USA: Physics Department, Reed College: Electrodynamics, Miscellaneous Essays, Exterior E&M, 1996, Accessed: 04.07.2022. [Online]. Available: <https://www.reed.edu/physics/faculty/wheeler/documents/index.html> (Pages 20, 50).
- [261] M. Wollitzer and T. Reum, “Coupling and Decoupling Device Between a Circuit Carrier and a Waveguide,” International Patent WO/2019/091 846, 2019, Accessed: 04.07.2022. [Online]. Available: <https://patentscope.wipo.int/search/en/detail.jsf?docId=WO2019091846> (Page 82).
- [262] I. Woyna, “Wideband Impedance Boundary Conditions for FE/DG Methods for Solving Maxwell Equations in Time Domain,” Ph.D. dissertation, Technische Universität Darmstadt, Darmstadt, Germany, 2014. (Pages 55, 72, 73, 77, 77, 88).
- [263] K.-H. Yang and K. T. McDonald, “Formal Expressions for the Electromagnetic Potentials in Any Gauge,” Princeton, New Jersey, USA: Joseph Henry Laboratories, Princeton University, 2019, Accessed: 04.07.2022. [Online]. Available: <https://puhep1.princeton.edu/~mcdonald/examples/gauge.pdf> (Page 50, 50).
- [264] Z. Yun and M. F. Iskander, “Ray Tracing for Radio Propagation Modeling: Principles and Applications,” *IEEE Access*, vol. 3, pp. 1089–1100, 2015. (Page 61).
- [265] J. A. W. Zenneck, *Wireless Telegraphy*, 1st ed. New York, USA: McGraw-Hill Book Company, Inc., 1915. (Page 15).
- [266] K. Zhang and D. Li, *Electromagnetic Theory for Microwaves and Optoelectronics*, 2nd ed. K. Zhang and D. Li (Eds.), Germany: Springer-Verlag Berlin Heidelberg, Ch. Metallic Waveguides and Resonant Cavities, 2008. (Page 102).
- [267] O. C. Zienkiewicz, “Achievements and some unsolved problems of the finite element method,” *International Journal for Numerical Methods in Engineering*, vol. 47, no. 1-3, pp. 9–28, 2000. (Page 90).
- [268] O. C. Zienkiewicz and R. L. Taylor, *The Finite Element Method - Volume 1: The Basis*, 5th ed. Woburn, Massachusetts, USA: Butterworth-Heinemann, 2000. (Page 64).
- [269] M. Ziółkowski, *Modern Methods for Selected Electromagnetic Field Problems*. Szczecin, Poland: West Pomeranian University of Technology, 2015. (Pages 33, 69, 70).
- [270] R. Zurmühl, *Matrizen und ihre technischen Anwendungen*, 4th ed. Germany: Springer-Verlag Berlin, Göttingen, Heidelberg, 1964. (Page 66).